PhD thesis

Institute of Physical Chemistry
Polish Academy of Sciences
Kasprzaka 44/52
01-224 Warszawa, Poland

Dioxygen electroreduction on enzyme modified carbon ceramic electrodes

Wojciech Nogala

PhD thesis

This dissertation was prepared within the International Ph.D. in Chemistry Studies at Institute of Physical Chemistry of the Polish Academy of Sciences

Supervisor: Prof. dr hab. Marcin Opallo

Department of Electrode Processes

Warszawa, July 2010

Acknowledgements

First and foremost, I would like to thank my supervisor Prof. Dr. Marcin Opallo for his indispensable guidance, substantial support, patience and for motivate me to complete this thesis.

I would like to thank Prof. Dr. Gunther Wittstock for his invaluable guidance during five months research work in his laboratory at Oldenburg University in Germany.

I would like to thank Prof. Dr. Jerzy Rogalski from Maria Curie-Sklodowska University in Lublin for isolation and purification of laccase.

I would like to thank Dr. Frank Marken for his guidance during one month research work in his laboratory at University of Bath in UK.

I would like to thank all my former and current colleagues in the Opallo Group for help and friendliness, especially Anna Celebanska and Katarzyna Szot for their active cooperation. I am very grateful to Dr. Ewa Rozniecka, Dr. Galyna Shul, Dr. Joanna Niedziolka-Jönsson, Dr. Izabela Brand and Monika Saczek-Maj for introducing me to the work in laboratory. I would like to acknowledge Prof. Dr. Piotr Zoltowski, Dr. Martin Jönsson-Niedziolka, Adam Lesniewski and Wojciech Adamiak for constructive scientific discussions. I am very grateful to Dr. Robert Lynch for correcting the manuscript.

I would also like to thank: Dr. Malte Burchardt and Dr. Carolina Nunes-Kirchner from Oldenburg University for introducing me to SECM and AFM, Dr. Grazyna Zukowska from Warsaw University of Technology for Raman spectra of electrodes, Dr. Yuriy Stepanenko and Bartlomiej Bialkowski from Institute of Physical Chemistry PAS for their help with the laser-assisted sample preparation, Adam Presz from Institute of High Pressure Physics PAS for SEM micrographs of electrodes.

I would like to thank all my friends from Warsaw for interesting scientific and widespread discussions throughout my PhD studies.

I would like to thank my daughter Olimpia and wife Malgorzata for their understanding, patience and emotional support during my long-lasting stay far from home. I am very grateful to my parents for their support for my school career.

Especially, I would like to acknowledge financial support from:

Institute of Physical Chemistry, Polish Academy of Sciences

Polish Ministry of Science and Higher Education grants: N N204 161936 and PBZ KBN-098/T09/2003

European Union within the European Regional Development Fund, through grant Innovative Economy (POIG.01.01.02-00-008/08)

Exchange programme of the German Academic Exchange Service (DAAD 323-bis PPP Polen)

Donation of bilirubin oxidase from Amano Enzyme Europe Ltd.

For chemists and physicists

Especially for electrochemists

Abstract

Modification of carbon ceramic electrodes with enzymes catalyzing dioxygen reduction – laccase or bilirubin oxidase – is reported. Laccase is immobilized within sol–gel processed hydrophilic silicate film on electrodes surfaces with immobilized mediators – 2,2'-azino-bis(3-ethylbenzothiazoline-6-sulfonate) or 3,5-dimethoxy-4-hydroxybenzaldehydrazine (syringaldazine). These electrodes exhibit mediated bioelectrocatalytic reduction of dioxygen. Electrodes with adsorbed bilirubin oxidase exhibit efficient mediatorless bioelectrocatalysis of dioxygen electroreduction. The efficiency of electrocatalysis and permeability for gaseous dioxygen are increased for electrodes enriched with hydrophilic carbon nanoparticles. Presented electrodes are examined as biocathodes in zinc-dioxygen cells. Current-voltage characteristics of these cells are determined using chronopotentiometry.

Bioelectrocatalytic process is studied by scanning electrochemical microscopy. Special attention is paid to the possible leaching of mediator and the effect of the electrode potential on the formation of reaction products. New variant of the scanning electrochemical microscopy feedback mode measurements of enzymatic dioxygen reduction is proposed. This mode is applied to study the distribution of laccase within sol–gel processed silicate films and for the comparison of laccase and bilirubin oxidase activity. Special attention is paid to increased activity at the edge of the film. Scanning electrochemical microscopy is also used for imaging of lateral distribution of the electrical conductivity and dioxygen permeability of the carbon ceramic electrode enriched with carbon nanoparticles.

Streszczenie

W pracy tej została przedstawiona modyfikacja ceramicznych elektrod węglowych enzymami katalizującymi redukcję ditlenu – lakazą lub oksydazą bilirubiny. Lakaza została unieruchomiona w cienkiej warstwie hydrofilowego polikrzemianu otrzymanego w procesie zol-żel. Warstwa ta została osadzona na powierzchni elektrod modyfikowanymi mediatorami: 2,2'-azino-bis(3-etylobenzotiazolino-6-sulfonianem) lub 3,5-dimetoksy-4-hydroksybenzaldehydrazyną (syryngaldazyną). Elektrody te wykazują mediatorową bioelektrokatalityczną redukcję ditlenu. Natomiast elektrody z zaadsorbowaną oksydazą bilirubiny wykazują bezmediatorową bioelektrokatalizę redukcji ditlenu. Efektywność procesu elektrokatalitycznego oraz przepuszczalność gazowego ditlenu są większe dla elektrod wzbogaconych hydrofilowymi nanocząstkami węgla. Zaprezentowane elektrody zostały wykorzystane jako biokatody w ogniwach cynkowo-ditlenowych, których charakterystyki prądowo-napięciowe zostały wyznaczone za pomocą chronopotencjometrii.

Proces bioelektrokatalityczny został także zbadany za pomocą skaningowej mikroskopii elektrochemicznej. Szczególną uwagę poświęcono wymywaniu mediatora oraz wpływowi potencjału elektrody na rodzaj powstałych produktów reakcji elektrodowej. Został również zaproponowany nowy sposób pomiarów za pomocą skaningowej mikroskopii elektrochemicznej, co umożliwiło zbadanie równomierności rozporoszenia lakazy unieruchomionej w cienkiej warstwie hydrofilowego polikrzemianu oraz porównanie aktywności lakazy z akytwnością oksydazy bilirubiny. Szczególną uwagę zwrócono na wyjaśnienie zwiększonej aktywności krawędzi warstwy. Skaningowa mikroskopia elektrochemiczna została również zastosowana do zobrazowania powierzchniowego zróżnicowania przewodności elektronowej oraz przepuszczalności ditlenowej ceramicznych elektrod węglowych wzbogaconych nanocząstkami węgla.

Abbreviations

Abbreviation	Meaning
AA	ascorbic acid
ABTS	2,2′-azino-bis(3-ethylbenzthiazoline-6-sulfonate)
ABTS-CCE	carbon ceramic electrode modified with ABTS
ABTS-CCE/Lc	carbon ceramic electrode modified with ABTS and laccase
AD/DA	analog-to-digital/digital-to-analog signal converter
AFM	atomic force microscopy
BDD	boron doped diamond
BOx	bilirubin oxidase
CCE	carbon ceramic electrode
CCE/BOx	carbon ceramic electrode modified with bilirubin oxidase
CCE-CNP	carbon nanoparticles doped carbon ceramic electrode
CCE-CNP/BOx	CCE-CNP modified with bilirubin oxidase
CCE-CNP10	carbon ceramic electrode doped with 10 % of carbon nanoparticles
CCE-CNP10/BOx	CCE-CNP10 modified with bilirubin oxidase
CCE-CNP20	carbon ceramic electrode doped with 20 % of carbon nanoparticles
CCE-CNP20/BOx	CCE-CNP20 modified with bilirubin oxidase
CCG	chemically converted graphene
CCGE	carbon ceramic gas electrode
CDH	cellobiose dehydrogenase
CE	counter electrode (auxiliary electrode)
CNT	carbon nanotube
CPE	carbon paste electrode
CueO	copper efflux oxidase
CV	cyclic voltammetry or cyclic voltammogram
DA	dopamine
DET	direct electron transfer
DPV	differential pulse voltammetry
EPR	electron paramagnetic resonance
FAD	flavin adenine dinucleotide
FB	feedback
GC	glassy carbon
HQS	8-hydroxyquinoline-5-sulfonic acid

Abbreviation	Meaning
IR	ohmic drop
Lc	laccase
MET	mediated electron transfer
MTMOS	methyltrimethoxysilane
MWCNT	multiwalled carbon nanotube
NA	numerical aperture
NADH	nicotinamide adenine dinucleotide
NHE	normal hydrogen electrode = SHE
NP	nanoparticle
OCP	open circuit potential
OCV	open circuit voltage
ORR	oxygen reduction reaction
PEFC	polymer electrolyte fuel cell
PQQ	pyrroloquinoline quinone
PS	polystyrene
PTFE	polytetrafluoroethylene
RDE	rotating disc electrode
RRDE	rotating ring-disc electrode
SAM	self assembled monolayer
SEM	scanning electron microscopy/microscope
SFM	scanning force microscopy/microscope
SG/TC	substrate generation/tip collection
SHE	standard hydrogen electrode = NHE
SNOM	scanning near field optical microscopy
SPM	scanning probe microscopy
STM	scanning tunneling microscopy/microscope
Syr	3,5-dimethoxy-4-hydroxybenzaldehydazine (syringaldazine)
Syr-CCE	carbon ceramic electrode modified with syringaldazine
Syr-CCE/Lc	carbon ceramic electrode modified with syringaldazine and laccase
TG/SC	tip generation/substrate collection
TMOS	tetramethoxysilane
TMOS-gel	tetramethoxysilane based gel
UA	uric acid
WE	working electrode
YSZ	yttria-stabilized zirconia

Table of content

1 Introduction

Electricity is an intrinsic element of everyday live of people in developed countries. The variety of electrical devices and energy consumption are continuously growing since the "Industrial Revolution". Most of the most usable form of energy – electricity – is produced by conversion of chemical energy stored in fuels. This can be carried out by a three step process: conversion into heat in combustion, conversion of heat into mechanical energy using turbines and eventually production of electricity in generators. The efficiency of the overall process is a product of the efficiency of each step. It is always lower than that of individual steps because these parameters are always below unity. This problem can be circumvented by direct conversion of chemical energy into electricity as is fulfilled in fuel cells [1, 2] or biofuel cells. The latter employ enzymes as catalysts (Chapter 5) and can operate at mild conditions (neutral pH) where noble metals are inefficient. Apart from fuel, these devices require continuous supply of oxidant (Fig. 1.1). Usually oxygen* is utilized for this purpose, because of its ubiquity.

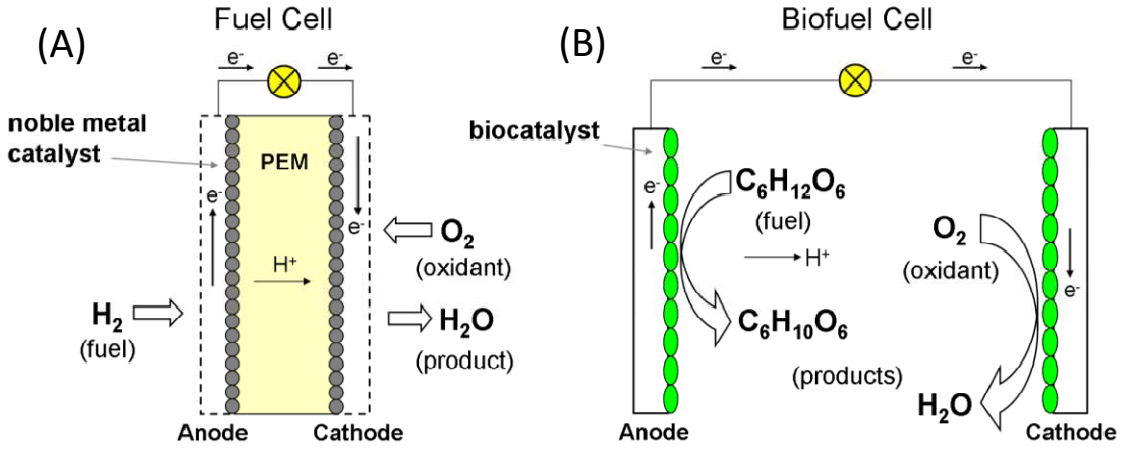

Fig. 1.1. Schematic presentation of conventional PEM fuel cell (A) and enzymatic biofuel cell (B) [3].

Biofuel cells can utilize glucose and oxygen dissolved in the body fluids of mammals as fuel and oxidant, respectively [4]. Thus, perspective biofuel cells could serve as power source for implanted devices such as: microvalves, drugs dispensers, pacemakers, sensors etc. For this reason development of electrodes for oxygen reduction modified with enzymes is an important task.

For this thesis, a carbon ceramic electrode (CCE) consisting of dispersed carbon-based material embedded in a silicate matrix is employed as a support for enzymes immobilization.

*For convenience the term "oxygen" instead of "dioxygen" is used in this thesis.

This electrode was developed in the early 1990's [5, 6] and is robust and easy to prepare. The hybrid material of the electrode is produced by a sol-gel process. The most typical example of CCE, prepared for the use in aqueous electrolyte is obtained by sol-gel processing of methyltrimethoxysilane mixed with carbon microparticles. Methyl groups attached to the silicate network render the pores of the material hydrophobic. Consequently the electrode body is not flooded when immersed into an aqueous solution. Moreover, the porous electrode material can be penetrated by oxygen.

Two enzymes used for modification of CCEs – laccase (Lc) and bilirubin oxidase (BOx) – that belong to the family of copper oxidoreductases. They are produced by plants, fungi, some bacteria and insects. When these enzymes are immobilized on the electrode surface and an efficient electron transfer path between the protein and the electrode is provided, the electrocatalytic process of oxygen reduction occurs at significantly higher potentials than at noble metal electrodes. This makes such electrodes attractive as cathodes for biofuel cells.

2 Electrochemical oxygen reduction

Electrochemical oxygen reduction reaction (ORR) is involved in metal-air batteries [7], fuel cells [1, 2], and electrochemical oxygen sensors [8]. In fuel cells this reaction occurs on the cathode parallel with fuel oxidation on the anode and electrons are flowing in external circuit. The power and efficiency of fuel cell is limited by the slowest process which in most cases is ORR [1, 2]. Not surprisingly, there is a current interest in improvement of oxygen cathodes. Such a work is mainly oriented towards the development of new catalysts, because of high cost of Pt considered for a long time as the best catalyst [9, 10]. Recently ORR composite catalysts more efficient than Pt were developed [9, 11]. However, their use is limited to extreme pH values. For neutral pH biocatalysts are more effective [12] than noble metals despite their lower stability.

2.1 Thermodynamics of oxygen reduction

Although ORR is chemically reversible it is strongly thermodynamically irreversible (non-Nerstian). This means that efficient reaction occurs at high overpotential. Similarly, the reverse reaction – oxygen evolution is also thermodynamically irreversible.

The products of ORR are dependent on the type of electrolyte. In molten carbonate fuel cell [13] CO_3^{2-} is produced in the presence of CO_2:

$$½\ O_2 + CO_2 + 2e^- \rightarrow CO_3^{2-} \qquad (2.1)$$

In solid oxide fuel cells [14] O_2 is reduced directly to O^{2-}:

$$½\ O_2 + 2e^- \rightarrow O^{2-} \qquad (2.2)$$

In aqueous electrolytes ORR pathways and products are pH-dependent. In acidic solutions O_2 can be reduced to H_2O (Eq. 2.3) whereas in alkaline media OH^- is a final product (Eq. 2.4).

$$O_2 + 4H^+ + 4e^- \rightarrow 2\ H_2O, \qquad (E^0)_{298} = 1.229\ V \qquad (2.3)$$

$$O_2 + 2H_2O + 4\ e^- \rightarrow 4OH^- \qquad (E^0)_{298} = 0.401\ V \qquad (2.4)$$

At neutral pH the ORR mechanism is described by equation (2.4).

Despite known standard potentials of reactions (2.3) and (2.4) arrows indicate thermodynamic irreversibility. One can calculate these potentials from thermodynamic data [10] or estimate by extrapolation of cathodic and anodic Tafel plots obtained from the polarization curves. Open-circuit potential (OCP) of noble metal electrode immersed into acid solution pH 0 with supplied oxygen under 1 atm partial pressure is always lower than reversible standard potential (E^0) – usually ca. 1 V. Nevertheless some researchers reported OCP of such electrode close to 1.23 V [15-18], but these results are considered as difficult to reproduce. In order to obtain efficient ORR, potential applied to electrode must be much lower than E^0.

The mechanism of reaction (2.3) applies also to cathode in polymer electrolyte fuel cells (PEFC) [19] with water-containing Nafion membrane as electrolyte and reaction (2.4) in alkaline fuel cells [20]. The mechanism of ORR in PEFC is similar to that in acidic aqueous solution, because of high proton concentration in polymer. Because of this similarity and simpler experimental setup, the research concerning cathode catalysts for PEFC are usually done in aqueous solutions [9].

As it was shown above, ORR is not simple one-step electrode process, where electroactive species just exchange electrons with electrode surface:

$$\mathrm{Ox} + \mathrm{ne}^- \rightleftarrows \mathrm{Red}^{\mathrm{n}-} \qquad (2.5)$$

It is strongly improbable that five species (O_2 molecule and four protons) will collide simultaneously with electrode surface at the same place to exchange electrons. Therefore the reaction (2.3) must involve intermediate steps [21]. Since diverse oxygen species may exist in aqueous solutions (Table 2.1), different intermediate electrode reactions are proposed. Their standard potentials E^0 can be calculated from standard Gibbs free energies ΔG^0 using Hess law [22] and following equation:

$$\Delta G^0_{\mathrm{r}} = -nFE^0 \qquad (2.6)$$

where ΔG^0_{r} is reaction Gibbs free energy change, n – number of electrons involved in reaction, F – Faraday constant (96485 C mol^{-1}), and E^0 – standard reaction potential versus standard hydrogen electrode (SHE).

Table 2.1. Selected thermodynamic data of oxygen species at 25 ℃ [10].

Formula	Standard state	ΔG^0 / kJ mol^{-1}	ΔH^0 / kJ mol^{-1}	S^0 / kJ mol^{-1} K^{-1}
O_2	Gas, 1 atm	0	0	205.3
H_2O	Pure liquid	-273.18	-285.83	69.91
OH^-	1 M, aq	-157.29	-230	-10.75
H_2O_2	1 M, aq	-134.1	-191.2	143.9
HO_2^-	1 M, aq	-67.36	-160.3	23.8
O_2^-	1 M, aq	27.4	-	-
HO_2	1 M, aq	5.09	-	-
OH	Gas, 1 atm	34.23	38.95	183.6

Table 2.2. Standard potentials of selected oxygen reactions [10].

Formula	E^0 / V *vs.* SHE
$O_2 + 4H^+ + 4e^- \rightarrow 2H_2O$	1.229
$O_2 + 2H_2O + 4e^- \rightarrow 4OH^-$	0.401
$O_2 + 2H^+ + 2e^- \rightarrow H_2O_2$	0.695
$O_2 + 2H_2O + 2e^- \rightarrow H_2O_2 + 2OH^-$	-0.133
$O_2 + H_2O + 2e^- \rightarrow HO_2^- + OH^-$	-0.065
$H_2O_2 + 2H^+ + 2e^- \rightarrow 2H_2O$	1.763
$H_2O_2 + 2e^- \rightarrow 2OH^-$	0.935
$HO_2^- + H_2O + 2e^- \rightarrow 3OH^-$	0.867
$O_2 + e^- \rightarrow O_2^-$	-0.284
$O_2 + H^+ + e^- \rightarrow HO_2$	-0.053
$HO_2 + e^- \rightarrow HO_2^-$	0.751
$HO_2 + H^+ + e^- \rightarrow H_2O_2$	1.443
$O_2^- + H_2O + e^- \rightarrow HO_2^- + OH^-$	0.155
$O_2^- + 2H_2O + 3e^- \rightarrow 4OH^-$	0.629
$HO_2 + 3H^+ + 3e^- \rightarrow 2H_2O$	1.656

The possible ORR paths in aqueous acidic and alkaline solutions with Gibbs free energies of intermediate species and standard reduction potentials are presented in Figure 2.2.

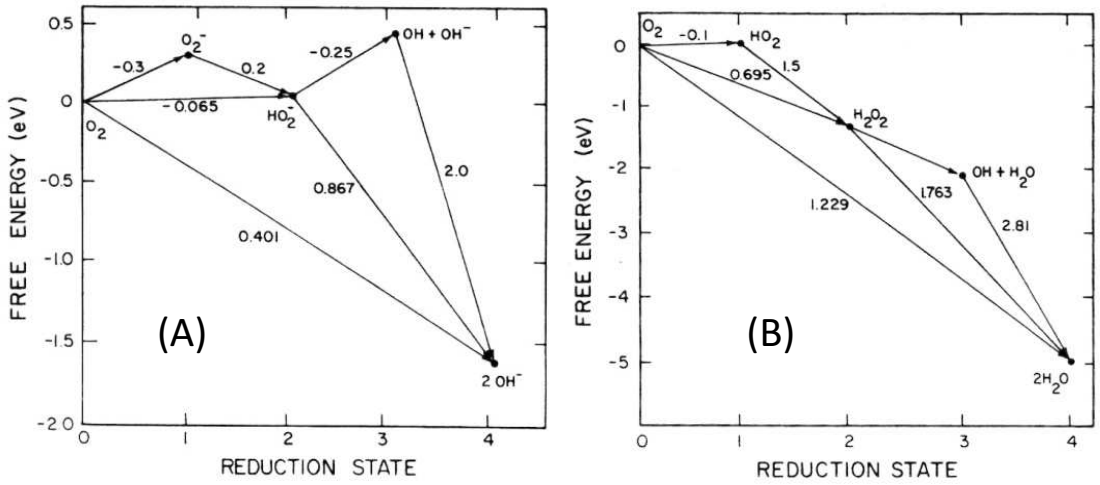

Fig. 2.2. Gibbs free energy relationships for the reduction of oxygen in acidic (A), and basic (B) solutions at 25 ℃. Standard potentials in volts are indicated on lines marking each step [10].

One can see that in acidic solutions Gibbs free energy change of the first step at -0.3 V and third step at -0.25 V are positive. This means that overall reaction requires activation, and temperature influences the overall reaction rate. Moreover, every next step must not occur at potential lower than the first one, so -0.3 V applied to electrode is sufficient to drive overall process. In basic solution the first step also determine overall ORR rate, but the activation energy is lower than in acidic solutions.

2.2 Parallel and consecutive reactions of oxygen and hydrogen peroxide

Recently ORR is more often studied in acidic solutions because of progressive development of PEFC. Typically, H_2O or H_2O_2 or their mixture are the products of this reaction. The composition of products mixture depends on cathode material, its potential and electrolyte composition (mainly pH). Platinum exhibits good selectivity as electrocatalyst for direct ORR to water and H_2O_2 reduction [23]. H_2O_2 is produced only at higher potentials in less acidic electrolytes. Other metallic catalysts are not as selective as Pt and larger fraction H_2O_2 is produced [23].

Several methods were applied to examine ORR mechanism and voltammetry on the rotating ring-disk electrode (RRDE) is among them [24]. The products generated on disk are transported hydrodynamically to the ring. If sufficiently high potential is applied to ring H_2O_2 can be there detected. The scheme of general consecutive-parallel reactions of O_2 and H_2O_2 is presented in Fig. 2.3.

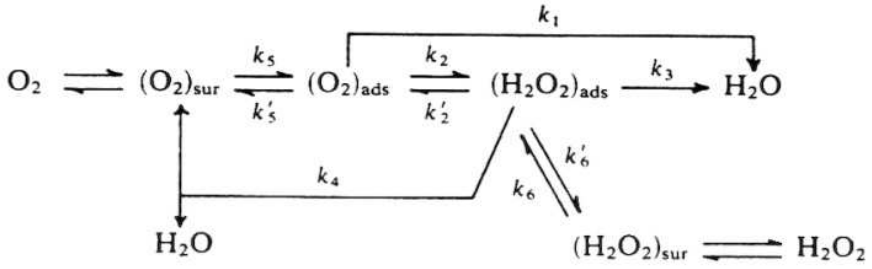

Fig. 2.3. A scheme of general consecutive-parallel reactions in ORR process. Species without subscript description – in the bulk solution, (sur) – in the vicinity of electrode surface, (ads) – adsorbed [10].

The experiments with ^{18}O and ^{16}O isotopes [25] shown that both oxygen atoms in a given H_2O_2 molecule come from the same O_2 molecule. Therefore, the oxidation of adsorbed $(H_2O_2)_{ads}$ is irreversible (Fig. 2.3).

The relationship between the ratio of disk and ring currents (i_D/i_R) and the RRDE rotation rate ω is as follows [10]:

$$\left(\frac{i_D}{i_R}\right)N = 1 + 2\frac{k_1}{k_2} + \left[\left(1 + 2\frac{k_1}{k_2}\right)\left(k_2' + k_3 + k_4\right) + \left(k_3 - k_2'\right)\right]\frac{1}{k_6'}$$
$$+ \left[\left(1 + 2\frac{k_1}{k_2}\right)\left(k_2' + k_3 + k_4\right) + \left(k_3 - k_2'\right)\right]\frac{k_6}{k_6'}\frac{1}{\gamma_B\sqrt{\omega}} \qquad (2.7)$$

$$\frac{i_A^\circ - (i_D + i_B)}{i_B} = 2\left(\frac{\gamma_A}{\gamma_B}\right)\left(\frac{k_5'}{k_5}\right)\left(\frac{k_6}{k_6'}\right)\left[\left(1 + \frac{k_1' + k_2}{k_5'}\right)\frac{k_2' + k_3 + k_4}{k_2} - \frac{\left(k_4 + 2k_2'\right)}{2k_2}\frac{k_2}{k_5'}\right] \cdot$$
$$\cdot \left[\left(1 + \frac{k_1 + k_2}{k_5'}\right) + \left(1 + \frac{k_2' + k_3 + k_4}{k_6'}\right)\frac{k_5'}{k_2} - \frac{k_4 + 2k_2'}{2k_6'}\right]\frac{k_5'}{k_2}\frac{2\gamma_A\sqrt{\omega}}{k_5'} \qquad (2.8)$$

where $i_B = i_R/N$, where N is the collection efficiency. i_A° is the diffusion-limited current density if all O_2 reaching the disk undergoes a four-electron reduction. The coefficients γ_A and γ_B relate the diffusion-limited currents for O_2 and H_2O_2 to the concentrations and rotation rates in equation:

$$i_A^\circ = 4F\gamma_A c_A^\circ\sqrt{\omega} \qquad (2.9)$$

and

$$i_B^\circ = 2F\gamma_B c_B^\circ\sqrt{\omega} \qquad (2.10)$$

where the subscripts A and B refer to O_2 and H_2O_2 respectively. The experimental data can be represented as a plot of i_D/i_R *vs.* $\omega^{-1/2}$ and $\left[i_A^\circ - (i_D + i_B)\right]/i_B$ versus $\omega^{1/2}$. Typical plots of i_D/i_R *vs.* $\omega^{-1/2}$ for Pt electrode are shown in Fig. 2.4. One can see that i_D/i_R is higher when

lower potential is applied to the disk. Literally, at lower potentials a larger fraction of O_2 is reduced directly to H_2O.

Another experimental method to examine products of ORR exploiting scanning electrochemical microscopy (SECM) was proposed by Shen *et al.*. Pt-microelectrode (SECM tip) positioned precisely in the vicinity of O_2-cathode (sample) [23] is kept at potential sufficiently high to oxidize H_2O_2 at the rate controlled by diffusion (Fig. 2.5).

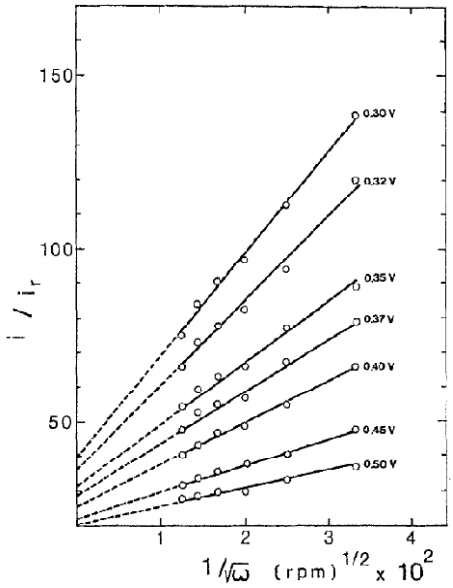

Fig. 2.4. RRDE data for O_2 reduction on Pt in 85% H_3PO_4 at 25 ℃. Pt-ring potentiostated at E_{RHE} = 1.2 V. N = 0.4 [26].

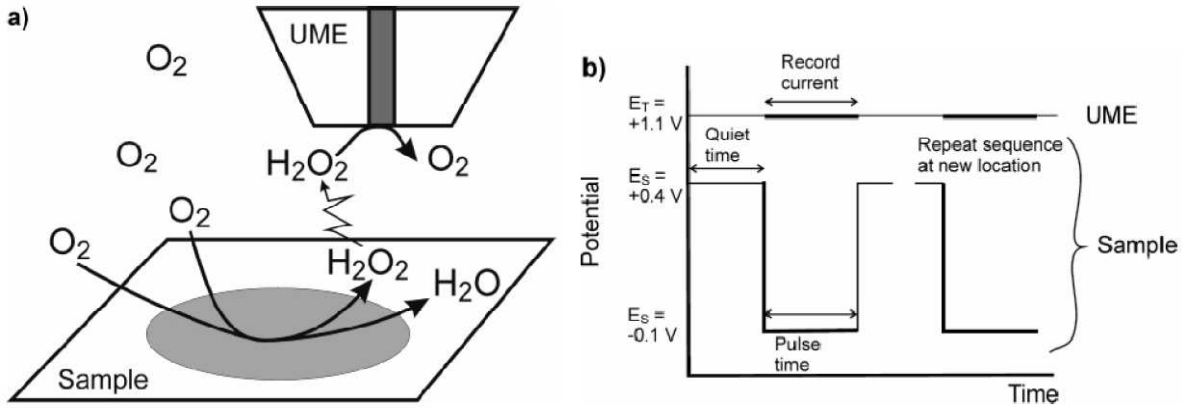

Fig. 2.5. Schematic illustration of the SECM operation in the examination of ORR products [23].

Since steady-state at microelectrode is achieved quickly this electrode works as amperometric H_2O_2 sensor. The current of H_2O_2 oxidation is proportional to its concentration; however, the concentration of the products of an electrochemical reaction at planar electrodes is transient because of extending diffusion length of substrate. When the sample is not polarized continuously but pulse potential is applied, determination of transient H_2O_2

concentrations profiles is possible. Fitting of parameters of theoretically developed equations to experimental H_2O_2 concentration profiles yields rate constants of reactions (2.3) and (2.4). Similar experiments were performed to obtain data presented in this thesis (see Section 13.5).

2.3 Non-platinum catalysts for oxygen reduction

Hardly available at high price platinum stimulate scientists for seeking for alternative efficient and stable catalysts. Apart from increasing of catalytic activity and lowering the amount of platinum in composite materials such as Pt-nanoparticles embedded on carbon support materials [27, 28], Pt/carbon nanotubes nanocomposite [29], Pt-nanoparticles functionalized graphene [30], and Pt monolayer deposited on non-noble metal monocrystals and nanoparticles [31]. During the last decade a lot of research and several review papers [9, 32-34] concerning non-platinum catalysts were published. Among them metal alloys are most interesting because of their high activity and stability [35, 36]. Fernandez *et al*. proposed synergic mechanism to explain enhanced ORR catalysis on bimetallic surfaces [37]. They noticed linear relationship (Fig. 2.6) between standard Gibbs free energy change of metal oxide formation reaction (assuming bulk oxide) (Eq. 2.11) and standard potential of electroreduction of this metal oxide in acidic media (Eq. 2.12).

$$2M + O_2 \rightleftarrows 2\,MO \tag{2.11}$$

$$2MO + 4H^+ + 4e^- \rightleftarrows 2M + 2H_2O \tag{2.12}$$

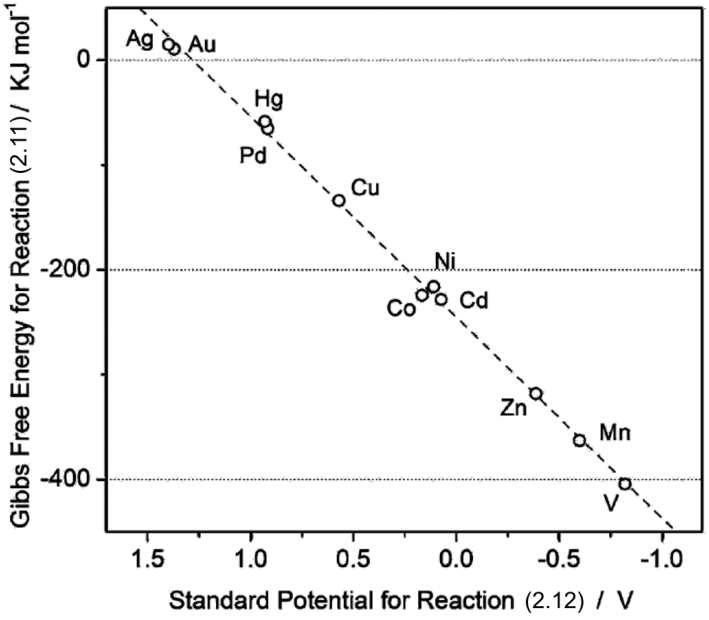

Fig. 2.6. Graph of the Gibbs free energy for reaction (2.11) versus the standard potential for reaction (2.12) [37].

The synergic mechanism of ORR catalysis on bimetallic surface can be explained as follows. Metals M in the lower right corner of Fig. 2.6 are favourable for the M-O bond creation. A reduction potential of MO is too low for power sources. On the other hand highly negative Gibbs free energy change of reaction (2.11) favours O=O bond breaking. Reaction (2.11) is thermodynamically unfavourable on metals in the upper left corner in Fig 2.6. These metals form less stable M'-O bonds that are easier to reduce as shown by higher reduction potentials for reaction (2.12). Based on the data shown in Fig. 2.6, authors proposed to couple a good oxygen bond breaking metal M with a second metal M' that is more efficient for ORR. It means that M'O reduction occurs at higher potential. Oxygen atom (O) can migrate from M to M' where reduction will occur (Fig. 2.7). One may ask why oxygen atom would migrate from the more stable oxide to the less stable one. However, migration from the top of M to a 3-fold site involving M' would be possible since oxygen could be more stable in such a 3-fold site.

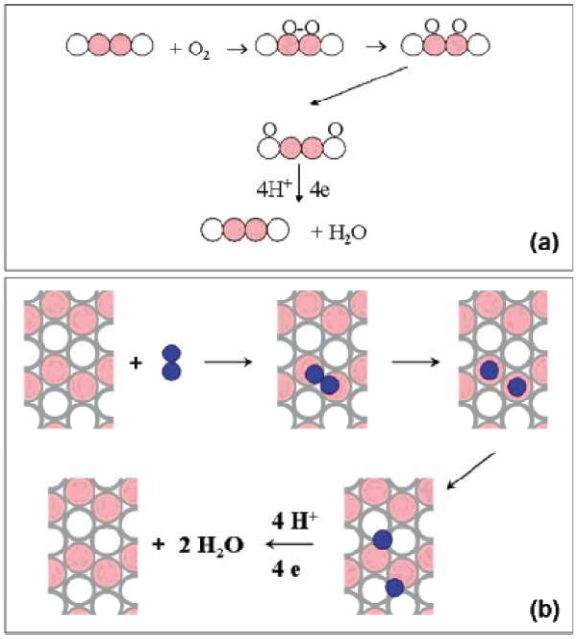

Fig. 2.7. (a) - Proposed synergetic mechanism for enhanced ORR electrocatalysis using bimetallic surfaces. (b) – schematic top view of the proposed mechanism. Pink circles represent atoms of metal M which oxidation is more favourable. White circles represent metal M' atoms that reduce adsorbed oxygen efficiently. Blue circles represent oxygen atoms [37].

An interesting example of determination of optimal composition of alloy by SECM was presented in the same paper [37]. An array of different atomic ratio Pd-Co alloy spots was deposited on glassy carbon electrode. Figure 2.8 represents SEM image of that array (A) and its ORR relative activity SECM image (B). The optimal atomic ratio Pd:Co is equal 9:1.

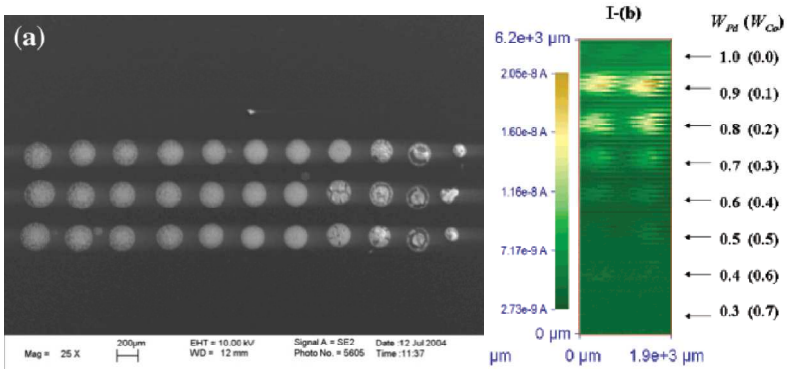

Fig. 2.8. A - SEM image of Pd-Co catalyst arrays. B - SECM TG/SC images of oxygen reduction activity measured on binary arrays in 0.5 M H_2SO_4. Tip-substrate distance - 30 µm, tip current - 160 nA, scan rate - 50 µm each 0.2 s, E_S - 0.7 V vs. HRE. W_M is the atomic ratio of metal M in the spot [37].

During the last decade some research was concentrated on nanoparticulate non-Pt ORR catalysts. These includes Pd nanoparticles deposited on Au electrode [38], carbon supported Ag nanoparticles [39], Au nanoclusters [40, 41], Pd-modified carbon nanotubes (CNT) [42], or Pd-Fe nanoparticles [43].

Carbon materials are another interesting example of cheap ORR catalyst [32, 44, 45]. Due to their low catalytic activity towards ORR (low potentials and low current densities) comparing to metallic catalysts, nowadays they are not studied. However, it is worth mentioning because carbon-based materials are used as a support for numerous inorganic, organic and biological catalyst of ORR. Also all electrodes presented in this thesis are carbon based. In the second half of XX century several works aimed for understanding the nature of the active sites of different carbon materials [10, 46-49] like examination of ORR on basal plane pyrolytic graphite (BPPG) and edge plane pyrolytic graphite (EPPG) in basic solution [47] were done (Fig. 2.9).

One can see a huge difference between catalytic activities of those two materials. Namely, current densities of ORR and hysteresis on EPPG are much higher than on BPPG. Moreover, the hysteresis increases at sufficiently low potentials when cathodic current flow. From peak-shaped CV-curves one can conclude that the surface of the graphite layers edges changes with applied potential and this affects catalytic activity. Basal planes exhibit much lower catalysis and no hysteresis. This implies that the ORR on carbon and graphite involves a strong interaction of O_2 with surface functional groups.

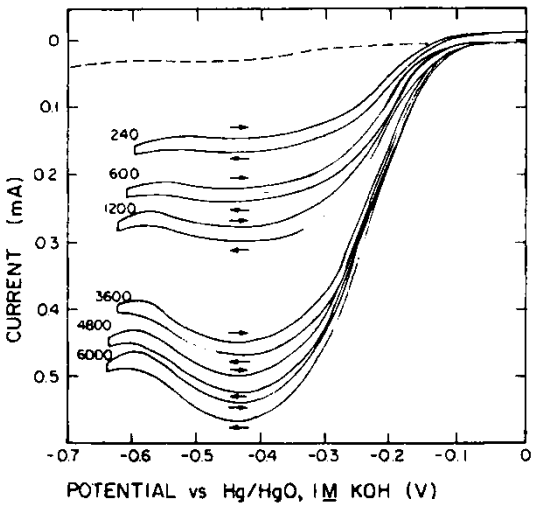

Fig. 2.9. ORR on (RDE) made of BPPG (dashed line) and EPPG (solid lines) in O2-saturated 0.1 M KOH. Electrode area: 0.2 cm2. Rotation rates in rpm's indicated near curves [47].

Garten and Weiss proposed mechanism of ORR at graphite edges illustrated in Fig. 2.10 [49]. The role of quinone groups was confirmed by catalytic activity of quinone modified BPPG [50] and other carbon materials [51].

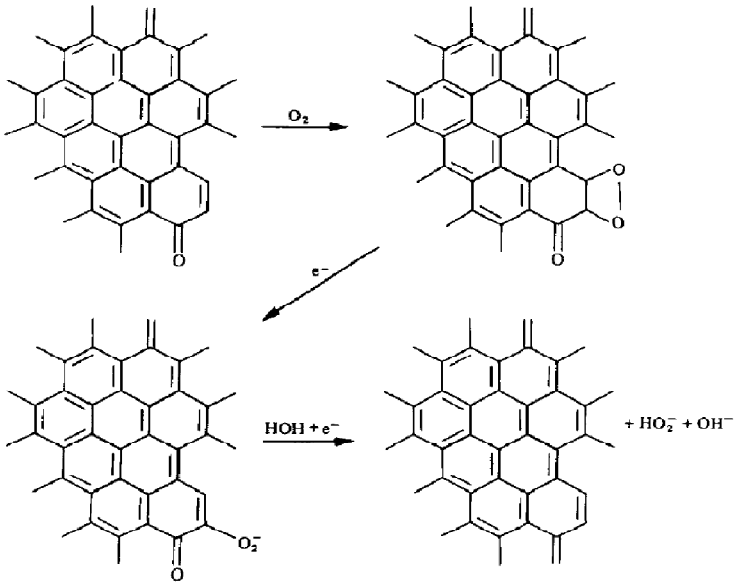

Fig. 2.10. Garten and Weiss mechanism for ORR on carbon surfaces [49].

Recently, in order to increase specific surface area and length of catalytically active graphite edges terminated with functional groups, graphene (individual layers of graphite) is used in a variety of electrochemical applications including ORR [30, 52, 53]. This material can be produced relatively easily by mechanical exfoliation of graphite [54], SiC heating [55], or by the reduction of graphite oxide [56]. The planes of graphite can be easily modified by non-covalent attachment of functionalized polycyclic hydrocarbons providing additional

catalytic active sites. Recently Li *et al.* proposed new sophisticated graphene-based catalyst for ORR [57]. Chemically converted graphene (CCG) was modified with perylene tetracarboxylic acid (PTCA) and Au-nanoparticles modified with ionic liquid (IL) (Fig. 2.11).

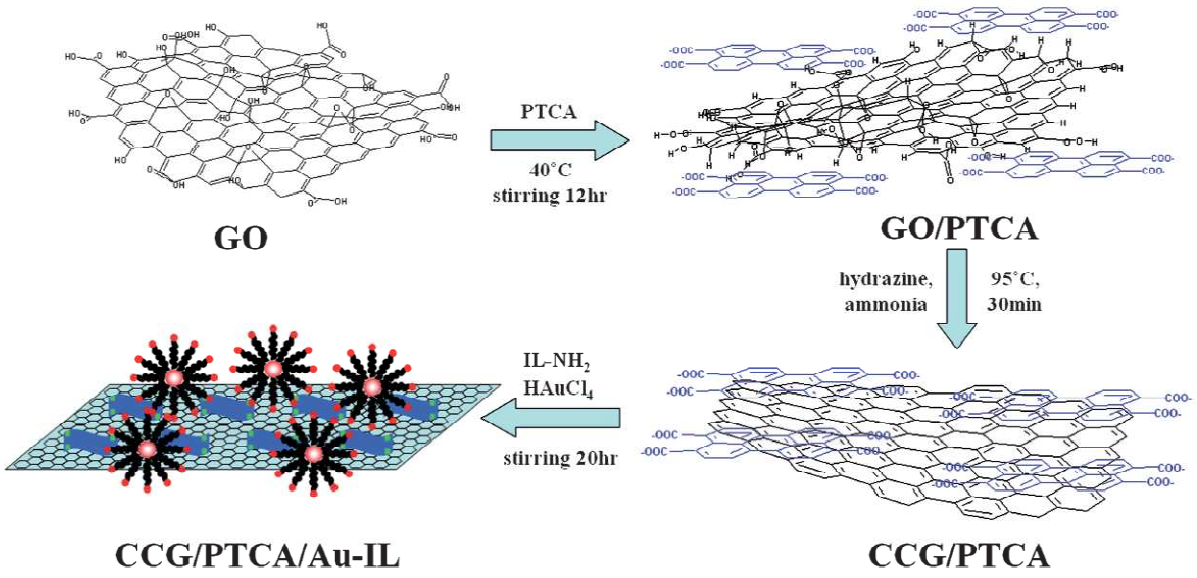

Fig. 2.11. Illustration of the preparation of CCG/PTCA/Au-IL composite [57].

In order to achieve high efficiency of oxygen cathode and the lack of by-products, the catalysts should reduce oxygen to water directly. The production of H_2O_2 causes depletion of cathode potential. In this case only two electrons take part in reduction of one O_2 molecule what results in lower current. Numerous transition metal complexes with macrocyclic ligands have been examined as oxygen reduction catalyst [58-63]. Most of them reduce oxygen via the two-electron pathway to hydrogen peroxide at relatively low potentials. Transition metal N_4-macrocycles such as porphyrins and phtalocyanines are also known to catalyze ORR under physiological conditions. Some of them act as catalyst for 4-electron ORR near the reversible thermodynamic potential [58, 63]. The most famous cofacial porphyrin catalyst was proposed by Collman *et al.* in 1980 [58]. They synthesized a series of dimeric metalloporphyrins with two porphyrin rings constrained parallel to one another by two amide bridges of varying length (Fig. 2.12A). This complex with cage of the size of O_2 molecule attached to the surface of graphite electrode exhibited ORR almost exclusively to water at exceptionally high potential (Fig. 2.12B).

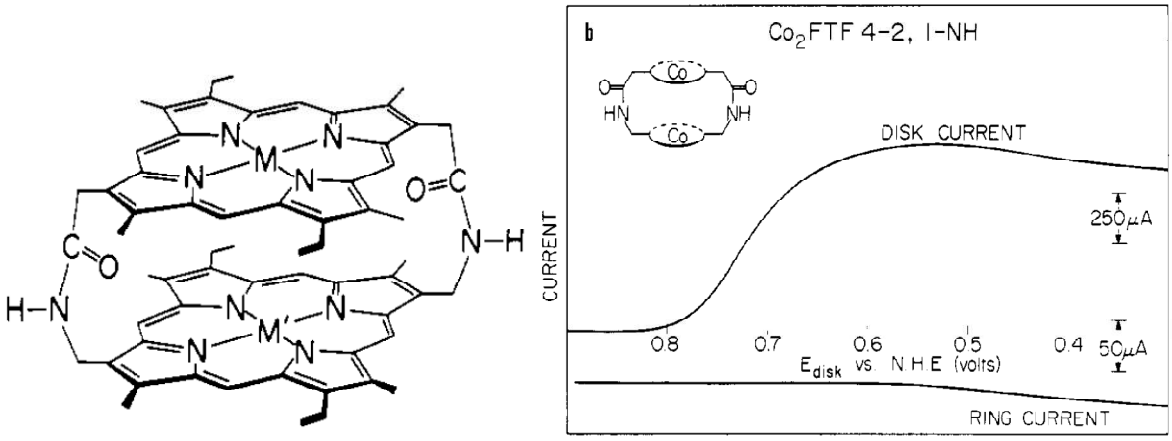

Fig. 2.12. A) - β-linked face-to-face porphyrin. B) - disk and ring current vs. the potential of the graphite disk coated with the dimeric dicobalt porphyrins. The Pt-ring was maintained at +1.4 V. Rotation rate: 250 rpm. Supporting electrolyte: 0.5 M CF_3COOH saturated with O_2 at 1 atm [58].

A possible mechanism for this reaction was suggested by Fukuzumi *et al.* (Fig. 2.13) [64]. Protons availability influences the ORR products and 4-electron process is favoured at lower pH.

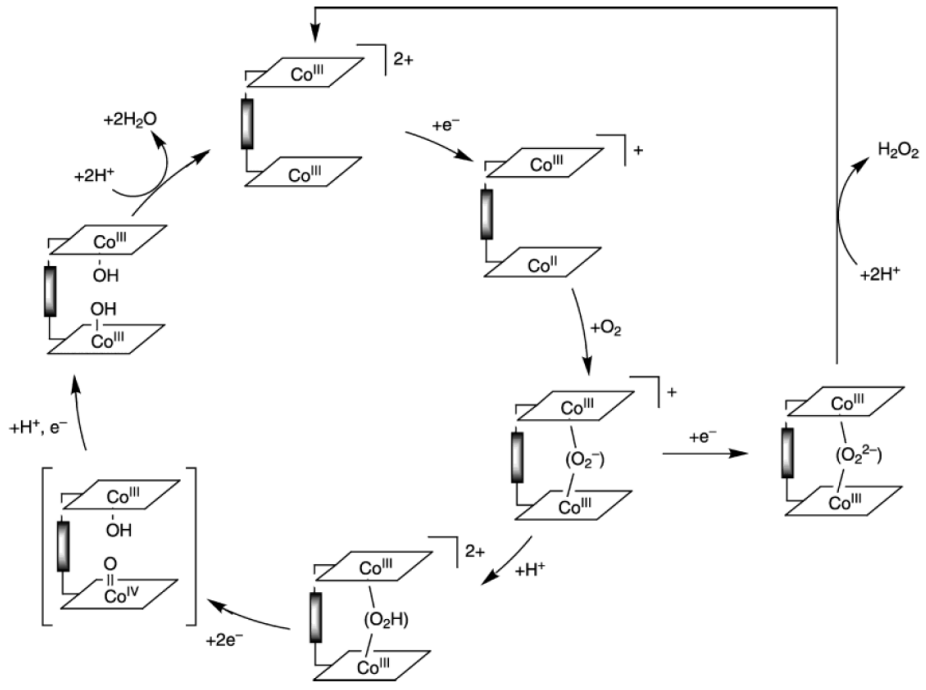

Fig. 2.13. A possible mechanism for the ORR catalyzed by cofacial dicobalt porphyrins[64].

Another important work concerning organometallic complex as ORR catalyst concerns iron(III) tetramethoxyphenyl porphyrin chloride adsorbed on the carbon black and heat-treated at temperatures from 200 to 1000 °C [65]. It was found that ORR its activity increases when material is pre-treated with high temperature. Authors do not find which

products of the heat treatment are responsible for the high activity of the catalyst, but they excluded the role of metallic Fe particles.

An interesting work is devoted to investigation of iron organometallic compounds which structure is similar to structure of enzymes prosthetic group. Collman *et al.* reported ORR using biomimetic analogues of cytochrome *c* oxidase as catalyst (Fig. 2.14) and $Ru(NH_3)_6^{2+}$ as mediator [59]. They observed reduction of O_2 to H_2O at pH 7.

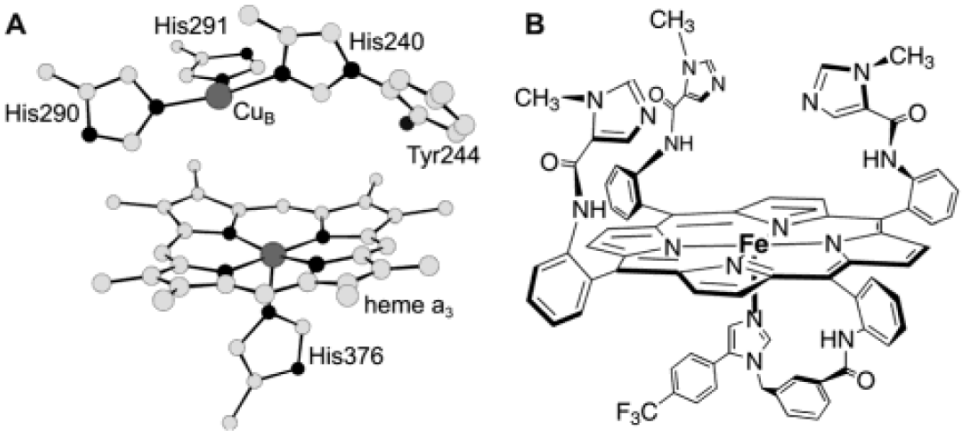

Fig. 2.14. (A) The catalytic site of cytochrome c oxidase. (B) Fe-based catalyst studied in ref. [59].

The ORR was also studied at semiconductor electrodes such as metal oxides. Mentus observed 2-electrons ORR on anodically formed TiO_2 in acidic media and 4-electron ORR in alkaline media [66], but current onset potential is only ca. 0.5 V higher than hydrogen evolution potential. Only in SOFC metal oxides are extensively used as cathode materials. This is because there are no other known conductive materials stable in the presence of gaseous oxygen at temperature ca. 1000 °C. Perovskite-like $La_{1-x}Sr_xCoO_3$ [67], $Ln_{0.4}Sr_{0.6}Co_{0.8}Fe_{0.2}O_3$ (Ln = La, Pr, Nd, Sm, Gd) [68] or $La_{1-x}Sr_xMnO_3$ [69] exhibit high electrical conductivity and good catalytic activity above 600 °C. In 2004 Shao and Haile presented SOFC with $Ba_{0.5}Sr_{0.5}Co_{0.8}Fe_{0.2}O_3$-based cathode which exhibits power densities 1.01 W cm^{-2} and 0.4 W cm^{-2} at 600 °C and 500 °C, respectively [70]. The main disadvantage of perovskites is a large thermal expansion mismatch between them and YSZ.

Except organometallic complexes neither non-platinum catalyst is sufficient for ORR at neutral conditions (ca. pH 7). They catalyze ORR efficiently in extremely acidic or basic environments. Another aspect is the lack of selectivity toward H_2O production. H_2O_2 as a product of ORR is harmful to physiological environment. Therefore a lot of scientific effort is put into research concerning biocatalysts for ORR, what is presented in next chapter.

3 Biocatalytic oxygen reduction

Enzymes as ORR catalysts at cathodes in biofuel cells (Chapter 5) have the number of advantages over inorganic catalysts. The main of them are: almost unity specificity toward O_2, biodegradability and lower ORR overpotential [71]. For example the overpotential of diffusion-controlled mediatorless oxygen reduction using laccase (pH 5) or bilirubin oxidase (pH 7) adsorbed on carbon aerogel electrode is reduced by 0.55 and 0.4 V, respectively, in comparison to Pt-electrode (Fig. 3.1) [72]. Moreover, enzymes availability is not as restricted as platinum. However, the use of biocatalysts has some disadvantages, such as low current density achieved on bioelectrodes, poor stability, restricted temperature range, difficulties in achieving good electronic coupling to the electrode. The adequate design of the biocathode may help to overcome these problems. However, there are also intrinsic enzymes disadvantages – susceptibility to various components of electrolyte, and long time of isolation and purification. The overcome of them is a challenge for biochemist and genetic engineers.

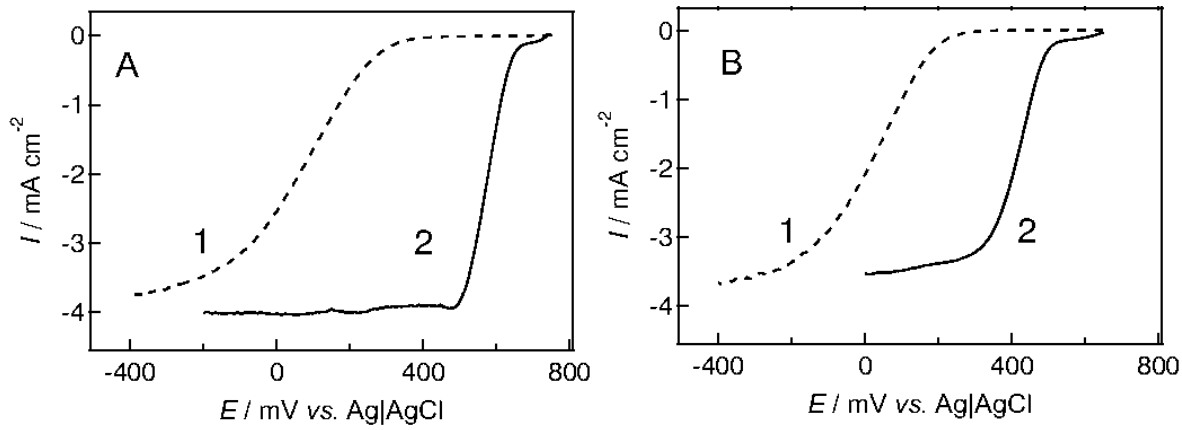

Fig. 3.1. Linear sweep voltammograms of (A) Pt (1) and laccase-adsorbed carbon aerogel electrode (2) in pH 5 McIlvaine buffer and (B) Pt (1) and bilirubin oxidase-adsorbed carbon aerogel electrode (2) in pH 7 phosphate buffer at 25 °C. The measurements were done under O_2-saturated conditions, at 1,000 rpm, and at a scan rate of 20 mV s^{-1} [72].

Efficient direct electron exchange between redox centre of the enzyme and electrode strongly depends on the electrode material properties such as hydrophobicity/hydrophilicity [73, 74] and nano-topography [75]. On the other hand, the electrode support and material encapsulating the enzyme are crucial for the enzyme stability.

There are two types of electronic communication between electrode material and enzyme – direct (mediatorless) (Section 3.3) and mediated (Section 3.2). Unfortunately, due to the variety of experimental conditions (i.e. different oxygen concentrations, electrolyte compositions and rotation rates of RDE) a straightforward comparison is difficult.

3.1 Enzymes for oxygen reduction

Common property of multicopper oxidases – laccase, bilirubin oxidase, or copper efflux oxidase (CueO) is their ability to catalyze four-electron oxygen reduction without generating any reactive intermediates (e.g. H_2O_2). Moreover, ORR catalyzed with these enzymes occurs at higher potential than on noble metals. These properties make them important candidates as catalysts for oxygen reduction in biofuel cells (Chapter 5). Another, less popular enzymes for modification of biocathodes for ORR are cytochrome oxidase [76, 77], and microperoxidase 11 [78]. The last one is two-electron ORR catalyst.

The most popular multicopper oxidases employed as ORR biocatalyst are laccases. This is because their isolation and purification methods are well developed and described in the literature [79]. Moreover, commercially available laccases are cheaper than other multicopper oxidases.

Tarasevich *et al.* [80] have first reported that some laccases adsorbed on carbon electrodes catalyze the four-electron reduction of O_2 without mediator. The current density of about 1 mA cm^{-2} was reported. However, the description was not enough for readers to reproduce the experiments [72]. Later, laccases became promising enzymes as cathode catalysts of biofuel cells, but a mediator – 2,2′-azino-bis(3-ethylbenzthiazoline-6-sulfonate) (ABTS), was used to shuttle electrons between the enzyme and electrode [81].

The catalysis carried out by all members of this family is guaranteed by the presence of different copper centres in the enzyme molecule. In particular, laccases are characterized by the presence one type-1 (T1) copper ion, together with one type-2 (T2) and two type-3 (T3) copper ions, arranged in a trinuclear cluster. The different copper centres can be identified on the basis of their spectroscopic properties. The T1 site is characterized by a strong absorption around 600 nm, whereas the T2 site exhibits only weak absorption in the visible region. The T2 site is electron paramagnetic resonance (EPR)-active, whereas the two copper ions of the T3 site are EPR-silent. The substrates are oxidized by the T1 copper and the extracted electrons are transferred, probably through His-Cys-His tripeptide, to the T2/ T3 site, where molecular oxygen is reduced to water (Fig. 3.2) [82].

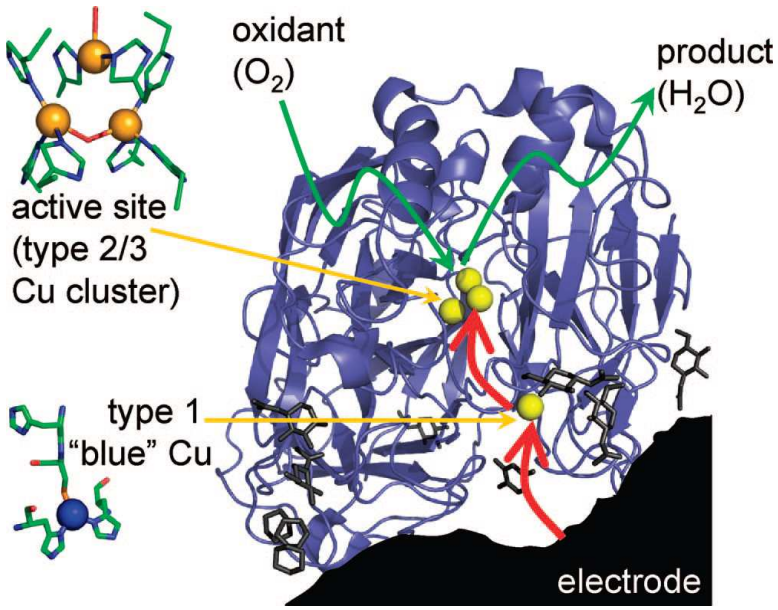

Fig. 3.2. The structure of T. versicolor laccase showing the protein superstructure in blue and the copper atoms as yellow spheres [83].

The redox potential of the enzyme is crucial for its application as cathode catalyst in biofuel cells. The redox potential of the electron-accepting T1 site of laccases is in the range 0.43–0.78 V vs. NHE [84, 85]. Because of this diversity, laccases can be divided into three groups: low-, medium-, and high-potential. The low-potential ones (isolated mainly from trees) are characterized by T1 redox potential ca. 0.43 V vs. NHE [86]. The intermediate ones with T1 redox potential in the range 0.47–0.71 V vs. NHE are isolated from fungi [87, 88]. The high-potential laccases, for example those from *T. hirsuta*, *T. versicolor* and *T. villosa*, all have a potential of the T1 site of about 0.78 V vs. NHE [85]. Obviously, the last group is most interesting for application in biocathodes. The redox potential of the T1 centre of laccase from *C. unicolor* used in this thesis is equal 0.75 V vs. NHE [89-91].

The T1 centre is responsible for accepting electrons from the substrate and its transfer to the T2/T3 cluster binding the oxygen molecule and reducing it to water [92]. The dependence of catalytic activity on the difference between redox potential of mediator and redox potential of the T1 centre suggests that the electron transfer to this copper ion is the rate-limiting step [93].

Another group of popular multicopper oxidases used as cathodic biocatalyst are bilirubin oxidases. Despite their more difficult isolation and purification method and higher price these enzymes are the best candidates for bioelectrocatalytic O_2 reduction at neutral pH [94]. Contrary to laccases BOx's are resistive to Cl^- ions, what make them interesting for devices operating under physiological conditions [95-97]. The crystallographic structure of

BOx is still unsolved probably because of difficulty in obtaining of proper monocrystal, but biochemical, spectral, and kinetic studies reveal that the T2/T3 cluster is surrounded by four histidine molecules while the T1 centre binds cysteine, histidine and methionine [98]. Earlier studies reported T1 redox potential of BOx isolated from Myrothecium verrucaria to be equal 0.49 V vs. NHE [98], whereas later studies provides higher value – 0.69 V vs. NHE [99]. The natural mediator of BOx is bilirubin which is oxidized to biliverdin, accompanied by reduction of oxygen to water [98, 100].

The last example of multicopper oxidoreductases – copper efflux oxidase (CueO) isolated from *Escherichia coli* bacteria has been recently employed as ORR biocatalyst by Kontani *et al.* [101]. Air diffusion biocathode composed of carbon black dispersed in O_2-permeable polytetrafluoroethylene (PTFE) with adsorbed CueO is able to reduce O_2 with the current density of 20 mA cm^{-2} at 0.2 V versus NHE in a citrate buffer pH 5 (Fig. 3.3).

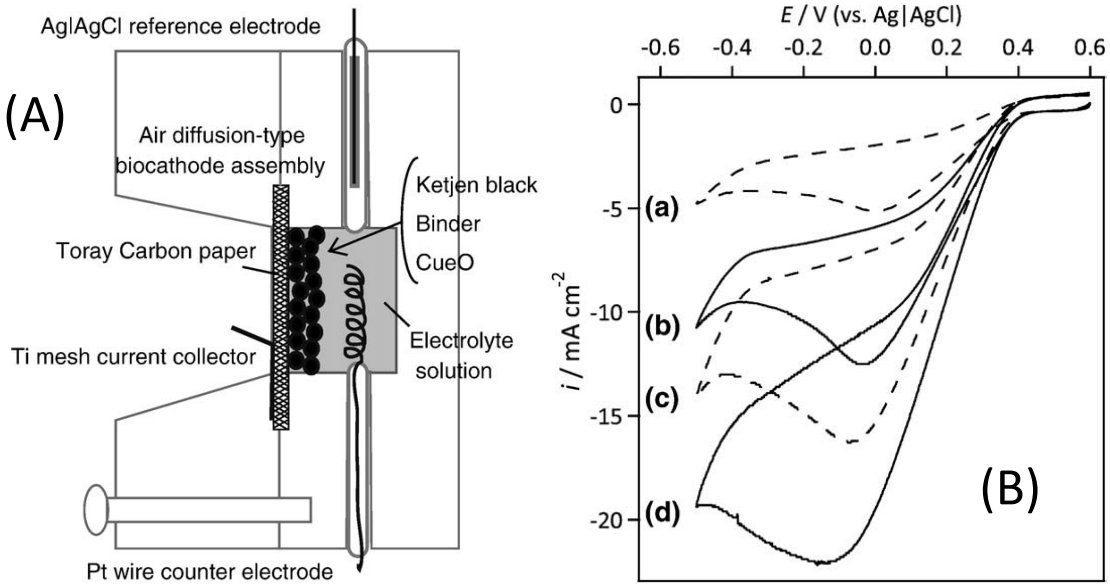

Fig. 3.3. A scheme of the air diffusion CueO-adsorbed on carbon black-based electrode (A), CVs of ORR at different concentrations of citrate (a) 0.05, (b) 0.1, (c) 0.5 and (d) 1.0 M (B) [101].

Unfortunately, the onset potential of ORR for this electrode being ca. 0.6 V versus NHE is lower comparing to laccases and bilirubin oxidases modified biocathodes. This is caused by lower T1 centre redox potential of CueO. Earlier, the same group has made an attempt to increase this potential by mutation of the T1 centre ligands, however, the decrease of the ORR overpotential on electrode modified with CueO mutant is only few milivolts (Fig. 3.4) [102]. However, because of much higher current densities biocathodes modified with this enzyme are interesting for application in devices with low-potential anodes e.g. zinc-air batteries [103].

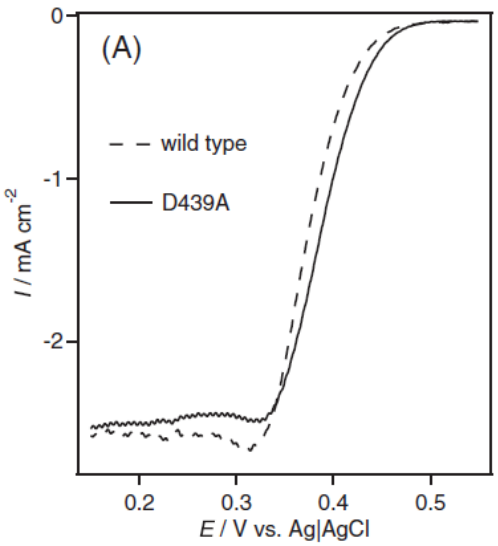

Fig. 3.4. Background-subtracted rotating disk voltammograms of mutant and wild-type CueOs modified electrode under O_2-saturated conditions at pH 5.0. The scan rate was 20 mV s^{-1} and a rotation rate 500 rpm [103].

3.2 Mediated electron transfer for bioelectrocatalytic oxygen reduction

In single-compartment (membraneless) BFC the application of mediator dissolved in electrolyte is impossible, because the potentials of anode and cathode would be almost equal resulting in negligible power density. The situation in double-compartment or double-stream microfluidic BFC, where electrodes are in contact with different electrolytes is different. Then the mediator can be dissolved in catholyte (without immobilization) providing its easy access to the immobilized enzyme. Then the electrons are exchanged with the electrode by diffusive mediator.

For shuttle electrons to ORR catalyzing oxidoreductases two types of mediators are most popular – 2,2'-azinobis (3-ethylbenzothiazoline-6-sulfonate) ($ABTS^{2-}$) (Fig. 3.5) [81] and $Os^{3+/2+}$ redox centre stabilized by ligands attached to polymer backbone [104].

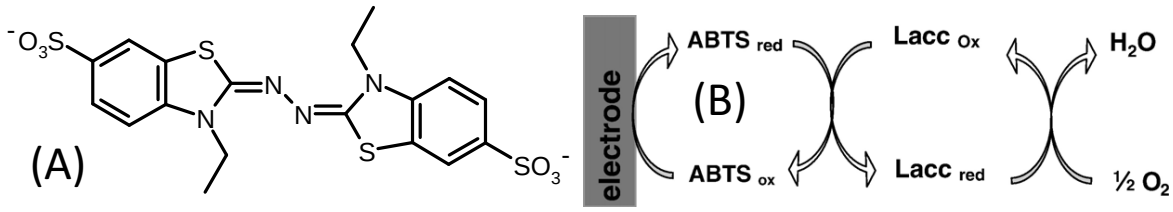

Fig. 3.5. 2,2'-azinobis (3-ethylbenzothiazoline-6-sulfonate) ($ABTS^{2-}$) (A), Reduction of oxygen with laccase /ABTS system (B) [105].

The advantage of osmium polymer or copolymer film is that it works as both electron relay and host for laccase or BOx (see Section 4.3). The redox centres are stabilized by a set of ligands containing heterocyclic nitrogen atoms (Fig. 3.6).

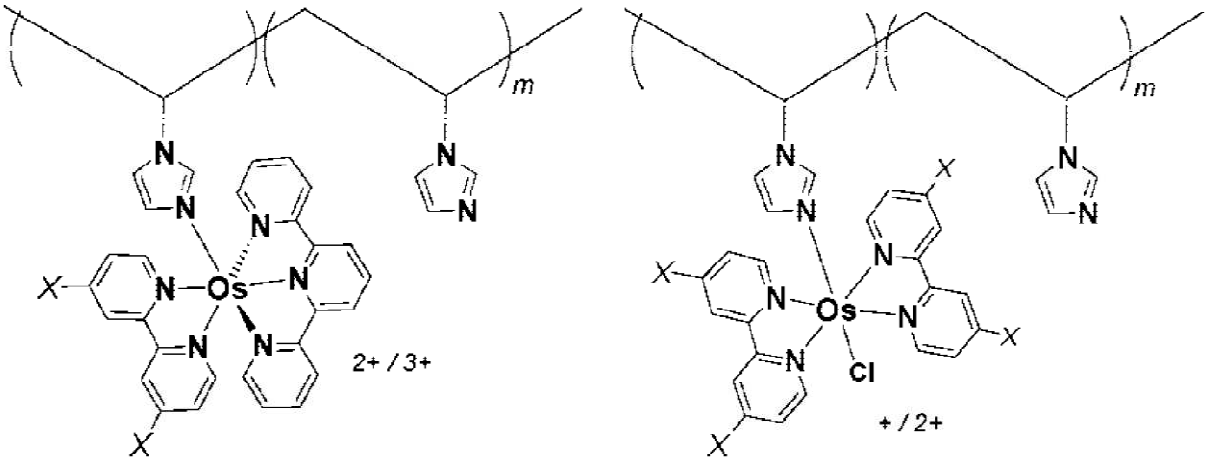

Fig. 3.6. General structure of the redox polymers with the backbone polymer polyvinyl pyridine (not shown) [93].

The redox potential of $Os^{3+/2+}$ redox couple is adjustable and can be optimized to be close to that of the active redox centre of the enzyme by proper selection of ligands [93]. These redox centres are connected to polymer backbone with chains as long as 10 carbon atoms and heteroatoms (e.g. N). Because of their flexibility, the distance between neighbouring oxidized and reduced redox centres can be shortened, allowing for efficient electron exchange on their collision [106]. The most important property of such polymers is the ability of $Os^{3+/2+}$ redox centres to exchange electrons with enzymes. Enzyme leakage is avoided not only by encapsulation of the large enzyme by crosslinked polymer backbones but also by electrostatic attraction between charged cationic redox groups of polymer and negatively charged protein moieties. Moreover, hydrophilic polymer matrix provides water-containing environment suitable for stable enzyme immobilization. It also allows for transport of dissolved oxygen to the redox centre of the enzyme.

The ORR rate depends on the standard potential of $Os^{3+/2+}$ redox polymer, which act as mediator (Fig. 3.7). Namely, higher difference between mediator and enzyme potentials results in higher catalytic currents. On the other hand lower cathode potential determined by mediator potential is unfavourable for BFC applications.

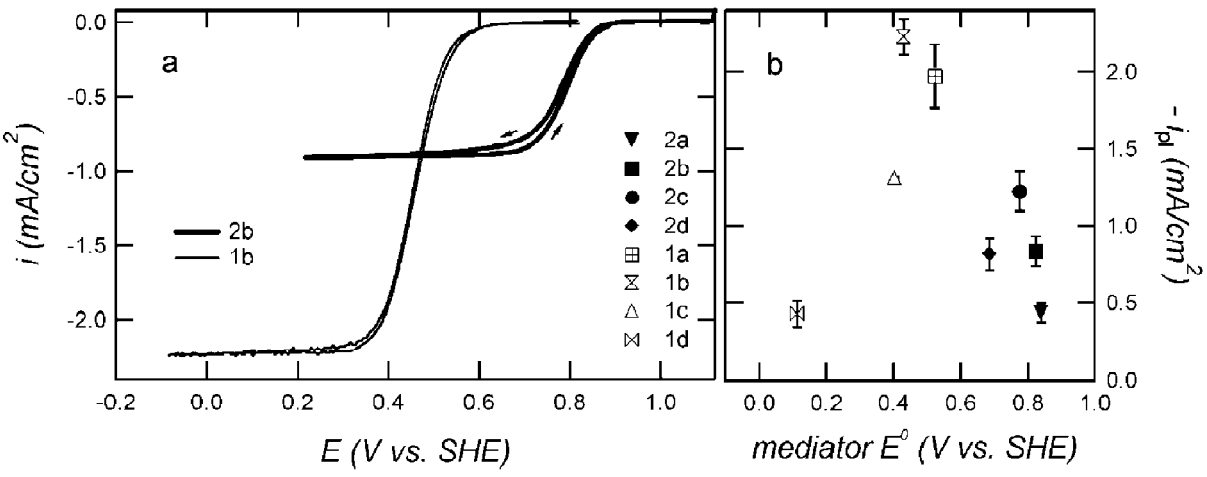

Fig. 3.7. CV curves of ORR on electrodes modified with laccase and two different redox polymers (a). ORR plateau current values for polymers characterized by their redox potential (b). Experiments conducted in 1 atm O_2-saturated citrate buffer at 900 rpm, scan rate 1 mV s^{-1} [93].

The electrodes modified with redox polymer serve as cathode for the membraneless biofuel cell, what is not always the case for the biocathodes based on ABTS mediator (Fig. 3.5) because of its water solubility. ABTS exhibits fast electron transfer kinetics between electrode and laccase and its standard potential is close to the T1 site potential. Palmore *et al.* [81] reported bioelectrocatalytic reduction of O_2 to water, where laccase from *Pyricularia oryzae* and ABTS were used in solution of acetate buffer at pH 4 without immobilization. ABTS has been also reported as an effective electron transfer mediator for bilirubin oxidase [94].

Although accelerated deactivation of both laccase or BOx in the presence of ABTS has been reported [107-109] (what can be attributed to the degradation of enzyme by $ABTS^{\bullet-}$ radical), this mediator is frequently used as a "model" system mainly because of its superiority to other water-soluble mediators in terms of higher potential and current density. ABTS is also used in experiments described in this thesis.

Several attempts of encapsulation of both ABTS and the enzyme were reported [110-115].

Burnel *et al.* reported BFC where laccase was co-immobilized with ABTS on cathode within electropolymerized polypyrrole [110] on which ORR current density ca. 130 µA cm^{-2} was achieved.

The electrostatic attraction between functional groups of ionomer film and $ABTS^{2-}$ [111] was used for mediator immobilization. The composite film consisting of ionomer–polyallylamine for $ABTS^{2-}$ immobilization and sol–gel processed silicate for laccase

encapsulation was proposed as biocathode material [112]. The lyotropic liquid-crystalline cubic phase (Fig. 3.8) film was employed to host laccase and ABTS [113]. The glassy carbon electrode modified with laccase and the mediator embedded in such film exhibits ORR current density ca. 18 μA cm^{-2} at 0.4 V versus NHE in 1 atm O_2-saturated phosphate buffer pH 7.

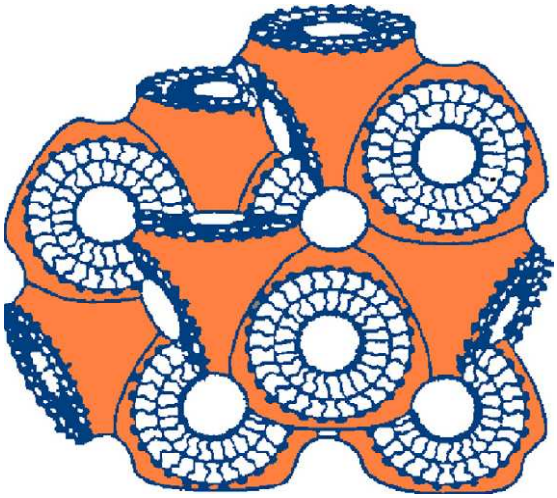

Fig. 3.8. Structure of the cubic phase [113].

Another method of ABTS immobilization is based on irreversible adsorption on MWCNTs. Adsorption occurs due to the interaction between delocalized π-electrons of ABTS and graphene structure of CNTs, which after this modification become water-soluble. The electrodes with immobilized such ABTS-modified CNTs after immobilization of laccase exhibit efficient oxygen catalysis [114-116].

Other than ABTS mediators for laccase and bilirubin oxidase were tested in biocatalyzed oxygen electroreduction. All redox species small enough, which can diffuse into prosthetic group of enzymes and exhibiting fast kinetic of electron transfer (e.g. cyanometallates, quinones and ferrocene derivatives) are suitable for this purpose, but the onset potential of catalytic current is too low for the glucose–air biofuel cell. Nevertheless, these mediators may be useful in hybrid devices (Section 5.5). The most efficient known nowadays diffusive mediator for laccase and BOx modified biocathodes for oxygen reduction remains ABTS, which was also used in experiments in this thesis.

3.3 Direct electron transfer for bioelectrocatalytic oxygen reduction

For direct bioelectrocatalysis good electronic communication between the T1 site of copper oxidases and electrode conductor has to be assured. This approach has some advantages over

mediated electrocatalysis. Namely, the problems with mediator stability, thermodynamic losses causing biocathode potential depletion, mediator cost, and safety for the environment are avoided [71]. On the other side current densities of ORR achieved on DET-utilizing biocathodes are usually lower in comparison to mediated electrocatalytic systems, because only the enzyme molecules in direct contact with conductive electrode material and properly oriented can act as catalyst (Fig. 3.2 and 3.9) [73, 74, 117].

Numerous studies show mediatorless catalysis with copper oxidoreductases on gold [118, 119] different types of carbon and graphite electrodes [78, 91, 102, 120-123] and boron doped diamond [124]. The mechanism of this process involves donation of electrons to the T2/T3 cluster through the T1 centre on the cathode. The oxygen reduction wave appears at 0.735 V versus NHE what is close to the standard potential of T1 site of the *Trametes versicolor* laccase (0.78 V versus NHE [125]). This reaction is controlled by catalysis rather than diffusion since the power output of BFC with such cathode was almost independent of stirring [126].

Anthracene-modified pyrolytic edge plane graphite substrate allowing fungal laccases to adsorb in a proper orientation represents another example of efficient mediatorless bioelectrocatalysis (>0.5 mA cm^{-2}) and remarkable biocathode stability (Fig. 3.9) [127, 128]. It seems that the anthracene groups interact with the hydrophobic part of the enzyme close to the T1 site of *Pycnoporus cinnabarinus* laccase.

The mediatorless bioelectrocatalysis with CueO was also observed on carbon materials [101, 102, 129]. The current density of 12 mA cm^{-2} was obtained at mesoporous carbon RDE [129]. On such biocathode consuming oxygen dissolved in the electrolyte the ORR current is limited by O_2 mass-transport because of weak solubility and low diffusion coefficient of oxygen. Recently, the ORR current density as high as 20 mA cm^{-2} was recently reported on CueO modified air diffusion biocathode with onset of the catalytic current around 0.35 V versus NHE [101].

Other materials frequently used for preparation of biocathode exhibiting mediatorless catalysis are CNTs. Their electronic properties are unique as they can be either metallic or semiconducting, depending on their structure [130]. CNTs immobilized on the electrode surface form an extended network and the electroactive surface is significantly increased (Fig. 3.10).

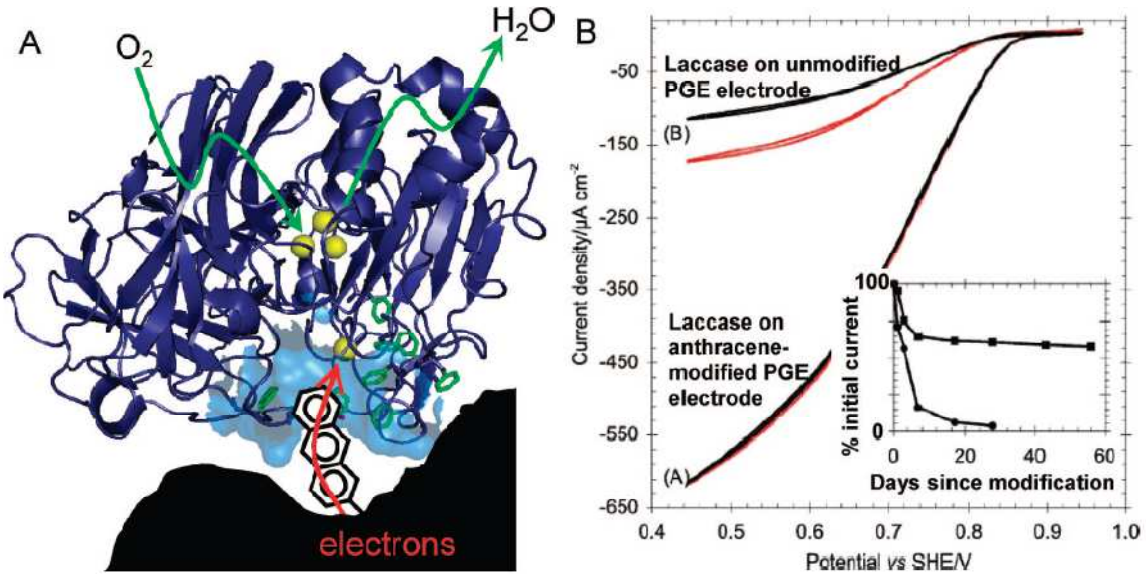

Fig. 3.9. (A) – A scheme of electron transfer via the 2-aminoanthracene linker to the T1 centre of laccase. The hydrophobic part is highlighted as a textured surface. (B) – Electrocatalysis of ORR by laccase on a 2-aminoanthracene modified pyrolytic graphite edge electrode and an unmodified electrode at 25 °C in pH 4. Red curves were recorded immediately after spotting laccase solution onto the electrode, while black curves were recorded after exchanging the electrochemical cell solution for enzyme-free buffer solution. Inset: The long-term change in catalytic current for a modified (■) and unmodified (●) electrode. The y-axis shows the change in current density at 0.44 V vs. SHE [83].

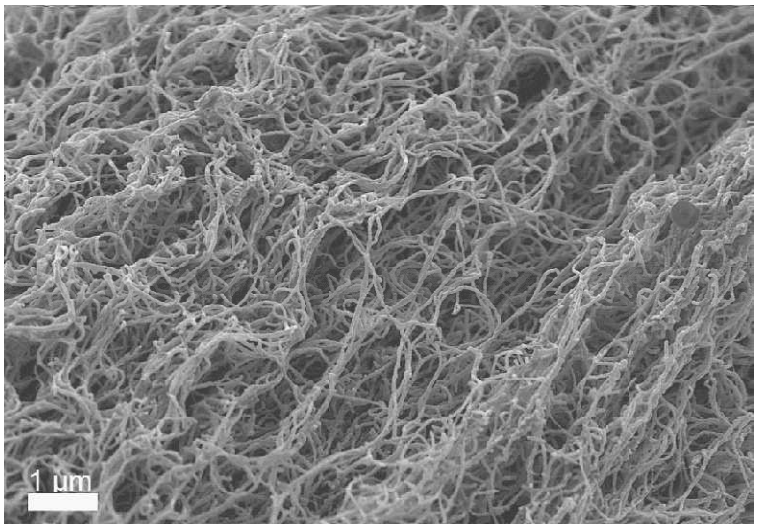

Fig. 3.10. SEM image of a CNTs agglomerate [116].

Both laccase and bilirubin oxidase were immobilized on CNT films by physical adsorption or covalent attachment [91, 115, 131-133]. This approach leads to a higher content of electrically contacted enzyme molecules per unit of geometric surface area of the electrode, thus higher catalytic current density is observed. The ORR current density on the electrode modified by laccase and SWCNTs can be significantly increased by functionalization of

nanotubes with pyrenesulfonate derivatives (Fig. 3.11) [131]. This functionalization increases SWCNT solubility in water and decreases aggregation during the film preparation.

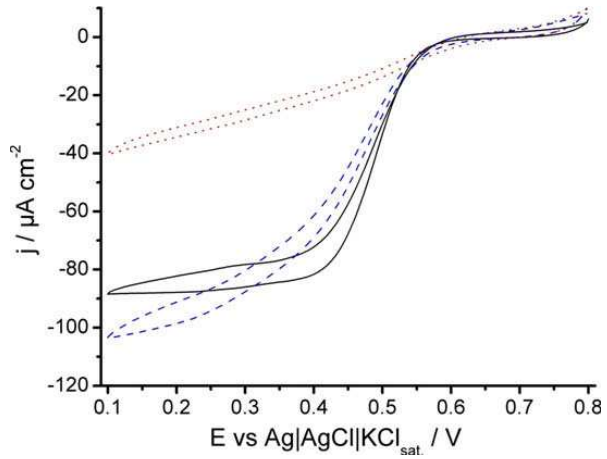

Fig. 3.11. SWCNTs unmodified (dotted lines) or modified by pyrenesulfonate (solid lines) and pyrene tetrasulfonate (dashed lines) [131].

The significant example of biocathode for ORR with high current density (Fig. 3.12B) is reported by Deng *et al.* [134]. A multilayer structured film consisting of MWCNTs and laccase with poly-L-lysine as a linker contain large amount of biocatalyst being in contact with electrode and accessible by O_2 dissolved in electrolyte (Fig. 3.12A).

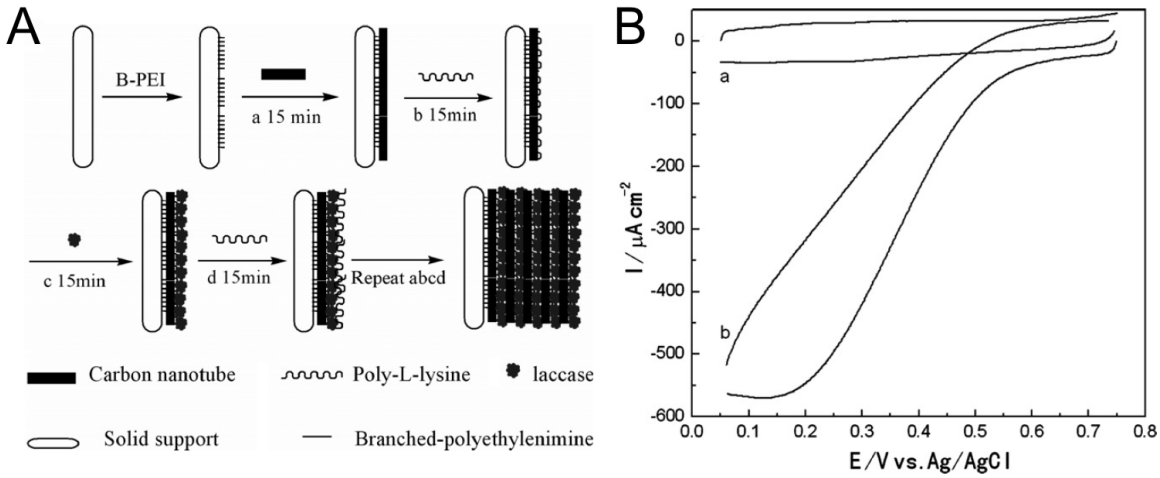

Fig. 3.12. (A) Assembly process of the (MWNT/PLL/laccase) multilayer film. (B) CVs of the MWNTs/PLL/laccase modified ITO electrodes in 0.1 M phosphate buffer (pH 6.0), under (a) N_2-saturated condition, and (b) air-saturated condition, respectively. Scan rate: 50 mV s^{-1}.

Recently, mediatorless ORR biocatalysis was reported on gold electrode modified with platinum nanoparticles (Pt-NPs) crosslinked with BOx [135]. ORR electrocatalytic current is observed at an onset potential of 0.72 V vs. NHE, which is ca. 180 mV higher comparing to the electrode without BOx. These results clearly indicate that the Pt-NP/BOx

composite electrode exhibits improved bioelectrocatalysis, and imply that BOx is electrically contacted with the electrode.

From a variety of electrode materials used for direct ORR biocatalysis carbon materials (especially carbon nanostructures) seems to be the best for achieving the highest current densities [72, 134]. Moreover, direct ORR catalysis with CueO was reported only on nanostructured carbon materials [101, 102, 129].

4 Enzymes immobilisation

Bioelectrocatalytic reaction can be observed when enzyme is not connected to electrode, but dissolved in electrolyte [136]. Then an addition of mediator (mobile redox probe, which shuttle electrons between the prosthetic group of enzyme and electrode surface) is necessary since there is no electrical contact between enzyme and electrode. Despite the fact that substantial current densities can be achieved with such system it cannot be applied in membraneless biofuel cell, because potentials of both electrodes (bioanode and biocathode) are determined by standard potential of mediator. With common mediator potential of anode would be close to cathode's resulting in negligible cell voltage. This problem can be circumvented by splitting the cell into anode and cathode compartments using a membrane and two different mediators, but such solution does not allow for miniaturization of the cell. Therefore, there is current interest for immobilization (the attachment of molecules to a surface resulting in loss of mobility) of enzyme and mediator (in the case of MET) on electrodes. Additionally, immobilization allows to employ lower amount of enzyme, what is especially important at biofuel cells working in flowing electrolyte and to achieve DET (Section 3.3) what allows to eliminate mediator.

In some cases, immobilization may lead to partial or complete loss of protein activity, due to random orientation and structural deformation. Apart from retaining the functionality of the biomolecule, the immobilization method must assure the accessibility of its active site. A close proximity between the active site of enzyme and the electrode is also desired in order to obtain an efficient electron transfer. The sensitivity, response time, long-term stability and reproducibility of the biosensor highly depend on the immobilization technique.

There are numerous problems connected with enzymes immobilization: loss of activity, leaking, random orientation and large diffusion barriers, what affects efficiency of electrodes as well as response time and sensitivity of biosensors. Currently the efforts are put

towards the development of procedures to control enzyme orientation through specific functional groups located at their surface. In this way, active sites are brought close to the electrode facilitating DET or in case of non-electrochemical applications towards the solution of substrates.

Many immobilization techniques have been developed in the past years, which are mainly based on the following three processes: physical adsorption, covalent bonding (and cross-linking) and encapsulation (entrapment).

4.1 Physical adsorption

The adsorption of enzymes on electrodes can proceed via different types of interactions. Enzymes with a large lipophilic surface area will be attracted by hydrophobic electrodes and large hydrophilic surface areas of the enzyme will interact with hydrophilic surfaces. The immobilization of the enzymes can be also ensured via ionic interactions, Van der Waals forces or hydrogen bonds. Electrostatic interactions play important role to immobilization by adsorption. The surface of the enzyme can be positively or negatively charged. It depends on the electrolyte pH and enzyme isoelectric point. To achieve efficient electrostatic attraction between enzyme and electrode surface, the latter should be charged oppositely to enzyme. It can be facilitated by modification of surface with negatively (e.g. carboxylate) or positively (e.g. protonated amino groups) functionalities.

A significant disadvantage of immobilization by adsorption is the enzyme leaching from the electrode surface.

4.2 Covalent bonding

Covalent binding of an enzyme to the electrode has the advantage that the enzyme is fixed. Thus leaching is minimized and no protein contamination of the electrolyte occurs. Moreover this method of immobilization may improve enzyme stability [137]. This is due to the fact that the formation of multiple covalent bonds between the enzyme and the electrode reduces conformational flexibility and thermal vibrations preventing protein unfolding and denaturation. A distinct disadvantage of covalent binding is the fact that the enzyme is chemically modified and this modification may affect its properties such as selectivity, specificity or efficiency. Mostly, the amino groups of the enzyme are employed for covalent immobilization (Fig. 4.1), however, other functional groups can also be utilised [138]. The

amino group as nucleophile can attack for instance an epoxide or an aldehyde. In the latter case the imine formed can subsequently be reduced, ensuring irreversible immobilisation [138]. Carbodiimides are also used, forming an amide bond with acid group on the electrode surface and vice versa [139].

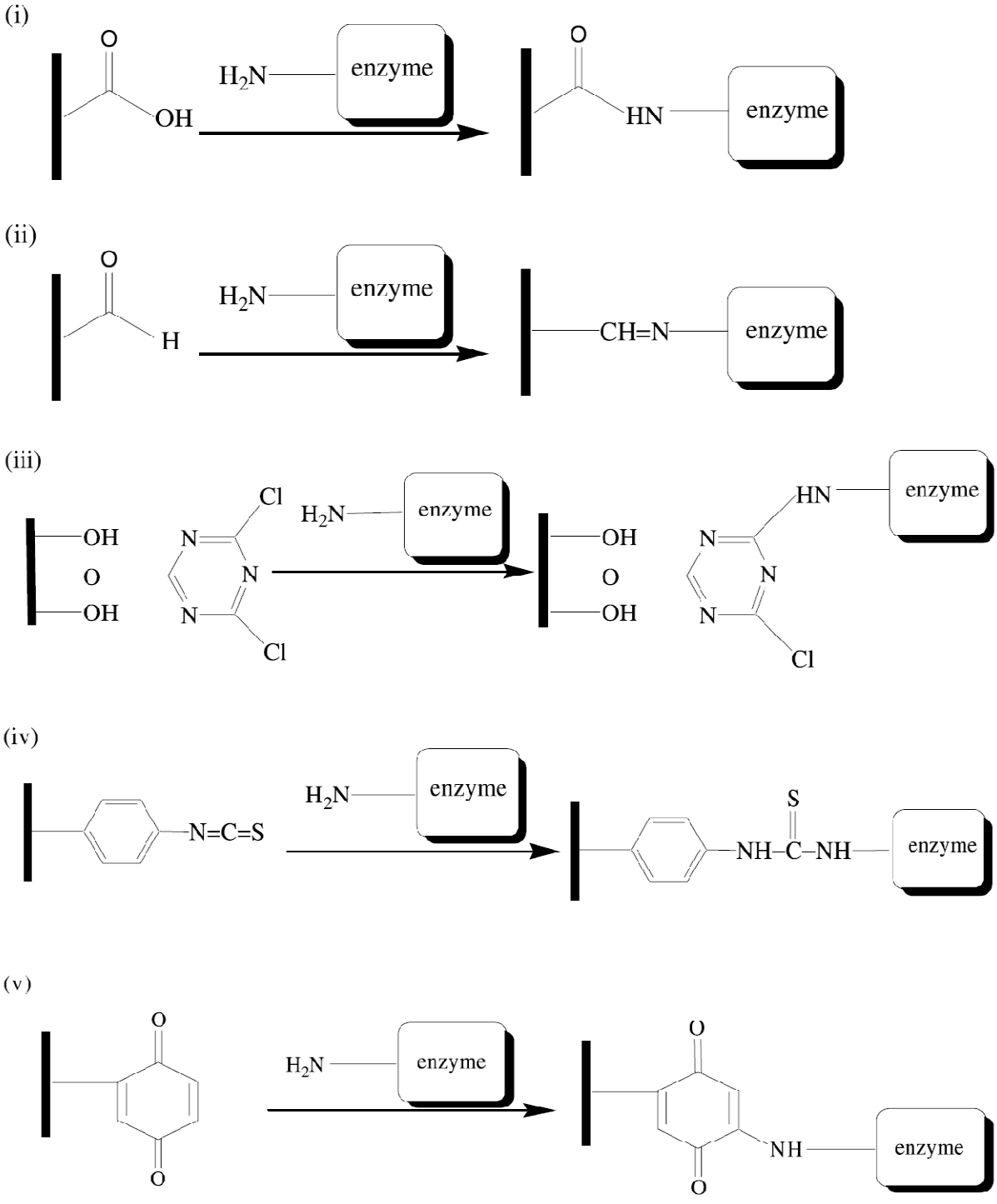

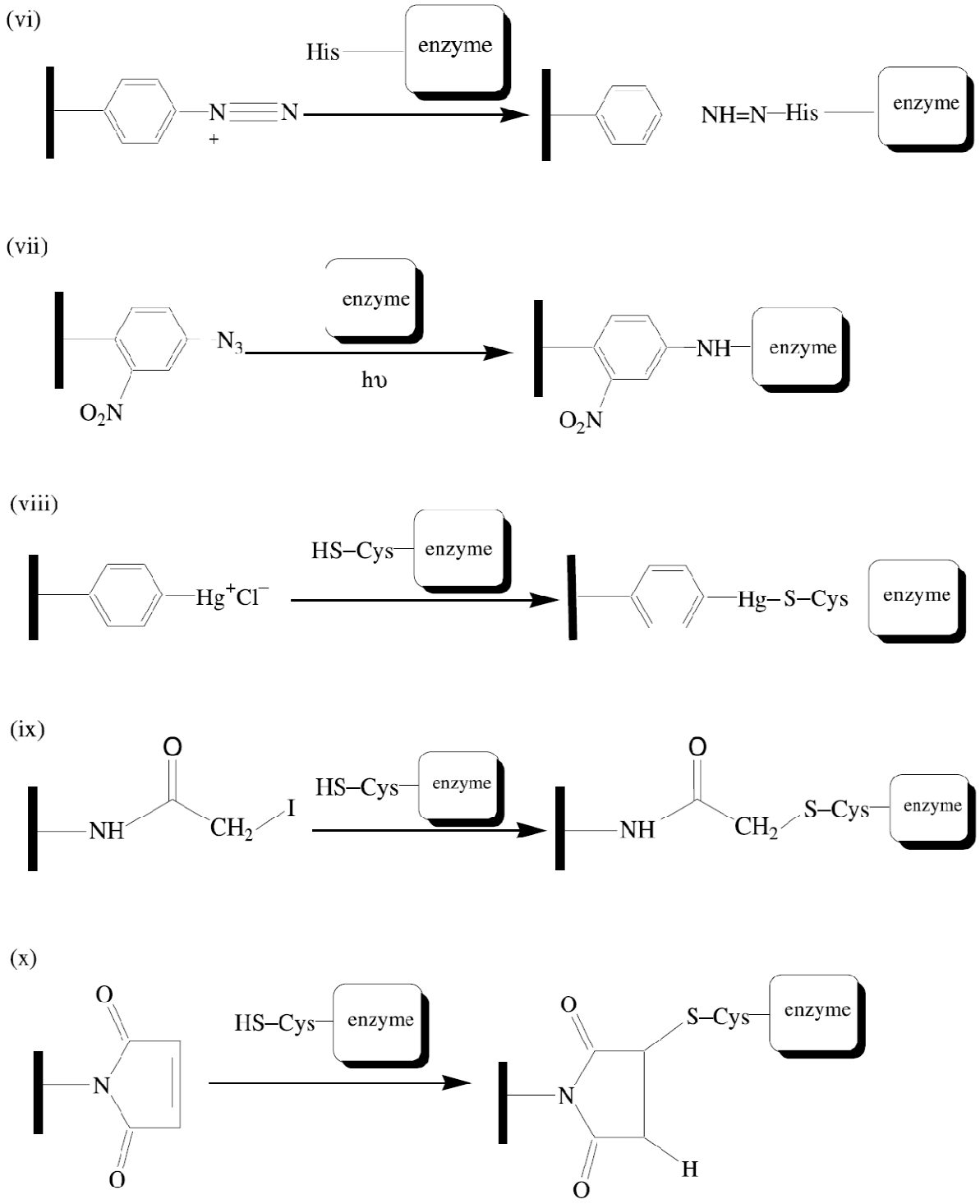

Fig. 4.1. Various surface functionalities for the covalent linkage of enzymes [140].

Self-assembled monolayers (SAMs) also provide a robust method of enzyme immobilization with some control over its orientation and distribution. The affinity of thiols for some metal surfaces, particularly gold, makes alkanethiols ideal for the preparation of modified electrodes. Alkanethiols adsorb spontaneously onto the surface of gold, silver, platinum and copper [141]. Their monolayers can be used to immobilize proteins close to the electrode surface [142, 143]. Gold is the most frequently used metal because it does not form

a stable oxide under ambient conditions. The thiol groups form with Au of a thiolate bond (Fig. 4.2) [144]. SAMs have been shown to be stable inside potential window between approximately -0.8 and +0.6 V versus Ag|AgCl [145]. Outside this range the thiols are reduced or oxidized and finally desorbed. There are two basic approaches to enzymes immobilization onto electrodes using alkanethiols. Either the enzyme can be bonded to an existing SAM [146] or the enzyme can be modified with thiol moieties which bond to the electrode [147]. Enzyme can be also attached to prepared SAM by electrostatic interactions [148].

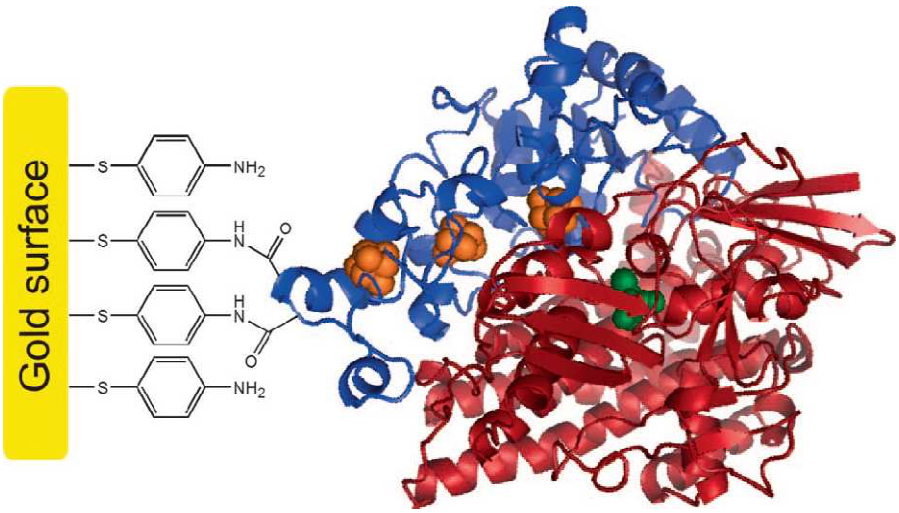

Fig. 4.2. Schematic view of hydrogenase covalently attached to Au surface modified with SAM [143].

An extreme case of covalent binding is crosslinking of enzymes by using a bi-functional agent (e.g. glutaraldehyde [149]). Instead of fixing the enzymes to the electrode, the biomolecules are connected together creating aggregates (Fig.4.3). After immobilization of aggregates on the electrode surface, enzyme surface concentration is superior to that obtained by other methods, but only those molecules which are in direct contact with the electrode can exchange electrons and for improving the efficiency the use of mediator is recommended.

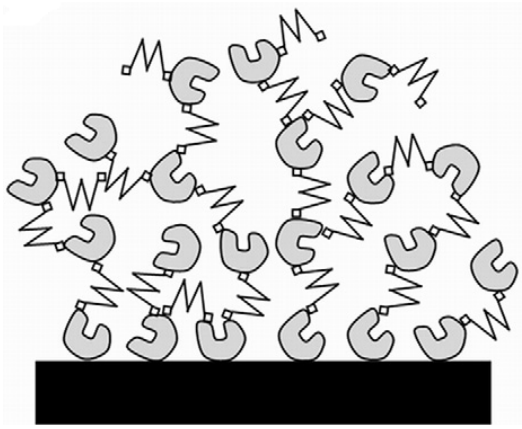

Fig. 4.3. Aggregate of cross-linked enzyme [150].

4.3 Encapsulation

The best method of enzyme immobilization which allows avoiding negative influence on the structure of an enzyme is encapsulation. Many encapsulation methods have been developed [151-155].

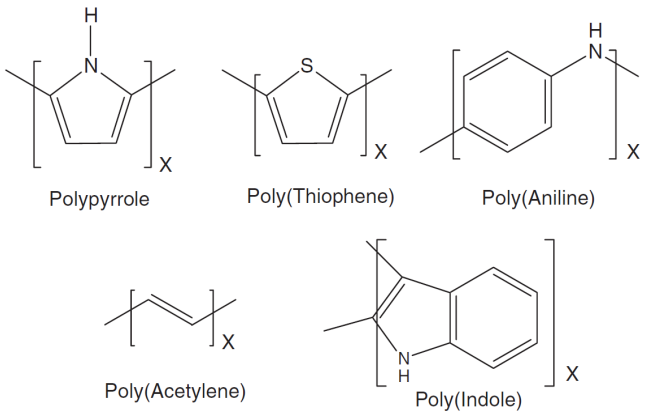

Fig. 4.4. Selected electronically conductive polymers.

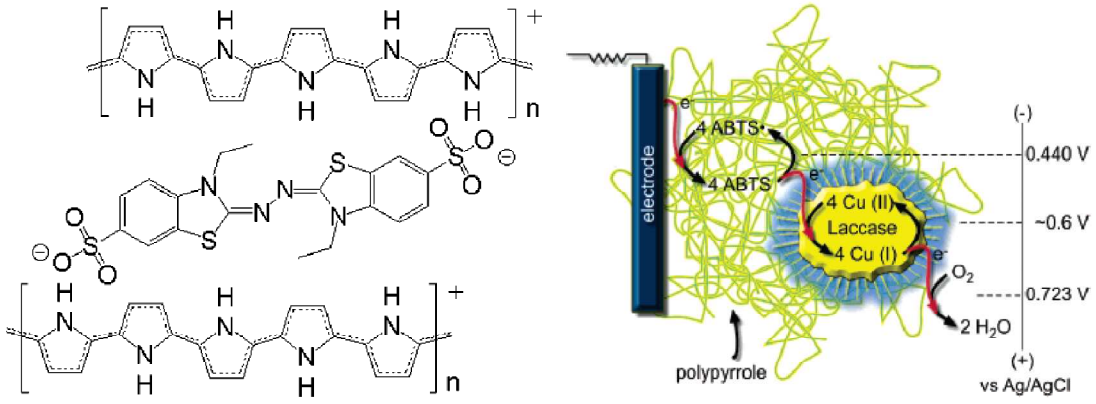

Fig. 4.5. Molecular structure of polypyrrole and ABTS composite and a scheme of bio-ORR at an electrode coated with this composite and laccase [151].

Electronically conductive polymers (Fig. 4.4) provide appropriate environment for enzyme immobilization and its interaction with conductive materials. These polymers can be

deposited electrochemically in the presence of enzyme in solution. For example polypyrrole was used to simultaneous immobilization of laccase and its mediator – ABTS (Fig. 4.5) [151].

Special approach to MET accomplishment is to immobilize an enzyme within a redox polymer, which consist of redox-active pendant moieties attached to a polymer backbone. The most used for enzyme incorporation are the polymers with osmium redox complexes moieties (Fig. 3.6) [93, 152]. Moreover, the presence of charged moieties facilitates enzyme immobilization providing electrostatic interactions. The concentration of these moieties, and their redox potential may be varied to control electron transport and reaction kinetics.

Another interesting matrix for enzyme encapsulation involving liquid-crystalline cubic phase (Fig. 3.8), which resembles the natural environment of membrane proteins, was recently proposed [113]. The cubic phase was prepared by mixing monoolein (1-oleoyl-rac-glycerol) with enzymes and different mediators, including tetrathiafulvalene (TTF) and ABTS.

Apart from polymers [93, 150, 152, 153] and carbohydrates [154, 155], the prominent one and widely used is the sol–gel method (Section 6.1).

Sol-gel processed thin film on the electrode surface act as a semi-permeable membrane, which allows to free passage of the substrate and product but confines the enzyme in a fixed cavity (Fig. 4.6). In order to obtain such membrane one can mix enzymes with sol-gel precursor and deposit this mixture by dip-coating [156], spin-coating [157] or sol drop evaporation [158]. As solvent evaporates, the sol-gel process takes place and the biomolecules are entrapped in the silica networks. However, such process suffers some disadvantages – it is time-consuming and despite porosity of obtained matrix, diffusion of substrate to the enzyme can be restricted. To increase porosity Yang *et al.* used recently electrochemically induced sol-gel process with simultaneous hydrogen evolution [159]. When a negative potential is applied to the working electrode, reduction of water of the precursor solution alters the local pH, which in turn induces the sol-gel process to form silica matrix with encapsulated enzyme. The evolved hydrogen bubbles help to form a porous structure.

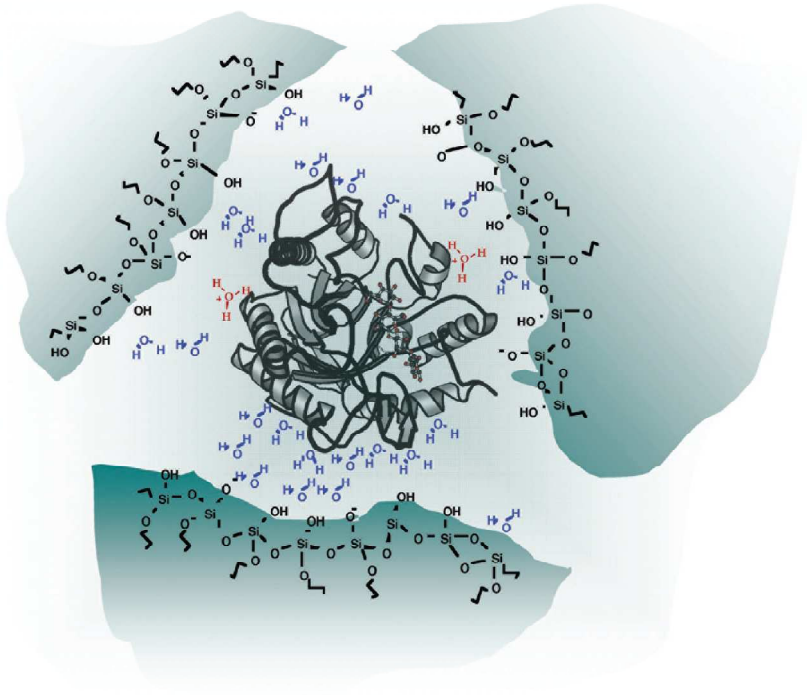

Fig. 4.6. Schematic view of the entrapped enzyme inside a pore in silicate matrix [160].

5 Enzymatic fuel cells

Enzymatic fuel cells unlike traditional fuel cell, which are mainly based on noble metal catalysts, employ enzymes as catalysts. Usually, the systems where both anode and cathode utilize biocomponents are referred as “biofuel cells” (BFCs). The device, where only one electrode compartment contain biocatalyst, is called as a “hybrid cell” [161]. If the enzyme is located inside living cell, such device is referred as “microbial fuel cell” [162]. The use of isolated enzymes allows to overcome the limits of microbial fuel cells, caused by mass transfer resistances across the cell membranes [163]. On the other side, enzymes still cannot compete with microbes in terms of long-term stability.

BFCs are predicted be used as an implantable power source for a variety of medical devices used in modern medicine such as drugs dispensers, and sensors monitoring body functions. The main advantage of BFCs over conventional fuel cells is lower cost of their components.

The working principle is the same as in conventional fuel cells, namely fuel is oxidized at the anode, and the electrons that are released from fuel by the oxidation reaction flow through an external electrical circuit generating electrical current. Finally, the electrons reach the cathode, where they are delivered to oxidant (mostly oxygen) (Fig. 1.1B).

Enzymes exhibit high turnover numbers, selectivity, specificity and activity under mild conditions (neutral pH and near-body temperature). The specificity results in decreased reactants crossover, what enables to construct a membraneless device. Moreover, biocatalysts allow oxidizing more complex fuels than hydrogen or methanol as in case of conventional fuel cells.

The main disadvantage of enzymes is the fact that they suffer from deactivation. Another drawback is the lower volumetric catalyst density. Single enzyme macromolecule, which provides only one catalytic site, is larger than active site of inorganic catalyst, so the number of active sites per volume is usually lower compared to conventional catalysts.

In last years the progress in biofuel cell research has often been reviewed in the literature [3, 83, 96, 163-177]. These papers provide a useful overview by discussing general aspects, fundamentals and classification in biofuel cell research.

5.1 Fuels

There are a number of fuels for enzymatic fuel cells including variety of sugars and low aliphatic alcohols. The main fuels and the enzymes which catalyze their oxidation are listed in Table 5.1.

The most often employed fuel for enzymatic biofuel cells is glucose [123, 136, 178]. Due to its versatility in nature and essential role in a variety of living organisms as a source of energy glucose is predicted to be an oxidant in implanted BFCs. Other sugars that have been employed as fuels in BFC are fructose [179], as well as lactose and cellobiose [180]. Other important fuels that have been used in enzymatic fuel cells are aliphatic alcohols such as methanol [181], ethanol [135] and glycerol [182]. Comparing to methanol and ethanol, the last one alcohol is characterized by higher energy density, lower vapour pressure and lower toxicity.

As one can notice, most enzymes do not catalyze total oxidation (to CO_2 and H_2O) of organic compounds. Bioanodes modified with only one enzyme limit the number of electrons gained from electrooxidation of one fuel molecule. The employment of enzyme cascades [165] allows to better utilization of the chemical energy of the fuel and can be used for its complete oxidation to CO_2. As a result increased the total current density can be attained.

5.2 Anodic enzymes

The most widely employed enzyme for anodes in BFCs is glucose oxidase (GOx). It catalyzes conversion of glucose to gluconolactone, which spontaneously hydrolyzes to gluconic acid (Fig. 1.1B). The redox co-factor responsible for the catalytic function of GOx is flavin adenine dinucleotide (FAD). The natural oxidant of GOx is oxygen, which is reduced to hydrogen peroxide [183]. In a membraneless BFC cathodic reagent – oxygen compete with anode for electrons released by GOx causing depletion of anodic current density.

Another enzyme for bioanode, recently introduced by Gorton and co-workers for BFCs applications is cellobiose dehydrogenase (CDH) [126, 184]. Its natural substrate is cellobiose but CDH can also oxidize lactose as well as glucose. Oxygen is not natural electron acceptor for CDH what makes this enzyme superior to GOx in membraneless BFCs applications. Prosthetic group of CDH contain flavin and heme domain.

Table 5.1. Fuels and enzymes used in enzymatic biofuel cells [3].

Fuel	Enzyme	Co-factor	Half-Cell Reaction
glucose	glucose oxidase, EC 1.1.3.4	FAD	glucose → glucono-1,5-lactone + $2H^+ + 2e^-$
	glucose dehydrogenase, EC 1.1.1.47	NAD	see above
	glucose dehydrogenase, EC 1.1.5.2	PQQ	see above
	cellobiose dehydrogenase, EC 1.1.99.18	FAD, heme	see above
fructose	fructose dehydrogenase, EC 1.1.99.11	FAD, heme	fructose → 5-dehydrofructose + $2H^+ + 2e^-$
cellobiose	cellobiose dehydrogenase, EC 1.1.99.18	FAD, heme	cellobiose → cellobiono-1,5-lactone + $2H^+ + 2e^-$
lactose	cellobiose dehydrogenase, EC 1.1.99.18	FAD, heme	lactose → 4-O-(galactopyranosyl)-glucono-1,5-lactone + $2H^+ + 2e^-$
methanol	alcohol dehydrogenase*, EC 1.1.1.1	NAD	alcohol → aldehyde + $2H^+ + 2e^-$
	aldehyde dehydrogenase*, EC 1.2.1.5	NAD	aldehyde + H_2O → acid + $2H^+ + 2e^-$
	formate dehydrogenase*, EC 1.2.1.2	NAD	formate → CO_2 + $2H^+ + 2e^-$
ethanol	alcohol dehydrogenase, EC 1.1.99.8	PQQ, heme	alcohol → aldehyde + $2H^+ + 2e^-$
	alcohol dehydrogenase*, EC 1.1.1.1	NAD	see above
	aldehyde dehydrogenase*, EC 1.2.1.5	NAD	see above
	alcohol dehydrogenase, EC 1.1.99.8	PQQ, heme	see above
glycerol	alcohol dehydrogenase*, -	PQQ, heme	alcohol → aldehyde + $2H^+ + 2e^-$
	aldehyde dehydrogenase*, -	PQQ, heme	aldehyde + H_2O → acid + + $2H^+ + 2e^-$
	oxalate oxidase*, EC 1.2.3.4	FAD, Mn	oxalate → $2CO_2$ + $2H^+ + 2e^-$
pyruvate	pyruvate dehydrogenase*, EC 1.2.4.1	NAD	pyruvate + CoA→ acetylCoA + $2H^+ + 2e^-$
hydrogen	membrane-bound hydrogenase, -	-	H_2 → $2H^+ + 2e^-$

*enzymes taking part in complete fuel oxidation

Other enzymes from the family of dehydrogenases that have been used in enzymatic biofuel cells are glucose dehydrogenase (GDH) [185] and fructose dehydrogenase (FDH) [179, 186] for oxidation of glucose and fructose, respectively.

Alcohols can be totally oxidized on bioanodes with enzyme cascades. A sequence of alcohol dehydrogenase (ADH), aldehyde dehydrogenase and formate dehydrogenase has been used for oxidation of methanol to CO_2 [165, 181, 187, 188].

5.3 Mediators

Similarly to biocathodes and ORR catalyzing enzymes, electronic communication between electrode and anodic enzyme can be assured by direct electron transfer or employment of mediator, which acts as acceptor of electrons from enzyme. Contrary to mediators for cathodic enzymes, redox potential of mediator for anodic catalyst cannot be lower than redox potential of enzyme prosthetic group. The most often used diffusive mediators for GOx are: ferrocene monocarboxylic acid [189], *p*-benzoquinone [190], pyrroloquinoline quinone (PQQ) [191], 8-hydroxyquinoline-5-sulfonic acid (HQS) [110] and tetrathiafulvalene [113]. HQS and was also co-entrapped with GOx in polypyrrole nanowires, grown on anodized aluminium oxide template [192]. Similar like in case of laccase and BOx based biocathodes, Os-based redox polymers was used as mediators and matrices for GOx immobilization [193-195].

Mediatorless electrocatalytic oxidation of glucose with GOx was also reported. Dong and co-workers employed CNT's-ionic liquid viscous gel as an matrix for GOx immobilization [196]. Wang *et al.* immobilized GOx on SWCNT's deposited on silicon substrate and the resulting electrode was employed in a membraneless and mediatorless biofuel cell [197]. Recently Mano *et al.* reported that the deglycosylated GOx is able to oxidize glucose on glassy carbon electrode without mediator (Fig. 5.1) [198]. Onset potential of -0.29 V versus SHE corresponds to the reversible potential of the $FAD/FADH_2$ couple.

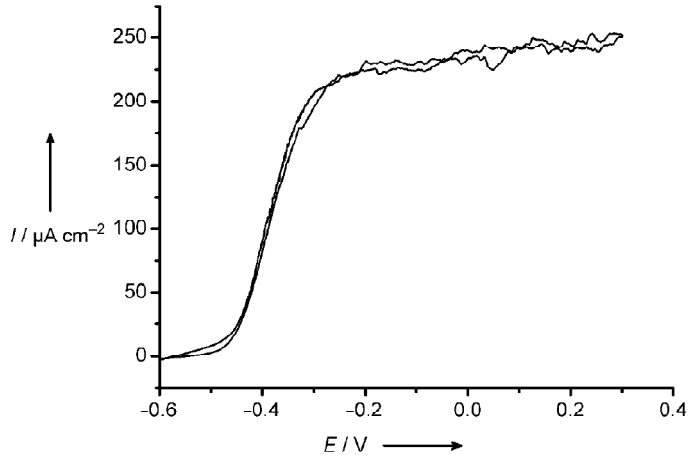

Fig. 5.1. Direct electrooxidation of 45 mM glucose on a monolayer of deglycosylated GOx adsorbed on a GC electrode (20 mM phosphate buffer, pH 7.4, scan rate: 5 mV s^{-1}, 500 rpm, argon atmosphere) [198].

5.4 Biofuel cells - examples

More than hundred examples of BFCs were reported in literature. Here, in my humble opinion only three of the most interesting are presented.

One of them, which utilize living plant energy was reported by Heller and co-workers in year 2003 [194]. Two electrodes prepared from (2 cm in length and 7 μm in diameter) modified with GOx (anode) and BOx (cathode) were implanted in a grape. The cell exhibited the highest power density (2.4 μW cm^{-2} at 0.52 V) when the cathode fibre was located near the skin of the grape, where the oxygen concentration is higher, than near the centre of the grape (Fig. 5.2).

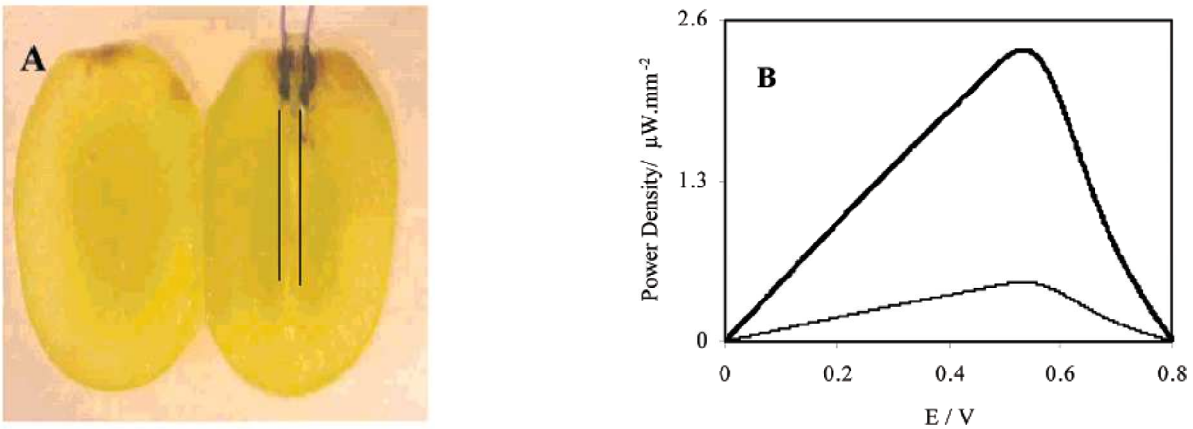

Fig. 5.2. Photograph of a grape with the implanted fibres and their electrical contacts. Because in the photographs the 7 μm diameter fibres were barely visible, lines are drawn to show their positions (A). Dependence of the power output on the cell voltage with the cathode fibre implanted near the skin of the grape (bold line) and near the centre of the grape (fine line) (B) [194].

Biofuel cell, which exhibits the highest reported power density to date (1.45 mW cm^{-2} at 0.3 V) was developed by Sakai *et al.* [178]. This device utilizes glucose as fuel on GDH-based bioanode, and O_2 as reductant on BOx-based gas-phase biocathode at pH 7 in presence of 0.4 M glucose under quiescent conditions. Enzymes and mediators are densely entrapped on carbon-fibre electrodes and the cathode structure is designed to supply O_2 efficiently. The cell units with a multi-stacked structure successfully operate a radio-controlled toy-car, what demonstrates the potential of biofuel cells in practical applications.

The only example of a membraneless BFC with a dissolved mediator is the microfluidic BFC [199] with two parallel streams: anolyte and catholyte consisting of dissolved ABTS and laccase. This system seems to be promising because the continuous supply of the enzyme solves the problem of its instability while laminar flow of two parallel streams allows for membraneless contact between the catholyte and the anolyte.

5.5 Enzymatic Zn-O_2 batteries

The main disadvantage of BFCs is weak enzymes stability. Potentially implantable caseless cell was suggested by Heller as an alternative to enzymes-containing BFCs [103]. Suggested cell consist of a miniature, Nafion-coated Zn anode [200] and a biocompatible hydrogel-shielded Ag/AgCl cathode or O_2-reducing biocathode. A model of that one with bioanode has been already constructed [201, 202]. During discharging of Zn anode in saline buffer a hopeite-phase ($Zn_3(PO_4)_2 \cdot 4H_2O$) is created on its surface providing Zn^{2+} conducting solid electrolyte film. The film blocks the transport of O_2 to the Zn, preventing its corrosion, while allowing the necessary transport of Zn^{2+}.

For example modern pacemakers consume ca. 1.3 µJ of energy per pulse [203]. Under assumption of average patients pulse 60 min^{-1} and 1 V of cell voltage, the pacemaker consume 41 C (11.4 mAh) of charge per year. This corresponds to 14 mg of Zn oxidized to Zn^{2+}. Due to low redox potential of Zn (E^0 = -0.76 V vs. NHE [204]) Zn-O2 cell voltage is higher than that of glucose-O_2 biofuel cell and exceeds 1 V.

Table. 5.2. Parameters of small commercially available batteries and conceptually implantable cells [103].

Cell	Li–MnO_2	Alkaline Zn–air	Alkaline Zn–MnO_2	Zn–AgCl (projected)	Zn–O_2 (projected)	Glucose–air (projected)
Availability	Commercial	Commercial	Commercial	Laboratory	Laboratory	Laboratory
Intended site of use	External electronics	External electronics	External electronics	Subcutaneous tissue	Subcutaneous tissue	Subcutaneous tissue
Package/case	Steel	Steel	Steel	None	None	None
Anode	Li	Zn	Zn	Zn	Zn	Wired GOx
Cathode	C(MnO_2)	C(Mn)	C(MnO_2)	Ag/AgCl	Wired BOD	Wired BOD
Electrolyte	Organic	6 M KOH	6 M KOH	Subcutaneous fluid	pH 7.4 saline buffer	pH 7.4 saline buffer
Smallest size, in mm^3	200	50	200	0.1	0.05	0.01
Power density, in W/L	300	150	200	50	10	1
Specific energy, in Wh/L	650	1800	600	500	5000	50,000
Operational life	3 years	1 month	1 year	1 month	2 weeks	2 weeks

The smallest commercially available implantable batteries and concept caseless cells are listed in Table 5.2. Despite operational lifetime all parameters for concept Zn-O_2 battery are advantageous. One can notice that improvement of operational lifetime of enzymatic cells is a challenge.

The electrodes studied in this thesis are tested as biocathodes in Zn-O_2 hybrid cells.

6 Carbon ceramic electrode

Carbon ceramic electrode was developed by Lev in 1994 [6] as an alternative to carbon paste electrode [205]. Apart from broad possibilities of modification, the main advantages of CCEs as working electrodes are: large potential window in aqueous electrolytes with low background current, fast kinetics for a number of mediators, high signal to background current, and high stability after prolonged immersion in electrolyte [206]. The carbon-ceramic composite material consists of interconnected carbon particles entrapped in continuous, porous silica matrix obtained in sol-gel process.

6.1 Sol-gel process

The name “sol-gel” is applied to process and materials concerning the strategy of preparation which include transformation from sol to gel. Sol is a suspension of colloidal solid particles within a liquid. A gel obtained from sol in so called sol-gel transition is a porous 3-dimensionally interconnected solid network that expands throughout a liquid medium [207, 208]. Apart from metal (e.g. Al, Ti, V, Zr) alkoxides, silicon alkoxides are the most popular precursors of sol-gel process. Their use results in creation of silicates which are components of electrodes and other samples described in this thesis. Therefore this section is focused on preparation of silica sol-gel materials.

Gel formation from alkoxides is known for more than 150 years. The first report concerning sol-gel processing – synthesis of silicate monoliths from a tetraethoxysilane precursor (made from tetrachlorosilane and ethanol) was done by a French scientist J. Ebelmen in 1846 [207]. In recent decades an increasing interest in the area of sol-gel derived materials and its application to (electro)analytical chemistry is observed. The main advantage of silica and organosilica materials is the possibility to control its structure, composition, morphology and porosity during low temperature processing. Nowadays, a concise literature concerning sol-gel science and its fundamentals is available [207, 208].

The starting mixture for sol-gel process usually include precursor (one or more), a solvent, a catalyst (acid or base), and water (can be from humid surroundings). Sol-gel processing of silica involves hydrolysis of silicon alkoxide precursors (in this thesis tetramethyoxysilane (TMOS) or methyltrimethoxysilane (MTMOS)):

$$Si(OCH_3)_4 + 4\ H_2O \rightarrow Si(OH)_4 + 4\ CH_3OH \qquad (6.1)$$

$$H_3C\text{-}Si(OCH_3)_3 + 3\ H_2O \rightarrow H_3C\text{-}Si(OH)_3 + 3\ CH_3OH \qquad (6.2)$$

and H^+ or OH^- catalysed condensation:

$$2\ Si(OH)_4 \rightarrow (OH)_3Si\text{-}O\text{-}Si(OH)_3 + H_2O \qquad (6.3)$$

$$2\ H_3C\text{-}Si(OH)_3 \rightarrow CH_3\text{-}Si(OH)_2\text{-}O\text{-}Si(OH)_2CH_3 + H_2O \qquad (6.4)$$

Finally in polyconcensation process a sol containing solid particles made of macromolecular network of siloxane bonds is created (Fig. 6.1).

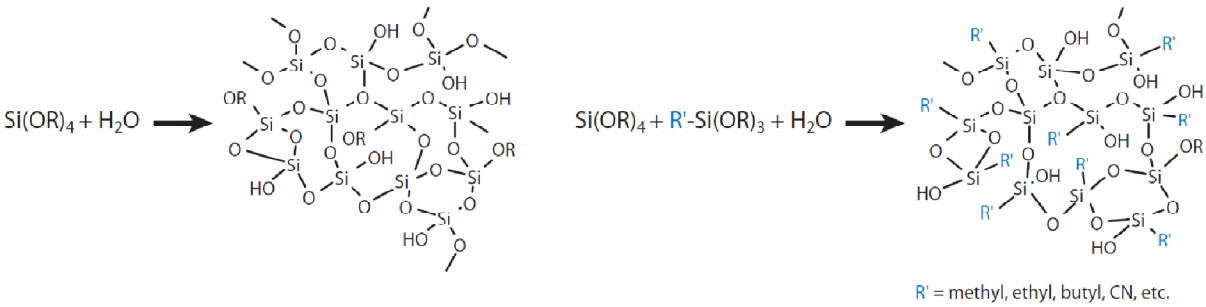

Fig. 6.1. A simplified view of sol-gel processing of silica and organosilica [209].

Next, in gelation step sol particles are connected creating 3-dimensional solid network with entrapped solvent. It is worth a mention that these steps are not only consecutive but also parallel.

The structure of obtained silicates depends not only on formation path, but also on further aging, drying, and sometimes heating steps (Fig. 6.2). Tuning of their experimental

parameters allows controlling the microstructure of the final material. Wide-open aerogels, highly porous monoliths or particles, less porous xerogels and silica thin films can be obtained [210]. One of the most efficient route to control porosity of ordered mesoporous silicates (pore size 1.5–10 nm, surface area > 1000 m^2 g^{-1}) is application of surfactant template [211]. Macropores can be introduced into the silicate matrix using colloidal ordered template of latex spheres ranging in diameter from 50 nm to 1 µm. After material formation the template is removed via calcination or chemical treatments [212] (Fig. 6.2).

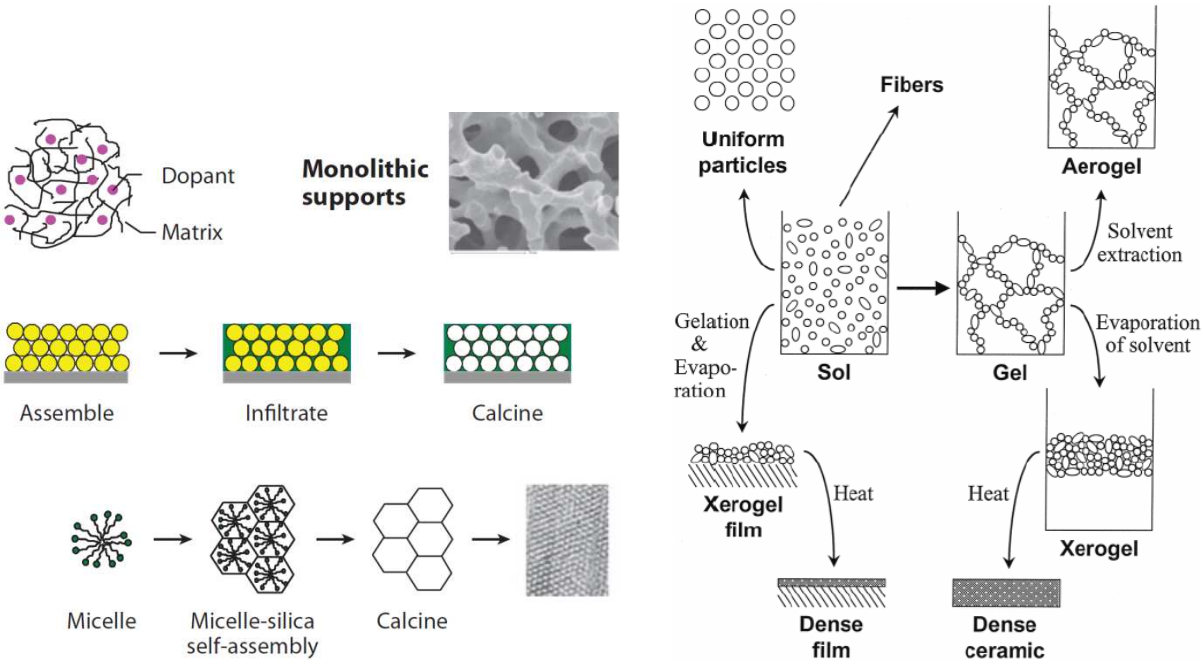

Fig. 6.2. Schematic representation of sol-gel materials processing [209].

Sol-gel chemistry is also a tool for the synthesis of inorganic-organic hybrid materials with special properties. They can be obtained by impregnation, doping, physical entrapment of organic compounds within sol-gel matrices, or via co-condensation of organosilane reagents [213].

6.2 Preparation of carbon ceramic electrodes

The first step of CCEs preparation is the dispersion of carbon powder within a silica sol. The sol is then allowed to form a gel and to dry forming a porous rigid matrix [6]. Usually after 24 hours of electrode aging electrode is ready to use. The silicate backbone provides better mechanical properties than these exhibited by carbon paste electrodes (CPE) [206]. Another aspect of wetted (hydrophilic) CCEs superiority over CPEs is the porosity of the binder, and

therefore their electrochemically active area is not confined to the outermost surface as in the CPE. Additionally, the surface of the CCEs can be renewed by mechanical polishing.

CCEs can be obtained in various configurations, including bulky cylinders, monolithic rods, at plates, miniature electrodes or even thin films [5, 214] and screen-printed electrodes [215].

Cordero-Rando *et al.* proposed another sol-gel-based procedure to obtain solid carbon composite electrodes called sonogel electrodes [216]. This procedure is based on the use of sonocatalysis to apply high-energy ultrasound directly to the precursors. This way, ultrasonic cavitation is achieved, so that hydrolysis with acidic water is promoted in the absence of any additional solvent and the time needed to get a unique phase is reduced.

The preparation of traditional CCEs requires long time for sol-gel process and drying (at least 24 h). Recently Abbaspour and Ghaffarinejad accelerated its preparation of CCE employing microwave irradiation, which requires only a few minutes [217].

6.3 Control of carbon ceramic electrodes properties

The physicochemical properties of silicates can be easily controlled by application of suitable sol-gel precursor, mixture of precursors or/and dopants (Section 6.2). For example it is possible to control electrode wettability by water. Application of hydrophobic organofunctional groups increases the hydrophobicity of the electrode, what is manifested by wide contact angle of water droplet (Table 6.1). A complete control of surface hydrophobicity (from completely wetted surface to hydrophobic electrode with very limited wettability) can be achieved by applications of sol-gel precursor with different functional groups. In the case of hydrophobic precursors (e.g. MTMOS) the resulting electrode repulses water leaving only carbon islands at the CCE surface in contact with the electrolyte.

Table 6.1. Contact angles of water droplets on CCEs prepared using different types of sol-gel precursors [206].

Silicate precursor	*Chemical formula*	*Molecular weight*	*Wetting angle,°*
Methyltrimethoxysilane	$[CH_3]Si(OCH_3)_3$	136	78
Ethyltrimethoxysilane	$[CH_3CH_2]Si(OCH_3)_3$	150	72
Phenyltrimethoxysilane	$[C_6H_5]Si(OCH_3)_3$	198	76
(3-Glycidoxypropyl)trimethoxysilane	$[CH_2(O)CHCH_2O(CH_2)_3]Si(OCH_3)_3$	235	21
(3-Glycidoxypropyl)trimethoxysilane/ methyltrimethoxysilane 1 : 1 (molar ratio)	$[CH_2(O)CHCH_2O(CH_2)_3]Si(OCH_3)_3$ / $[CH_3]Si(OCH_3)_3$	235 / 136	45
n-Octyltrimethoxysilane	$[CH_3(CH_2)_7]Si(OCH_3)_3$	234	72
3-Methacryloxypropyl-trimethoxysilane	$[CH_2=C(CH_3)C(O)O(CH_2)_3]Si(OCH_3)_3$	248	63
Tetramethoxysilane	$Si(OCH_3)_4$	152	Totally wetted
3-Cyanopropyltriethoxysilane	$[CN(CH_2)_3]Si(OC_2H_5)_3$	231	Totally wetted

From hydrophilic precursors (e.g. TMOS) a flooded CCEs is obtained and electrolyte penetrates into the bulk of the electrode. For catalytic and biocatalytic applications, flooded electrodes are superior compared to flat surface electrodes because larger catalyst surface can be exposed to the electrolyte than on the outer surface of an electrode.

The second component – interconnected carbon grains provide electron conductivity along percolation paths. The properties of the CCEs depend significantly on the type of carbon powder mixed with sol-gel precursors. Depending on the grain size, the conductivity percolation threshold varies from a few weight percent for carbon black to ca. 30% for large grains (Fig. 6.3). Moreover, the presence of carbon provides diverse possibilities of its covalent modification [218].

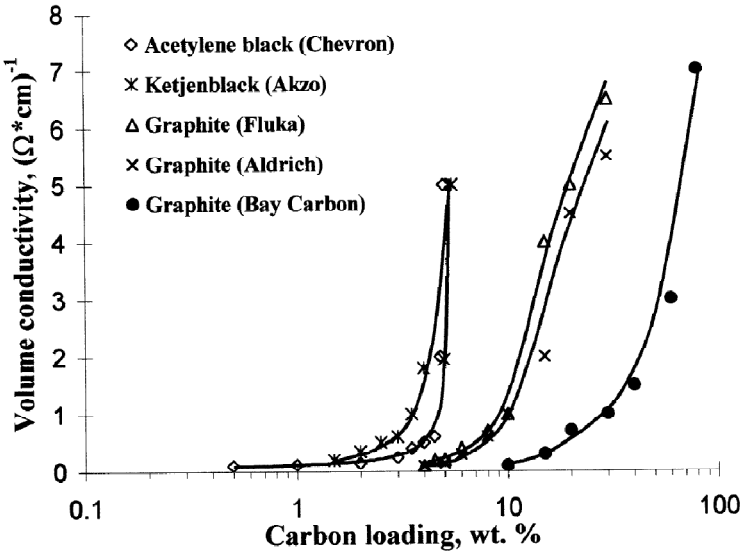

Fig. 6.3. Dependence of the specific conductivity of CCEs on carbon loading for different carbon powders[206].

6.4 Redox modification of carbon ceramic electrodes

A number of publications is devoted to redox modifications of CCEs mainly for fundamental research of interfacial ion transfer [219, 220], sensing applications and providing electrons shuttle to enzymes [221]. Redox active groups can be introduced to CCEs in different ways, such as doping the redox species to the sol used for electrode preparation [222], binding the redox-active groups to the precursors [206], impregnation with the redox liquid [219, 220], covalent modification of carbon particles [218], or adsorption of the redox modifier on their surface [223].

6.5 Electroanalytical applications of carbon ceramic electrodes

Many applications of CCEs were devoted to amperometric electroanalysis. These CCE-sensors can be modified by redox mediators [219, 220], ligands [224], catalysts [225, 226] and biocatalysts [221, 227, 228]. Since CCE had been proposed a numerous papers involving its application as sensors and biosensors (sensitive to biological analyte or containing biological component) were published. Some of them was devoted to sensing: acetaminophenol [229], adrenaline [229, 230], ascorbic acid [229-231], bromate [232, 233], chlorate [234], cysteine [229, 235, 236], cystine [237], dopamine [229, 230], glucose [238-241], glutathione [242], hydrazine [243], hydrogen peroxide [228, 244, 245], insulin [246], iodate [247], methionine [237], NADH [248-250], oxygen [225], pH [6, 251], phenolic compounds [252-257], pyridoxine (vitamin B6) [258], silver [259, 260], sulfide and sulfur oxoanions [261], uric acid [229, 230].

Two of these sensors are pH-sensitive [6, 251]. The idea of voltammetric pH measurement is to measure the redox potential (usually mid-peak potential in CV or peak potential in differential pulse voltammetry (DPV)) of a pH-sensitive redox probe attached to the electrode. If protons are involved in electrochemical reaction:

$$\mathrm{Ox} + n\mathrm{e}^- + m\mathrm{H}^+ \leftrightarrows \mathrm{R} \tag{6.5}$$

then according to Nernst equation, redox potential depends linearly on pH:

$$E = E^{0'} + \frac{RT}{nF}\ln\frac{[\mathrm{Ox}]}{[\mathrm{R}]} - \frac{m}{n}0.059\mathrm{pH} \tag{6.6}$$

Voltammetric pH measurement with CCE was demonstrated by Tsionsky *et al.* with 9,10-phenanthrenequinone doped CCEs [6]. An almost Nernestian dependence of the anodic peak current on pH is found over a wide pH range (0-7): d*E*/dpH = 60.2 mV. Quinhydrone modified electrodes exhibited a larger linear pH range (0-9). Small leaching of the quinones from the electrode during prolonged continuous cycling does not affect its accuracy because a potential shift (pH-determining) does not depend on the peak current.

An interesting CCE-based sensor, proposed by Salimi *et al.* [230], is capable to simultaneous voltammetric determination of ascorbic acid (AA), dopamine (DA) and uric acid (UA) (Fig. 6.4).

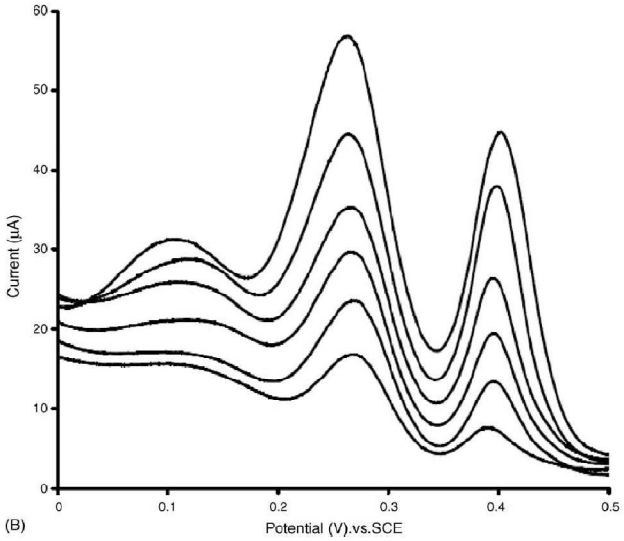

Fig. 6.4. Square wave voltammograms of 10 µM of AA, 1 µM DA, and 2 µM UA at CCE in 0.1M phosphate buffer pH 5. Concentrations of AA, DA, and UA are simultaneously changed: 10, 20, 30, 40, 50 µM of AA and 1, 2, 3, 4, 5 and 6 µM DA and UA [230].

CCE has been also modified to obtain antibody-antigen interactions-based immunosensor [224]. Several potentiometric applications were also demonstrated. Ion sensitive CCEs were constructed by incorporation of $AgNO_3$ into the starting sol-gel solution and silver reduction after gelation [6]. The resulting electrode exhibited a linear (49 mV/decade) potential dependence on chloride ion for 1-100 mM range. Such Ag|AgCl-CCE can also serve as reference electrode. Because its active surface is rather high, it can be used in a two-electrode cell even under significant current densities.

6.6 Application of carbon ceramic electrodes for energy conversion and storage

As it was said earlier, graphite (intrinsic component of CCE) exhibits poor electrocatalytic activity towards ORR (Section 2.3). However, the addition of metallic or organometallic catalysts to the electrode body improves its performance. CCE because of its porous structure can work as gas electrodes – permeable for gaseous compounds so that the gas (e.g. O_2 for fuel cell cathode) feed can be introduced to the back side of the electrode, diffuse through it, and react at the solid-liquid interface (Fig. 15.10). CCEs modified with cobalt porphyrin [262, 263], Pd [264, 265], Pt [225, 226] and naphtoquinone [222] were reported as oxygen cathodes. CCE was also modified with laccase [214, 254] or horseradish peroxidase [227]. These electrodes were used as phenolic compounds sensor [254] and biocathode for oxygen [214] or hydrogen peroxide [227] reduction from aqueous phase.

Another application of CCE for energy conversion is anode for fuel cell. Razmi *et al.* reported CCE modified with Pt nanoparticles for electrocatalytic oxidation of methanol and ethanol [266, 267].

Recently Ranganathan and Easton found CCE as high performance anode for use in the Cu-Cl thermochemical cycle for hydrogen production [268]. A thermochemical cycle is a process consisting of the closed loop of thermally driven chemical reactions where water is decomposed into hydrogen and oxygen. All the chemicals used in these cycles are regenerated and remain in the system (Fig. 6.5). The copper chloride (Cu–Cl) thermochemical cycle is promising due the close match of its temperature requirements (ca. 550 °C) to the super critical water-cooled nuclear reactor.

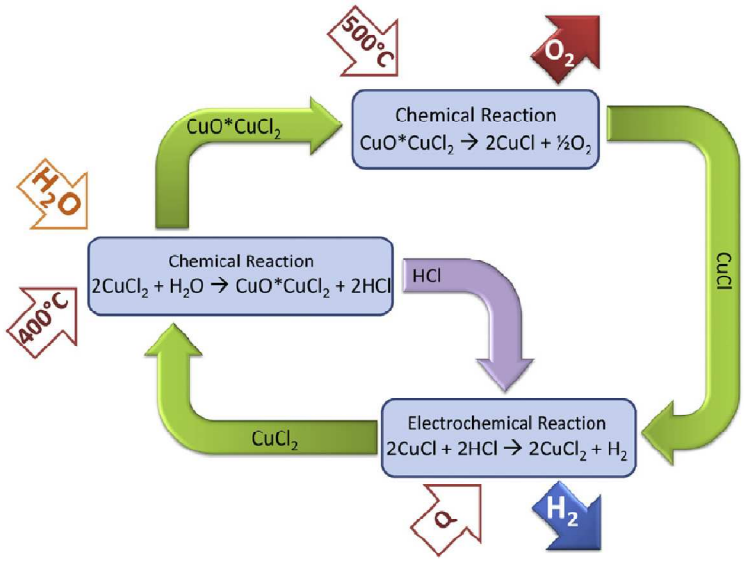

Fig. 6.5. The Cu-Cl thermochemical cycle [268].

7 Scanning electrochemical microscopy

Scanning electrochemical microscopy (SECM) is one of the most important electroanalytical methods used in this work. This technique belongs to a larger family of scanning probe microscopies (SPM) which includes such techniques as atomic force microscopy (AFM) (section 8.8) also known as scanning force microscopy (SFM), scanning electron microscopy (SEM) (Section 8.7), scanning tunneling microscopy (STM) [269], and scanning near-field optical microscopy (SNOM) [270].

SECM allows mapping the topography as well as the lateral variations of the (electro) chemical activity, measure local solute concentration, investigating heterogeneous kinetics, and inducing local electrochemical modification. In SECM microelectrode mounted on *xyz*-positioner act as amperometric or potentiometric sensor. It can be applied to investigate a variety of interfaces including solid-liquid , liquid-liquid, and liquid-gas [271-274]. The analyzed sample can be insulator, conductor or semiconductor. The lateral resolution of SECM is limited by the size of the probe and is usually worse than resolution of other SPM techniques, but large area can be analyzed. SECM can be used to probe activity of immobilized enzymes [275].

The first SECM experiment was reported by Engstrom *et al.* [276]. They used amperometric microelectrode to measure concentration profiles close to a macroscopic sample electrode. At the same time Bard *et al.* [277] recorded large faradaic current using electrochemical scanning tunneling microscopy (ECSTM) when the sample-tip distance was too large to achieve tunneling current. Although these two experiments are considered to be the first use of SECM, this technique was popularized after development of the feedback concept by Kwak and Bard [278, 279]. They developed theory describing the diffusion-limited faradaic current at a microelectrode as a function of the distance *d* between a macroscopic planar sample and this microelectrode. Further development of SECM concerning different operation modes is described in several reviews [271-274, 278, 280].

7.1 Instrumentation

The microelectrode which is moved by a positioning system relative to the sample is the central element of an SECM. The microelectrode is connected to a potentiostat or bipotentiostat together with the reference (RE) electrode and the counter electrode (CE). Then a three-electrode cell is established (Fig. 7.1).

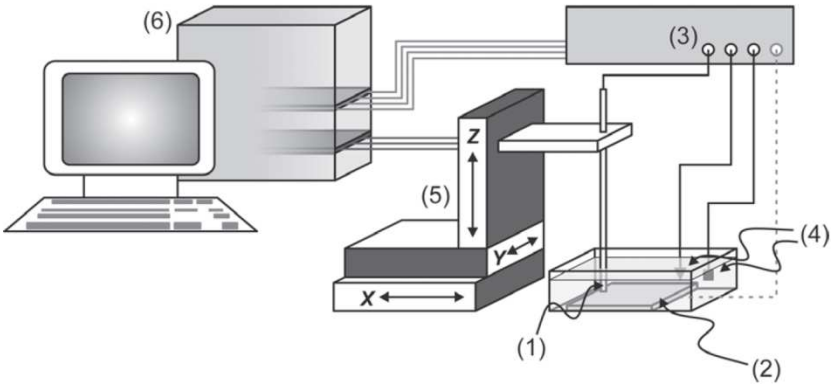

Fig. 7.1. Schematic setup of SECM. (1) microelectrode, (2) sample, (3) (bi)potentiostat, (4) reference and counter electrodes, (5) positioning system, (6) control PC [274].

Conductive or semiconductive sample can be connected as the second working electrode to a bipotentiostat. There is an essential difference between SECM and ECSTM. Both techniques share similarities in the basic setup, but the mode of action and the obtained information are quite different. In SECM, the current between probe and sample is mediated by dissolved substances which undergoes electrochemical reactions at the microelectrode and the sample surface and are transported between them by diffusion. This allows (and requires) the microelectrode to move in further from the sample than in ECSTM. The obtained information is also quite different. SECM provides information about the local heterogeneous reaction rate. In ECSTM, the current originates from the quantum-mechanical tunneling effect. It means that there is no need for an electrochemical conversion at the probe or sample.

7.2 Microelectrodes

The SECM probe as in other SPM techniques is commonly called “tip”. Usually, it is an amperometric disk-shaped microelectrode which is embedded in an insulating sheath, typically made of glass. The most often used microelectrodes are made of Pt, Au, other noble metals and carbon fibres. Potentiometric ion-selective [281-285] and pH-sensitive [286, 287] electrodes have also been used as SECM probes.

The term “microelectrode” is used for amperometric electrodes whose characteristic dimension (e.g. radius) is, under the given experimental conditions, comparable to or smaller than the diffusion layer thickness [288]. Under these conditions, a steady state is attained. For typical redox species in aqueous electrolyte and disk electrode such conditions are met when its diameter is equal or less than 25 μm. Commonly, and also in this thesis the microelectrode radius r_T, potential E_T, and current i_T are indexed with “T” (refers to tip) and accordingly the

quantities indexed with "S" are related to the sample. The geometry of a disk-shaped microelectrode can be characterized by: the radius r_T of the active electrode area and the radius r_g of the insulating glass sheath (Fig. 7.2). The ratio $RG = r_g / r_T$ is an important parameter which influences i_T and the shape of feedback mode approach curves - the curves representing i_T versus d. (Section 7.3).

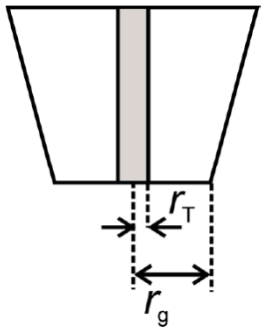

Fig. 7.2. Dimensions of microelectrode [274].

The microelectrode can be characterised by optical microscopy, cyclic voltammetry (CV), and by recording approach curves to an inert, insulating sample [289] (Fig. 7.3).

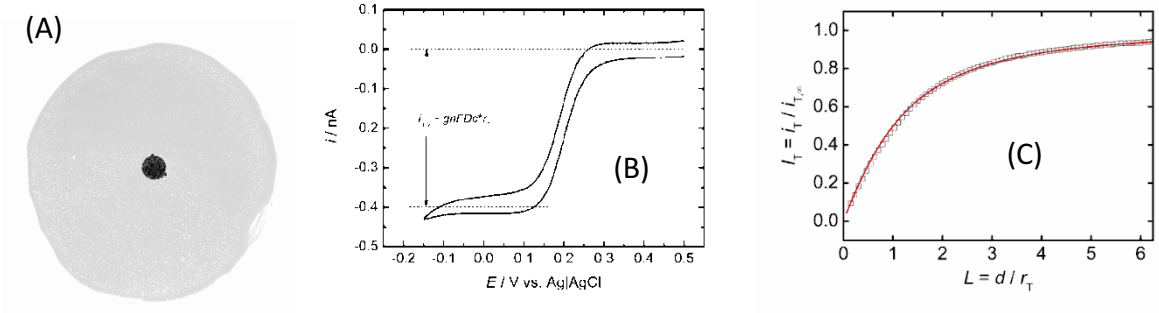

Fig. 7.3. (A) Optical micrograph of the Au microelectrode shows r_T = 12,5 µm and RG = 9.97, (B) CV of the same microelectrode resulted in a $r_T \approx$ 13.4 µm according to Eq. (7.2) (redox probe: 0.1 mM $[Fe(CN)_6]^{3-}$ in 0.1 phosphate buffer pH 4.8, v = 10 mV s^{-1}), (C) SECM approach curve to a glass surface using the same microelectrode. The theoretical parameters fit with RG = 9.97 yields r_T = 12.48 µm.

In comparison to macroelectrodes where planar diffusion occurs, with use of microelectrodes the mass transport due to hemispherical diffusion is enhanced and IR drop is reduced. The hemispherical diffusion assures large current densities in quiescent solution and the steady state current is achieved in short time ($\sim r_T^2/D$). This allows the treatment of i_T recording at the scanning probe with velocity $v \leq 15$ µm s^{-1} by the theory derived for a stationary electrode [274].

When the microelectrode is polarised at a potential E_T sufficiently low to cause the diffusion-controlled reduction of oxidized species Ox, its conversion occurs:

$$\mathrm{Ox} + n\mathrm{e}^- \leftrightarrows \mathrm{R} \quad (7.1)$$

The steady-state, diffusion-controlled current plateau on microelectrode ($i_{T,\infty}$) is obtained (Fig. 7.3B) if the microelectrode is at a quasi-infinite distance from the sample ($d > 20\ r_T$) [274]:

$$i_{T,\infty} = gnFDc^* r_T \quad (7.2)$$

where n is the number of transferred electrons per molecule, F – the Faraday constant, D – the diffusion coefficient, c^* - the bulk concentration of the redox probe, r_T – the radius of the disk-shaped active electrode area, and g – the geometry-dependent factor that assumes different values of *RG* (Table 7.1) [290].

Table 7.1. Selected geometry-dependent factors g values with respect to RG [290].

RG	∞	10	2	1.2
g	4	4.07	4.44	4.95

One can see that higher diffusion-controlled currents are achieved on lower *RG* microelectrodes. This is because of rather spherical than hemispherical diffusion.

7.3 Feedback mode

The term “feedback” in SECM is used to indicate that the i_T is influenced by the redox substrate regeneration rate at the sample and must not be confused with the feedback-loop system used to control probe vertical position in SPM techniques. In such SECM experiment electrolyte contain one form of a redox couple (reduced (R) or oxidized (Ox)), which can be consumed on microelectrode with diffusion-controlled rate. To clarify, let’s consider that only Ox is present in electrolyte. The mathematical models developed for SECM do not take into account migration and convection. Therefore, Ox is usually added in milimolar concentration to an excess of inert supporting electrolyte to ensure that the Ox mass transport occurs predominantly by diffusion.

In SECM electrochemical cell the microelectrode acts as working electrode (WE). CE is placed far from the microelectrode to prevent access of CE reaction products to WE. The microelectrode potential (E_T) is controlled versus a stable RE. The conductive sample can be connected as a second working electrode (WE2). In this case bipotentiostat is necessary.

Vertical translation of the microelectrode towards the sample allows to detailed kinetic investigation of the reaction R → Ox + ne^- at a specific location of the sample. The SECM approach curve represents recorded i_T as a function of the microelectrode-sample separation d. For unification, i_T is normalized to $i_{T,\infty}$ ($I_T = i_T / i_{T,\infty}$), and d is normalized to r_T ($L = d/r_T$). The normalized currents are independent of c^*, D and r_T. There are two limiting cases for approaching a quasi-infinitely large sample:

- when the sample is an inert, insulating surface (Fig 7.4A),
- when the sample is a conducting surface where species R generated at the microelectrode are regenerated to Ox at a diffusion-controlled rate (Fig. 7.4B)

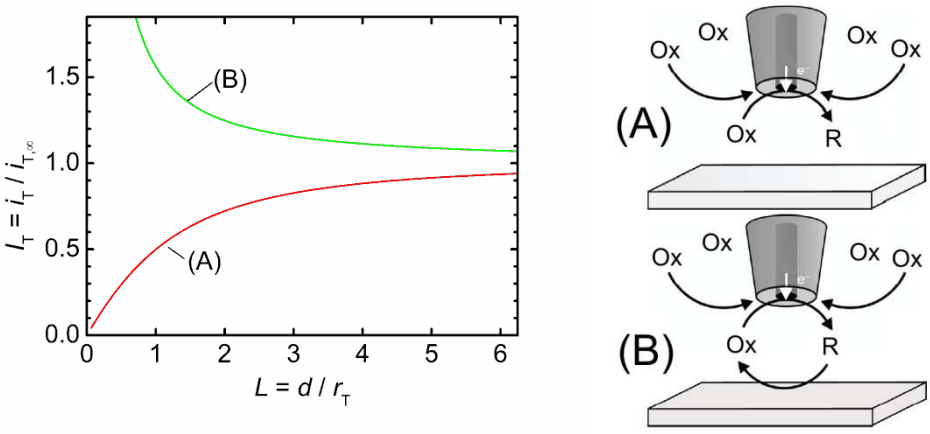

Fig. 7.4. Principle of feedback mode. (A) – normalized approach curve for hindered diffusion when the microelectrode approaches an inert, insulating sample (negative feedback), (B) – normalized approach curve for mediator regeneration by a fast heterogeneous reaction at the sample surface (positive feedback).

If the microelectrode approaches an inert, insulating sample, e.g. glass, the diffusion of Ox toward the microelectrode is hindered by the insulating microelectrode sheath and the sample surface. Thus, the faradaic current i_T falls below $i_{T,\infty}$ as d decreases (Fig. 7.4A). The diffusional flux of Ox toward the microelectrode is also hindered as the *RG* increases. This type of response is called "negative feedback" [278]. However, if the microelectrode approaches a sample where the R species generated at the microelectrode are reoxidized chemically or electrochemically, the sample acts as an additional source of Ox. In this case i_T increases during approaching and exceeds $i_{T,\infty}$ (Fig. 7.4B). Such response is called "positive feedback" [278].

Quantitative description of approach curves can be obtained by solving the diffusion equations for disk-shaped microelectrode. The simulation results for various values of d can

be described by analytical approximation for both limiting cases [279, 291]. An analytical approximation for an inert, insulating surface is described by following equation:

$$I_T^{\mathrm{ins}}(L) = \frac{i_{\mathrm{T}}}{i_{\mathrm{T},\infty}} = \frac{1}{k_1 + \frac{k_2}{L} + k_3 \exp\left(\frac{k_4}{L}\right)} \tag{7.3}$$

The contribution (*RG*-dependent values of k_1, k_2, k_3 and k_4) for the normalized current at the microelectrode approaching insulating sample ($I_{\mathrm{T}}^{\mathrm{ins}}$) can be find in ref. [291].

This approximation provides a way to determine *d* from experimental approach curves. For this purpose one can use even an irreversible reaction at the microelectrode (e.g. ORR). Then the approach curve is independent of the nature of the sample. By fitting parameters in Eq. (7.3) to experimental approach curve, *d* can be obtained as adjustable parameter. The knowledge of the distance between the microelectrode and the sample is essential for quantitative SECM measurements.

The upper limit of i_{T}, when the microelectrode approaches conducting sample and the reactions both at the microelectrode and the sample are diffusion-controlled is described by following equation [291]:

$$I_{\mathrm{T}}^{\mathrm{cond}}(L) = \frac{i_{\mathrm{T}}}{i_{\mathrm{T},\infty}} = k_1 + \frac{k_2}{L} + k_3 \exp\left(\frac{k_4}{L}\right) \tag{7.4}$$

The *RG*-dependent parameters $k_1 - k_4$ can be found in ref. [291].

Typically the conducting sample at which R produced at the microelectrode is reoxidized to Ox is connected to a bipotentiostat. However, in some cases it is not necessary. If the sample is much larger than the microelectrode or is connected to a larger conducting region in contact with the electrolyte, then concentration of R is enhanced in the close proximity of the microelectrode. Thus, local sample potential in the microelectrode proximity is lower according to the Nernst equation:

$$E_{\mathrm{S}} = E^{\circ} - \frac{RT}{nF} \ln\left(\frac{[\mathrm{R}]}{[\mathrm{Ox}]}\right) \tag{7.5}$$

where E° is the standard potential of the redox couple, *R* the gas constant, *T* the absolute, [R] and [Ox] are the molar concentrations of the reduced and oxidized form of the redox mediator respectively. If the bulk electrolyte contains only Ox as illustrated in Fig. 7.5B, a local concentration cell is created leading to oxidation of R to Ox underneath the microelectrode. An equal amount of Ox is reduced to R at the sample far away from the microelectrode (Fig. 7.5B). If standard heterogeneous rate constant k_0 of used mediator is high enough, oxidation

of R underneath the microelectrode occurs under nearly diffusion-controlled conditions. Instead of diffusion of R into the bulk electrolyte electrons are transported from the vicinity of the microelectrode through the conducting sample.

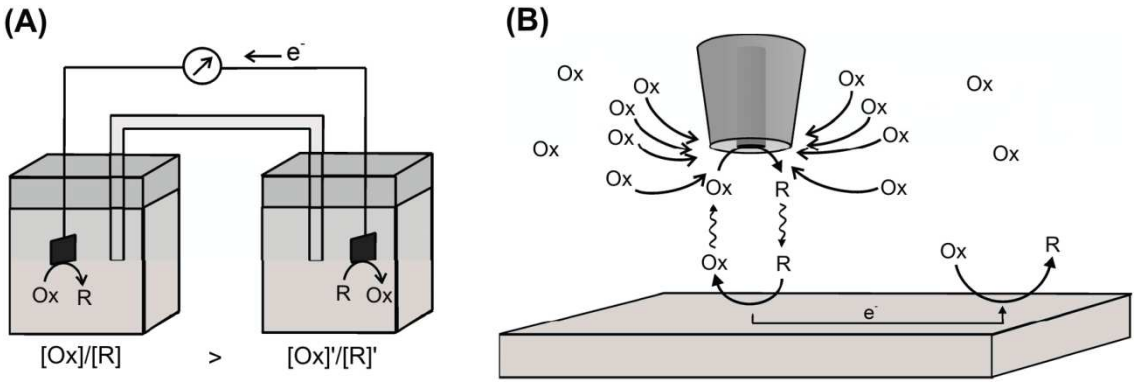

Fig. 7.5. (A) – conventional electrochemical concentration cell, (B) – formation of a concentration cell in feedback mode SECM experiment.

If the electrochemical mediator regeneration at the sample is not diffusion-controlled, but limited by the heterogeneous electron transfer rate at the sample, a unique approach curve can be found for a given rate constant [292]. Such curves are described by analytical approximation for finite kinetics at the sample and diffusion-limited current at the microelectrode (Eq. (7.6)). This analytical approximation can be used for $RG \leq 20$ and $L \geq 0.1$.

$$I_{\mathrm{T}}(L,\kappa,RG) = I_{\mathrm{T}}^{\mathrm{cond}}\left(L+\frac{1}{\kappa},RG\right) + \frac{I_{\mathrm{T}}^{\mathrm{ins}}(L,RG)-1}{(1+2.47RG^{0.31}L\kappa)(1+L^{\gamma}\kappa^{-\sigma})} \tag{7.6}$$

with

$$I_{\mathrm{T}}^{\mathrm{cond}}\left(L+\frac{1}{\kappa},RG\right) = \alpha(RG) + \frac{1}{2\beta(RG)\xi\left(L+\frac{1}{\kappa}\right)} + \left(1-\alpha(RG)-\frac{1}{2\beta(RG)}\right)\xi\left(L+\frac{1}{\kappa}\right) \tag{7.7}$$

$$I_{\mathrm{T}}^{\mathrm{ins}}(L,RG) = \frac{\frac{2.08}{RG^{0.358}}\left(L-\frac{0.145}{RG}\right)+1.585}{\frac{2.08}{RG^{0.358}}(L+0.0023RG)+1.57+\frac{\ln RG}{L}+\frac{2}{\pi RG}\ln\left(1+\frac{\pi RG}{2L}\right)} \tag{7.8}$$

$$\alpha(RG) = \ln 2 + \ln 2\left(1-\frac{2}{\pi}\cos^{-1}\left(\frac{1}{RG}\right)\right) - \ln 2\left(1-\left(\frac{2}{\pi}\cos^{-1}\left(\frac{1}{RG}\right)\right)^2\right) \tag{7.9}$$

$$\beta(RG) = 1 + 0.639\left(1-\frac{2}{\pi}\cos^{-1}\left(\frac{1}{RG}\right)\right) - 0.186\left(1-\left(\frac{2}{\pi}\cos^{-1}\left(\frac{1}{RG}\right)\right)^2\right) \tag{7.10}$$

$$\xi\left(L+\frac{1}{\kappa}\right) = \frac{2}{\pi}\tan^{-1}\left(L+\frac{1}{\kappa}\right) \tag{7.11}$$

$$\gamma = 0.006RG + 0.113 \tag{7.12}$$

$$\sigma = 0.0236RG + 0.91 \quad (7.13)$$

The magnitude of the feedback depends on the rate of mediator regeneration at the sample, hence the approach curve provides information about kinetics at the sample by the value κ in Eq. (7.6). This parameter can be related to normalized heterogeneous first order rate constant k_{eff}:

$$k_{\text{eff}} = \kappa \frac{D}{r_{\text{T}}} \quad (7.14)$$

Knowing r_{T} and diffusion coefficient of mediator D (assuming that for Ox and R is equal) an effective heterogeneous first order rate constant k_{eff} can be derived.

In this thesis the FB mode was used to extract kinetic information from experimental approach curves (Section 14.3.4) as well as to imaging lateral distribution of sample activity (Section 14.3) and conductivity (Section 15.5).

7.4 Generation-Collection mode

In contrast to feedback mode, the generation-collection mode (GC) the electrolyte initially does not contain any a substance which can be electrochemically oxidized or reduced at the microelectrode at applied E_{T}. This mode can be used to monitor heterogeneous processes such as catalytic reactions [280, 293, 294], corrosion [280, 295, 296], mass transport across permeable samples [284, 285, 297] and phase interfaces [298-300]. There are two types of GC mode (Fig. 7.6): sample-generation/tip-collection (SG/TC) and tip-generation/sample-collection (TG/SC).

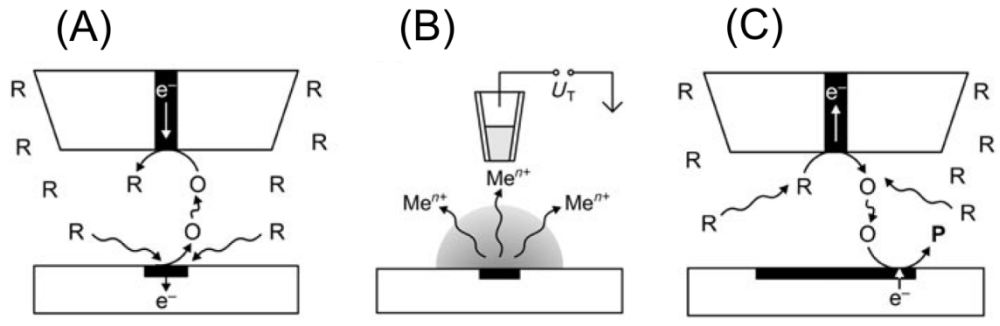

Fig. 7.6. Principle of the generation-collection mode. (A) – SG/TC mode with an amperometric microelectrode, (B) – SG/TC with a potentiometric microelectrode (e.g. ion-selective electrode), (C) – TG/SC mode [274].

The SG/TC mode can be performed with either amperometric (Fig. 7.6A) or potentiometric (Fig. 7.6B) microelectrodes. The sample surface generates a redox-active

species, probed by the microelectrode, when it is placed close to the active sample region. When the microelectrode translates above the region where the redox-active species are generated, the i_T depends on the local concentration of this species generated at the sample surface. The SG/TC seems to be a simple experiment, however, it has some disadvantages:

- a steady-state concentration profile of electroactive species generated at the sample is achieved only if the active regions are well separated microstructures. If the size of active area is large the concentration is transient.
- The concentration profile of the electroactive species generated at the sample is disturbed by the presence of the microelectrode.
- If the product of electrochemical reaction at the microelectrode is a substrate for the sample, there might be feedback caused current enhancement for $d \leq 5r_T$.

In order to minimize the feedback effect and the disturbance of the diffusion layer, one has to use microelectrode with smaller r_T and *RG*.

In TG/SC mode the microelectrode is held at a potential E_T where an electrochemical reaction occurs or the current flow is forced in galvanostatic mode. The potential set on the sample is capable to probe the microelectrode reaction product (Fig. 7.6C). An image is constructed by plotting the sample current i_S versus the microelectrode position. Usually, in TG/SC mode the sample is larger than the microelectrode and the collection efficiency is close to 100 %. Using this mode the sample surface area has to be small enough not to mask the current relevant with “collection” of electroactive species generated at the microelectrode. This mode has been used to image ORR on metallic [37] and enzymatic catalysts arrays [301]. The lateral resolution of GC mode imaging is inferior to FB mode, but the sensitivity of GC mode is higher. This mode is used when FB mode is not sensitive enough or impossible to apply.

Quantitative measurements using GC mode is possible only if the active sample regions are well separated microstructures which can deliver steady-state concentration profiles. The signal over the active sample region can be described by a model developed for mediator diffusing from an isolated disk-shaped pore in membrane [297, 302]. This model is based on Fick’s laws of diffusion and relates the microelectrode current to the local flux of molecules generated by the active region of the sample. It assumes that the microelectrode does not interact with the system being measured (i.e. acts as a passive probe and its presence does not disturb concentration profile). The current i_T depends on the radius of the active region of the sample r_S, microelectrode radius r_T, the concentration of the analysed species at the surface of

the sample $[A]_S$, and the dilution factor describing the diffusion from the active sample region into electrolyte:

$$i_T = gnFDr_T[A]_S\zeta \tag{7.15}$$

The dimensionless factor ζ describes the concentration decrease of the released redox-active species as a function of the lateral distance Δx from the centre of the active sample region ($\Delta x = x - x_0$, where x_0 is the x-coordinate of the spot centre), the vertical distance d from the active centre of the sample and r_S:

$$\zeta = \frac{2}{\pi}\tan^{-1}\frac{\sqrt{2}r_S}{\left(\sqrt{\left(\Delta x^2+d^2-r_S^2\right)+\sqrt{\left(\Delta x^2+d^2-r_S^2\right)^2+4d^2r_S^2}}\right)} \tag{7.16}$$

A fit of the parameters in Eq. (7.15) and (7.16) (i_T = f(x, d = const)) to the experimental horizontal line scan yields r_S and $[A]_S$. Then the total flux Ω from the active region can be calculated from [297]:

$$\Omega = 4Dr_S[A]_S \tag{7.17}$$

By assuming a uniform flux over the whole active sample region and a circular area $A = \pi r_S^2$, a generation rate J can be determined according to the following equation:

$$J = \frac{\Omega}{\pi \cdot r_S^2} \tag{7.18}$$

This treatment is used in this thesis (Section 14.2) in order to evaluate the flux of the product of the enzymatic reaction coming from the immobilized enzyme, and to evaluate O_2 permeability through the silicate (Section 15.5). The SG/TC mode imaging was used for enzyme aggregates (Section 14.2) and for detection of oxygen permeability through the sample electrode (Section 15.5).

7.5 Redox competition mode

The redox competition (RC) mode (Figure 7.7) was proposed recently by Eckhard *et al.* [303]. In this mode, the microelectrode and the sample are polarized at the same potential. Then the sample and the microelectrode compete for the same reagent. The main advantage of this mode is its ability to investigate irreversible reactions, e.g. ORR. It provides an interesting alternative to the TG/SC mode. At each grid point of the image, the microelectrode is pulsed

to a potential high enough to locally generate O_2, which is re-reduced as soon as the pulse ends. The E_T switches to a potential where oxygen reduction occurs (Fig. 7.7).

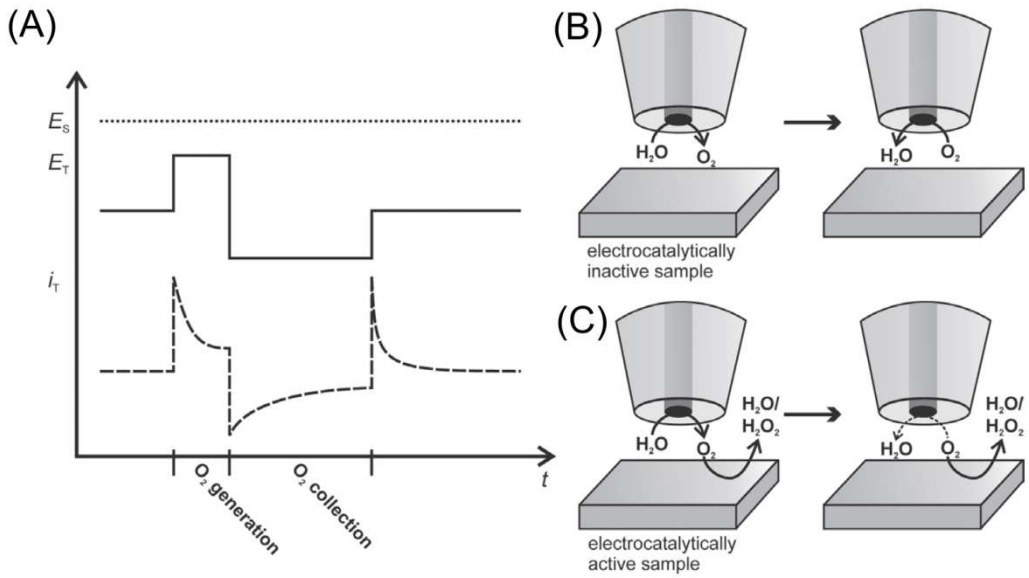

Fig. 7.7. General principle of the RC mode. (A) – Pulse program at the microelectrode, (B) – O_2 is generated and re-reduced at the microelectrode above an electrocatalytically inactive substrate, (C) – O_2 is generated at the microelectrode and partly consumed at an electrocatalytically active substrate [280].

If the sample beneath the microelectrode is electrocatalytically active, some oxygen is consumed by the sample instead of being reduced at the microelectrode. Then i_T is lower when the microelectrode is positioned above the areas of higher electrocatalytic activity of the sample. In contrast to TG/SC mode, the RC mode does not impose limitations on the sample size and the activity of the support. The ability of this mode has been proven on highly dispersed spots of gold and platinum [303] and on spot of BOx [304]. A quantitative description of the signals seems extremely difficult and is not available yet. In this thesis RC mode was used to investigate ORR on electrodes modified with enzymes (Section 13.5 and 15.4).

7.6 Direct mode

The direct mode has mainly been used for local surface modification, e.g. deposition [305] or etching [306]. The sample acts as the working electrode (WE) and the microelectrode as counter electrode (CE). The microelectrode is positioned close to the sample surface forming a thin layer cell and a current flow between them to cause faradaic reactions at the sample surface and at the microelectrode. Due to electrolyte non-zero resistance, current lines are formed between the electrodes. The current value determines the amount of formed deposit.

Fig. 7.8. represents a scheme of a typical metal deposition by direct mode. As the current flow is limited to the gap between the microelectrode and the sample, the modification or deposition is restricted to the region underneath the microelectrode.

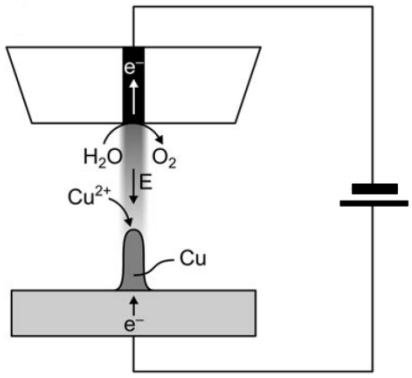

Fig. 7.8. Schematic representation of cooper needle generated using SECM direct mode [274].

7.7 Constant distance mode

Conventional SECM imaging experiments measures the microelectrode current when it translates across the sample surface at a constant height. In order to increase imaging resolution, smaller microelectrodes (even nanoelectrodes) must be used and positioned at a suitable working distance. The working distance *d* has to be of the order of the active probe area diameter to ensure high resolution imaging and good collection efficiency. Constant-height mode SECM imaging has some disadvantages. For samples with variations in conductivity and topography, variations in i_T response can not be exactly assigned to differences in topography or local activity. Another problem is that the sample tilt and protruding sample features can cause undesirable physical contact of the microelectrode and the sample. In order to overcome these problems a shear force distance control system may be used. Using this technique the microelectrode-sample distance is measured and this value is used as a setpoint to keep the distance constant. Thus, sample topography and reactivity can be measured simultaneously. Shear force rely on measurement of the changes in resonance frequency, amplitude or phase shift of a nanometer-sized microelectrode. There are two variations of shear force systems. In the first, a quartz tuning fork is attached to the microelectrode by one leg and the resonance frequency is determined by a quartz resonator [307]. The changes of resonance frequency, amplitude or phase shift can be recorded either by projection of a diffraction pattern onto a split photodiode using laser beam [308] or by attaching a second piezoelectric plate to the microelectrode (Fig. 7.9) [309].

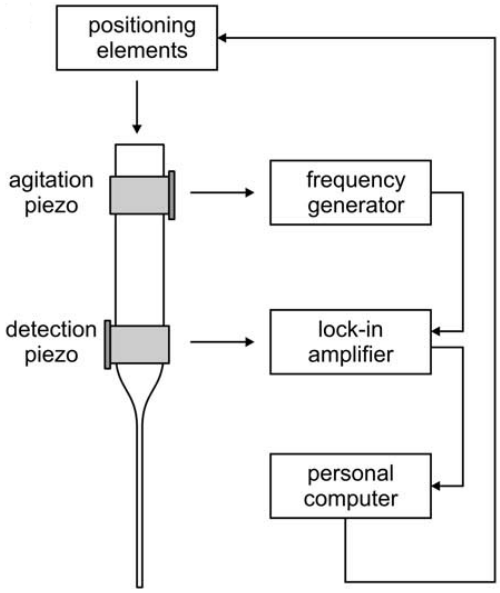

Fig. 7.9. The scheme of piezoelectric detection system for shear force system [274].

The upper plate is used to excite the SECM probe causing it to vibrate, and the lower detects the shear forces between the microelectrode and the sample, hence variations in amplitude of the microelectrode oscillation. The detection piezoelectric plate is connected to a lock-in amplifier which amplifies the distance-dependent signal. A closed-loop feedback controller reacts to changes in amplitude by moving a piezo actuator (to which the microelectrode is attached) in vertical direction keeping the resonance frequency constant.

7.8 Summary

A number of schemes can be used to monitor the activity of oxygen-reducing electrodes. If H_2O_2 is formed, this compound can be detected in SG/TC mode [310]. In order to obtain quantitative data in SG/TC mode the analysed sample must be a microstructure by itself, in order to form a steady-state diffusion layer. The four electron ORR favourable for biofuel cells is not possible to detect using SG/TC mode, since the reaction product (H_2O) is the solvent. Such catalysis can be monitored in TG/SC mode [37, 301] in an O_2-free solution when O_2 is generated at the microelectrode by water electrolysis. The locally available O_2 is then consumed by the enzyme-modified electrode. In such experiment the sample should be as small as possible to minimize background current. Another mode sufficient for ORR monitoring is double potential step RC mode (Section 7.5). In this mode, active areas on the sample and the microelectrode compete for dissolved O_2. In all above mentioned imaging modes a signal is recorded only if the enzyme is active under the experimental conditions and that the enzyme can transfer the electrons to the substrate electrode.

SECM is also able to detect the activity of O_2-reducting enzymes immobilized on insulating supports. Such imaging can be accomplished in the SG/TC, simple RC and FB mode by detection of mediator concentration changes. In this case the response of the surface does not require any electron transfer to a substrate electrode and would even interfere with the imaging of the enzyme activity. The possibility for quantitative kinetic analysis of 4 electron enzymatic ORR gives only FB mode.

Goal

The ultimate aim of this work is to construct electrodes for efficient bioelectrocatalytic oxygen reduction and to understand the mechanisms of processes occurring during their operation and preparation. Another goal is to find the factors which influence efficiency of the oxygen reduction process on constructed electrodes by affecting their stability and finally to indicate a way of improving electrode design. Moreover, a design of scanning electrochemical microscopy procedures for imaging, kinetics measurement and enzymatic activity comparison is also intended.

Two enzymes known as oxygen reduction catalysts – laccase and bilirubin oxidase – were chosen for modification of carbon ceramic electrodes. This type of electrode provides favourable conditions for enzymes adsorption (graphite particles) and act as a container for mediator (silicate matrix). Moreover, silicate thin films – that are a suitable environment for enzyme encapsulation – can be easily embedded on carbon ceramic electrode surface.

8 Methods

8.1 Cyclic voltammetry

Cyclic voltammetry (CV) and other voltammetric experiments are usually carried out in three-electrode cell. The apparatus known as a "potentiostat" adjust the voltage between the working electrode (WE) and counter electrode (CE) to maintain the potential difference between the WE and non-polarized reference electrode (RE) in accord with the program defined by a function generator (Fig. 8.1). Modern potentiostats are integrated to electrochemical workstations together with galvanostats, function generators and data acquisition modules controlled by microcomputer.

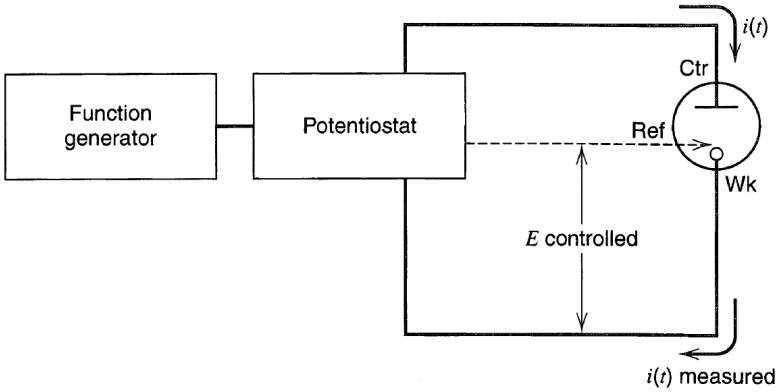

Fig. 8.1. A scheme of potential-controlled experiment setup [204].

Most of electrochemical experiments are carried out in electrolytes containing analyte in milimolar concentration and supporting electrolyte. The concentration of the latter one has to be at least one order of magnitude higher than that of analyte in order to provide sufficient electrolyte conductivity and to eliminate the migration of charged analyte molecules.

In CV a linear potential sweep is applied to WE. After reaching a switching potential E_λ, the sweep is reversed. Figure 8.2 represents an example of CV potential program and corresponding cyclic voltammogram obtained on planar WE when only oxidizable species (R) are present in electrolyte. In this example both redox forms (R and Ox) undergo reversible electrochemical processes and electrode size is larger than analyte diffusion length in this time scale causing transient current. Different situation is observed when electrode size is comparable diffusion length or smaller. Then the steady-state current is attained (Chapter 7.2).

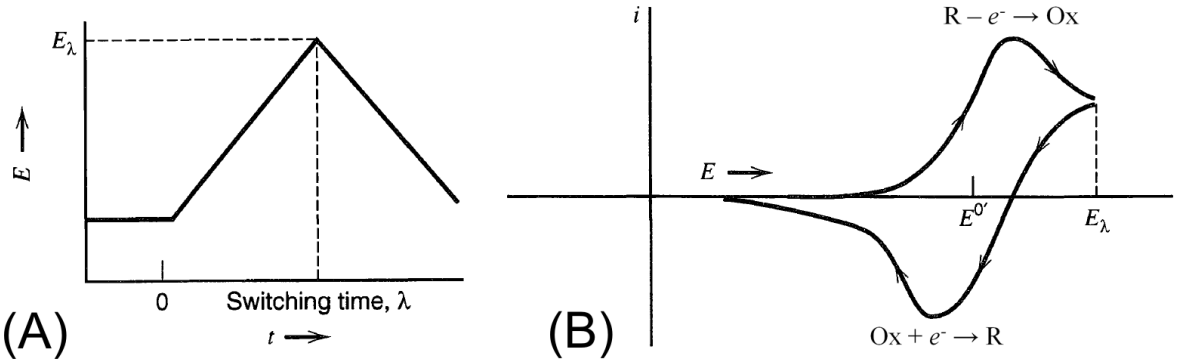

Fig. 8.2. (A) – Potential program in CV. (B) – Resulting cyclic voltammogram. From ref. [204] modified to be in accordance with IUPAC recommendations.

The shape of cyclic voltammograms depends on many factors such as chemical reversibility, adsorption, coupled homogeneous reactions, kinetics, adsorption or R and Ox diffusion coefficients differences. If kinetics of both electrooxidation and electroreduction is fast enough to maintain R and Ox concentrations ratio at the electrode surface to be in accordance with Nernst equation (usually when standard heterogeneous rate constant $k^0 > 10^{-1}$ cm s^{-1}), then the peaks separation is equal 57/*n* mV at 25 °C where *n* is a stochiometric number of electrons involved in an electrode reaction [204]. For slower reactions peaks separation is larger.

The scan rate $v = dE/dt$ is one of the most important parameters in CV controlling the time scale of experiment and capacitive current. The last one is proportional to the electrochemical double layer capacitance and scan rate ($i_C = vC_{dl}$). The peak current i_p when a substrate is diffusing from bulk electrolyte is proportional to square root of scan rate according to Randles-Sevcik equation, which at 25 °C, for *A* in cm^2, *D* in cm^2 s^{-1}, C* in mol cm^{-3}, *v* in V s^{-1} and i_p in amperes is following [204]:

$$i_p = (2.69 \cdot 10^5) n^{3/2} A D_R^{1/2} C_R^* v^{1/2} \quad (8.1)$$

In the case of adsorbed substrate or restricted diffusion length i_p is proportional to *v*.

In this thesis CV was used for measurements of all examined electrodes and SECM tips testing.

8.2 Differential pulse voltammetry

Differential pulse voltammetry (DPV) belongs to the group of potential-step voltammetric techniques, whose distinctive feature is the fact that the current is measured when potential of

WE is held constant. This reduces or eliminates capacitive current. The diagram of the applied DPV potential waveform as a function of time and the current sampling scheme are presented in figure 8.3. WE potential is changed from initial potential (Init E) toward final potential (Final E). The current before the potential pulse and at the end of the potential pulse is sampled. The difference between these two currents is recorded as a function of potential giving a peaked output (Fig. 13.3A). Under assumption that diffusion coefficients of reduced and oxidized forms of the analyte are equal, the peak position corresponds to analyte standard potential [204]. The peak width provides also information about kinetics of redox processes. Slower kinetic results wider DPV peak.

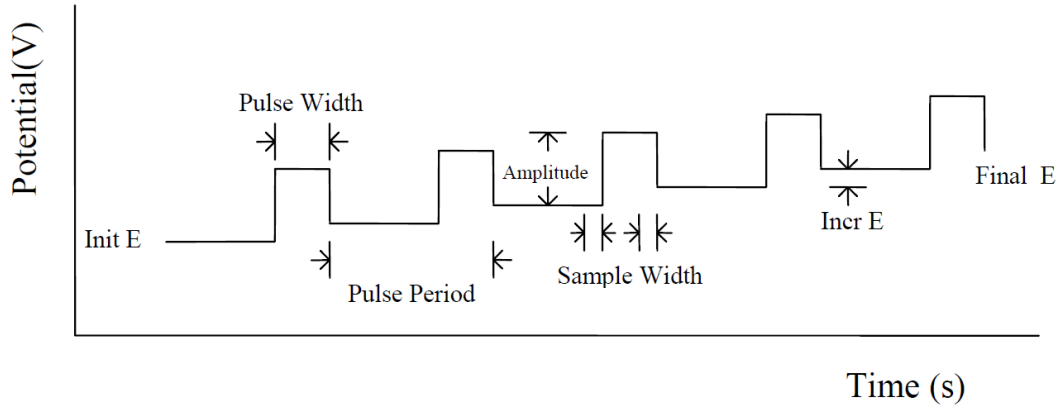

Fig. 8.3. Potential program in DPV experiment.

8.3 Chronoamperometry

Chronoamperometry (CA) is another potential-step voltammetric technique which consist in application to WE a constant potential and current measurement versus time. The diagram of CA potential program and schematic example of current response on planar electrode immersed onto electrolyte containing only oxidizable species are presented in figure 8.4.

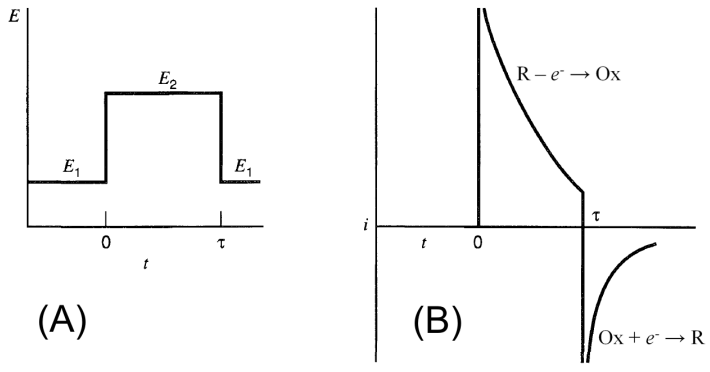

Fig. 8.4. A typical CA potential program (A) and current response (B). From ref. [204] modified to be in accordance with IUPAC recommendations.

At potential E_1 no reaction occurs what results in zero current. At $t = 0$ potential step to E_2 is applied. E_2 is sufficiently high to cause diffusion-controlled oxidation of R. Faradaic current versus time is described by Cottrell equation (eq. 8.2), which was developed from diffusion laws for planar electrode in unstirred electrolyte [204]. After potential switching back to E_1 at $t = \tau$ oxidized species Ox generated during previous step are re-reduced. Non-zero current $i(t)$ in this step shows chemical reversibility of redox process:

$$i(t) = \frac{nFAD_{\mathrm{R}}^{1/2}C_{\mathrm{R}}^{*}}{\pi^{1/2}t^{1/2}} \tag{8.2}$$

CA is usually employed for determination of diffusion coefficients or electrode area. In this thesis CA was used for electrodes stability tests.

8.4 Chronopotentiometry

In chronopotentiometry (CP) potential is measured as a function of time. Such experiment is usually carried out in traditional three-electrodes cell connected to apparatus called galvanostat, which is implemented into modern electrochemical stations. A voltage applied between WE and CE is controlled by operational amplifier to maintain current at constant setpoint value or to be in accordance with program defined by function generator. The potential of WE is measured versus RE. In this thesis constant-current CP was employed to register current-voltage characteristics of zinc-oxygen batteries. Here potential of WE was measured in two-electrodes cell versus CE when steady-state was attained (Section 11.12).

8.5 Confocal laser scanning microscopy

Contrary to traditional microscopy where whole sample is illuminated and reflected or transmitted light is gathered by objective from the whole cross-section of the sample (even out of focal plane), in confocal laser scanning microscopy (CLSM) a laser beam is focused on particular part of the sample and reflected, scattered or fluorescent light gathered by objective goes to detector (Fig. 8.5). A pinhole aperture that is situated between objective and detector cut out-of-focus rays allowing passing only light emitted by part of sample situated in focal plane. Incident laser beam is focused using the same objective which is used for detection what causes that illumination and detection is in a conjugate (confocal) plane. This is possible due to translucent mirror (see Fig. 8.5), which is connected to piezoelectric actuator allowing to scan the laser beam across confocal plane. A signal recorded by a detector plotted as a function of lateral laser beam position represents sample cross section image. The thickness of

such cross-section depends on the objective numerical aperture and is close to the laser wavelength.

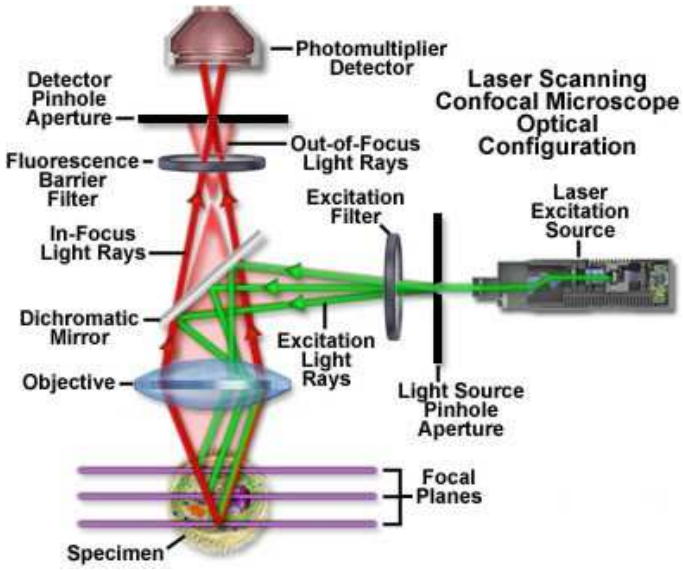

Fig. 8.5. A scheme of CLSM [311].

The distance between the sample and objective can be changed. Usually, a sample holder is embedded in piezoelectric actuator which allows changing the sample-lens distance with resolution better than laser wavelength. Then confocal plane cross a sample in different positions and an stack of cross-section images is processed resulting in three-dimensional (3D) sample image. 3D CLSM imaging is often used by biologist to biological cells investigation, what is facilitated by their transparency.

In this thesis CLSM was used to investigate both transparent (Section 14.2) and opaque samples (Section 15.2).

8.6 Raman Spectroscopy

Molecular vibrational energy levels can be explored by examining the frequencies present in the radiation scattered by molecules in Raman spectroscopy. Molecules are irradiated by visible monochromatic radiation with frequency ν_0. Then interatomic bonds act as oscillating induced dipoles and emit radiation consisting of three electromagnetic waves [312]. One of these waves (the most intense) with a frequency ν_0 corresponds to Raileigh scattering. The second one with a frequency $\nu_0 - \nu$, and the last one $\nu_0 + \nu$ are Stokes and anti-Stokes bands, respectively. This phenomenon can be compared to frequency-modulated radio wave, where antenna transmits high-frequency carrier wave modulated with low-frequency waves. Similarly, visible electromagnetic radiation scattered in Raman spectroscopy is “modulated”

with waves of frequencies corresponding to those emitted by vibrating moieties. A scheme of molecular energy levels with Raman transitions are presented in figure 8.6. The incident photons with frequency v_0 not fitted to electronic levels energy difference and are only scattered. If a molecule after interaction with a quantum hv_0 go back to the same energy level, such phenomenon is called Rayleigh scattering and the wave frequency is not changed. Some molecules after such interaction go to higher vibronic level and then the frequency of scattered radiation is $v_0 - v$, where v corresponds to vibronic levels difference. The Raman spectrum contain then Stokes radiation band. If the molecule before interaction with incident photon occupy higher vibronic level, it is highly possible that this interaction will transfer the molecule to ground state. Then scattered radiation exhibit the frequency $\nu_0 + \nu$ and is called anti-Stokes shift.

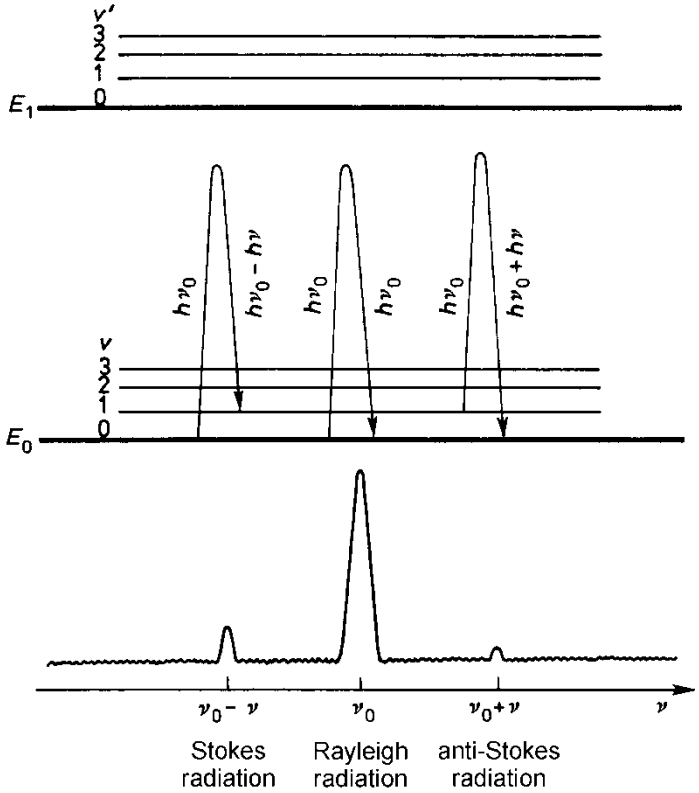

Fig. 8.6. Raman transitions between energy levels of diatomic molecule and corresponding Raman spectrum. E_0 – ground electronic state, E_1 – excited electronic state, v and v' – vibronic energy levels [312].

The intensity of Stokes radiation bands is usually ca. three orders of magnitude lower than intensity of Rayleigh bands but is higher than intensity of anti-Stokes bands [312]. The analysis of Stokes radiation bands shifts delivers the information about vibronic energy levels what allows determining molecular structure of compounds present on the examined surface.

In this thesis Raman spectroscopy was employed to determine surface composition of electrodes examined *in situ* in electrochemical cell under controlled potential (Section 13.3).

8.7 Scanning electron microscopy

The minimal distance Δd between two light-shining points that can be distinguished by optical microscopy is restricted because of diffraction of electromagnetic waves. This distance is described by equation developed by Ernst Abbe and Lord Rayleigh independently:

——— (8.3)

Where λ is a wavelength, n – refractive index of sample surrounding medium, θ – angle between optical axis of microscope objective and straight line between the sample and lens edge. Denominator of eq. (8.3) right side is called “numerical aperture” which is a parameter characterizing objective. The lowest Δd for visible light optical microscopy is ca. 300 nm.

This distance is much lower in scanning electron microscopy (SEM), because of shorter λ. According to de Broglie relation ($\lambda = h/p$, where p is particles momentum) higher energy photons corresponds to shorter λ. In SEM the electron beam emitted by electrons gun (accelerated in electric field) is focused on sample using electromagnetic lenses (Fig. 8.7) to a spot whose size is smaller than 5 nm. The beam of electrons is deflected by electromagnetic coils or a pair of deflector plates in such a way that it scans the sample surface line-by-line like the screen of cathode ray tube monitor.

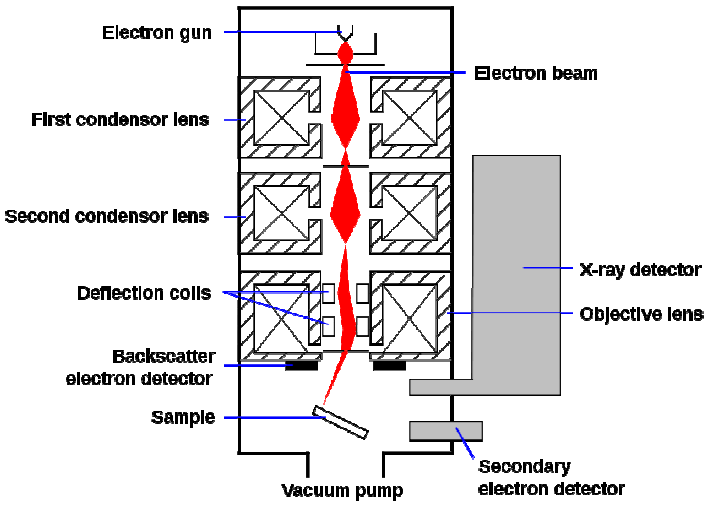

Fig. 8.7. Schematic diagram of an SEM [313].

The sample bombarded with electrons emits different types of radiation such as X-rays, visible light (cathodoluminescence), back-scattered electrons and secondary electrons, whose intensity is measured by dedicated detectors. The analysis of emitted X-rays and back-

scattered electrons provides information about local surface composition. The plot of secondary electrons intensity versus incident beam position provides high-resolution image of the sample topography with relatively large depth of field.

In this thesis SEM Was used to examine CCEs modified with carbon nanoparticles.

8.8 Atomic force microscopy

Atomic force microscopy (AFM) is another method for high-resolution surface topography investigation. It uses a fine tip at the end of a cantilever to probe the surface similarly to phonograph needle. The cantilever is connected into piezoelectric actuator which is used to scan the tip across the sample surface and to control *z*-position (Fig. 8.8). The curvature of the tip is in the order of nanometres what defines lateral resolution of AFM. The vertical resolution is usually below 0.1 nm. A laser beam is focused on the backside of the cantilever and reflected to a photodiode. When the cantilever is deflected, this beam is aimed at different part of photodiode. The photodiode output is an input signal to feedback-loop maintaining this value constant, changing vertical position of the cantilever holder.

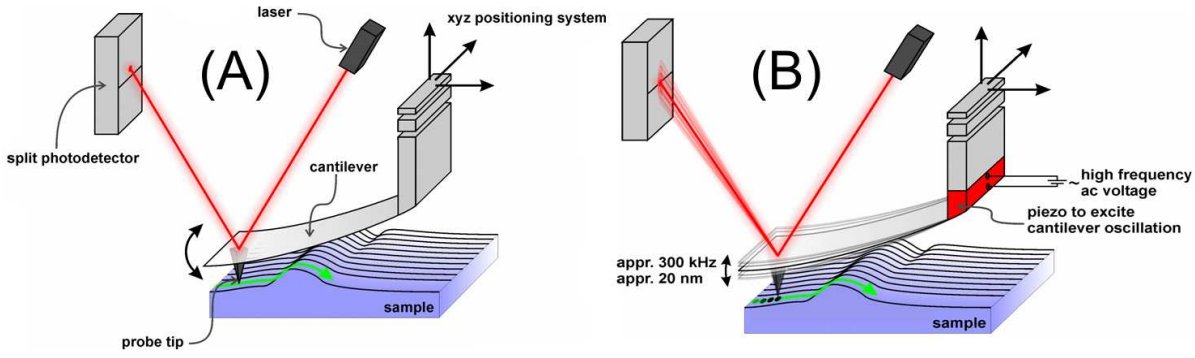

Fig. 8.8. A schematic diagrams of contact mode (A) and tapping mode (B) AFM setups [314].

There are two different AFM modes – contact and tapping mode. In contact mode during scanning across the sample the force exerted on the sample surface is maintained constant by keeping constant cantilever deflection. This mode is commonly used for hard surfaces. In the tapping mode additional piezoelectric actuator connected to the cantilever (Fig. 8.8B) oscillates it in vertical direction with its resonance frequency. The amplitude of the oscillation decreases as the tip approaches the probe. The tip slightly tap the surface during scanning and the magnitude of interaction with the sample surface is maintained constant by feedback loop keeping constant amplitude of cantilever oscillation by varying the *z*-position. Topography of soft surfaces can be visualized this way without their damage.

9 Chemicals and materials

All chemicals were analytical grade and were used as received without further purification.

- 2,2'-azino-bis(3-ethylbenzothiazoline-6-sulfonate) diammonium salt (ABTS, Sigma-Aldrich)
- 3,5-dimethoxy-4-hydroxybenzaldehydazine (syringaldazine, Sigma-Aldrich)
- Argon (N5.0, Multax)
- Bilirubin oxidase from *Myrothecium sp.* fungus (EC 1.3.3.5, Amano Enzyme Inc.)
- Borosilicate glass capillaries (Hilgenberg GmbH)
- Carbon nanoparticles with phenylsulfonic acid surface functionalities (ca. 7.8 nm mean diameter, Emperor 2000, Cabot Corporation)
- Disodium hydrogen phosphate (Na_2HPO_4, POCH)
- Ethanol (C_2H_5OH, 96 %, Chempur)
- Glassy carbon (GC) disc (3 mm diameter, nLab)
- Gold wire (25 µm diameter, Goodfellow)
- Graphite powder (MO-300, average particle size 20 µm, Carbon GmbH)
- Hexaammineruthenium(III) chloride ($[Ru(NH_3)_6]Cl_3$, Sigma-Aldrich)
- Hydrochloric acid (HCl, 35 %, POCH)
- Laccase from *Cerrena unicolor* fungus (EC 1.10.3.2, isolated and purified by Prof. Jerzy Rogalski group according to procedure described in literature [315, 316])
- Methyltrimethoxysilane (MTMOS, Sigma-Aldrich)
- Microscope glass slides (Menzel-Glaeser)
- Monosodium phosphate hydrate ($NaH_2PO_4 \cdot H_2O$, POCH)
- Nafion (5 % solution in 2-propanol, Sigma-Aldrich)
- Oxygen (N5.0, Multax)
- Petri dishes made of polystyrene (Carl Roth GmbH)
- Phosphoric acid (H_3PO_3, 85 %, Chempur)
- Platinum wire (10 µm diameter, Goodfellow)
- Potassium chloride (KCl, Sigma-Aldrich)
- Potassium hexacyanoferrate(II) trihydrate ($K_4[Fe(CN)_6] \cdot 3H_2O$, POCH)
- Potassium hexacyanoferrate(III) ($K_3[Fe(CN)_6]$, Sigma-Aldrich)
- Silver nitrate ($AgNO_3$, Sigma-Aldrich)

- Sodium chloride (NaCl, Sigma-Aldrich)
- Sodium hydroxide (NaOH, POCH)
- Tetramethoxysilane (TMOS, Sigma-Aldrich)
- Water (H_2O, >15 Ω·cm, demineralized with ELIX system, Milipore)
- Zinc wire (250 µm diameter, Goodfellow)

10 Instrumentation

Potentiostats, bipotentiostats and galvanostats

- Autolab PGSTAT30 (Eco Chemie)
- µAutolab III (Eco Chemie)
- CHI900B (CH Instruments)
- CHI7001B (CH Instruments)
- Ivium CompactStat (Ivium Technologies)
- µBIP (Schramm, Heinrich Heine University, Düsseldorf, Germany)
- Jaissle PG10 (Jaissle Elektronik GmbH)

Optical microscopes

- Nikon Eclipse LV150 metallographic microscope with LU Plan 10× (NA = 0.8) objective (Nikon)
- Olympus MIC-D

Confocal laser scanning microscope

- CSLM TCS SP2 AOBS with 488 nm Ar laser, HC PL FLUOTAR 10× (NA = 0.3), HC PLAN APO 20× objective (NA = 0.7) and HC PL FLUOTAR 50× (NA = 0.80) objectives (Leica Microsystems GmbH)

Atomic force microscope

- Veeco Dimension 3100 microscope and Nanoscope IIIA controller (Veeco Instruments Inc.)

Scanning electrochemical microscopes

- CHI900B (CH Instruments, for study of CCE-CNP conductivity, O_2-permeability and MTMOS-based silicate)
- Home-built (for study of laccase aggregates using SG/TC mode)
    - PI – HERA positioning system (PhysikInstrumente)
    - Analog µP3 analogue potentiostat (M. Schramm, Heinrich Heine University of Düsseldorf)
    - PCI-DDA8 and PCI-DAS1602/16 analog-digital converter boards (Plug-in Electronic GmbH)
- Home-built (for study of laccase aggregates using SG/TC and RC modes)
    - Closed-loop piezoelectric positioning system (mechOnics AG)
    - Ivium CompactStat potentiostat (Ivium Technologies)
- Home-built (for study of ABTS-CCE/Lc, Syr-CCE/Lc and CCE-CNP/BOx)
    - Stepper motor positioning system (Märzhäuser Wetzlar GmbH & Co KG)
    - PCI-DAS 1602/16 analog-digital converter board (Plug-in Electronic GmbH)
    - Analog µBiP3 bipotentiostat (M. Schramm, Heinrich Heine University of Düsseldorf)
- Home-built (for FB mode imaging of laccase aggregates)
    - Closed-loop piezoelectric positioning system (mechOnics AG) placed in a 2 L volume cell with controlled atmosphere [317]
    - Analog potentiostat Jaissle PG10 (Jaissle Elektronik GmbH)
    - PCI-DAS1602/16 analog-digital converter board (Plug-in Electronic GmbH)

Motors positioning and data acquisition in all home-built SECMs are controlled by the homemade SECMx software [318]. Data analysis was performed with the in house developed package MIRA [319].

Raman spectrometer

- Nicolet Almega with CLSM and CCD detector (Thermo Fisher Scientific)

Scanning electron microscope

- SEM SUPRA (Carl Zeiss SMT Inc.)

Evaporation chamber

- Mini-Coater (Tectra GmbH)

pH-meter

- CG 837 pH-meter (SCHOTT)
- pH-meter 605 (Metrohom GmbH)

Balance

- AB204-S analytical balance (Mettler Toledo)
- CP124S analytical balance (Satorius AG)

Ultraconic bath

- Sonorex RK 31 (Bandelin electronic GmbH & Co.)

Thermostat

- U4 Type (VEB MLV Labortechnik)

11 Procedures and cells assembly

11.1 ABTS-CCE and Syr-CCE preparation

The hydrophobic sol-gel matrix for CCE was prepared as described elsewhere [6, 206]. The hydrolysed sol was obtained by mixing 1 mL of MTMOS with 1.5 mL of methanol. For ABTS-CCE and for Syr-CCE preparation 12 mg of ABTS or 78 mg of syringaldazine was added to the sol, respectively. After addition of 50 µL of 11 M aqueous HCl it was sonicated for 2 min. Next, 1.25 g of graphite powder was added and the obtained mash was sonicated for another minute. Next, it was immediately placed into a 2 mm deep cavity of the 1.55 mm inner diameter glass tubing filled tightly with a copper wire. The electrode was left for drying at room temperature for at least 48 hours and then polished with printing paper. The geometric surface area of the exposed disc electrode is 0.019 cm^2.

11.2 CCE-CNP preparation

The hydrophobic sol-gel matrix was prepared in the same way as for ABTS-CCE and Syr-CCE (Section 11.1) The hydrolyzed sol was obtained by mixing 500 µL of MTMOS with 750 µL of methanol. After addition of 25 µL of 11 M HCl, it was sonicated for 2 min. Afterward, 625 mg of graphite microparticles or its mixture with CNPs in mass ratios 9:1 or 8:2 was added and the obtained mash was sonicated for another minute. It was then immediately placed into a 2 mm deep cavity of the 1.55 mm inner diameter glass tubing filled tightly with a copper wire. After drying at room temperature for at least 48 h, it was polished with printing paper, rinsed with water and dried. The geometric surface area of the exposed disc is 0.019 cm^2. The obtained electrodes will be referred to later as CCE and CCE-CNP10 and CCE-CNP20.

11.3 CCGE preparation

The hydrophobic sol-gel matrix was prepared in the same way as for ABTS-CCE, Syr-CCE and CCE-CNP (Sections 11.1 and 11.4). The hydrolyzed sol was obtained by mixing 500 µL of MTMOS with 750 µL of methanol. After addition of 25 µL of 11 M HCl, it was sonicated for 2 min. Afterward, 500 mg of graphite microparticles and 125 mg of CNPs were added and the obtained mash was sonicated for another minute. It was then immediately placed into the 5.7 mm inner diameter glass tube to fill it to 3 mm in depth. After drying at room temperature for at least 48 h, it was polished with printing paper, rinsed with water and dried. The geometric surface area of the exposed disc was 0.255 cm^2. The electrodes were immersed in 1 g L^{-1} solution of BOx in 0.1 M phosphate buffer pH 5.0 at +4 ºC for 2 h and rinsed with water.

11.4 Encapsulation of enzymes in the hydrophilic gel film

The hydrophilic gel film (TMOSgel) for encapsulation of active enzyme was prepared according to slightly modified literature procedure [158, 320]. TMOS, H_2O and 0.04 M aqueous HCl were mixed in volume ratio 18 : 4.5 : 1. This mixture was sonicated for 20 minutes and next mixed with water, in volume ratio 1 : 1. This stock sol was sonicated for 3 minutes, diluted with water in 1 : 100 volume ratio and sonicated for another 3 minutes. Finally, 145 µg of laccase (lac) from *Cerrena unicolor* or bilirubin oxidase from *Myrothecium sp.* was added to 250 µL of diluted stock sol. 10 µL of 1:100 diluted sol was placed on the CCE electrodes or the glass and gold surfaces. For sol-gel processing and drying these

electrodes were left for 20 hours at room temperature, at air humidity equal 40 – 50 %. For comparison of enzymes activity, a silicate-entrapped laccase spot and a silicate-entrapped BOx spot were placed on one Plexiglas slide by a glass micropipette attached to micromanipulators and filled with the corresponding enzyme-sol. The movement was controlled by an inverted optical microscope. The diameter of the micropipette tip was ca. 50 µm, and the diameters of the resulting spots were also ca. 50 µm.

11.5 Gold evaporation on glass

Glass microscope slides were cleaned subsequently with water and ethanol in an ultrasonic bath for 3 minutes and dried with argon. Next, the slides were coated subsequently with 30 nm of Cr and 200 nm of Au using evaporation chamber. The thicknesses of Cr and Au layers were controlled by quartz crystal microbalance mounted inside the camber.

11.6 Synthesis of hexaaminoruthenium(III) nitrate

$[Ru(NH_3)_6](NO_3)_3$ was obtained by metathesis as a filtrate after AgCl precipitation using stoichiometric amounts of $[Ru(NH_3)_6]Cl_3$ and $AgNO_3$. This synthesis was done to eliminate chloride anions, which are known as laccase inhibitor (section 3.1).

11.7 Bilirubin oxidase adsorption

The CCE-CNP electrodes were immersed in 1 g L^{-1} solution of BOx in 0.1 M phosphate buffer pH 5.0 at +4 ºC and rinsed with water. The enzyme adsorption time was optimised in the range 0.5-48 h on the basis of voltammetric signal of the BOx-modified electrodes in aerated solution. The same test showed maximal catalytic current for electrodes obtained from 1 g L^{-1} BOx solution in comparison to 0.1 g L^{-1} and 10 g L^{-1}.

11.8 Preparation of microhole in PS plate filled with silicate

For determination of oxygen permeability of MTMOS-based silicate a hole (c.a. 100 µm diameter) in 0.8 mm thick polystyrene (PS) plate (Petri dish) was burned using a homemade 800 nm wavelength laser (100 fs, 300 µJ pulses, repetition rate 1 kHz) during 0.5 s. The hole was filled only with MTMOS-based sol by touching its droplet and left for drying at room temperature for at least 48 h.

11.9 Preparation of zinc anode

The anodes for Zn-O_2 batteries were zinc wires (0.25 mm diameter) coated with a Nafion film by dipping in 0.5% Nafion solution in 2-propanol and dried for 5 minutes in ambient conditions. The length of these electrodes was adjusted to the same surface area as cathodes.

11.10 Experimental setup for CV and DPV

Cyclic voltammetric (CV) experiments were done with potentiostats listed in Chapter 10 in conventional three-electrode cells. Studied electrodes were connected as working electrodes. Saturated Ag|AgCl|sat.-KCl electrode and Pt wire served as reference and counter electrode respectively. Experiments were performed in 0.1 M phosphate buffers whose pH was checked using pH-meter. In some cases mediators were used with 0.1 mM concentration in the same buffers. The experiments were carried out in O_2-, air-, or Ar-saturated solutions with proper gas passing above the electrolyte. The temperature of the cell was equal room temperature 20-22 °C. All potentials are referred to used reference electrode.

11.11 Experimental setup for SECM measurement

SECM measurements of enzymes immobilized on insulating surfaces were performed in a three electrode cells consisting of a Pt or Au microelectrodes as working electrode, a Pt wire as counter electrode and a silver wire (SG/TC and RC modes) or Ag|AgCl|3M KCl as quasi-reference and reference electrode respectively. The microelectrodes were prepared by sealing a Pt or Au wire (10 or 25 µm diameter) into borosilicate glass capillaries and shaping the apex according to literature procedure [321]. The ratios *RG* between the radius of the insulating glass and the radius r_T of the active electrode area was approximately 10. 0.1 M phosphate buffers were used as working solution. In some cases mediators were present in working solutions. If not stated otherwise, their concentration was 0.1 mM. Ar, O_2 or air were passed over the cell. Oxidation or reduction of mediators were carried out at potentials sufficient for diffusion-controlled reaction. The working distance *d* was adjusted by withdrawing the microelectrode by a defined distance after touching to insulating sample support near the measured area. Some SECM measurements were carried out with simultaneous observation of transparent samples by CLSM.

SECM measurements of electrodes were performed in a four electrode cells consisting of a disk-shaped Pt microelectrode and sample as first and second working electrodes, respectively. A Pt wire and Ag|AgCl|3M KCl served as auxiliary and reference electrodes, respectively. The microelectrode was obtained by sealing a Pt wire (25 µm diameter) into borosilicate glass capillaries. Its apex was shaped according to literature procedure [321]. The ratio *RG* between the radius of the insulting glass and the radius r_T of the active area for Pt microelectrode was ca. 4.6. The distance between probe and sample was $d \approx 20$ µm and was adjusted by withdrawing the microelectrode by a defined distance after touching to the sample support near the measured area.

11.12 Experimental setup for Zn-O_2 cell measurement

Current density-voltage characteristics of the Zn-O_2 cell were determined by chronopotentiometry. The studied cell acts as an active element of the electric circuit and the galvanostat is a passive element which allows the current to flow with a certain setpoint value. The cell voltage for each current setpoint was recorded 100 seconds after current setting. It was observed that after this period the voltage was stabilized. Then the galvanostat acts as resistor with voltmeter and ammeter and results are comparable to those obtained by variable resistor method. The advantage of chronopotentiometry is that it is fully automated.

11.13 Experimental setup for Raman spectroscopy

Raman spectra were recorded using Nicolet Almega Dispersive Spectrometer with confocal microscope and CCD detector. Spectra were recorded using two 780 nm diode laser and 1200 grooves mm^{-1} grating. The laser power was reduced to 13 % in order to avoid overheating. The typical exposure time was between 15 and 30 s. For selected samples, namely non-polarised and polarised at 0.2 V electrodes spectra were additionally recorded using 532 nm exciting line and 2400 grooves mm^{-1} grating, with power of the laser reduced to 1%. The exposure time was between 30 and 180 s, depending on sample. The experimental setup is presented in Figure 11.1.

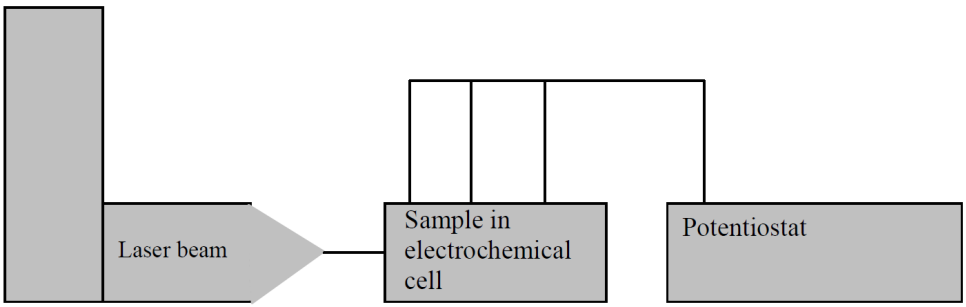

Fig. 11.1. A schematic diagram of experimental setup for Raman spectroscopy investigation of electrode surface under controlled potential.

Samples were placed inside the spectroelectrochemical cell designed by Ventacon Ltd. Voltammetric experiments were done in a conventional three-electrode cell. Hg|Hg_2Cl_2|sat.-KCl electrode and Pt wire served as reference and counter electrode, respectively. The laser beam of the Raman spectrometer was directly aimed in the front glass plate of the spectroelectrochemical cell. Position of the sample was manually adjusted toward obtaining best quality of optical images.

11.14 Fitting of heterogeneous kinetic parameters to SECM approach curves

Normalized heterogeneous rate constants κ have been extracted from experimental approach curves by fitting analytical approximation of simulated data evaluated by Cornut and Lefrou [292] to experimental curves.

Input parameters

The radius of the active part of the microelectrode, r_T, the ratio of insulating sheath r_{glass} and r_T, *RG*, and the point of closest approach d_0 have been determined from independent experiments. *RG* was determined by optical microscopy; r_T and d_0 were determined from approach curves to glass and fitting them to theoretical curves proposed by Amphlett and Denuault [291].

Fitting

Experimental approach curves $i_T(z)$ where normalised. Current I_T and distance L have been calculated using Eq. (11.1) and Eq. (11.2) or Eq. (11.3). Eq. (11.2) applies for increasing motor position z for decreasing microelectrode-to-sample distance d (case A in Fig. 11.2). Eq. (11.3) applies for decreasing z for decreasing d (case B in Fig. 11.2).

$$I_T = \frac{i_T}{i_{T,\infty}} \tag{11.1}$$

$$L = \frac{z - z_{offset}}{-r_T} \tag{11.2}$$

$$L = \frac{z - z_{offset}}{r_T} \tag{11.3}$$

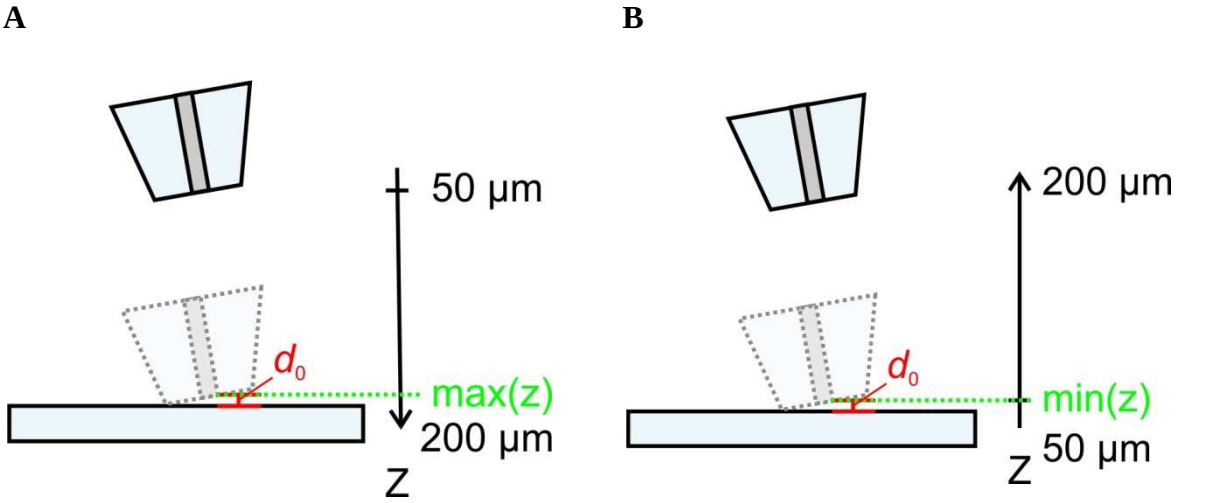

Fig. 11.2. Determination of z_{offset} and L for (A) increasing z for decreasing d and (B) decreasing z for decreasing d.

z_{offset} is calculated according to Eq. (11.4) and (11.5) which corresponds to case A or B, respectively. d_0 is the distance of the active microelectrode area to the sample when the insulating sheath touches the surface.

$$z_{offset} = \max(z) + d_0 \tag{11.4}$$

$$z_{offset} = \min(z) - d_0 \tag{11.5}$$

The analytical approximation of Cornut and Lefrou [292] was used for calculating a theoretical current I_T for each experimental, normalised distance L.

$$I_T(L,\kappa,RG) = I_T^{cond}\left(L+\frac{1}{\kappa},RG\right) + \frac{I_T^{ins}(L,RG)-1}{\left(1+2.47RG^{0.31}L\kappa\right)\left(1+L^{0.006RG+0.113}\kappa^{-0.0236RG+0.91}\right)} \tag{11.6}$$

with

$$I_T^{cond}\left(L+\frac{1}{\kappa},RG\right) = \alpha(RG) + \frac{1}{2\beta(RG)\xi\left(L+\frac{1}{\kappa}\right)} + \left(1-\alpha(RG)-\frac{1}{2\beta(RG)}\right)\xi\left(L+\frac{1}{\kappa}\right) \tag{11.7}$$

$$I_T^{ins}(L,RG)=\frac{\frac{2.08}{RG^{0.358}}\left(L-\frac{0.145}{RG}\right)+1.585}{\frac{2.08}{RG^{0.358}}(L+0.0023RG)+1.57+\frac{\ln RG}{L}+\frac{2}{\pi RG}\ln\left(1+\frac{\pi RG}{2L}\right)} \tag{11.8}$$

$$\alpha(RG)=\ln 2+\ln 2\left(1-\frac{2}{\pi}\arccos\left(\frac{1}{RG}\right)\right)-\ln 2\left(1-\left(\frac{2}{\pi}\arccos\left(\frac{1}{RG}\right)\right)^2\right) \tag{11.9}$$

$$\beta(RG)=1+0.639\left(1-\frac{2}{\pi}\arccos\left(\frac{1}{RG}\right)\right)-0.186\left(1-\left(\frac{2}{\pi}\arccos\left(\frac{1}{RG}\right)\right)^2\right) \tag{11.10}$$

$$\xi\left(L+\frac{1}{\kappa}\right)=\frac{2}{\pi}\arctan\left(L+\frac{1}{\kappa}\right) \tag{11.11}$$

$$\kappa=\frac{k_{\mathrm{eff}}r_T}{D} \tag{11.12}$$

κ, $i_{T,inf}$ and d_0 were varied in order to fit the experimental approach curves.

Heterogeneous rate constant k_{eff} was calculated from κ:

$$k_{eff}=\frac{\kappa D}{r_T} \tag{11.13}$$

12 Carbon ceramic electrode modified with ABTS and laccase

12.1 Introduction

For mediated electron transfer numerous molecules serving as electron relay between the electrode and protein were already examined [98]. Water soluble 2,2'-azino-bis(3-ethylbenzothiazoline-6-sulfonate) ($ABTS^{2-}$) is one of the most popular [81, 108, 158, 322, 323].

Here simple procedure of the non-covalent immobilization of $ABTS^{2-}$ and laccase is proposed. Mediator is immobilized into porous silicate-carbon heterogeneous structure of carbon ceramic electrode. Hydrophobic silicate matrix allows for stable confinement of $ABTS^{2-}$ molecules by their addition to the sol. In the next step, laccase is immobilized in hydrophilic silicate thin film deposited on the $ABTS^{2-}$ modified CCE surface. Such a matrix prevents laccase leaching to surrounding solution [108, 158, 323]. Additionally, the sol-gel processing of silicate film on the top of silicate based heterogeneous material of CCE allows for strong bonding between both parts of the electrode.

In order to evaluate ABTS-CCE voltammetric stability and electrocatalytic properties towards oxygen its electrochemical properties were studied in the absence and presence of the enzyme in silicate film. These experiments were done at pH = 4.8 corresponding to maximum electrocatalytic activity of laccase from *Cerrena unicolor* encapsulated in silicate matrix [158]. Special attention is paid to the possible leaching of mediator as earlier detected by SECM experiments [324]. Here, it was found that $ABTS^{2-}$ leaching could only be detected after application of sufficiently low potentials to the sample while at open circuit potential (OCP) this process is not observed.

12.2 Voltammetric measurements of ABTS-CCE

At first the electrochemical properties of ABTS-CCE were examined. Its voltammetric response indicates surface confined redox process (Fig. 12.1B), because of linear dependence of peak current on scan rate (Fig. 12.2A). The set of anodic and cathodic peaks with redox potential equal 0.401 V corresponds to the reversible process:

$$ABTS^{2-} \leftrightarrows ABTS^{\bullet-} + e^{-} \qquad (12.1)$$

This voltammogram is much better defined and the current densities are much higher than in the case of electrode modified with ABTS polymer [325]. Interestingly, both peaks are shifted into cathodic direction in comparison to that obtained on unmodified CCE with $ABTS^{2-}$ present in solution (Fig. 12.1A). This may indicate stronger adsorption of oxidized form of the mediator. At slowest scan rate (1 or 2 mV s^{-1}) another anodic peak at higher potential (0.62 V) appears (Fig. 12.1A). It may indicate some irreversible electrode process – possibly further oxidation of adsorbed $ABTS^{\bullet-}$ to neutral molecule. Although for dissolved mediator this process occurs at higher potential, here it may be shifted, because of substrate adsorption. This also may explain why the ratio of anodic to cathodic charge is larger than unity and depends on the scan rate (Fig. 12.2B).

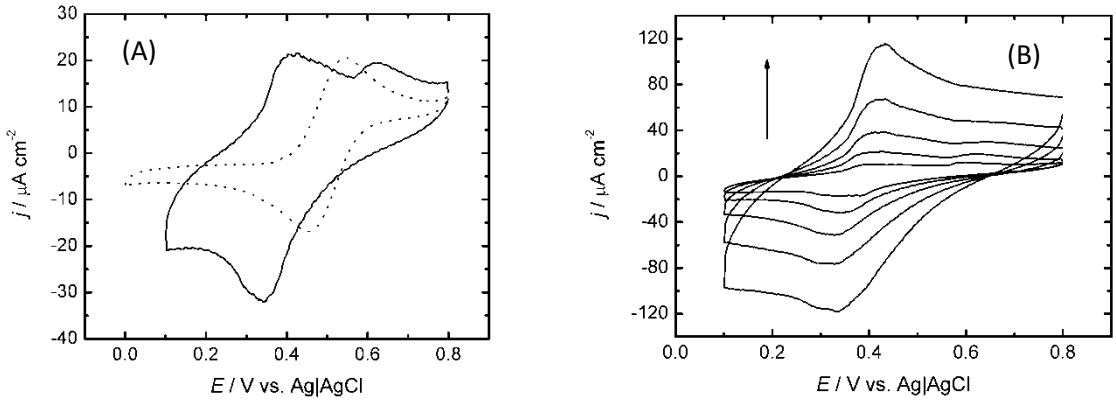

Fig. 12.1. (A) - Cyclic voltammograms of TMOS-gel coated ABTS modified CCE immersed in O_2-saturated 0.1 M phosphate buffer (pH 4.8 (solid line) and TMOS-gel coated CCE immersed in 0.1 mM ABTS solution in the same electrolyte (dotted line). Scan rate 2 mV s^{-1}. (B) - Cyclic voltammograms of TMOS-gel coated ABTS-CCE obtained at different scan rates: 1, 2, 4, 8 and 16 mV s^{-1}. Electrode was immersed in O_2-saturated 0.1 M phosphate buffer pH 4.8. Arrow indicates increasing scan rate.

The voltammograms obtained with ABTS-CCE are stable during continuous scanning indicating long-lasting immobilization of substrate and product of reaction (12.1) within pores of hydrophobic silicate matrix. The presence of methyl groups connected to silicon atoms prevents the dissolution of mediator in the aqueous phase. This is confirmed by failure of its immobilization within hydrophilic TMOS based matrix. The surface coverage calculated from the cathodic voltammetric charge at scan rate 8 mV s^{-1} and based on estimated surface area of $ABTS^{2-}$ (1.7 nm^2) [326] corresponds to approximately four layers covering geometric area of the electrode. This indicates that only small fraction of the mediator immobilized next to the electrolyte is electrochemically active.

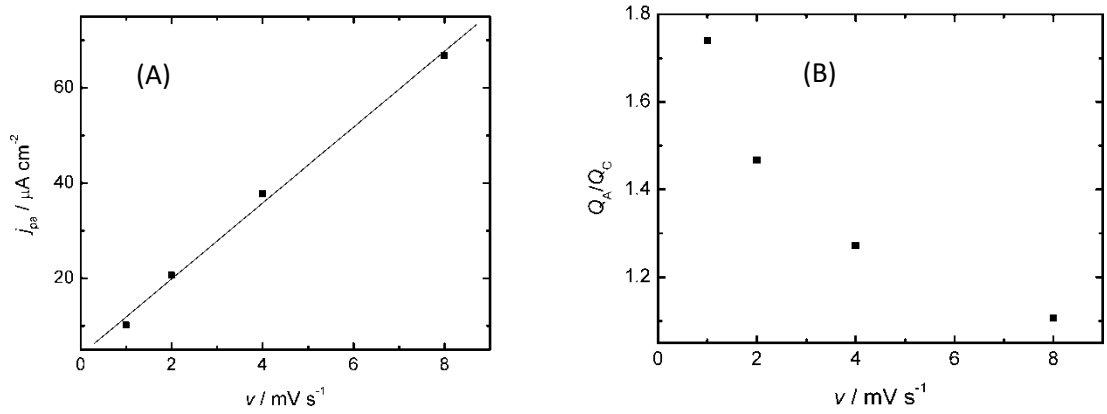

Fig. 12.2. Scan rate dependence of anodic peak current (A) and anodic to cathodic charge ratio (B) of CVs from Fig. 12.1B.

This results from the heterogeneous structure of the electrode (Fig. 12.3) and possible precipitation of $ABTS^{2-}$ salt. One can conclude that only mediator molecules present close to three phase junction graphite particle|silicate matrix|aqueous solution participate in the electrode process.

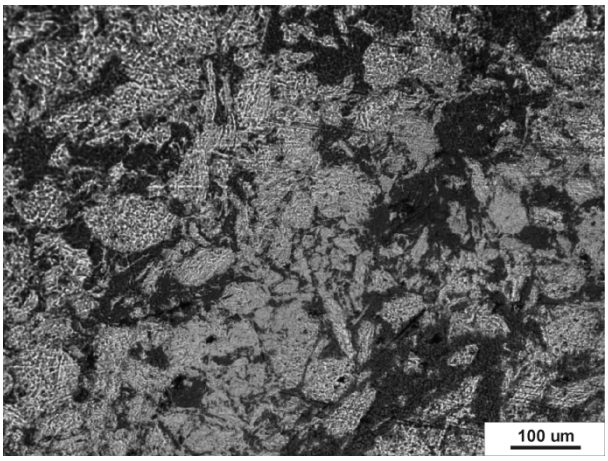

Fig. 12.3. Optical micrograph of CCE surface. Dark places correspond to silicate matrix and bright to light reflected from graphite particles.

12.3 Voltammetric measurements of electrode modified with laccase

Next voltammetric experiments were done with laccase encapsulated in thin silicate film on the top of ABTS-CCE surface in oxygen saturated solution. The observed sigmoidal shape of cyclic voltammograms and the larger magnitude of the cathodic current (Fig. 12.4A) are typical features of electrocatalytic reduction of O_2 by laccase mediated by $ABTS^{2-}$ [327]:

$$4\ ABTS^{2-} + O_2 + 4\ H^+ \qquad 2\ H_2O + 4\ ABTS^{\bullet-} \qquad (12.2)$$

Obviously some fraction of mediator and the enzyme immobilized in adjacent hydrophobic and hydrophilic silicate matrices remains in close contact. The catalytic current is observed immediately after immersion of the electrode indicating that the enzymatic reaction starts without delay. Repeated voltammetry of this system results in decrease of catalytic current (Fig. 12.4A). Its approximately 30% decrease is observed in third scan at 1 mV s^{-1}. This is probably because $ABTS^{\bullet-}$ anion radical produced by silicate encapsulated laccase may shorten its lifetime due to denaturation [328-330].

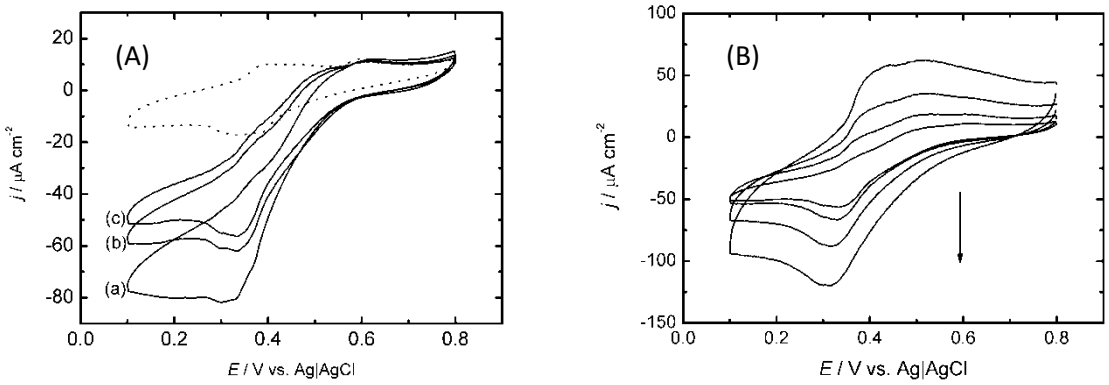

Fig. 12.4. (A) - Cyclic voltammograms of $TMOS_{gel}$ coated ABTS modified CCE in the absence (·····) and presence (—) of laccase in silicate film: (a) 1st scan, (b) 2nd scan, (c) 3rd scan. Both electrodes were immersed in O_2-saturated 0.1 mol dm^{-3} phosphate buffer pH 4.8. Scan rate: 1 mV s^{-1}. (B) - Cyclic voltammograms (3rd scan) of laccase-containing TMOS-gel coated ABTS-CCE at different scan rates: 1, 2, 4 and 8 mV s^{-1}. Arrow indicates increasing scan rate.

The shape of cyclic voltammograms obtained with laccase modified ABTS-CCE depends strongly on time scale of the experiment (Fig. 12.4B). At scan rate faster than 2 mV s^{-1} anodic peak reappears and the ratio of cathodic to anodic charge decreases indicating slow rate of catalytic reaction. This was earlier observed for bioelectrocatalysis with ABTS present in solution [158].

Interestingly, the potential corresponding to the largest slope of the catalytic voltammetric curve obtained with immobilized mediator is negatively shifted by ca. 0.12 V comparing to situation when $ABTS^{2-}$ is present in the electrolyte (Fig. 12.5). It is typically governed by matching of the redox potential of the mediator and laccase. The value of the latter is equal 0.51 V [108] which is 0.1 V higher than observed for ABTS-CCE. This small difference promotes the electron exchange (See section 4.3). However, this may not be the only reason of this effect. Different local concentrations of mediator and its distribution in the electrode material may also play important role.

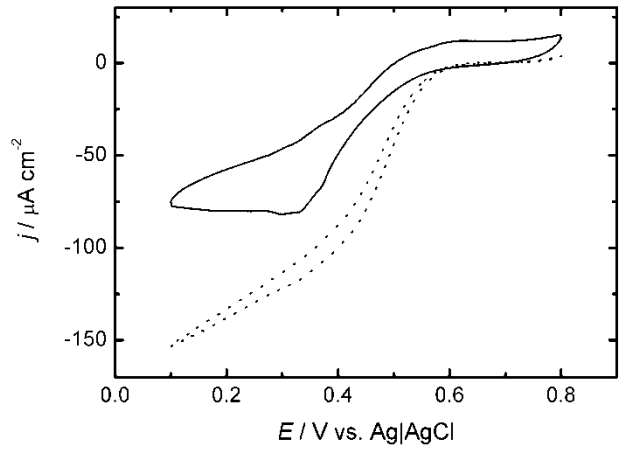

Fig. 12.5. Cyclic voltammograms (1st scan) of laccase – TMOS-gel ABTS-CCE immersed in O_2-saturated 0.1 M phosphate buffer pH 4.8; (—) and of laccase – TMOS-gel modified CCE immersed in 0.1 M ABTS solution in the same electrolyte (·····). Scan rate = 1 mV s^{-1}.

12.4 SECM measurements

The mediation in composite enzyme electrodes can be based on slow dissolution of the mediator [324]. The dissolved mediators shuttles electrons between the active site of the enzyme and the conducting parts of the composite. Because of the short diffusion length this process can be very effective despite the low concentration of dissolved mediator (Fig. 12.6). The possible leaching of the mediator is compensated by the large reservoir of solid mediator in the composite. Nevertheless, mediator leaching may lead to contamination that can be problematic depending on the application. Therefore, SG/TC mode SECM experiments were used to probe possible mediator leaching and its distribution at this electrode. Following earlier published methodology [324], the microelectrode was positioned close to the sample. After applying a potential sufficiently low to observe bioelectrocatalytic oxygen reduction at the ABTS-CCE/Lc substrate electrode (E_S = 0.25 V), a cyclic voltammogram is recorded at the tip.

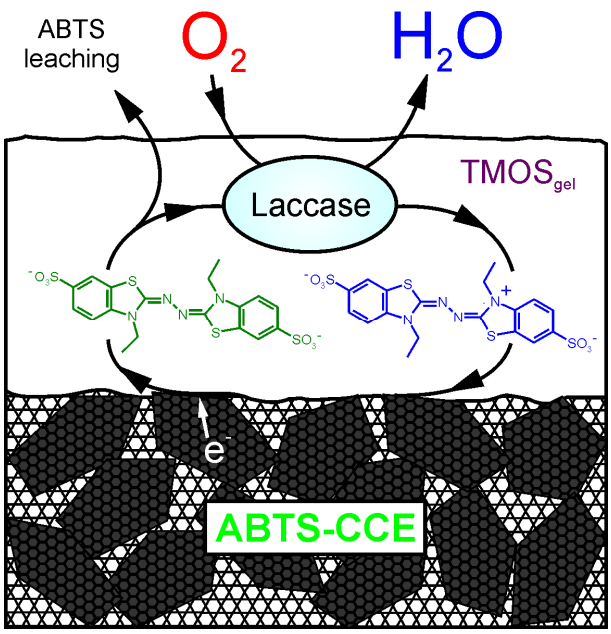

Fig. 12.6. A schematic diagram of the structure of ABTS-CCE covered by a thin film of sol–gel processed hydrophilic TMOS-gel based silicate with encapsulated laccase and the mechanism of mediated ORR.

In this way the electrochemical signature of any compound released from the electrode can be identified before diffusion into the bulk phase of the solution, what would lead to a dilution below the detection limit of cyclic voltammetry. The cyclic voltammogram performed at the SECM probe above ABTS-CCE/Lc electrode reveals a two step electrooxidation process (Fig. 12.7A).

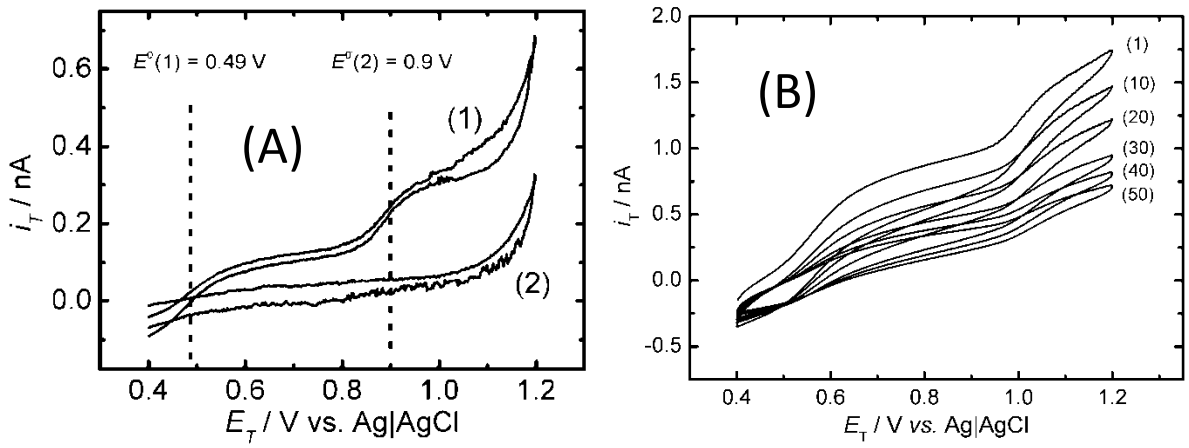

Fig. 12.7. (A) – Cyclic voltammograms obtained at the Pt-microelectrode positioned 20 µm above ABTS-CCE/Lc in 0.1 M phosphate buffer pH 4.8. Curve (1) – sample at E_S = 0.25 V; scan rate 20 mV s^{-1}. Curve (2) same as before but sample at OCP. Dashed vertical lines indicate standard potentials for reaction (12.1) and (12.13). (B) – Cyclic voltammograms obtained at the Pt-microelectrode positioned 20 µm above ABTS-CCE/Lc in 0.1 M phosphate buffer pH 5. Scan numbers marked. E_S = 0.25 V; scan rate 20 mV s^{-1}.

The positions of the signals (E°'(1) = 0.49V, E°'2 = 0.9 V) are in agreement with the redox potentials of the oxidation of $ABTS^{2-}$ according to reaction (12.1) and (12.13), respectively.

$$ABTS^{\bullet-} \leftrightarrows ABTS + e^{-} \quad (12.13)$$

The values of the standard potentials of reaction (12.1) and (12.13) correspond to those reported earlier [331]. The voltammetric signals at the microelectrodes are absent when no external potential is applied to the ABTS-CCE/Lc electrode (Fig. 12.7A). This indicates that the application of the potential causes $ABTS^{2-}$ leaching from the electrode to the electrolyte solution. The signal registered at the tip decreases continuously (Figure 12.7B). The depletion of the mediator inside the ABTS-CCE body results in the decrease of the electrode activity (Fig. 12.4A). Because $ABTS^{2-}$ salt is present in CCE body, the OCP should be in the range where the this form of mediator is stable, i.e. below 0.49 V (Fig. 12.7A). Therefore, the potential dependent release cannot be explained by a change in the redox state of $ABTS^{2-}$. The laccase catalyzed reaction (12.2) seems to have no direct influence on the leaching because the cyclic voltammogram in Fig. 12.7A shows that mainly the $ABTS^{2-}$ form is released from the sample surface, because the anodic currents at 0.6 V (oxidation of $ABTS^{2-}$) are much larger than the cathodic ones at 0.4 V (reduction of $ABTS^{\bullet-}$ and ABTS).

The remaining influence of the potential may result from migration of the $ABTS^{2-}$ anion. In the bulk of the electrolyte transport of mediator would mainly be controlled by diffusion due to the excess of the phosphate ions in the buffer. Within the body of the CCE charge transport occurs mainly by electronic conduction via the network of interconnected carbon particles. However in the enzyme loaded gel film on the top of CCE, the content and mobility of ions is not precisely known. Furthermore, considerable compositional gradients may exist. Immobile charges at the pore backbone of the silicate network further complicate the situation in comparison to the solution bulk. In this situation migration of $ABTS^{2-}$ may play an important role in the charge transport across the gel film. To provide a more direct proof for this mechanisms, anodic current on SECM probe positioned in the vicinity of ABTS-CCE covered with film without laccase was measured at E_T = 1 V versus the sample potential (Fig. 12.8). The sample potential was changed slowly (1 mV s^{-1}). One can notice that tip current (processes (12.1) and (12.13)) starts to increase shortly after net cathodic current starts to flow on the sample. The delay (ca. 6 mV corresponding to 6 s) is caused by diffusion of $ABTS^{2-}$ from the sample to the tip. We exclude any substantial feedback contribution (re-reduction of $ABTS^{\bullet-}$ on the sample electrode), because no $ABTS^{2-}$ is detected when the sample electrode is not connected to bipotentiostat.

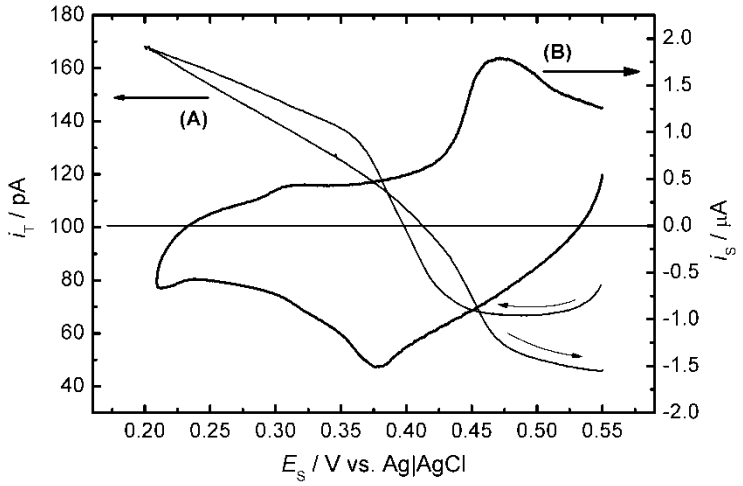

Fig. 12.8. Cyclic voltammograms: (A) – current at Pt-microelectrode (r_T = 12.5 µm, E_T = 1 V) positioned 20 µm above ABTS-CCE as a function of ABTS-CCE potential (E_S), (B) – current at ABTS-CCE as a function of its potential (E_S). Electrolyte: 0.1 M phosphate buffer pH 5, v = 1 mV s^{-1}.

The enzymatic reaction should have an indirect influence on such migration process via the current distribution at the composite electrode. At regions of higher enzymatic activity increased leaching of mediator is expected due to higher current density. Experiments with CCE modified with a redox liquid [332] also showed that leaching of the mediator may be inhomogeneously distributed across the surface on the micrometer scale. The local leaching of the product of the electrode reaction [332] or mediator [324] can be monitored by SECM. Therefore, SG/TC SECM imaging of ABTS-CCE/Lc was performed and the results are presented in Fig. 12.9.

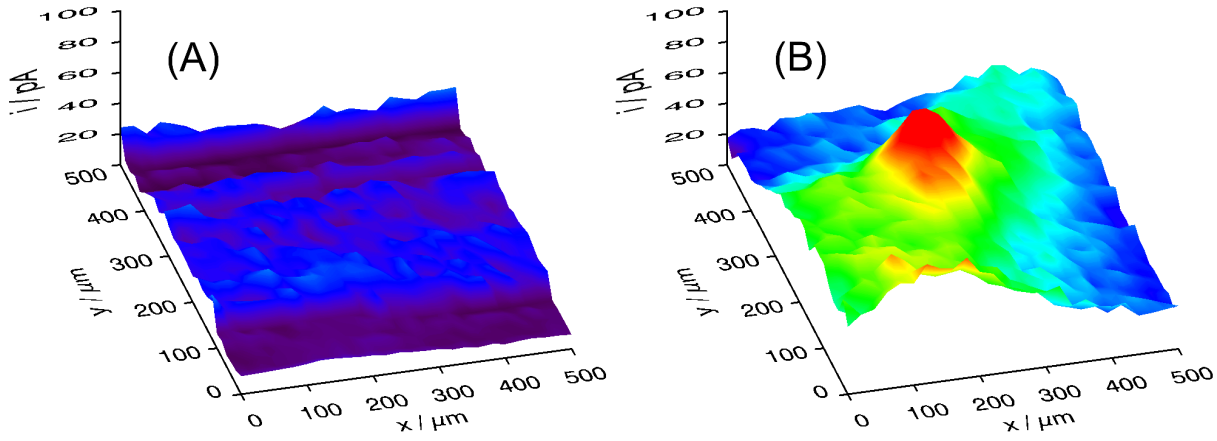

Fig. 12.9. SECM images of electrooxidation of $ABTS^{2-}$ leaching from ABTS-CCE/Lc in 0.1 M phosphate buffer pH 4.8. A) E_S = OCP, E_T = 1 V, r_T = 13.2 µm, RG = 10.3, d = 20 µm, v_T = 8.7 µm s^{-1}; (B) same as (A) but with the sample at 0.25 V.

Regions with higher anodic currents in Fig. 12.9B compared to Fig. 12.9A are caused by the faradaic processes (12.1) and (12.13) at the microelectrode. The variation of the current

may have two reasons. It might be due to the local availability of $ABTS^{2-}$ above the ABTS-CCE/Lc electrode, thus reflecting the local release of $ABTS^{2-}$ from the substrate electrode. In addition, current variation would be enhanced by possible electrochemical feedback effects if $ABTS^{\bullet-}$ is re-reduced at the carbon particles. In such case the current variations would depend strongly on the working distance [333]. In this experiment the working distance *d* was 20 µm with an microelectrode radius r_T = 13.2 µm. The current at the peak in Fig. 12.9B is about 4 times higher than the current level in the surrounding or in the control image shown in Fig. 3B. apart from the distance variations a very small average *d* would be required in order to relate the current variation exclusively to topographic effects. Considering the working distance of *d* = 20 µm and the fact that the CCE electrode was covered by ca. 150 nm (Fig. 14.4) of a gel film not containing carbon particles excludes the possibility that such small *d* were effective in this experiment. A realistic estimate of the roughness of ceramic electrodes is 5 µm (as exemplarily measured for Syr-CCE/Lc electrode, Fig. 13.13). Hence topographic effects alone cannot be responsible for the current variation in Fig. 12.9B. In a control experiment with the ABTS-CCE/Lc at OCP, no systematic current variations were observed (Fig. 12.9A) on the identical sample region although the background currents was almost equal to that in Fig. 12.9B. For a possible electrochemical re-reduction of ABTS or $ABTS^{\bullet-}$ at the carbon particles at OCP, one would expect an almost diffusion-controlled reaction rate. In case of feedback contributions to the image due to variations in working distance and re-reduction of ABTS at carbon particles this effect should be visible in Fig 12.9A as well. The complete absence of these features is another argument for a strongly localized release of $ABTS^{2-}$. By combining the results of Fig. 12.7 and the observation of localized release in Fig. 12.9B, the localized release is related to the current distribution of the catalytic reduction inside the film. The lateral variations in currents density can be caused by locally different concentration of the solid $ABTS^{2-}$ salts in the composite, variations in the enzyme concentration or variation in the effectiveness of mediation for instance due to different distances of the enzyme to the carbon particle network.

12.5 Zn-O_2 membraneless hybrid cell

ABTS-CCE/Lc was tested as biocathode in Zn-O_2 hybrid cell (Section 5.5). To show the influence of biocatalysis current-voltage characteristics of the cells with bare CCE as the cathode and ABTS-CCE/Lc as the biocathode are compared in Fig. 12.10A. One can notice that ORR occurs also at bare CCE at much lower potentials, so activation voltage drop is

much higher for Zn-O_2 cell with CCE cathode than for cell with ABTS-CCE/Lc biocathode. This is because of lower overpotential of bioelectrocatalytic ORR.

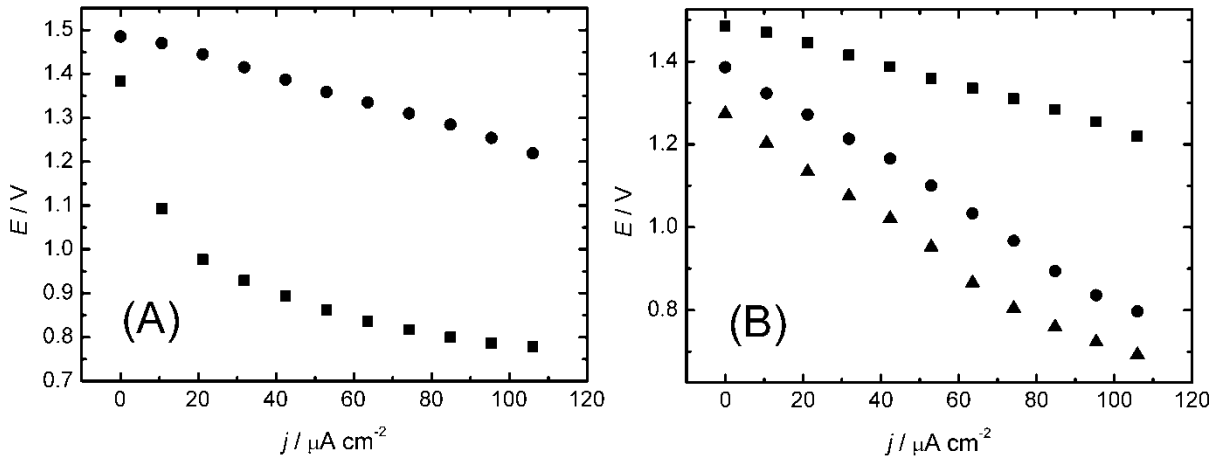

Fig. 12.10. (A) Current density-voltage characteristics of a cell consisting of Nafion coated Zn wire and CCE (■) or ABTS-CCE/Lc (●) immersed in O_2-saturated 0.1 M phosphate buffer pH 5. (B) Current density-voltage characteristics of a cell consisting of Nafion coated Zn wire and ABTS-CCE/Lc immersed in 0.1 M phosphate buffer pH 5 (■), pH 7.4, or artificial serum (▲).

Due to the interest in application of Zn-O_2 battery as an implantable power source this cell was also examined at pH 7.4 and in artificial serum consisting of 20 mM phosphate buffer pH 7.4 and 0.15 M NaCl. Current density-voltage characteristics of cells consisting of Nafion coated Zn wire and ABTS-CCE/Lc immersed in O_2-saturated electrolytes with different compositions are presented in Fig. 12.10B. The most effective is the cell with 0.1 M phosphate buffer pH 5, less effective at pH 7.4 and the lowest voltages are recorded for the cell with artificial serum. This is because of strong pH-dependence of laccase activity [158]. At pH 5 laccase exhibits almost maximal activity whereas at pH 7.4 is much lower. Despite this fact ORR may also occur at graphite, which is a component of ABTS-CCE/Lc, but at lower potential. This causes the cell voltage losses. Chloride anions, known as laccase inhibitor (Section 3.1), present in artificial serum cause additional potential drop (Fig. 12.10B).

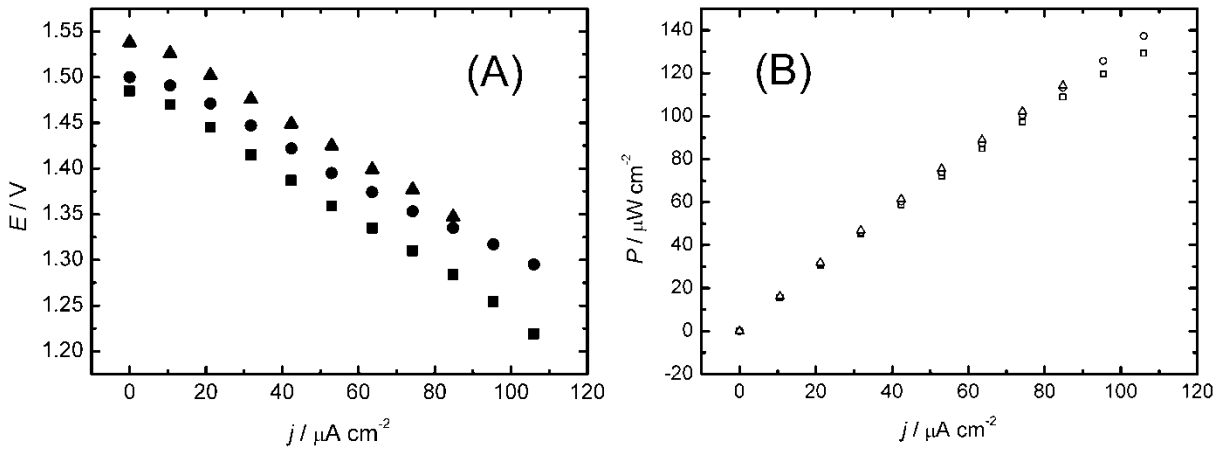

Fig. 12.11. Current density-voltage (A) and current density-power density (B) characteristics of a cell consisting of Nafion coated Zn wire and ABTS-CCE/Lc immersed in O_2-saturated 0.1 M phosphate buffer pH 5 at different temperatures: 24 °C (■,□), 37 °C (●,○) and 50 °C (▲,Δ).

Due to requirement for implantable battery to operate at 37 °C, current-voltage characteristics of Zn-O_2 cell with ABTS-CCE/Lc biocathode were also measured at different temperatures (Fig. 12.11A). The temperature increase causes slight improvement of cell voltage what has negligible influence on power density (Fig. 12.11B). As one can see there is no maximum in power-current characteristic measured in this current range. At higher current densities O_2 is reduced at graphite microparticles which are an ingredient of ABTS-CCE/Lc composite. Then ORR may proceed as 2 electrons reaction causing H_2O_2 generation. In order to eliminate ORR on graphite the cells were loaded at current densities lower than obtained in voltammetric measurements of ABTS-CCE/Lc (Section 12.3). This ensures that cathode potential is higher than H_2O_2 evolution potential (see Section 13.5).

12.6 Conclusions

ABTS-CCE with laccase encapsulation within silicate matrix deposited on its surface exhibits electrocatalytic activity towards oxygen reduction. The immobilization procedure of both mediator and enzyme is simple and does not require polymerization of the mediator and covalent linkage of the enzyme to the electrode surface. Negative potential shift of ORR on ABTS-CCE/Lc may be caused by stronger adsorption of $ABTS^{2-}$ on graphite than that of $ABTS^{\bullet-}$ causes. However, this electrode still suffers from deactivation of laccase by ABTS anion radical. The results obtained by means of SECM imaging and combined sample-probe voltammetry shed new light on reaction mechanism and deactivation of ABTS-CCE/Lc process. The leakage of mediator during the operation of ABTS-CCE/Lc electrode was experimentally verified by SECM and may explain the decrease of its activity with time.

13 Carbon ceramic electrode modified with syringaldazine and laccase

13.1 Introduction

3,5-dimethoxy-4-hydroxybenzaldehydazine (syringaldazine) is commonly used for laccase activity determination [334, 335] and identification [328]. When dissolved in solution it is able to shuttle electrons between oxidized laccase and electrode [327, 336]. Due to weak solubility of syringaldazine in aqueous solutions, it was chosen as potential mediator to prepare more stable electrode than ABTS-CCE/Lc.

In this section a simple procedure of the non covalent immobilization of syringaldazine and laccase is presented. As in the case of ABTS-CCE/Lc (Section 12.3) syringaldazine is immobilized into hydrophobic porous silicate – carbon heterogeneous structure of CCE. For comparison syringaldazine was also immobilized on the CCE surface by spontaneous adsorption from phosphate buffer with addition of ethanol.

In order to evaluate syringaldazine modified CCE (Syr-CCE) electrochemical properties cyclic voltammetry and differential pulse voltammetry were performed at different pH, because of expected participation of protons in the electrode reaction [327]. This property was also confirmed by Raman spectroscopy.

In the next step, laccase was immobilized in hydrophilic silicate thin film deposited on the Syr-CCE surface in the same way as on ABTS-CCE and the experiments were conducted in oxygen saturated solution at different pH. This is because of pH dependent activity of fungal laccase [158] and interest in biocathode performance at neutral pH [103]. The measurements of lateral activity toward ORR on Syr-CCE/Lc surface and detection of reaction products were done with SECM. Voltammetric experiments with syringaldazine dissolved in buffer solution were also performed.

13.2 Electrochemical behaviour of syringaldazine modified CCE

Typical optical micrograph of Syr-CCE showing the network of carbon particles and the hydrophobic silica matrix with immobilized syringaldazine is presented in Fig. 13.1. Immobilized mediator can be seen as red islands indicating uneven distribution of mediator within heterogeneous material.

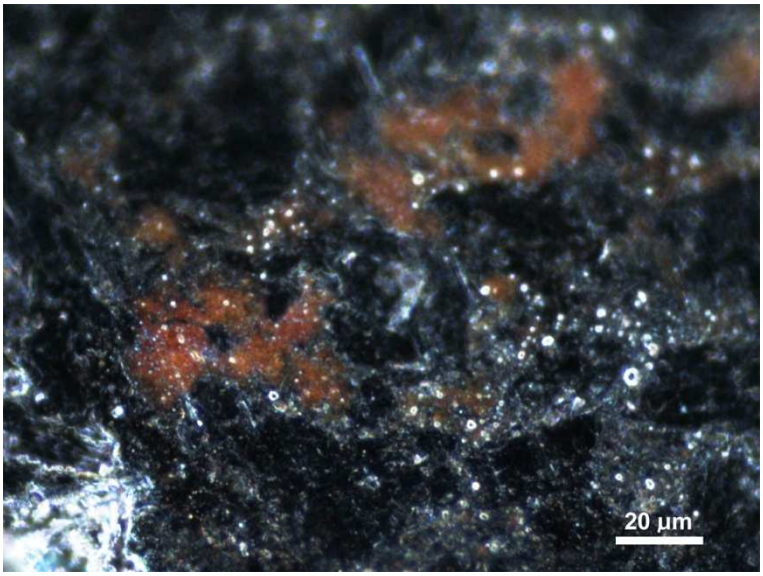

Fig. 13.1. Optical micrograph of syringaldazine modified CCE surface. Red islands correspond to syringaldazine deposit.

The voltammetric response of Syr-CCE indicates surface confined process because of linear dependence of peak current on scan rate (Fig. 13.2). The set of anodic and cathodic peaks of similar current magnitude corresponds to the reversible process and the obtained voltammogram is stable during continuous cycling. This is because both oxidized and reduced forms of syringaldazine are electroneutral and water insoluble. Therefore they both stay within hydrophobic silicate matrix.

The ratio of anodic to cathodic charge is equal unity and independent of the scan rate. The voltammograms obtained with Syr-CCE are stable during continuous scanning indicating long-lasting immobilization of substrate and product of electrode reaction within carbon–hydrophobic silica heterogeneous material. This was expected, because of the presence of methyl groups connected to silicon atoms within the pores of silicate matrix and very low solubility of mediator in the aqueous phase.

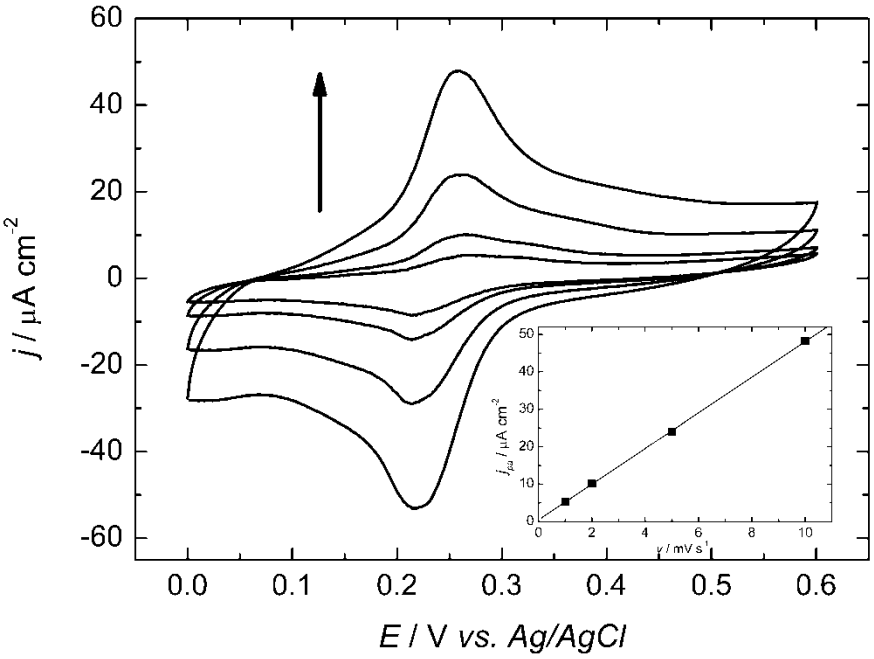

Fig. 13.2. Cyclic voltammograms of TMOS-gel coated syringaldazine modified CCE immersed in O_2-saturated 0.1 M phosphate buffer (pH 7) obtained at different scan rates: 1, 2, 5, 10 mV s^{-1}. Arrow indicates increasing scan rate. Insert shows anodic peak current dependence on scan rate.

The surface coverage calculated from the anodic charge corresponds to electrochemical activity of c.a. 34 layers of syringaldazine molecules in a flat position (surface area = 2 nm^2 [337]), covering geometric area of the electrode. This indicates that only molecules located close to three phase junction graphite particle|silicate matrix|aqueous solution participate in the electrode process. Comparing this surface coverage to ABTS-CCE (4 layers) one can conclude that Syr is more stable immobilized on CCE surface than ABTS.

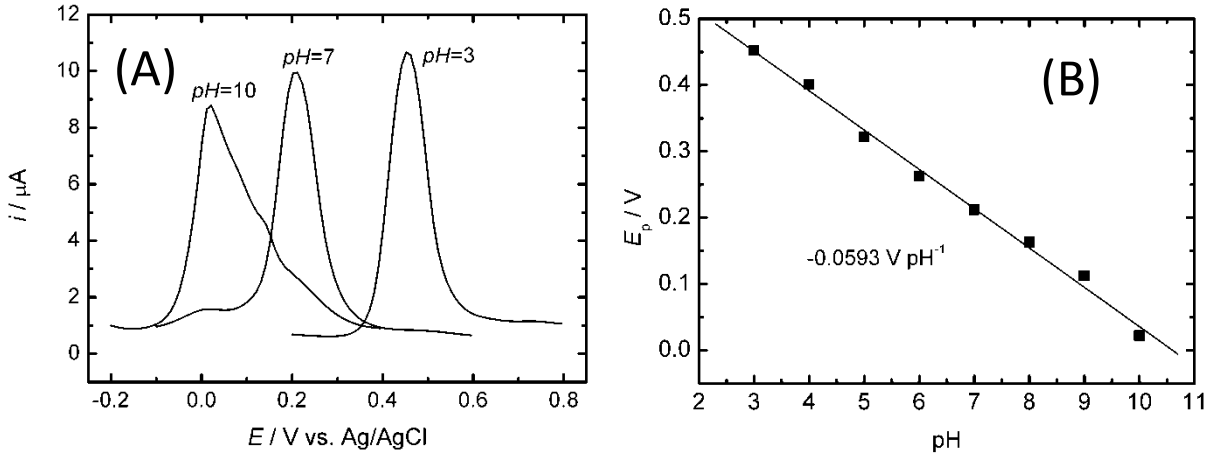

Fig. 13.3. (A) – Differential pulse voltammograms of TMOS-gel coated Syr-CCE immersed in O_2-saturated 0.1 M phosphate buffer at different pH. (B) – The plot of peak potentials (E_p) versus pH.

In order to examine the mechanism of electrooxidation of syringaldazine differential pulse voltammetry experiments in different pH were done. The peak potential (E_p) depends linearly on pH in wide (3-10) range (Fig. 13.3). The slope of this dependence is equal –59.3 mV. Therefore, this result can be described by following equation:

$$E_p = E^0 + \frac{RT}{nF}\ln\frac{[Ox]}{[Red]} - \frac{2}{n}0.059\,pH \qquad (13.1)$$

Therefore during electrooxidation of syringaldazine molecule two electrons and two protons are detached as is shown in Figure 13.4. The effect of pH is similar to that observed for syringaldazine dissolved in acetate buffer [327] indicating that immobilization of this compound within hydrophobic carbon silica material does not affect its electrochemical behaviour which is not always the case [338]. Earlier, pH sensitivity was reported for CCE doped with 9,10-phenantrenequinone [6] or modified with silicate appended naphtoquinone group [222].

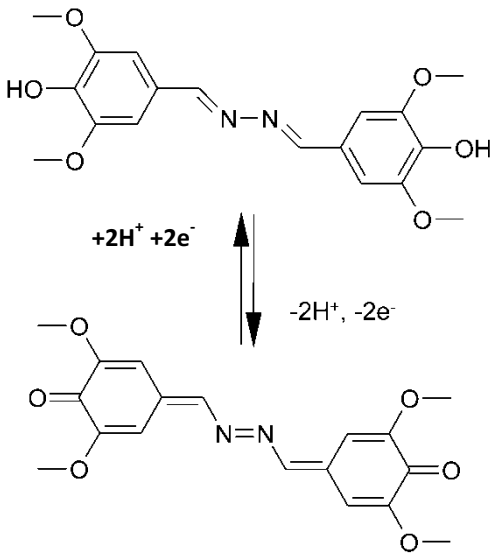

Fig. 13.4. The mechanism of syringaldazine electrode reaction.

13.3 Raman spectroscopy studies of Syr-CCE

Raman spectroscopy (Section 8.6) was chosen for Syr-CCE investigation, because it is proper technique for structural study of variety of chemical compounds. Syringaldazine upon oxidation changes colour into purple, whose structure is presented in Fig. 13.4. This coloration was indeed observed in many spots of the surface. Figure 13.5 represents a Raman spectrum of pristine syringaldazine.

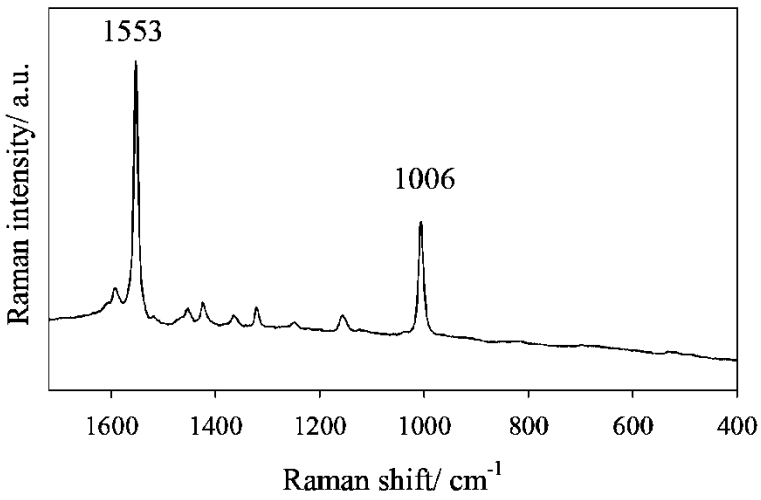

Fig. 13.5. Raman spectrum of crystalline syringaldazine

On the surface of Syr-CCE before immersing in buffer solution no aggregates of mediator has been seen. However, Raman mapping results performed for Syr-CCE electrode revealed presence of mediator clusters in certain parts of the electrode. Surprisingly, recorded spectra were not the same as those for pristine syringaldazine. The strong peaks in the spectrum of syringaldazine, with maxima at 1553cm^{-1} (C=N stretching) and 1006 cm^{-1} (N-N stretching), typical for conjugated aryl azines [339]. Figure 13.6AB shows distribution of syringaldazine in CCE electrode and typical spectrum of syringaldazine entrapped in graphite. The diameter of aggregates is kept between 10 and 20 μm and the distance between them varied from 50 to more than 500 μm. Bands attributed to ring stretching and N-N stretching vibrations are both shifted to higher wavenumbers. In particular, maximum of $\nu_{N\text{-}N}$ band is shifted from 1006 cm^{-1} for crystalline syringaldazine (Fig. 13.5) to 1056 cm^{-1} for Syr-CCE (Fig. 13.6C).

Such an effect indicates significant strengthening of the N-N bond. Presence of the weak band at 1646 cm^{-1} which can be ascribed to mixed C=O and C=C stretching vibrations suggests that this form of syringaldazine can be either partially oxidized, protonated or can interact with graphite. Most probably, a bright yellow coloration of syringaldazine clusters observed on the surface of freshly prepared Syr-CCE is due to the protonation of azine group. This is because hydrochloric acid was used as sol-gel catalyst for electrode preparation. Similar and reversible colour change was found by Bauer *et al.* [340] in water-isopropanol solution at pH 6-7.

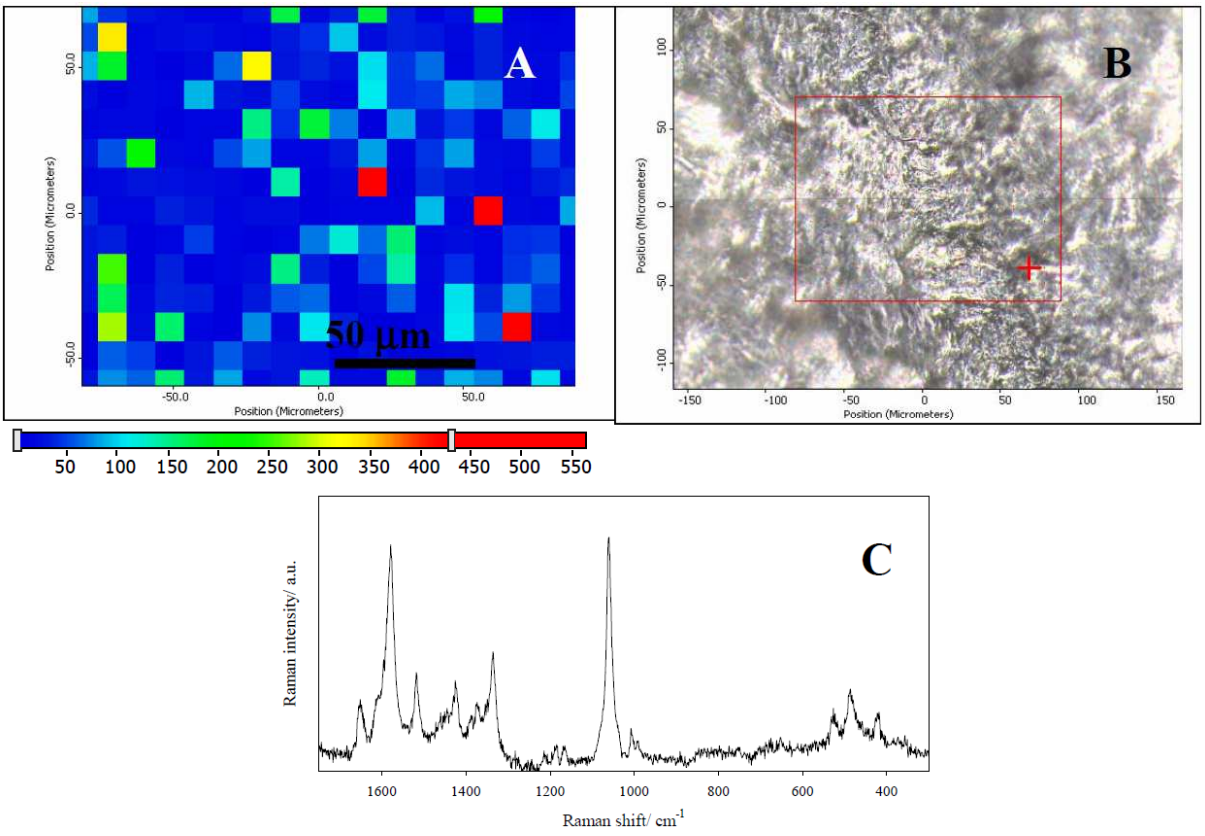

Fig. 13.6. (A) Raman map recorded at 532 nm, showing distribution of syringaldazine in Syr-CCE. Red colour indicates the highest concentration of syringaldazine, blue colour- the lowest. (B) Optical micrograph of the mapped surface. (C) Raman spectra recorded in the spot indicated by a cross.

Figure 13.7 represents set of *in situ* Raman spectra recorded at -0.2V in the same spot immediately after potential applying and after 5 and 15 minutes.

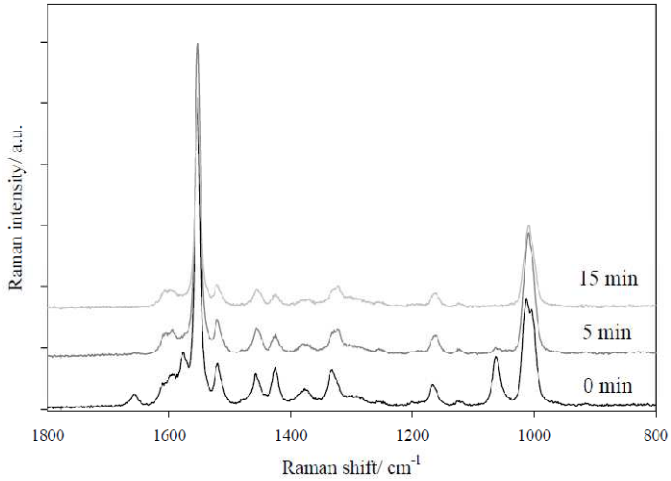

Fig. 13.7. Raman spectra of syringaldazine clusters in Syr-CCE polarized at -0.2 V.

The optical micrograph, presented in Figure 13.8, shows orange coloration in the middle of the cluster and the spectrum is a mixture of those typical for the reduced form of

syringaldazine and for the protonated orange-yellow form (Figure 13.8A). After 5 minutes of polarization at -0.2 V, the intensity of the peak at 1062 cm^{-1} (typical for the protonated form) began to decrease, and after 15 minutes only bands of the reduced form were seen. The colour of the syringaldazine cluster changed to white indicating the complete reduction of the mediator. When the potential +0.3 V was applied, after 5 minutes bands of the oxidized form at 969 cm^{-1} and 1042 cm^{-1} appeared and their intensity increases with increase in the time of the polarization. At the same time darkening on the edge of the syringaldazine cluster was observed (Fig. 13.8C). However, bands of the reduced form still prevail after 15 minutes of anodic polarization.

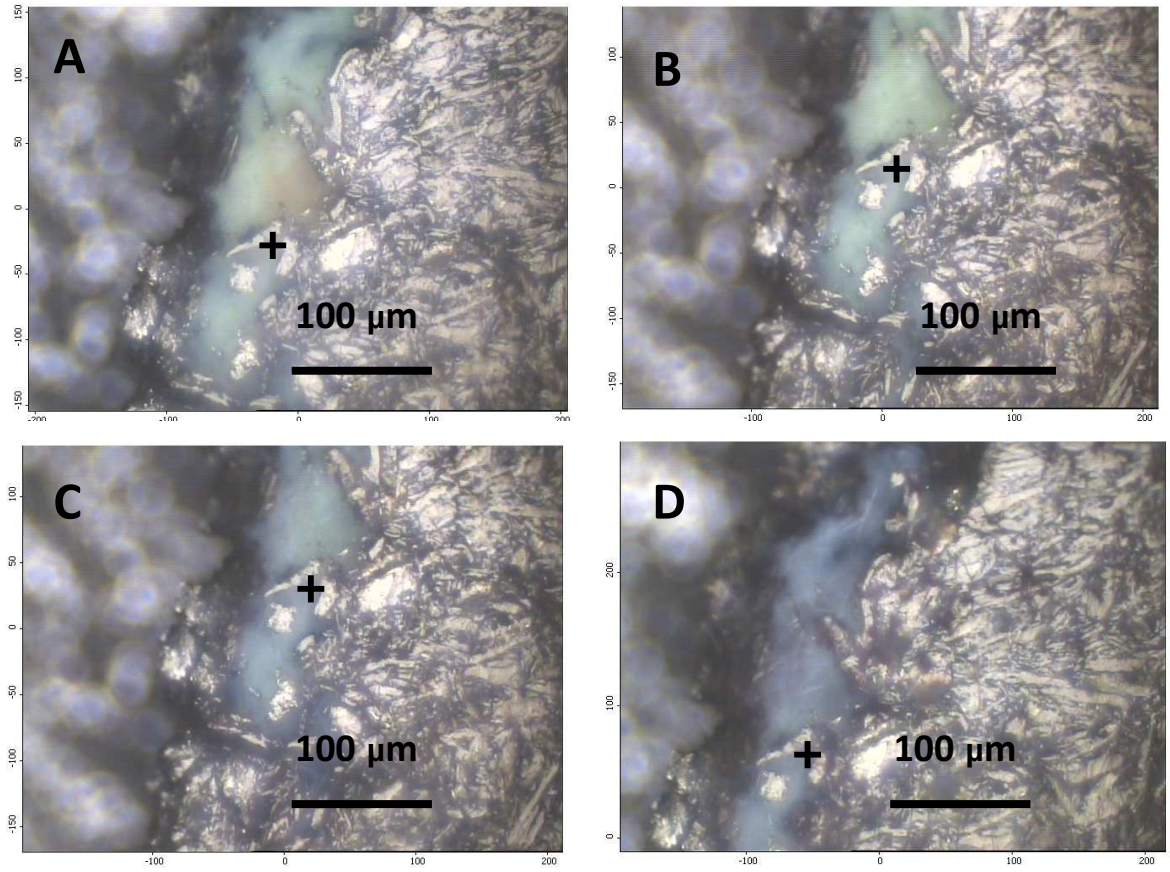

Fig. 13.8. Optical micrographs of Syr-CCE surface: (A) before experiment, (B) after 15 minutes of polarisation at -0.2V, (C) after 15 minutes of polarization at +0.3V, (D) after 30 minutes of polarization at +0.6V.

After further increase of the potential up to +0.6 V gradual oxidation of the mediator was observed, but the content of the fully oxidized form depends on the size of the clusters and polarization time. For small aggregates (up to 10 µm), after 15 minutes of polarization at +0.6V only the oxidized form was found, while the bands of both oxidized and reduced form were observed for bigger ones.

Figure 13.9 represents comparison of Raman spectra recorded for the same spot, at the potential +0.6V after different elapsed time. It is seen that for the bulky clusters the content of oxidized form of syringaldazine increases slowly with the time of polarization. After 17 hours the oxidized form dominates, but some reduces syringaldazine still remains. Results of this experiment show that the transfer of electrons between the oxidized and reduced form is rather slow and bulky clusters of mediator never undergo the complete oxidation. Therefore only small fraction of Syr encapsulated in CCE can participate in bioelectrocatalysis (see next section)

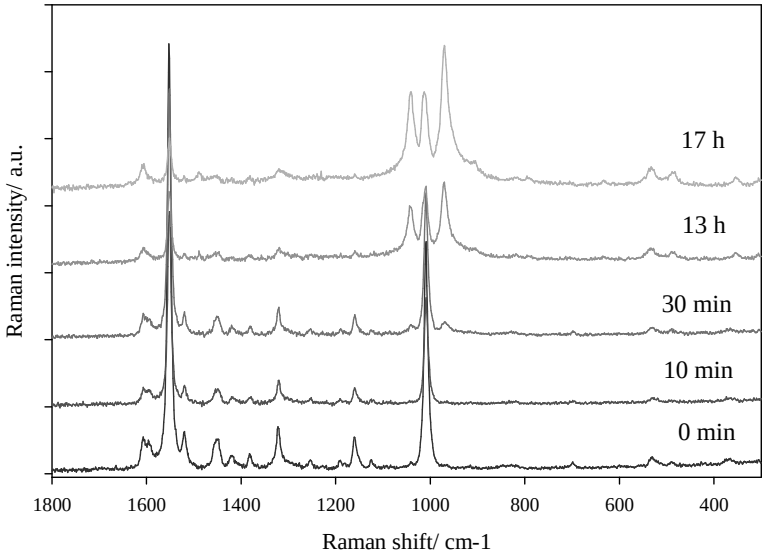

Fig. 13.9. Raman spectra of syringaldazine clusters in Syr-CCE polarized at +0.6 V.

13.4 Electrochemical behaviour of syringaldazine and laccase modified CCE

Next experiments were done with laccase encapsulated in thin silicate film on the Syr-CCE surface in oxygen saturated solution. The change of the shape of cyclic voltammograms, namely the increase of the ratio of the cathodic to anodic current (Fig. 13.10A) is a typical features of electrocatalytic reaction. No catalytic current is observed when syringaldazine is not immobilized in CCE body indicating the absence of direct electron transfer between immobilized laccase and graphite particles. Catalytic chemical reaction – syringaldazine oxidation by the enzyme and laccase regeneration by oxygen is followed by electrochemical regeneration of mediator:

$$2\ Syr_{Red}(H_2) + O_2 \xrightarrow{\text{enzyme}} 2\ H_2O + 2\ Syr_{Ox} \qquad (13.2)$$

Obviously, some fraction of the immobilized mediator molecules, and some fraction of proteins immobilized in adjacent hydrophobic and hydrophilic silicate matrices respectively remains in close contact as in the case of ABTS-CCE/Lc. Therefore this electrode architecture is favourable for efficient electron transport between the enzyme, mediator and graphite particles. However, this case shows that no dissolution of mediator is necessary for mediated electrocatalysis.

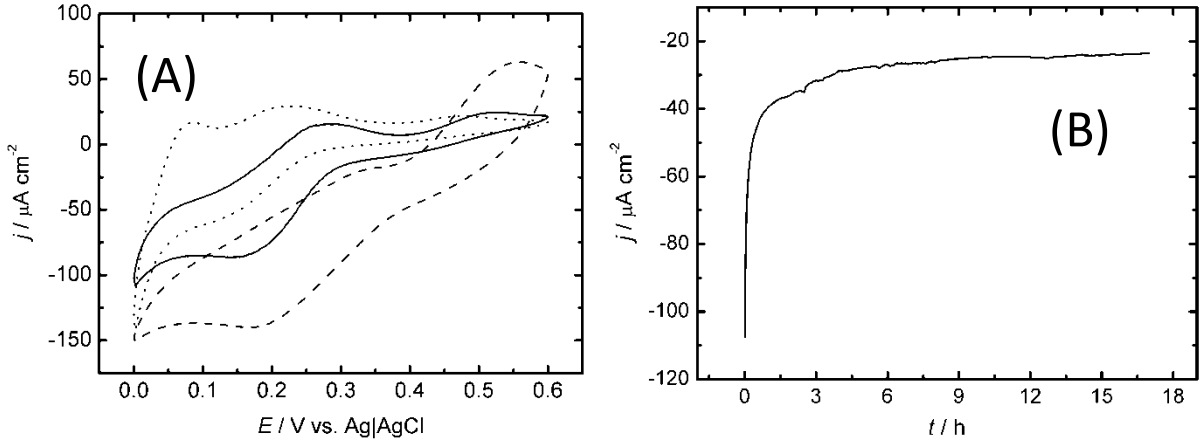

Fig. 13.10. (A) - Cyclic voltammograms of Syr-CCE/Lc immersed in O_2-saturated 0.1 M phosphate buffer at different pH: (dashed) pH 4.85, (solid) pH 6.7, (dotted) pH 7.62. (B) - Chronoamperogram of Syr-CCE/Lc immersed in O_2-saturated 0.1 M phosphate buffer pH 4.85 obtained after potential step to +0.1 V.

The catalytic current is observed immediately after immersion of the electrode indicating that the enzymatic reaction starts without any delay. The voltammogram recorded at pH 4.85 (corresponding to maximum enzyme activity [158]) is stable during continuous scanning. Namely, after 10 scans at 1 mV s^{-1} 1 % decrease of the current was observed. This is different than for ABTS–CCE/Lc (Section 12.3), because of different mechanism of the redox reaction of mediator. In contrast to ABTS modified electrode where radical formation accelerates deactivation of protein [73] neither syringaldazine nor its oxidation product do not affect laccase stability.

The current density and potential of electrocatalytic oxygen reduction decrease with increasing pH (Fig. 13.10A). However at pH > 7 catalytic effect is still visible, but the current decreases during continuous scanning. The appearance of small anodic peak on voltammograms recorded at higher pH indicates that the rate of catalytic reaction is smaller. This effect can be caused by different factors. There is clear evidence of relationship between laccase activity and the difference between the redox potentials of mediator and its T1 site [176, 341]. On the other hand the latter value is almost pH independent [176]. Therefore the

smaller efficiency of catalytic process at higher pH probably results from decreasing of laccase activity.

The performance of Syr-CCE/Lc was examined in potentiostatic experiment at +0.1 V. The potential close to this value is expected when electrode will be used as cathode in biofuel cell. The initial decrease of the catalytic current (Fig. 13.10B) together with significant hystheresis of voltammograms (Fig. 13.10A) also observed with ABTS-CCE/Lc electrode (Section 12.3) may be caused by depletion of oxygen at reaction site. However, results of investigation with mediator dissolved in electrolyte [158], where no hysteresis was observed, indicate that this is not the case. Perhaps this effect is connected with immobilization of mediator and its access to enzyme. After 10 hours the current density of catalytic oxygen reduction decreases to stable value ca. 25 µA cm^{-2} (Fig. 13.10B).

It was also observed that the shape of cyclic voltammograms obtained with Syr-CCE/Lc depends strongly on time scale of the experiment (Fig. 13.11). At scan rate faster than
2 mV s^{-1} anodic peak reappears and the ratio of cathodic to anodic charge decreases indicating slow rate of catalytic reaction. In this respect the electrocatalytic behaviour of Syr-CCE/Lc electrode is similar to ABTS-CCE/Lc (Section 12.3).

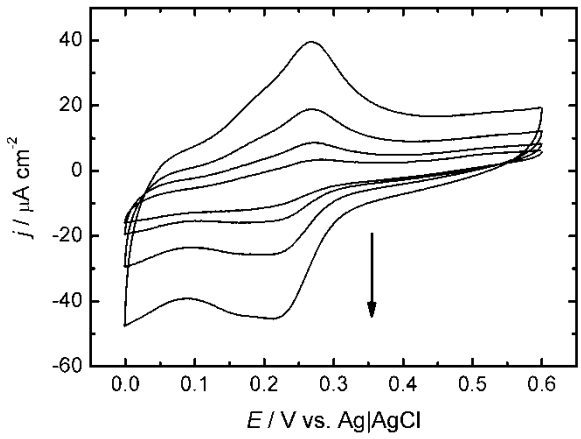

Fig. 13.11. Cyclic voltammograms of Syr-CCE/Lc immersed in O_2-saturated 0.1 M phosphate buffer pH 7 at different scan rates: 1, 2, 4 and 8 mV s^{-1}. Arrow indicates increasing scan rate.

The rate of ORR on Syr-CCE/Lc depends on temperature what means that this reaction needs activation. In order to evaluate activation energy the temperature studies were performed at pH 4.8 corresponding to maximum laccase activity. Chronoamperometry experiments at +0.1 V during 60 s were done at different temperatures in temperature range

21–60 °C. Then the catalytic charges (Q) as the measures of the rate of the enzymatic reaction were calculated by integration of these chronoamperograms. From these data the temperature dependence of Q was prepared (Fig. 13.12A). The catalytic charge increases with temperature. However, above 52 °C this effect is reduced probably due to protein denaturation.

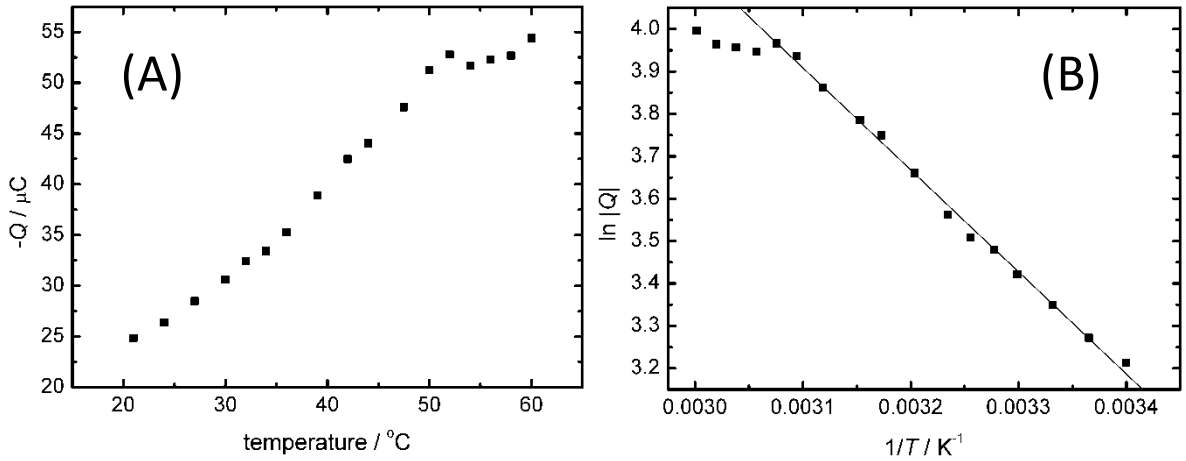

Fig. 13.12. Temperature dependence of catalytic charge of ORR on Syr-CCE/Lc (A) and its Arrhenius plot (B).

The data obtained at temperatures up to 52 °C fit to Arrhenius equation with standard deviation equal 0.997 (Fig. 13.12B):

$$\ln|Q| = A - E_a/RT \tag{13.3}$$

$$\ln|Q| = 11.3 - 2385/T \tag{13.4}$$

The slope results in activation energy (E_a) equal 19.8 kJ mol^{-1}. This value is much lower than that of the same laccase determined using ABTS as mediator, which is 52 kJ/mol^{-1} [158].

13.5 SECM measurements of Syr-CCE/Lc

Contrary to the ABTS-CCE/Lc electrode (Section 12.3), monitoring of the bioelectrocatalytic activity of Syr-CCE/Lc by SECM is possible, because Syr is almost water-insoluble and hence does not leak into solution with a detectable flux. The experiments were performed in double potential step redox competition mode (RC-SECM) (Section 7.5). Both, microelectrode and the closely spaced Syr-CCE/Lc electrode compete for dissolved oxygen. In order to avoid its depletion, a two-step potential program is applied to the microelectrode at every grid point. In the first step, oxygen is generated at the microelectrode by setting its potential E_T to 1.35 V for 3 s. Next, E_T is shifted to -0.40 V in order to cause a diffusion-controlled ORR at the microelectrode for another 3 s.

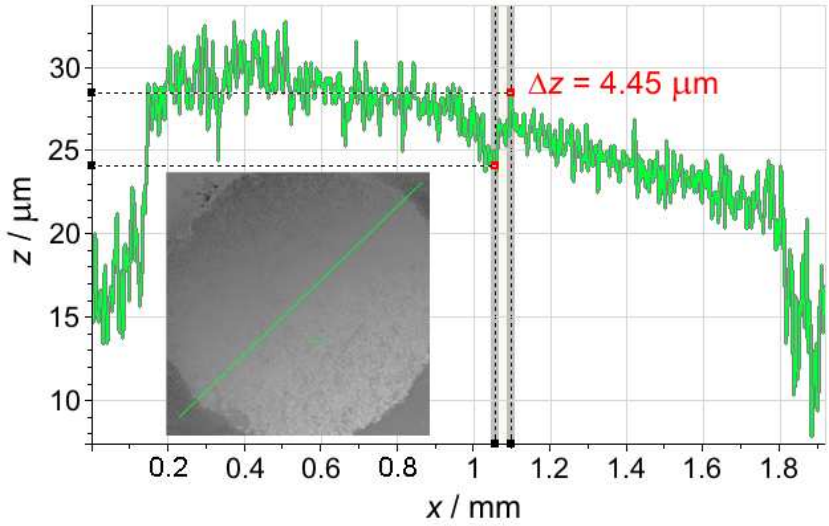

Fig. 13.13. Cross section of topography image (inset) of Syr-CCE obtained with CLSM.

Above the active enzyme layer, the ORR current of the microelectrode is expected to be smaller because of oxygen consumption by laccase at the substrate electrode. A two-dimensional image is constructed by plotting the average microelectrode current $\langle i_T \rangle(x,y)$ between t = 0.3 s and t = 1.0 s after changing the potential to E_T = -0.4 V at every point over the Syr-CCE/Lc electrode. A low absolute i_T represents locally high bioelectrocatalytic activity of the sample. This image can be influenced by topographic features as they would affect the O_2 diffusion between the electrodes. Indeed, the roughness of the polished Syr-CCE/Lc is estimated using reflection mode CLSM as ca. 4.5 µm (Fig. 13.13). In order to minimize the influence of topographic features of the sample, the result with a Syr-CCE/Lc electrode polarized at the potential corresponding to oxygen reduction (E_S = 0.1 V) is compared to a control experiment without external polarization.

The results shown in Figure 13.14B confirm that a topographic effect is present as deduced from the image of the Syr-CCE/Lc electrode but cannot explain all the variation observed at the identical electrode region when an external potential E_S = 0.1 V is applied. In the RC SECM experiments, i_T above the active areas of Syr-CCE/Lc is expected to be lower compared to i_T in the control experiment. The difference between the images of the Syr-CCE/Lc electrode at OCP and with E_S = 0.1 V is presented as a differential image (Fig. 13.15), where a larger current difference corresponds to higher local laccase activity.

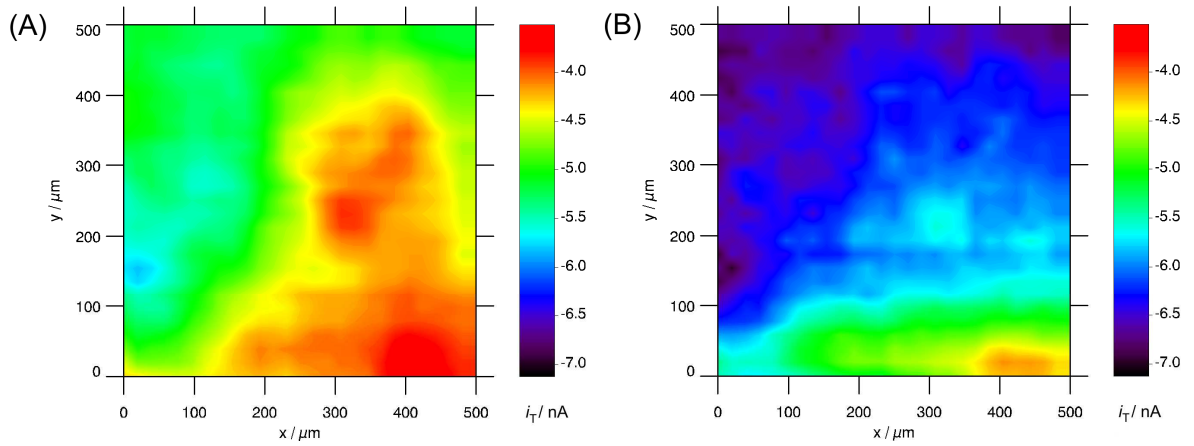

Fig. 13.14. SECM (RC mode) visualization of lateral activity distribution of Syr-CCE/lac in 0.1 M phosphate buffer (pH 4.8) saturated with air. r_T = 13.2 µm, d = 20 µm, v_T = 10 µm s^{-1}. E_T = 1.35 V (3 s) and -0.4 V (3 s); grid spacing is 20 µm. Images are constructed by plotting the average microelectrode current $\langle i_T \rangle (x,y,t)$ between t = 0.3 s and t = 1.0 s after stepping to E_T = -0.4 V. The image (A) is recorded with E_S = 0.1 V; and (B) with the sample disconnected from bipotentiostat.

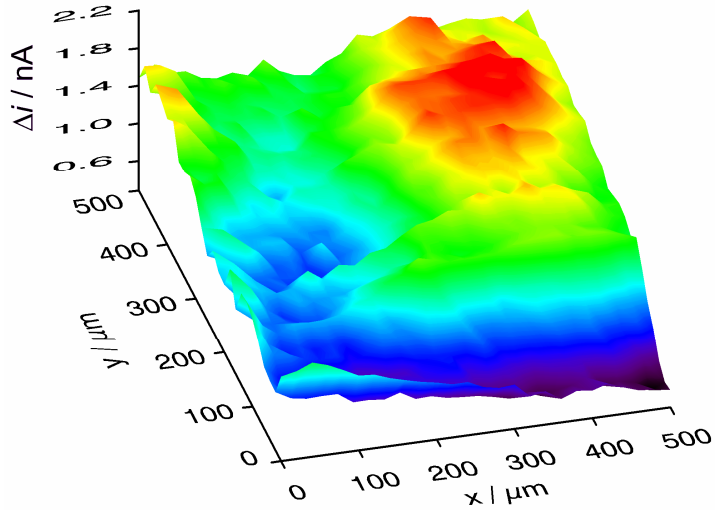

Fig. 13.15. SECM (RC mode) visualization of lateral activity distribution of Syr-CCE/Lc in 0.1 M phosphate buffer (pH 4.8) saturated with air. The image is a plot of the differences between currents obtained when sample is disconnected and with E_S = 0.1 V (see Fig. 13.14 A and B for individual images).

The measurement shows a strongly non-homogenous lateral distribution of the Syr-CCE reaction rate. This is consistent with the non-uniform mediator distribution observed by optical microscopy (Fig. 13.1) and localised Raman spectroscopy (Fig. 13.6). Another possible explanation for the observed inhomogenity in the reaction rate is the formation of aggregates of laccase in the silicate film (see Chapter 14), or a combination of both effects. Since the image measures the overall reaction rate, this can only be high where a good communication between enzyme, mediator and a percolation path in the network of carbon particles is established. Larger crystals of syringaldazine are likely to interrupt this

communication even if the local variation of the mediator in the film may be slightly enhanced.

In order to confirm 4 electron mechanism, an attempt to detect H_2O_2 as a product of the ORR at the Syr-CCE/Lc electrode was also made. For this purpose SG/TC SECM (Section 7.4) was employed. Results presented in Figure 13.16 show that although the oxygen electroreduction on Syr-CCE/Lc commences at E_S ca. 0.35 V, no H_2O_2 is generated at E_S higher than ca. 0.05 V. At lower potential O_2 is reduced at the graphite and H_2O_2 is produced and can be detected by the microelectrode. This experiment also shows the ability of SG/TC SECM to detect small quantities of H_2O_2.

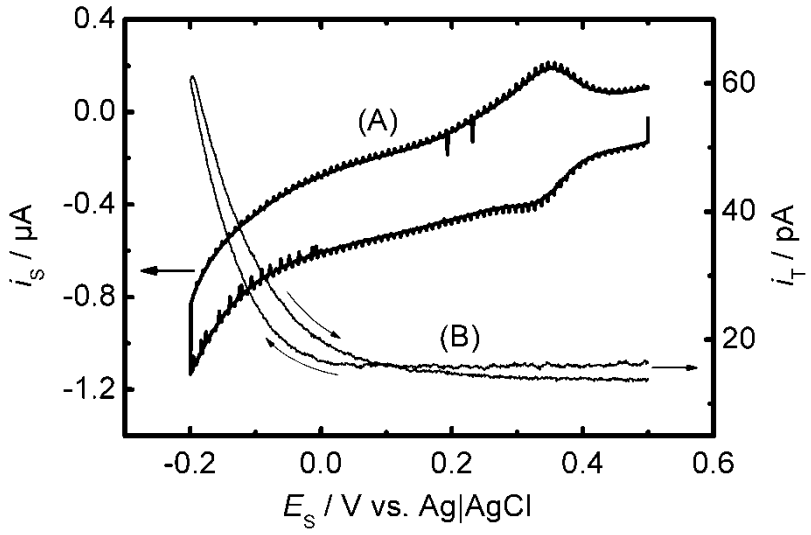

Fig. 13.16. Cyclic voltammograms: (A) – current registered at Syr-CCE/Lc (i_S) as a function of its potential (E_S), (B) – current registered at Pt-microelectrode positioned 20 µm above Syr-CCE/Lc as a function of E_S. Electrolyte: air-saturated 0.1 M phosphate buffer pH 4.8, v = 1 mV s^{-1}.

13.6 Electrochemical behaviour of CCE modified with adsorbed syringaldazine

The study of analogous system with syringaldazine dissolved in buffer solution was also done. For these experiments, because of the limited solubility of mediator in phosphate buffer, syringaldazine solution in 0.1 M phosphate buffer with 10 % ethanol addition were prepared. It turned out that mediator adsorbs on CCE and this process can be monitored by cyclic voltammetry (Fig. 13.18). After this experiment electrode was immersed in pure phosphate buffer solution and stable voltammetric response was observed. The linear relationship between peak current and scan rate indicates that voltammograms are connected with electrode process of adsorbed syringaldazine.

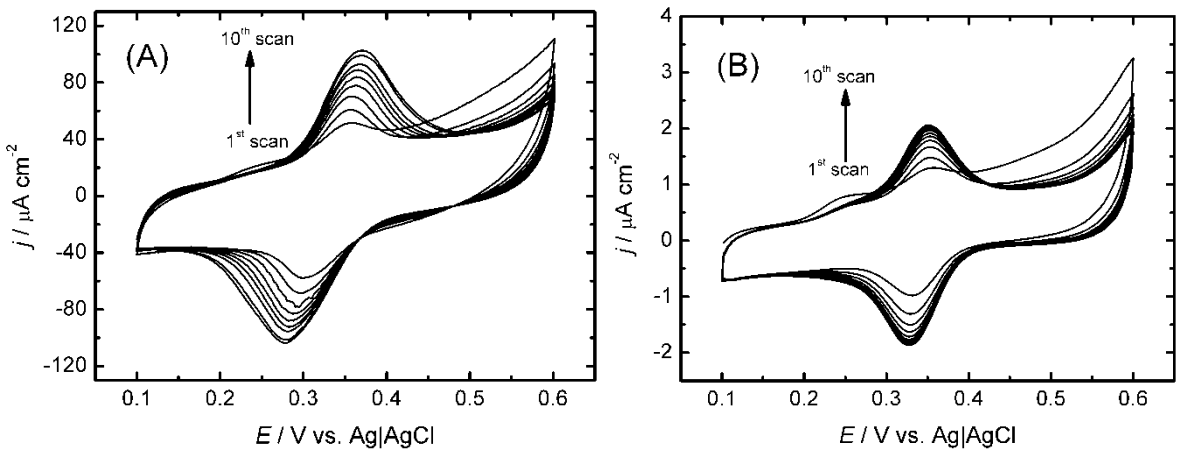

Fig. 13.17. Subsequent cyclic voltammograms of CCE (A) and GC (B) immersed in 0.1 mM syringaldazine solution in 0.1 M phosphate buffer (pH 7) mixed with ethanol (9:1). Scan rate: 10 mV s^{-1}. Arrow indicates the order of voltammograms.

The magnitude of voltammetric signal obtained after saturation is almost two times larger than that obtained on Syr-CCE (Fig. 13.2). The adsorption process is irreversible because the magnitude of the signal is not affected after transfer of the electrode to solution where syringaldazine is absent. However the difference between peak potentials is higher (100 mV (Fig. 13.17A) in comparison to 40 mV (Fig. 13.17B)) indicating slower electron transfer and electron transport across adsorbed layer. The value of peak current density is approximately 50 times larger than obtained with GC electrode with adsorbed syringaldazine (Fig. 13.17B) indicating significant effect of heterogeneous structure of the electrode.

When CCE electrode modified with adsorbed syringaldazine was covered with laccase encapsulated in silicate film the catalysis of oxygen electroreduction is observed (Fig. 13.18). Contrary to Syr-CCE the clear signature of electrocatalytic process – the difference between cathodic and anodic charges can be seen only at very slow scan rate (0.2 mV s^{-1}). This indicates much slower catalytic reactions probably caused by less favourable mutual position of adsorbed mediator and the enzyme. This obviously results in lower magnitude of catalytic current with adsorbed mediator. Interestingly, such low catalytic activity is observed at electrode with higher (about 90 mV) redox potential of mediator. It seems that the position adsorbed syringaldazine is less favourable for efficient electron exchange with laccase encapsulated in silicate matrix.

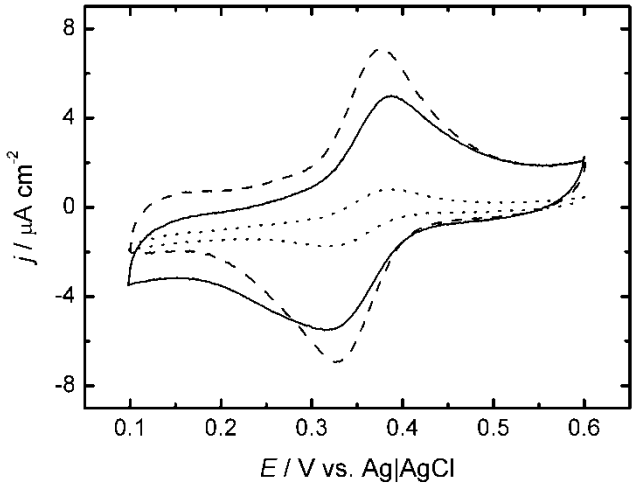

Fig. 13.18. Cyclic voltammograms of laccase containing TMOS-gel coated CCE modified with adsorbed syringaldazine immersed in O_2-saturated 0.1 M phosphate buffer pH 7 at scan rates: 0.2 (dotted line) and 1 mV s^{-1} (solid line). The voltammogram obtained in the absence of silicate film encapsulated laccase with scan rate: 1 mV s^{-1} is marked by dashed line.

13.7 Zn-O_2 membraneless hybrid cell

Due to low potential of ORR on Syr-CCE/Lc this electrode is not suitable for application as biocathode in glucose-O_2 biofuel cell. However, because of much lower potential of zinc anode than glucose bioanode (see Chapter 5) Syr-CCE/Lc can be applied as biocathode in hybrid cell (Section 5.5), similarly to ABTS-CCE/Lc (Section 12.3).

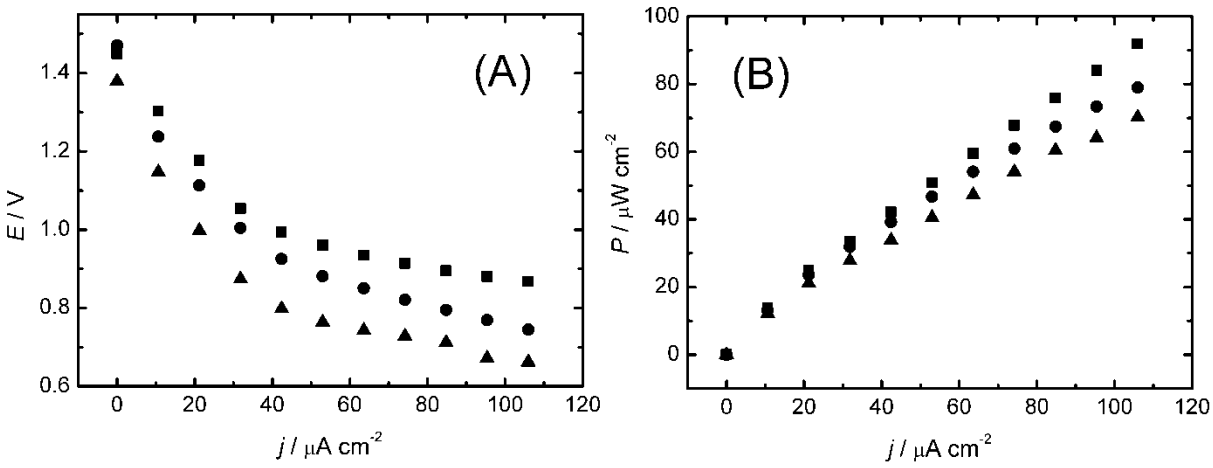

Fig. 13.19. Current density-voltage (A) and current density-power density (B) characteristics of a cell consisting of Nafion coated Zn wire and Syr-CCE/Lc immersed in 0.1 M phosphate buffer pH 5 (■), pH 7.4 (●), or artificial serum (▲).

Current-voltage and power-voltage characteristics of Zn-O_2 battery consisting of Nafion-coated zinc wire and Syr-CCE/Lc are presented in Fig. 13.19. Following pH-dependence of laccase activity the voltage of the cell decreases with increasing pH of the electrolyte up to 7.4. Inhibition of laccase by chloride anions causes further decrease of the cell voltage. This means that decrease of biocathode catalytic properties is superior to improvement of efficiency of zinc anode in presence of chloride [200].

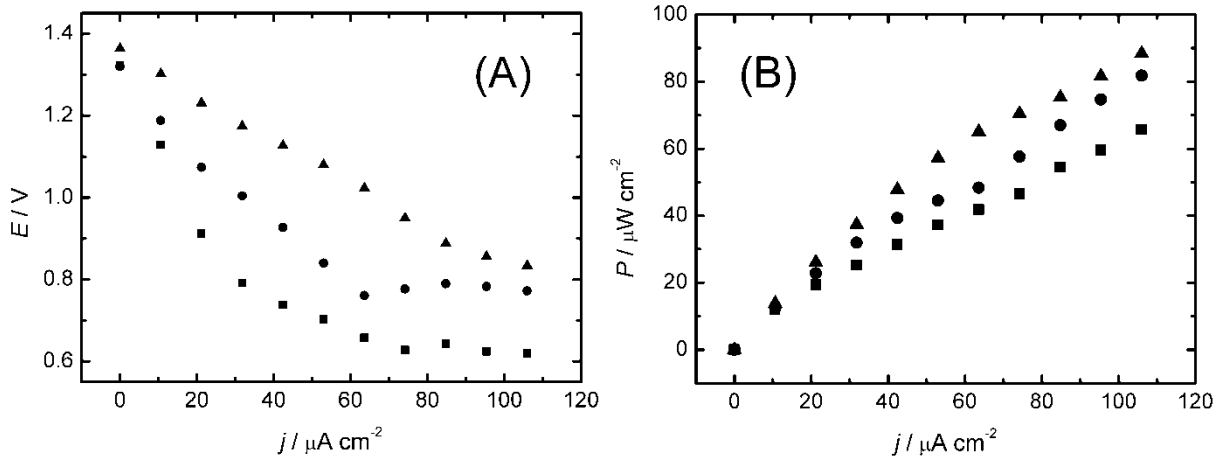

Fig. 13.20. Current density-voltage (A) and current density-power density (B) characteristics of a cell consisting of Nafion coated Zn wire and Syr-CCE/Lc immersed in O_2-saturated artificial serum at different temperatures: 24 °C (■), 37 °C (●) and 50 °C (▲).

Similar to Zn-O_2 cell with ABTS-CCE/Lc as biocathode both voltage and generated power density increases with temperature (Fig. 13.20). Here this dependence is stronger what is consistent with lower activation energy of ORR on Syr-CCE/Lc than for biocatalysis mediated with ABTS (Section 13.4). One can notice unusual increase of cell voltage with application of higher current density (> 60 μA cm^{-2}) at 37 °C. This can be relevant with decrease of anode potential caused by its activation.

13.8 Conclusions

Voltammetric response of CCE doped with syringaldazine depends on pH what is connected with mechanism of the electrode reaction, what is also confirmed by Raman spectra of electrochemically oxidized syringaldazine. Replacement of ABTS immobilized in hydrophobic heterogeneous material (Chapter 12) by syringaldazine as mediator for bioelectrocatalysis of oxygen reduction results in much stable behaviour. From the point of view of efficiency of catalytic process the addition of mediator to the sol used for electrode preparation is superior in comparison to its adsorption from solution.

SECM imaging of Syr-CCE/Lc electrodes indicate a non-uniform distribution of its enzymatic activity which is probably connected to enzyme aggregation in the sol-gel silicate matrix and/or non-homogeneous distribution of the mediator in electrode material. Other experiments with this electrode confirm that no H_2O_2 is produced during enzymatic oxygen electroreduction at low overpotentials.

Unfortunately, low redox potential of syringaldazine and its pH dependence is disadvantageous for biofuel cell application. Nevertheless, Syr-CCE/Lc can be applied in hybrid system with Zn anode [103]. The use of this electrode for pH-sensing can be also envisaged.

14 SECM study of silicate film with immobilized laccase or bilirubin oxidase

14.1 Introduction

Among other factors (e.g. specific laccase activity) the distribution of laccase immobilized in a silicate thin film on ABTS-CCE or Syr-CCE surface affects the efficiency of the resulting electrodes. This is a reason for interest in imaging enzyme activity immobilized in such a way. The four electron reduction - favourable for (bio)fuel cells is not straight forward to detect by SECM, since the reaction product H_2O is the solvent. Nevertheless, a number of SECM schemes can be used to monitor the lateral distribution of oxygen-reducing enzymes (Section 7.8).

In this section investigations of laccase distribution within sol-gel processed silicate films by SECM is presented. A glass plate and polystyrene surface were used as support because of its flat surface, strong affinity to silicate films and insulating character. The SECM measurements were performed in the SG/TC mode and the RC mode detecting amperometrically either $ABTS^{\bullet-}$ or $ABTS^{2-}$ at the microelectrode scanned over the laccase film. A new variation of the feedback mode in which oxygen is used as the native electron acceptor and the feedback loop is established via the electron donor for the enzymatic reaction was also performed. While an electron transfer to the substrate in FB mode is not required and would even interfere with the imaging of the enzyme activity, it eliminates the problem of rising background current. Special attention is paid to increased activity at the edge of the film and effective heterogeneous rate constants were determined at different areas of the sample. Moreover, FB mode was also applied for the comparison of laccase and BOx activity.

14.2 SG/TC and RC mode SECM measurements with $ABTS^{2-}$

The CLSM investigation of thin films of laccase immobilized in sol-gel matrices (Fig. 14.1A) reveals features that are considered to be aggregates of laccase. In order to confirm this assignment, combined SECM/CSLM experiments were performed that correlated the optically detectable features in the laccase/silicate film with electrochemical signals (Fig. 14.1). Several spots are visible in the CLSM image recorded in the reflection mode (Fig. 14.1A). The inverted setup of the CLSM allowed to observe the sample during SECM imaging. This feature was used to position the microelectrode of the SECM close to the features of interest by means of optical observation.

The microelectrode is visible at the starting point of the experiment as a white spot at the bottom right corner of Fig. 14.1A. The microelectrode to sample distance d was adjusted to $d = 4r_T = 20$ µm. The image frame corresponds to the bright region in the optical image in Fig. 14.1A.

The SECM experiments were carried out in the SG/TC mode (Fig. 14.1B). A solution of $ABTS^{2-}$ in phosphate buffer was used. $ABTS^{2-}$ serves as the electron donator in the enzymatically driven reduction of oxygen (Eq. (12.2)). The reaction product, $ABTS^{\bullet-}$, diffuses into the solution and forms a diffusion layer. At the microelectrode a potential sufficiently low to reduce $ABTS^{\bullet-}$ (Eq. 12.1) is applied.

$ABTS^{2-}$ was selected as electron donor, because of its good solubility in water, its ability to diffuse through the silicate film [158] and efficient exchange electrons with the prosthetic group of laccase. The insulating nature of the glass support eliminates positive feedback contribution in SG/TC experiment.

When the microelectrode scans across the surface, an increased cathodic current i_T is observed at the microelectrode (Fig. 14.1C) when it is scanned across the features visible in the CLSM image Fig. 14.1A. A rising background is observed in because the macroscopic silicate film contains laccase also in areas outside the scanned surface. After assembling all parts, oxygen from air was allowed to diffuse through previously deaerated electrolyte into the sample. Then the macroscopic laccase-silicate film provides an increasing flux of $ABTS^{\bullet-}$ leading to a steadily increasing bulk concentration. In order to highlight the signals from the additional flux above the laccase aggregates on the rising background, the colour scale (but not the vertical position of the datapoints) was corrected by subtracting a background (Fig. 14.1C and Fig. 14.1E).

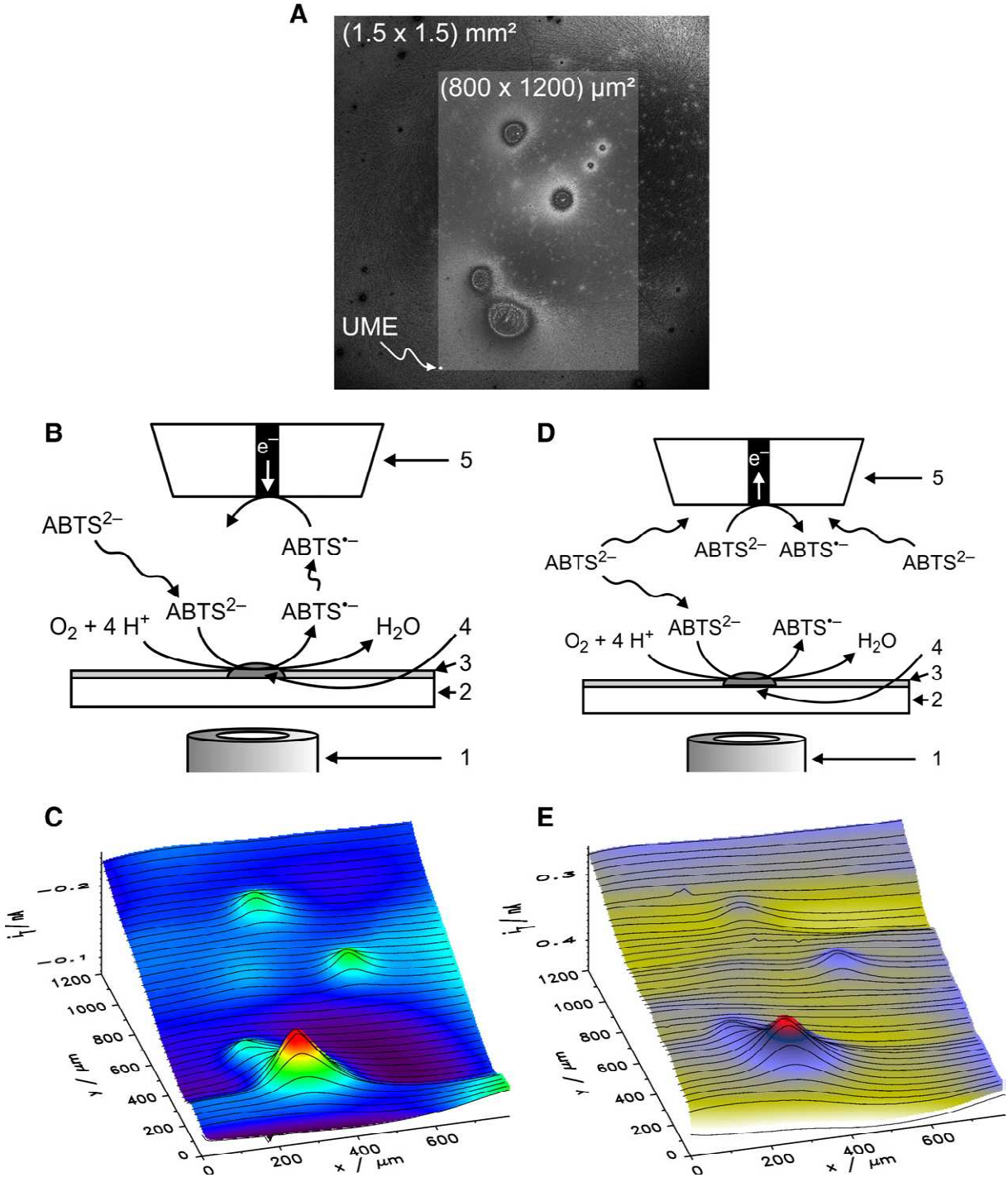

Fig. 14.1. Combined SECM/CLSM mapping of laccase aggregates. A) Reflection mode CLSM image; B) a scheme of SG/TC mode SECM imaging; 1) microscope objective; 2) glass slide; 3) laccase-silicate film; 4) laccase aggregate; 5) microelectrode; C) SG/TC mode SECM image; E_T = -0.1 V, r_T = 5 µm, 1 mM $ABTS^{2-}$ in 0.1 M phosphate buffer (pH 4.8), v_T = 7.7 µm s^{-1}; D) a scheme of RC mode SECM imaging; E) RC mode SECM image, E_T = +0.4 V. Current scales in C and E are inverted to show high activity as "hills".

A control experiment was performed in order to exclude that topographic features lead to variations of i_T (Fig. 14.1C) and may be mistakenly interpreted as enzymatic activity. In the SG/TC mode experiment an increased reduction current is also expected if small amounts of

$ABTS^{\bullet-}$ are present in the bulk solution and d is increase for instance when scanning over a depression in the silicate film. In this case an enhanced diffusion of $ABTS^{\bullet-}$ to the microelectrode would take place because the shielding of sample and insulating sheath of the microelectrode is reduced at larger d. For the control experiment, potential sufficiently high to diffusion-controlled oxidation of $ABTS^{2-}$ was applied to the microelectrode in the same working solution. Due to the consumption $ABTS^{2-}$ by the enzymatic reaction at the sample, a decrease of i_T is expected if the microelectrode is scanned over an area with increased laccase activity (Fig. 14.1D). For a qualitative detection of enzyme activity the sensitivity was sufficient here to detect an additional contribution of the laccase aggregates (Fig. 14.1E). Possible topographic features of the silicate film would lead to the same signal variations as in the SG/TC mode: an increase of d leads to an increase of the oxidation current at the microelectrode. The opposite trend is observed in Fig. 14.1E: the reduced oxidation current above the enzyme aggregate indicates the consumption of $ABTS^{2-}$ by the enzymatic reaction. This observation is supported by AFM micrographs (Fig. 14.3). In those topographic data, only small features are observed that can not be responsible for the signals in the SG/TC mode or RC mode experiments at the given $d = 4r_T$ where topographic effects do not play an important role.

For quantification of the additional flux from the laccase aggregate, a cross section above the centre of the spot has been extracted from a SECM image (Fig. 14.2). The parameters in Eqs. (14.1 and 7.16) has been fitted to resulting profile.

$$i_T = 4nFD(ABTS^{\bullet-})\, r_T\, [ABTS^{\bullet-}]_S\, \zeta \qquad (14.1)$$

where $n = 1$ is the number of transferred electrons per $ABTS^{\bullet-}$ molecule, $D(ABTS^{\bullet-}) = 3.2 \times 10^{-6}$ cm^2 s^{-1} [81] is the diffusion coefficient of $ABTS^{\bullet-}$, $r_T = 5$ µm is the microelectrode radius, r_S is the radius of the enzyme aggregate, $[ABTS^{\bullet-}]_S$ is the additional concentration of $ABTS^{\bullet-}$ at the enzyme aggregate surface. Non-linear fitting yielded the following adjustable parameters: $4Dr_Tc_S = 1.583 \times 10^{-15}$ mol s^{-1}, $x_0 = 126.92$ µm, $d = 23.31$ µm, $r_S = 14.54$ µm, $i_{offset} = 0.0484$ nA (Fig. 14.2, curve 1).

The fitted value of $d = 23.3$ µm agrees well with the working distance retracted from the surface. The fitted $r_S = 14.5$ µm is consistent with the optical microscopic observation that yielded $r_S = 13.5$ µm. The small offset current is a consequence of the slowly increasing bulk concentration of $ABTS^{\bullet-}$. Fitting of the profile by fixing the parameters d an r_S to the independently determined values leads to results deviating less than 10 % from the results of

the other fitting strategy ($4Dr_Tc_S$ = 1.4631 × 10^{-15} mol s^{-1}, x_0 = 126.80 µm, i_{offset} = 0.0508 nA; Fig. 14.2, curve 2). Therefore, derived values will be reported only for the fit with adjustable r_S and d because the derived values are also within a 10 % uncertainty interval.

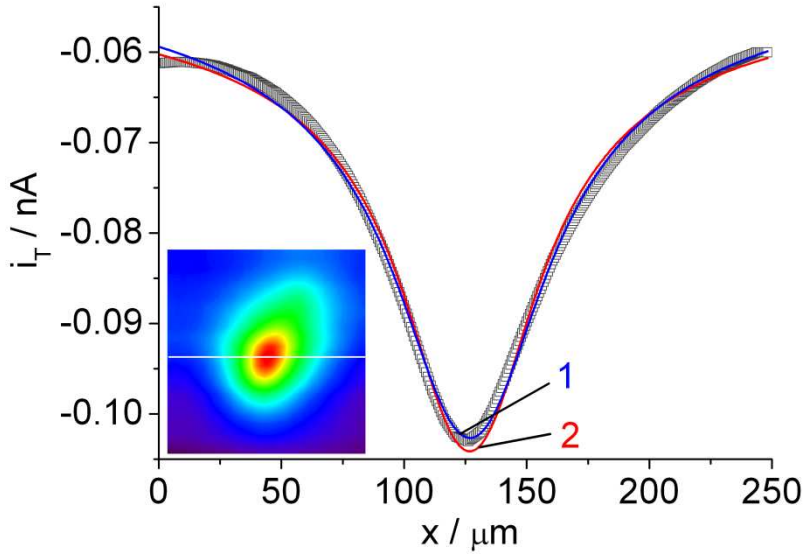

Fig. 14.2. Extracted line profile along the white line in the inset and fits of parameters in Eqs. (14.1 and 7.16) from which the flux of $ABTS^{\bullet-}$; curve 1) - fitted curve using $4Dr_Tc_S$ = 1.583 × 10^{-15} mol s^{-1}, x_0 = 126.92 µm, d = 23.31 µm, r_S = 14.54 µm, i_{offset} = 0.0484 nA, curve 2) fitted result using $4Dr_Tc_S$ = 1.4631 × 10^{-15} mol s^{-1}, x_0 = 126.80 µm, d = 20 µm, r_S = 13.5 µm, i_{offset} = 0.0508 nA (d and r_S fixed). Experimental parameters: scan area 250 µm × 250 µm, E_T = -0.1 V, r_T = 5 µm, 1 mM $ABTS^{2-}$ + 0.1 M phosphate buffer (pH 4.8), v_T = 4.2 µm s^{-1}.

The additional surface concentration $[ABTS^{\bullet-}]_S$ can be estimated to be 9.8 × 10^{-4} M. From this value, the flux of $ABTS^{\bullet-}$ Ω from the enzyme aggregate can be calculated [297]:

$$\Omega = 4D(ABTS^{\bullet-})\, r_S\, [ABTS^{\bullet-}]_S = 1.7 \times 10^{-14} \text{ mol s}^{-1} \quad (14.2)$$

Assuming a uniform flux over the enzyme aggregate a generation rate J can be determined according to following equation:

$$J = \Omega/(\pi r_S^2) = 3.0 \times 10^{-9} \text{ mol s}^{-1} \text{ cm}^{-2} \quad (14.3)$$

To further investigate the laccase aggregates, AFM micrographs of some aggregates were recorded (Fig. 14.3). The radius of the particular spot shown in Fig. 14.3A is approximately 7 µm and the height is 1.8 µm. As discussed above, these height variations are not sufficient to cause the current variations in SG/TC mode investigations at $d \approx 20$ µm. The aggregate is surrounded by a dendrite-like structure that is approximately 100 nm high.

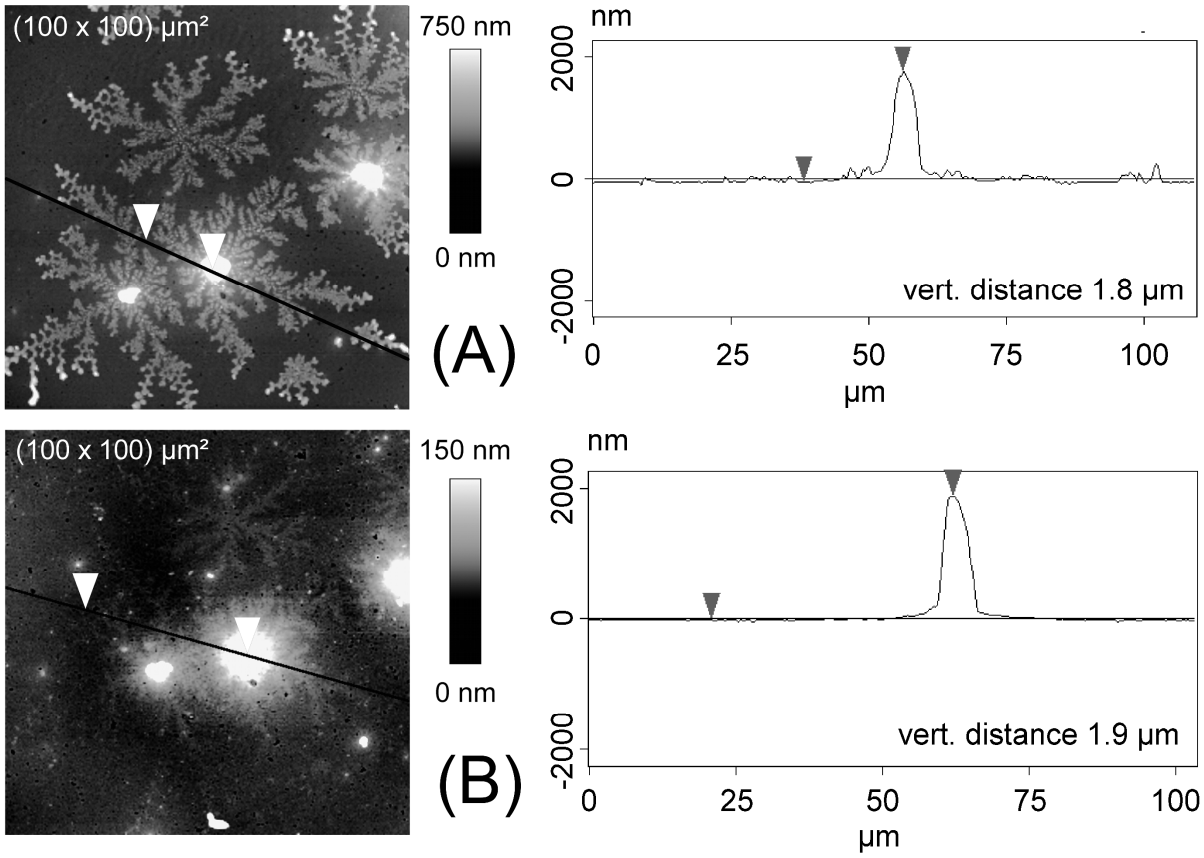

Fig. 14.3. AFM micrographs of laccase aggregates. (A) Topography representation of the aggregate of a freshly prepared sample and cross section along the black line. (B) Topography representation of the same aggregate after 22 h exposure to 1 mM $ABTS^{2-}$ in 0.1 M phosphate buffer (pH 4.8) and cross section along black line. Note the different greyscales of height in (A) and (B).

After exposure of the sample to 1 mM $ABTS^{2-}$ in 0.1 M phosphate buffer (pH 4.8) for 22 h and drying it, the same area was imaged again (Fig. 14.3B). The lateral dimension of the central aggregate has not been changed significantly compared to Fig. 14.3A. The height of the surrounding dendrite-like structure has significantly been reduced to a few nanometres indicating that some material has been dissolved during the exposure to the aqueous buffer.

Moreover, the probe of the film thickness evaluation was done using AFM (Fig. 14.4). A sample with TMOS-gel based film with immobilized laccase embedded on glass surface was scratched using steel tweezers in such a way that a part of a film was removed without glass support injury. AFM images in Fig. 14.4 represent glass support surface (left part of images) and unscratched silicate film with laccase (right part of images). Step heights are calculated as differences between mean height of selected areas as indicated in AFM images.

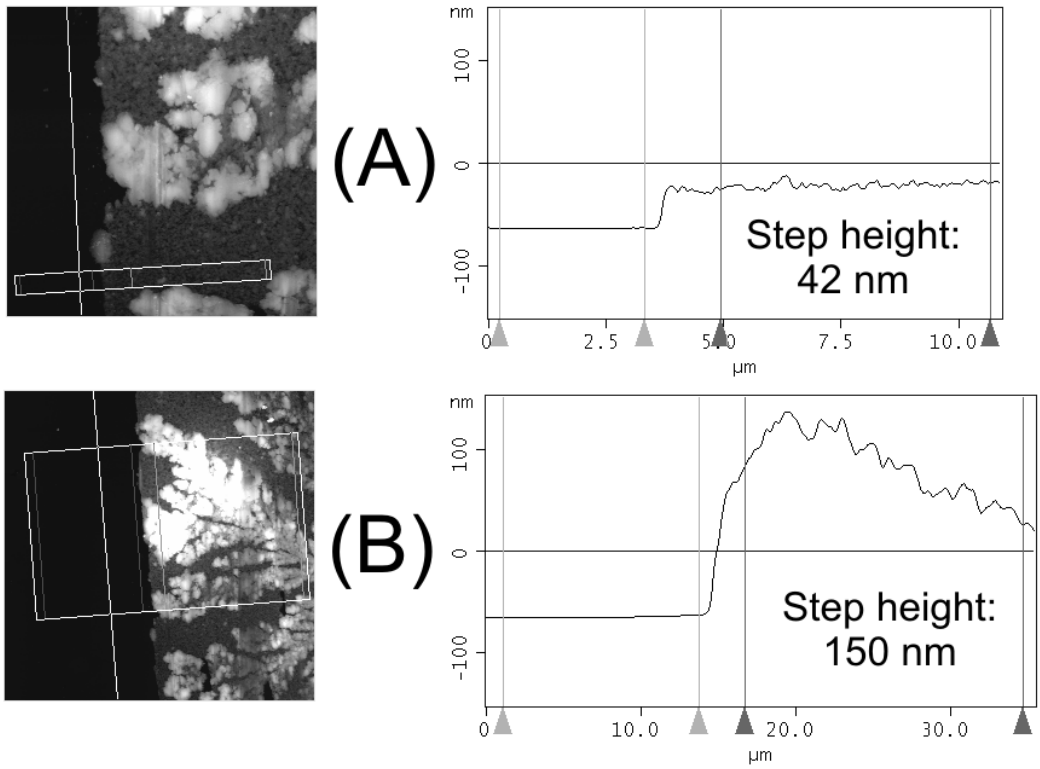

Fig. 14.4. AFM images and cross sections of TMOS-gel based film with laccase embedded on glass surface. A part of film was removed my mechanical scratching. (A) – Evaluation of film thickness between laccase aggregates. (B) – Evaluation of film with laccase aggregate thickness.

14.3 FB mode SECM measurements of TMOS-gel film with laccase

14.3.1 Selection of mediator

In order to employ the SECM feedback mode to study enzymatic oxygen reduction, the oxidised form of an appropriate mediator is needed. The redox potential of this mediator should be lower than the one of the T1 centre of enzyme. However, the redox potential of the mediator should be high enough to appear inside the potential window of the SECM microelectrode in a non-deaerated electrolyte. Namely, oxygen electroreduction on SECM microelectrode should not occur at higher potentials than the diffusion-controlled mediator electroreduction. Moreover, the mediator molecule should be small enough to reach the prosthetic group within the enzyme in order to act as electron shuttle. Furthermore, it should be water soluble at least in millimolar concentration.

Four different compounds were examined: $K_3[Fe(CN)_6]$, $[Ru(NH_3)_6]Cl_3$, $[Ru(NH_3)_6](NO_3)_3$ and *p*-benzoquinone. These mediators were dissolved in electrolyte (aerated 0.1 M phosphate buffer pH 4.8) in 0.2 mM concentration. Figure 14.5 represents CVs obtained at macroscopic gold electrodes (0.5 cm^2) covered with laccase-containing silicate

film. Sigmoidal-shaped signals are due to mediated catalytic oxygen reduction. CVs obtained with $[Ru(NH_3)_6]Cl_3$ and $[Ru(NH_3)_6](NO_3)_3$ are very similar, indicating that activity of laccase immobilized in silicate film is not very sensitive to 0.6 mM chloride.

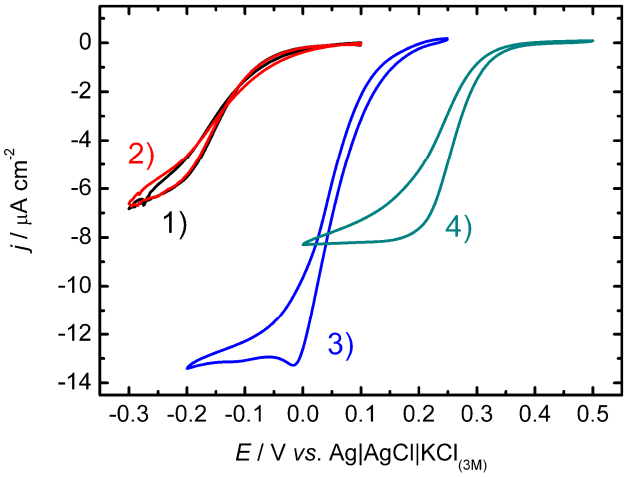

Fig. 14.5. Cyclic voltammograms obtained at a Au planar electrode with laccase immobilized in hydrophilic silicate film. Electrolytes: 1) 0.2 mM $[Ru(NH3)_6]Cl_3$, 2) $[Ru(NH_3)_6](NO_3)_3$, 3) p-benzoquinone, 4) and $K_3[Fe(CN)_6]$ in 0.1 M phosphate buffer pH 4.8. Electrode area: ca. 0.5 cm^2, Scan rate: 2 mV s^{-1}.

The catalytic oxygen electroreduction current obtained with *p*-benzoquinone as mediator is about two times higher than that in $[Ru(NH_3)_6]^{3+}$ and $[Fe(CN)_6]^{3-}$ solution of the same concentration. This is probably because *p*-benzoquinone/hydroquinone redox process is a two-electron process while the reductions of $[Ru(NH_3)_6]^{3+}$ and $[Fe(CN)_6]^{3-}$ are one-electron processes. The size, shape and charge of mediator molecule may also play a minor role in the efficiency of the catalytic process. At the potential of the $[Fe(CN)_6]^{3-}/[Fe(CN)_6]^{4-}$ couple no appreciable O_2 reduction occurs at Au electrodes. Therefore, $[Fe(CN)_6]^{3-}$ was chosen as mediator for feedback mode SECM measurements. A diffusion controlled steady-state current of $[Fe(CN)_6]^{3-}$ electroreduction was achieved at an Au microelectrode in oxygen-containing acidic electrolyte. The use of conventional Pt microelectrodes is not possible because oxygen electroreduction occurs at higher potentials at Pt than the diffusion-controlled $[Fe(CN)_6]^{3-}$ electroreduction.

In order to visualise and evaluate local kinetics of the immobilized enzyme, SECM imaging and approach curves in the feedback mode were used. In these experiments, the electron donor was $[Fe(CN)_6]^{4-}$ generated at the microelectrode by reaction (14.4) from $[Fe(CN)_6]^{3-}$ present in 0.1 mM or 0.2 mM concentrations in the working solution.

microelectrode: $[Fe(CN)_6]^{3-} + e^- \rightarrow [Fe(CN)_6]^{4-}$ (14.4)

$[Fe(CN)_6]^{4-}$ acts as an one-electron donor for the enzyme-catalysed oxygen reduction:

$$\text{sample surface: } O_2 + 4H^+ + 4[Fe(CN)_6]^{4-} \xrightarrow{\text{enzyme}} 2H_2O + 4[Fe(CN)_6]^{3-} \quad (14.5)$$

The flux of $[Fe(CN)_6]^{4-}$ consumed (and thus the flux of $[Fe(CN)_6]^{3-}$ regenerated) by the enzyme at the sample surface is detected as an additional source of $[Fe(CN)_6]^{3-}$. This leads to an enhanced cathodic current at the microelectrode (Figure 14.6).

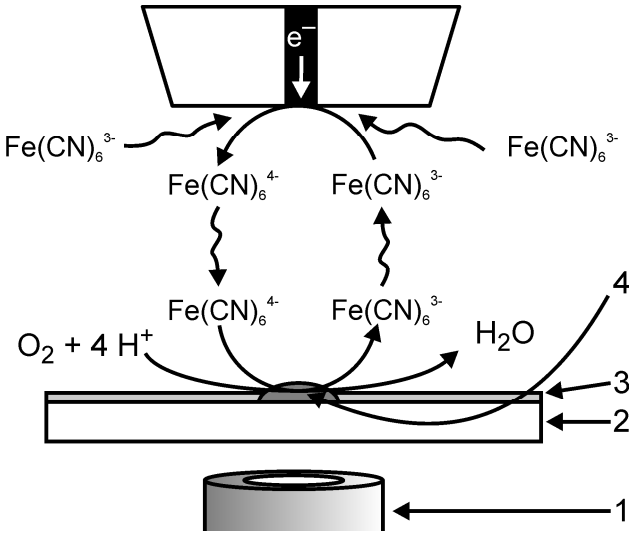

Fig. 14.6. Schematic setup of the feedback mode SECM experiments combined with CLSM. 1 - CLSM objective; 2 - insulating and transparent support; 3 – enzyme-silicate film; 4 – enzyme aggregate.

14.3.2 SECM feedback measurements of laccase aggregates

For FB imaging of laccase aggregates two experiments were conducted using a small positioning system completely enclosed in a controlled gas atmosphere. First with O_2-free atmosphere (Figure 14.7A) and next with O_2-atmosphere, Figure 14.7B). After switching to oxygen atmosphere, an increase of the cathodic current at the microelectrode is observed, confirming the involvement of oxygen in the heterogeneous reaction at the sample. Some contrast is also observed in the case of the deaerated electrolyte because of topographic influence. Therefore, it cannot be excluded that traces of oxygen are still present in the chamber of electrolyte.

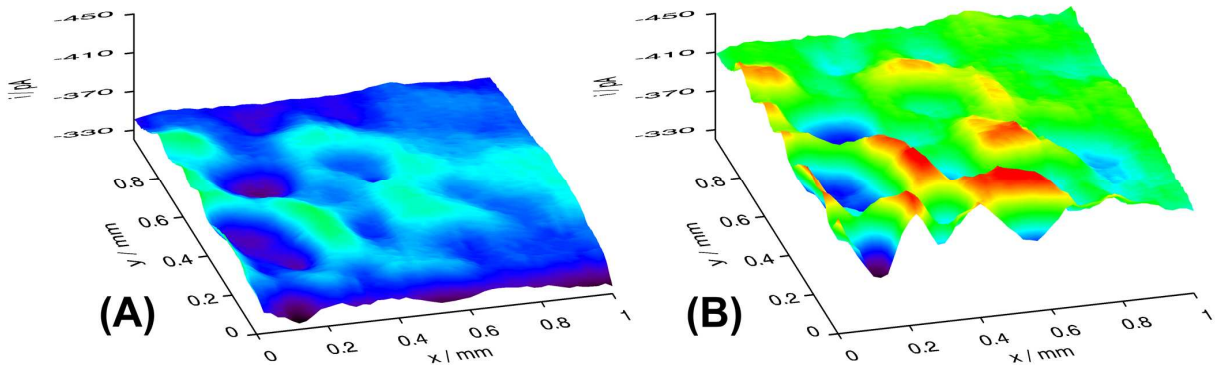

Fig. 14.7. SECM images of laccase-silicate film deposited on glass in 0.1 mM $K_3[Fe(CN)_6]$ in 0.1 M phosphate buffer pH 4.8, E_T = 0 V, r_T = 12.5 µm, RG ≈ 10, v_T = 7.7 µm s^{-1}, d ≈ 20 µm. (A) – Ar-saturated and (B) – O_2-saturated solution. Higher activity is shown as hills.

In SG/TC and RC images of similar sample the lateral resolution was lower and the rising backgrounds is a substantial problem because the enzymatic reaction occurs on the whole sample independent of the microelectrode position. This is not the case in the feedback imaging presented here because the enzymatic reaction is proceeding only directly under the microelectrode where the microelectrode generated electron donor is available.

14.3.3 SECM feedback measurements of laccase aggregates at the film edge

An interesting phenomenon was observed during scanning the area comprising both the silicate thin film with immobilized laccase and the insulating glass support. Figure 14.8A represents a CLSM image of thin silicate film edge. Newton's rings are visible close to the edge of the silicate film due to the variation of thickness with the radius. On the left part of image, the microelectrode is visible which is placed at a distance *d* = 15 µm above the glass support. The bright rectangular area corresponds the 500 µm × 500 µm image frame (Fig. 14.8A) used for the SECM experiments shown in Fig. 14.8B. Figure 14.8C represents a SECM image in a *x*-*z* plane perpendicular to the film surface along the red line marked in Figure 14.8A. In Figures 14.8B and 14.8C one can see larger positive feedback currents for microelectrode positions above the film border than above the centre of the laccase-silicate film. Such behaviour can be explained as a sum of two effects. The first one (probably having a stronger influence) is based on a higher local surface concentration of the enzyme in the silicate film close to the film border. The second influence is the so called edge effect [342] – caused by nonlinear oxygen concentration profiles close to the border yielding higher oxygen fluxes at the film edge.

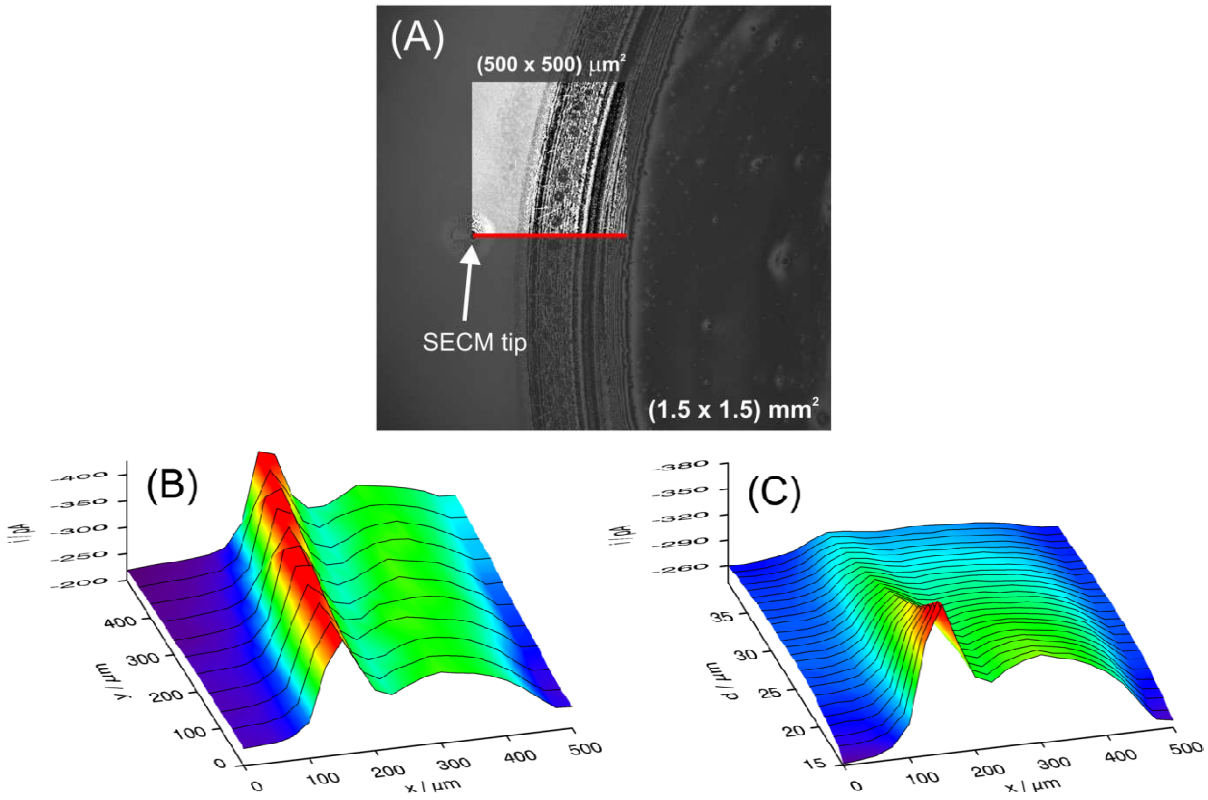

Fig. 14.8. Combined SECM/CLSM imaging of the edge of the laccase-silicate film deposited on glass. (A) – reflection mode CLSM image, (B) – lateral (x-y) SECM image, (C) – perpendicular to the sample surface (x-d) SECM image in aerated 0.1 mM $K_3[Fe(CN)_6]$ in 0.1 M phosphate buffer pH 4.8. E_T = 0 V, r_T = 12.5 µm, RG ≈ 10, v_T = 8.9 µm s^{-1}, d ≈ 15 µm.

14.3.4 SECM approach curves to laccase film in feedback mode.

Usually, the following (simplified) reaction mechanism is used to analyse the enzymatic reaction of laccase with oxygen and a one-electron mediator [343]:

$$\mathrm{Enz(4Cu^{+}) + O_2 \underset{k_{-1}}{\overset{k_1}{\rightleftharpoons}} [Enz(4Cu^{+})\cdots O_2]} \tag{14.6}$$

$$\mathrm{[Enz(4Cu^{+})\cdots O_2] + 4H^{+} \xrightarrow{k_2} Enz(4Cu^{2+}) + 2H_2O} \tag{14.7}$$

$$\mathrm{Enz(4Cu^{2+}) + 4[Fe(CN)_6]^{4-} \xrightarrow{k_3} Enz(4Cu^{+}) + 4[Fe(CN)_6]^{3-}} \tag{14.8}$$

The reaction mechanism can be transferred to a rate law following earlier reports [343, 344].

$$\frac{\partial c_{[Fe(CN_6)]^{4-}}}{\partial t} = \frac{4 k_2 \Gamma_{enz}}{\frac{K_{M,O_2}}{c_{O_2}} + \frac{K_{M,[Fe(CN)_6]^{4-}}}{c_{[Fe(CN)_6]^{4-}}} + 1} \tag{14.9}$$

with

$$K_{M,O_2} = \frac{k_{-1} + k_2}{k_1} \tag{14.10}$$

$$K_{M,[Fe(CN)_6]^{4-}} = \frac{k_2}{k_3} \tag{14.11}$$

Equation (14.9) can be simplified if $c_{O_2} >> K_{M,O_2}$ and an apparent pseudo first order kinetics with respect to the SECM mediator is expected if $c_{[Fe(CN)_6]^{4-}} << K_{M,[Fe(CN)_6]^{4-}}$. Under this situation a fit of the theory for first order irreversible kinetics at the sample provides kinetic information about the enzymatic reaction.

In order to evaluate local activity of the centre and the edge of the film, approach curves were recorded (Figure 14.9). The response of the laccase-modified silicate film (Figure 14.9, curve 1 and 2) can be compared to a system without enzymatic reaction at the sample. Such a control is conveniently obtained by recording an approach curve to an insulating surface without immobilized enzyme using $[Fe(CN)_6]^{3-}$ as mediator (Figure 14.9, curve 3). In this case the enzymatic reaction cannot proceed and the microelectrode current is determined exclusively by the hindered diffusion of the $[Fe(CN)_6]^{3-}$ from the solution bulk to the microelectrode.

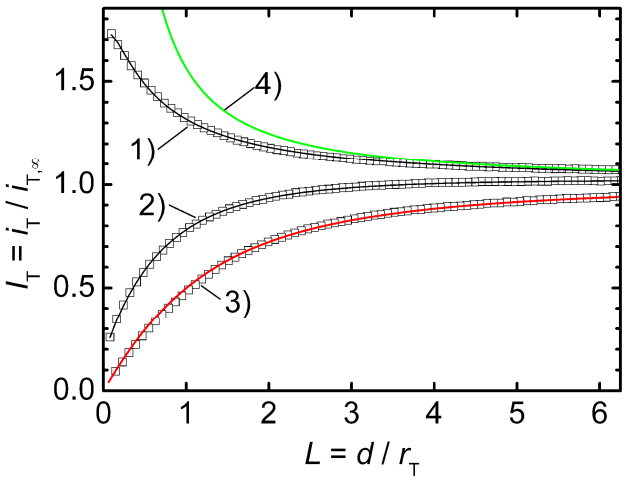

Fig. 14.9. Experimental SECM approach curves (symbols) to 1) the edge and 2) the centre of the laccase-silicate film deposited on glass. Curve 3) is an approach curve to bare glass. Electrolyte: O_2-saturated 0.1 mM $K_3[Fe(CN)_6]$ in 0.1 M phosphate buffer pH 4.8; E_T = 0 V, r_T = 12.5 µm, RG ≈ 10; v_T = 0.77 µm s^{-1}. Lines are fitted curves for irreversible first order reaction at the sample with a normalised rate constant κ = 1.86 (curve 1) and κ = 0.11 (curve 2). Curve 4) represents limiting case for diffusion-controlled reaction at the sample surface.

Normalised rate constants $\kappa = 0.11$ for the central part of the laccase-silicate film and $\kappa = 1.86$ for the edge of the film were extracted by fitting to the analytical approximation of Cornut and Lefrou [292] for $RG = 9.97$, and $r_T = 12.48$ µm as detailed in Section 11.14.

The local surface concentration of the enzyme at the border of the film is higher than in its centre probably because of "coffee ring effect" [345, 346]. During evaporation, the droplet covers roughly the same area of the support (glass slide). The situation is schematically illustrated in Figure 14.10A. As a consequence of the solvent evaporation of the continuous phase (water) at the air-liquid interface, the concentrations of enzyme and dispersed particles are increased close to the air-liquid interface. The concentration gradient causes diffusion of enzyme molecules and silicate particles towards the bulk of the droplet. The droplet shape imposes larger restrictions to this process in the vicinity of the droplet edge. Because of higher concentrations of the reagents in this regions, the sol-gel process is faster and more silicate with entrapped enzyme is deposited at the edge. The resulting increased film thickness at the droplet edge can be seen from CLSM reflection measurements (Figure 14.10B). The film on the border is about 10 µm thicker than in the centre.

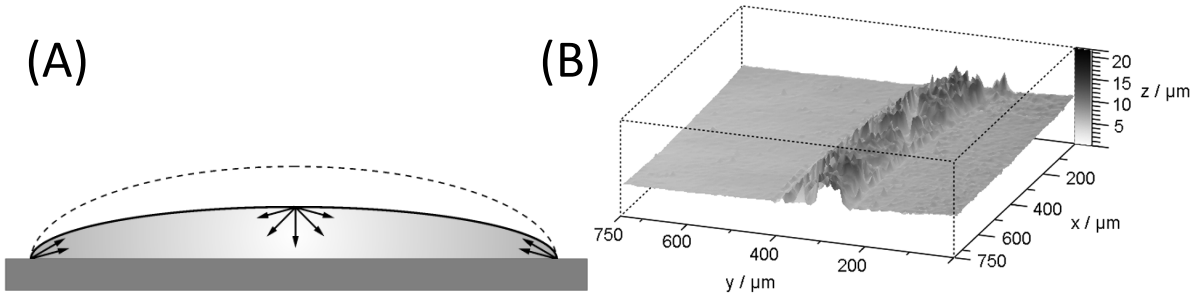

Fig. 14.10. (A) - Schematic representation of hindered solute diffusion in an evaporating drop. (B) - Topography reconstruction of the edge of the laccase-silicate film deposited on glass obtained from a reflection mode CLSM images stack.

This leads also to different working distances if an image is recorded at a fixed vertical microelectrode position (Figure 14.8B). However, topography is only a minor contribution to the large contrast in Figure 14.8B. As can bee seen from an image in the *x-z* plane (Figure 14.8C), i.e. each line scan is effectively an approach curve, the behaviour at the different regions is qualitatively very different with the current rising when approaching the edge of the silicate spot while decreasing when over the spot centre.

14.4 Comparison of laccase and bilirubin oxidase deposits activities

In order to compare activities of laccase and bilirubin oxidase, SECM feedback-mode images

of neighbouring silicate-entrapped enzymes spots were recorded. The main advantage of such measurement compared to voltammetric analysis of different electrodes is the fact that the samples are examined exactly at the same time and under the same physical and chemical condition. Two silicate spots with diameters of around 50 µm containing equal masses of entrapped laccase (in one spot), and bilirubin oxidase (in the other spot) were placed on a PS surface. The hydrophobicity of this material allows preparing silicate film spots with diameters of 50 µm. The distance between the centres of the spots was 130 µm. With the help of the CLSM (Figure 14.11A), both spots could be placed in relatively small scan area (500 µm × 500 µm, brighter area in Figure 14.11A). The active part of SECM microelectrode is visible as a white circle in bottom left corner of this area, which is the start position of the SECM images (Figure 14.11B and 14.11C). This procedure helps to limit the time for recording an image frame and making tilt adjustment less critical than for larger scan areas. Larger scanning areas would be required for larger enzyme-silicate spots or for generation-collection images because of their lower lateral resolution. Because the molar masses of *Cerrena unicolor* laccase and BOx are almost equal ($M_{Lc} \approx 57$ - 64 kDa [347], $M_{BOx} \approx 60$ kDa [94, 348]), the molar amounts of both enzymes are also similar. Laccase exhibits its maximum activity at pH 4.8 [158, 202], and bilirubin oxidase at pH 5.0 [94]. Figure 14.11B shows enhanced microelectrode currents in SECM feedback imaging for both enzymes in 0.1 mM $[Fe(CN)_6]^{3-}$ as mediator in 0.1 M phosphate buffer, pH 4.8. Although the pH is at the pH optimum of laccase and slightly off the pH optimum of BOx. The BOx spot exhibits a several times higher activity than the laccase spot.

Of particular interest is a comparison at neutral pH due to the relevance for biofuel cells operating close to physiological pH. After changing the electrolyte to 0.1 mM $K_3[Fe(CN)_6]$ in 0.1 M phosphate buffer at pH 7 using a peristaltic pump, the feedback image of BOx activity of the same sample is almost unchanged (Figure 14.11C). In contrast, the activity of laccase is almost not detectable at this pH. Thus BOx is a much better candidate as cathodic biocatalyst for biofuel cells especially if operation at neutral pH is required.

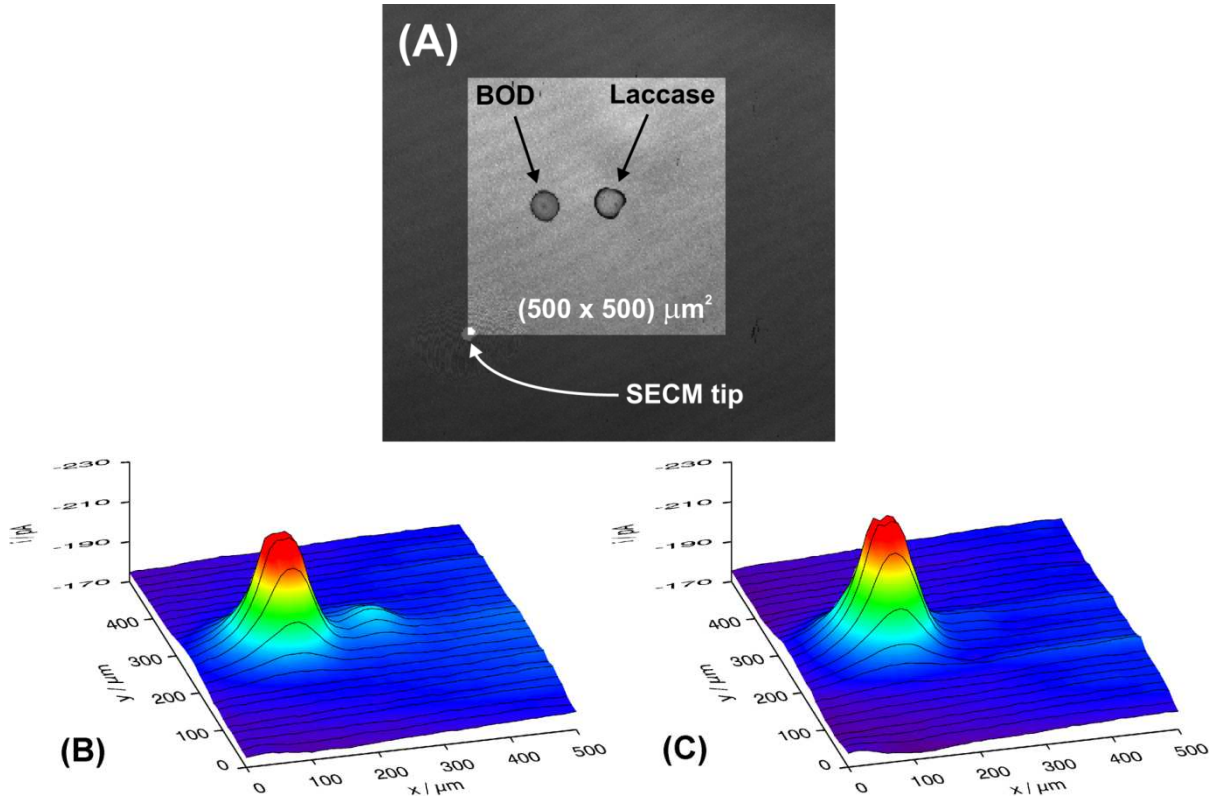

Fig. 14.11. Combined SECM/CLSM mapping of BOx and laccase immobilized in silicate spots on PS surface. (A) reflection mode CLSM image; (B) SECM feedback image in aerated 0.1 mM $K_3[Fe(CN)_6]$ in 0.1 M phosphate buffer pH 4.8; (C) SECM feedback image in aerated 0.1 mM $K_3[Fe(CN)_6]$ in 0.1 M phosphate buffer pH 7.0. Other experimental conditions for (B) and (C): E_T = 0.0 V, r_T = 12.5 µm, RG ≈ 10, v_T = 10 µm s^{-1}, d ≈ 15 µm.

14.5 Conclusions

The hydrophilic silicate film obtained by the sol gel process using TMOS as precursor with immobilized laccase exhibits laterally non homogeneous distribution of oxygen reduction activity. The laccase aggregates present in the film extend ca. 2 µm above the film. Around the aggregates a dendrite-like phase is often observed. The highest activity was detected at the edge of the film mainly because of higher surface laccase load caused by the formation of thicker films during evaporation of the continuous phase of the sol. Such behaviour is probably connected to hindered diffusion of enzyme and silicate particles close to sol droplet border. SECM feedback measurement of the activity of oxygen-reducing enzymes can be performed using Au microelectrode and $[Fe(CN)_6]^{3-}$ as redox mediator.

A sample containing both, BOx and laccase immobilized in separate spots with similar amounts, showed that BOx has a several times higher activity at pH 4.8. Laccase lost its

catalytic activity at pH 7 while to BOx which can still catalyse oxygen reduction at this pH. This observation is consistent with literature reports [94, 158, 202].

15 Carbon ceramic electrode modified with bilirubin oxidase

15.1 Introduction

Despite the fact that BOx catalyzed ORR overpotential decrease is smaller than laccase [72] BOx is superior in terms of activity under simulated physiological conditions, i.e. at neutral pH and in the presence of Cl^- anions [97]. Carbon-based electrode materials have been already proved to provide favourable conditions for direct electron exchange with BOx [109, 125, 349] and for mediatorless oxygen reduction catalysis with this enzyme [120, 132, 133, 349, 350].

In this section CCE modified by adsorbed BOx from *Myrothecium sp*. exhibiting efficient mediatorless bioelectrocatalysis of oxygen electroreduction is presented. The efficiency of electrocatalysis is increased for electrodes enriched with hydrophilic CNP's. The construction and performance of carbon ceramic gas electrode (CCGE) modified with BOx that make use of oxygen from the gas phase (Fig. 15.10) is also presented.

The electrodes were examined by CLSM, AFM, CV, CA and SECM. The last technique was used for imaging of lateral distribution of the enzymatic activity, electrical conductivity and oxygen permeability of the CCGE. These experiments were supplemented by SECM examination of oxygen permeability through a microhole filled with MTMOS-based silicate. CCGE was applied as biocathode in a zinc-oxygen cell with a bare zinc anode and deaerated electrolyte. Current-voltage characteristics of this cell were determined using chronopotentiometry.

15.2 Microscopic examination

At first the surface of electrodes were studied by CLSM (Fig. 15.1). In the examination of these images we took advantage of better reflectivity of carbon microparticles (compared to CNPs) for visible light. The grey scale represents the maximal reflected light intensity from stacks of images recorded with focal planes in the range of topographic features of samples. The brighter areas correspond to exposed graphite microparticles and darker areas to CNPs. It

is clear that the presence of CNP in bulk electrode material resulted in their appearance on the electrode surface.

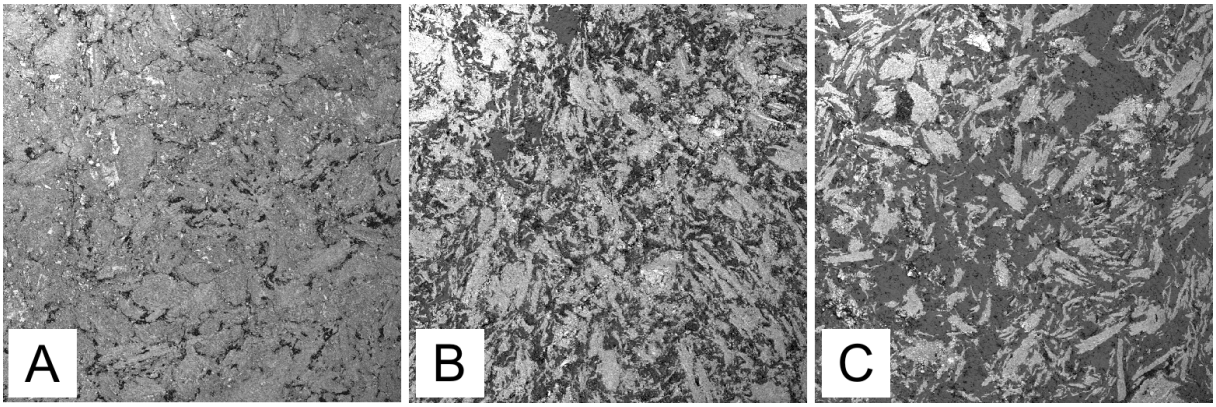

Fig. 15.1. Reflection mode CLSM images of CCE (A), CCE-CNP10 (B) and CCE-CNP20 (C). Each image covers 300×300 μm^2.

Apart from development of the electrode surface area, and delivery of the direct electron transfer possibility, addition of hydrophilic CNPs causes the increase of porosity (Fig. 15.2), what should have an influence on the enhancement of oxygen transport through the CCE-CNP. No such pores were observed for CCE without CNPs. Such composite is hydrophobic enough to prevent penetration of submicrometer size pores by aqueous electrolyte, what is seen in Fig. 15.3. This figure represents attempts to evaluation of water droplets contact angle on CCE, CCE-CNP10 and CCE-CNP20 surfaces, which are: 61.5° ± 3.2°, 59.5° ± 3.1° and 57.5° ± 3.2°, respectively. This result shows partial loss of hydrophobicity with CNPs addition.

Next BOx was adsorbed on CCE surface from enzyme solution. Such a procedure was earlier found to be useful for the immobilization of this enzyme on carbon-based materials [89]. Here an attempt was made to follow the adsorption process by AFM (Fig. 15.4). After taking AFM images of pristine CCE-CNP20 electrode at different magnifications that allowed relocation of the specific region, it was immersed into BOx solution in phosphate buffer (Fig. 15.4A-C).

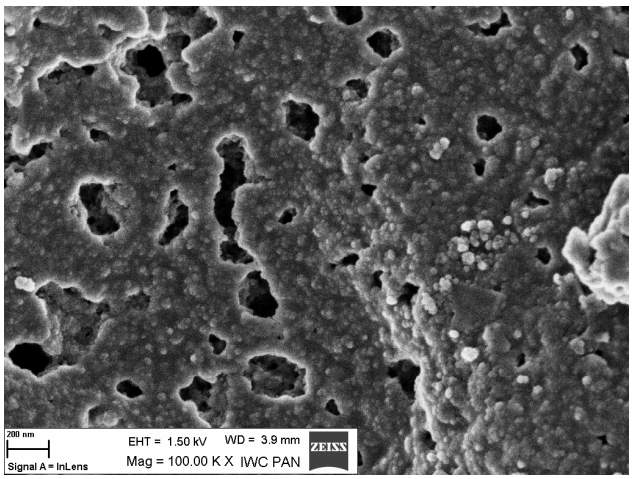

Fig. 15.2. SEM image of the CCE-CNP20 surface.

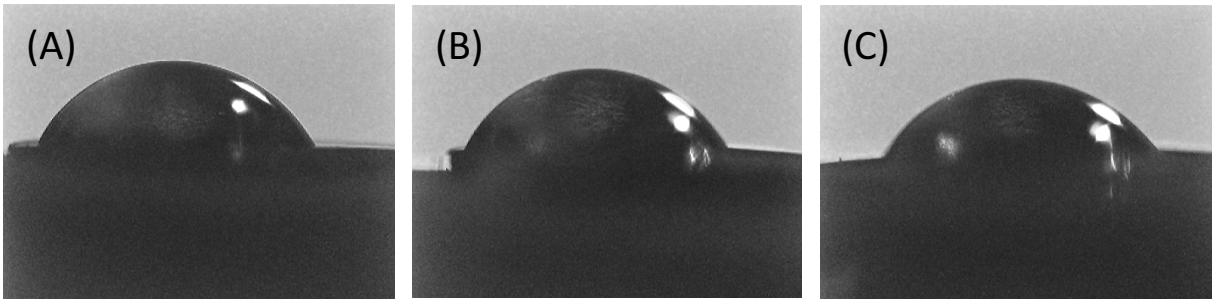

Fig. 15.3. Optical micrographs of water droplets on CCE (A), CCE-CNP10 (B) and CCE-CNP 20 (C) surfaces. Corresponding contact angles: 61.5° ±3.2° (A), 59.5° ±3.1° (B) and 57.5° ±3.2° (C).

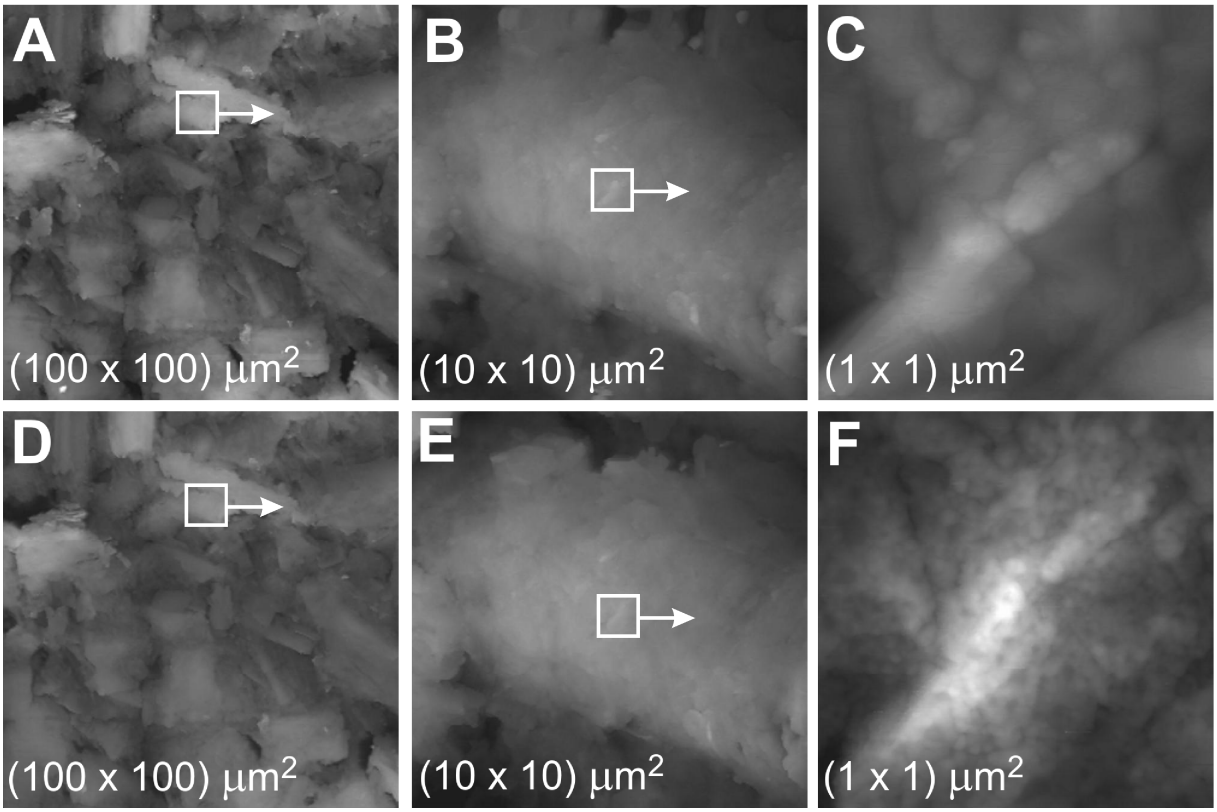

Fig. 15.4. AFM images of CCE-CNP20 taken before (A,B,C) and after (D,E.F) BOx adsorption in the order of decreased imaging area (100×100), (10×10) and (1×1) μm^2. The white squares represent area restricted in subsequent experiments B, C and E, F.

Then AFM imaging was again performed (Fig. 15.4D-F). The topographic features visible on different scale images allowed the relocation of an identical scan area after the enzyme adsorption. Most importantly comparing figures 15.4C and 15.4F, one can identify additional topographic differences corresponding to adsorbed enzyme aggregates.

15.3 Bioelectrocatalytic activity

CV sigmoidal signal with minor hysteresis is observed for CCE modified with adsorbed BOx and the catalytic current is proportional to oxygen concentration (Fig. 15.5A). The onset potential of catalytic current is at ca. 0.6 V, close to the redox potential of the T_1 centre of BOx [99]. This indicates that carbon microparticles provide favourable conditions for mediatorless bioelectrocatalytic activity towards oxygen reduction. This electrode exhibits higher activity than CCE modified with laccase from basidiomycete *Trametes hirsuta* [254]. In deaerated solution no signal from the redox transition of the adsorbed protein is observed. However, the shape of the voltammograms obtained under these conditions is typical for an electrocatalytic process. This is probably due to the electroreduction of oxygen trapped in the porous electrode material being in contact with deaerated aqueous electrolyte occurring at the three phase boundary carbon microparticle|air|electrolyte. The transition from air-saturated to oxygen-saturated solution results in an approximately five-fold increase of the catalytic current density from 15 to 80 µA cm^{-2} (Fig. 15.5A, curve (ii) and (iii)). This was estimated at 0.3 V after "background catalytic current density" of 15 µA cm^{-2} substraction (Fig. 15.5A, curve i).

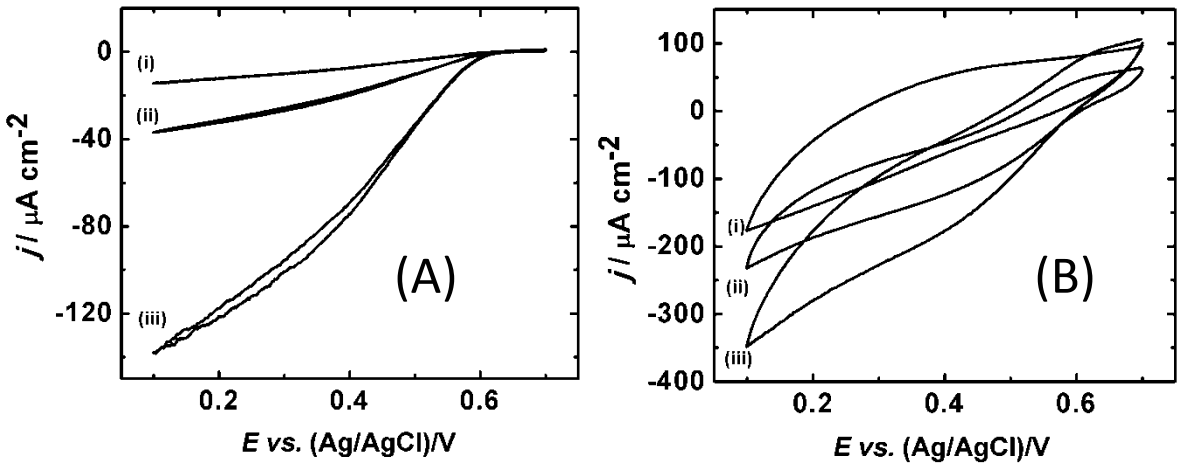

Fig. 15.5. (A) Cyclic voltammograms (2nd scans) obtained with BOx modified CCE electrode in 0.1 M phosphate buffer (pH 5) saturated with (i) Ar (ii) air (iii) O_2.(B) Cyclic voltammograms (2nd scans) obtained with BOx modified CCE-CNP10 electrode in 0.1 M phosphate buffer (pH 5) saturated with (i) argon (ii) air (iii) oxygen. Scan rate: 1 mV s^{-1}.

Next an attempt to replace carbon microparticles with CNPs in the volume of the CCE was made. Unfortunately, no stable bulk material was obtained from MTMOS and CNPs. However, stable electrode materials were obtained with up to 20% CNPs load. Indeed such electrode material exhibits higher activity than standard CCE (Fig. 15.5B).

However, for CCE-CNP10 electrode significant catalytic currents (120 µA cm^{-2} at 0.3 V) are observed when immersed in argon-saturated solution. Therefore, the current increase is to a significant part due to increased capacitive current caused by the increase of the real surface area and electroreduction of oxygen trapped in the porous electrode body. A further effect is the better development of three phase boundaries carbon microparticle|air|electrolyte solution by nanoparticulate carbon. Interestingly, the catalytic current obtained with CCE-CNP10 at 0.3 V in air-saturated solution is four times larger than with CCE. However, for oxygen-saturated solutions only two-fold increase is observed. In contrast to the CCE, the increase of the catalytic current at the CCE-CNP10 electrode is not proportional to the concentration of oxygen. A further increase of the CNP fraction in the electrode material up to 20% resulted in a further increase of the catalytic currents. However, the effect is not very significant (Fig. 15.6). This can be caused by depletion of oxygen dissolved in electrolyte and flooding of the electrode material due to the presence of hydrophilic nanoparticles. Peak-shaped cathodic CV scan (Fig. 15.6, curve iii) is caused by such oxygen mass transport limitation.

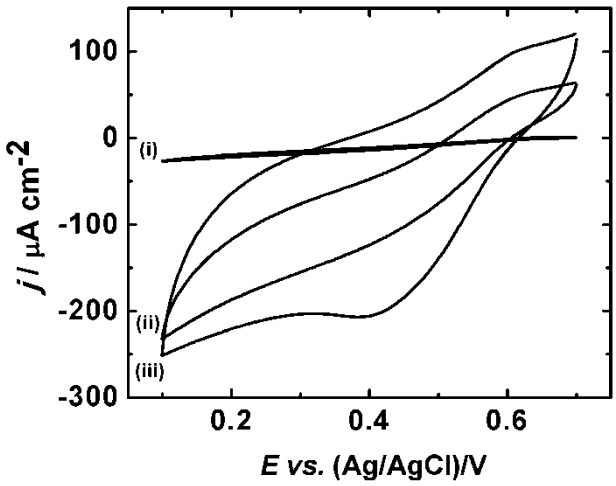

Fig. 15.6. Cyclic voltammograms (2nd scan) obtained with BOx modified (i) CCE, (ii) CCE-CNP10 and (iii) CCE-CNP20 electrode in air-saturated 0.1 M phosphate buffer (pH 5). Scan rate 1 mV s^{-1}.

The magnitude of the catalytic current is pH-dependent. This is understandable, because this parameter affects the enzyme activity [99]. For example at pH 7 the CCE-CNP10

electrode retained about 50% of its activity at pH 5 (Fig. 15.7) making it a good candidate for a cathode in biofuel cell working under physiological conditions.

The stability test of the electrode showed a significant activity decrease during the first 2 hours (Fig. 15.8). This could be connected with depletion of oxygen in the solution next to the electrode. The desorption of the enzyme cannot be excluded until a new equilibrium is established. This effect is similar in the absence and in the presence of CNPs in the electrode material. However at longer times (t > 5 h) CNPs clearly contribute to the larger catalytic current density (Fig. 15.8).

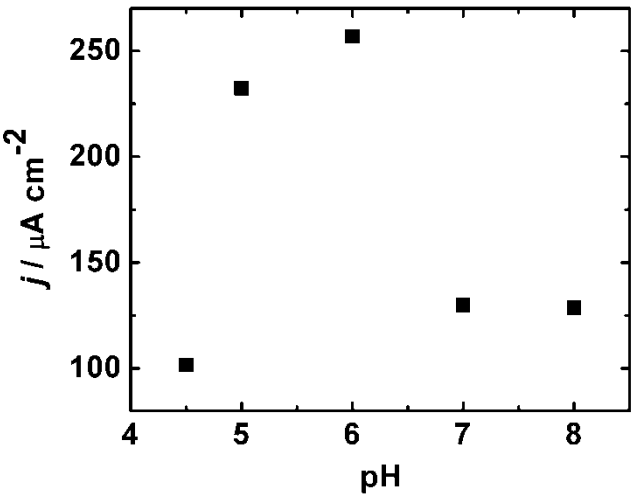

Fig. 15.7. pH dependence of absolute cathodic current density for second scans (cathodic sweep, scan rate: 1 mV s^{-1}) at 0.2 V on CCE-CNP10 electrode in air-saturated 0.1 M phosphate buffers.

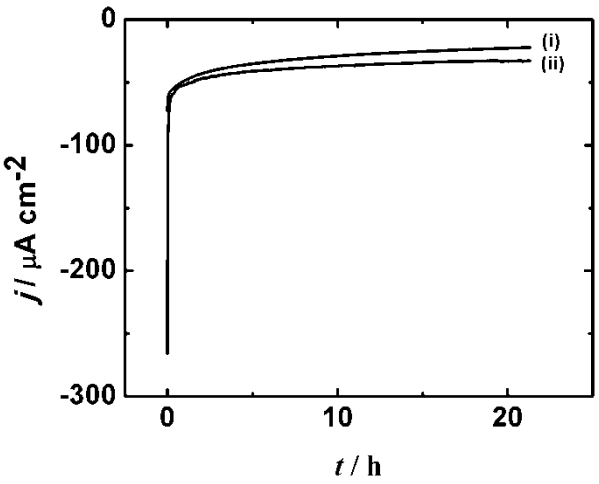

Fig. 15.8. Current density versus time dependence obtained with BOx modified CCE (i) and CCE-CNP10 (ii) electrode in air-saturated 0.1 M phosphate buffer (pH 5) after potential step from 0.8 to 0.2 V.

15.4 SECM measurements

The RC-SECM mode experiments were performed in deaerated 0.1 M phosphate buffer pH 5 and argon was passed above the cell during the measurements. A three-step potential program is applied to the microelectrode at every grid point of the image. In the first step, the microelectrode potential E_T is set to 1.37 V for 0.3 s causing oxygen generation by water oxidation. Next, E_T is shifted to -0.40 V for diffusion-controlled oxygen reduction reaction for 0.5 s. Next, E_T is shifted to 0.50 V for 0.5 s where no faradaic reaction occurs. This step was added for equilibration of the system before movement of the microelectrode to the next grid point. This allows for diffusion of oxygen generated in the first step to the solution bulk.

In order to minimize the influence of tilt and of topographic features of the CCE (Fig. 13.13) on O_2 diffusion between the electrodes, two maps were constructed (see Section 13.5). The first map was constructed by collecting the average microelectrode current during the second potential step (E_T = -0.4 V) between t = 0.08 s and t = 0.35 s. It is influenced by the oxygen consumption by the bioelectrocatalytic reduction at the sample. The second map was constructed from a control experiment in which microelectrode current was collected with the sample electrode disconnected from the bipotentiostat. Finally, a differential images for several electrode materials (Fig. 15.9) were calculated from the current difference obtained in experiments described above.

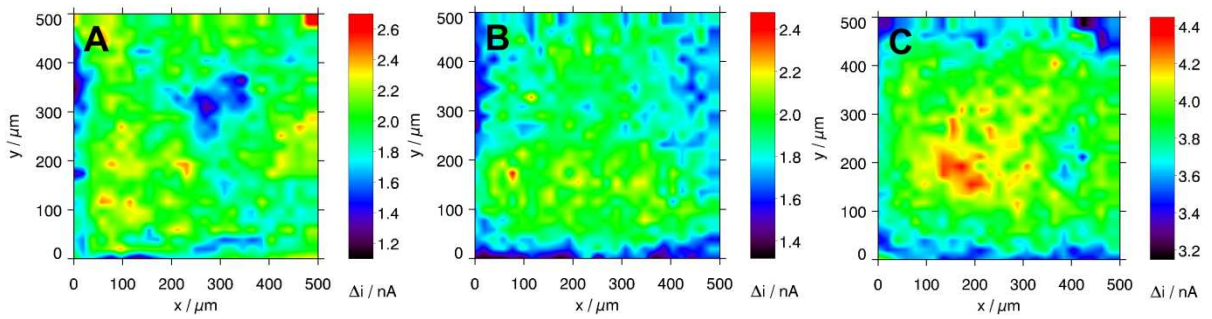

Fig. 15.9. SECM visualization of lateral activity distribution at (A) BOx-modified CCE, (B) CCE-CNP10 and (C) CCE-CNP20. Electrolyte: 0.1 M phosphate buffer (pH 5) saturated with Ar. r_T = 12.5 µm, d =20 µm.

The areas with higher current differences correspond to higher local activity. Higher current differences for CCE-CNP20 (Fig. 15.9C) comparing to CCE (Fig. 15.9A) and CCE-CNP10 (Fig. 15.9B) can be caused by higher oxygen permeability through CCE-CNP20. Then more oxygen is reduced at the microelectrode in a control experiment. It is clear that the surface activity of all electrodes for oxygen reduction is more or less evenly distributed on the length scale of the used microelectrode (r_T = 12.5 µm) and no significant effect of electrode material is observed. Such distribution of the enzyme was earlier found as important for mediatorless bioelectrocatalysis of oxygen reduction with laccase.

In order to confirm the four electron mechanism of mediatorless bioelectrocatalysis with BOx, SG/TC experiments similar to this presented in Fig. 13.16 were done and no H_2O_2 was detected as the product of this reaction when sample potential was higher than 0.2 V.

15.5 Gas diffusion CCE-CNP/BOx

Because the efficiency of mediatorless oxygen reduction electrocatalysis on CCE modified with adsorbed BOx is increased by addition of hydrophilic CNPs to the electrode material, CCGE doped with 20 % of CNPs was examined.

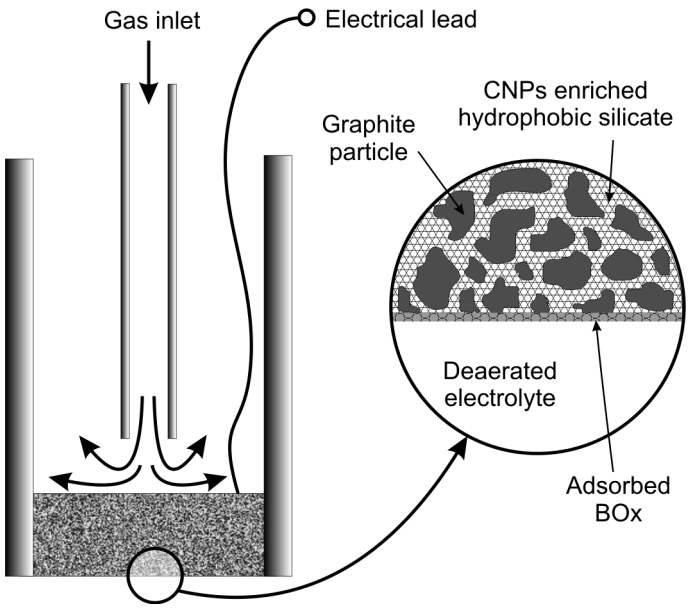

Fig. 15.10. A scheme of CCGE for bioelectrocatalytic reduction of oxygen supplied from the gas phase.

Methyl groups attached to the silicate network render the pores of the material hydrophobic. Consequently the electrode body is not flooded when immersed into an aqueous solution. Moreover, the porous electrode material can be penetrated by gaseous oxygen up to the matrix|aqueous electrolyte interface inside the electrode body and this flux can be superior to O_2 diffusion in electrolyte and higher current densities can be obtained [131]. Additionally, it allows to use oxygen-free electrolytes what improves the operation of some devices. For example, in oxygen–glucose biofuel cells [113, 167, 169], electron transfer to the anode from the mostly employed anode biocatalyst – glucose oxidase competes with electron acceptance by oxygen dissolved in the electrolyte [183]. Supply of oxygen from outer gas phase eliminates this problem. Moreover, if both cathodic and anodic biocatalysts are immobilized on the electrodes, the use of oxygen free electrolyte allows for construction of simpler membrane-free devices like biofuel cells or Zn-O2 cells.

Permeation of oxygen across porous MTMOS-based silicate matrix, being the gas permeable CCGE component is an important factor because the transport of oxygen can be the rate determining step of the bioelectrocatalytic ORR [101, 351]. In order to visualize and estimate oxygen permeability of this silicate material a hole (Fig. 15.11A) (ca. 150 µm in diameter) in 0.8 mm thick polystyrene plate filled with this material was studied by SECM. In order to provide the most shallow depth of field the topography of the sample was characterized by optical microscopy with totally opened aperture. Both silicate and polystyrene are at the same distance from objective of microscope, because the micrograph is well focused on both materials (Fig. 15.11B). This is also observed from the opposite side of the sample (not shown). Therefore, one may conclude that the entire hole is filled with sol-gel processed silicate. Only two polystyrene hills extend out of the focal plane. This is probably caused by a distorted laser beam focused using a 100 mm converging lens during manufacturing, because the incident beam is not perfectly parallel to the optical axis of the lens accentuating coma and astigmatism. The height of these topographic defects is ca. 6 µm as estimated using optical microscopy. These features are difficult to remove by polishing of the tiny polymer plate. Therefore, we decided to use them for SECM experiments bearing in mind that they can affect the obtained currents.

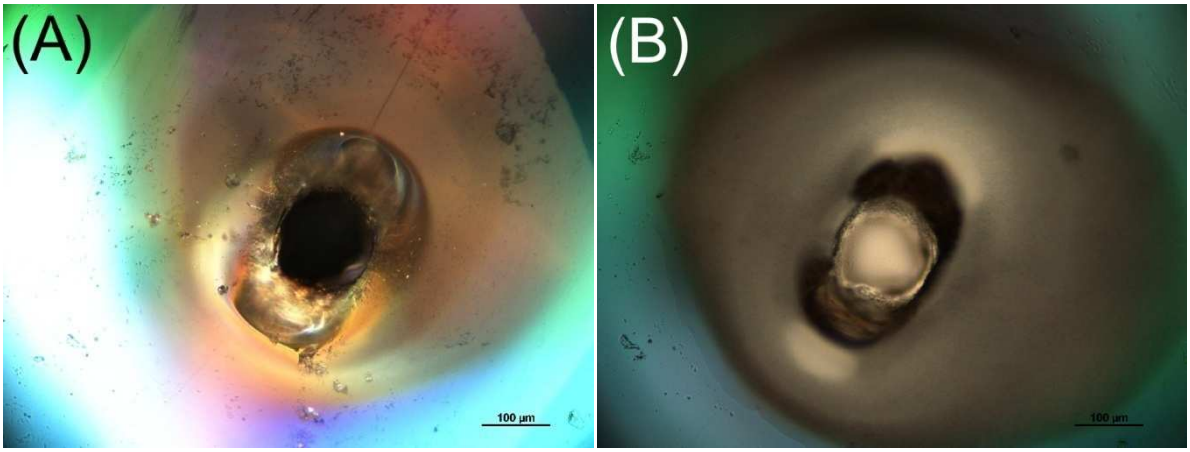

Fig. 15.11. Micrographs of a hole in a PS plate (A), filled with MTMOS-based silicate (B).

Initially SECM imaging were performed in aqueous $K_4[Fe(CN)_6]$ solution with the microelectrode polarized at +0.5 V to achieve a diffusion-controlled oxidation of $[Fe(CN)_6]^{4-}$ (Fig. 15.12A). The microelectrode current does not depend on the microelectrode position except for the two small hills of polystyrene mentioned above. Over these spots the current decrease due more efficient blocking of the diffusion of the $[Fe(CN)_6]^{4-}$ to the microelectrode above the impermeable elevated structures. The lack of any current difference between the position of the hole (between the hills) and the surrounding PS plate indicates that the hole is

completely filled with silicate.

Subsequently, an image was recorded after the microelectrode potential had been switched to -0.4 V in order to achieve diffusion-controlled oxygen reduction at the Pt microelectrode (Fig. 15.12B). A larger cathodic current is observed over the silicate filled hole indicating that oxygen concentration is higher comparing to other parts of the sample surface. This indicates the ingress of oxygen from the backside of the gel-closed hole into the deaerated electrolyte.

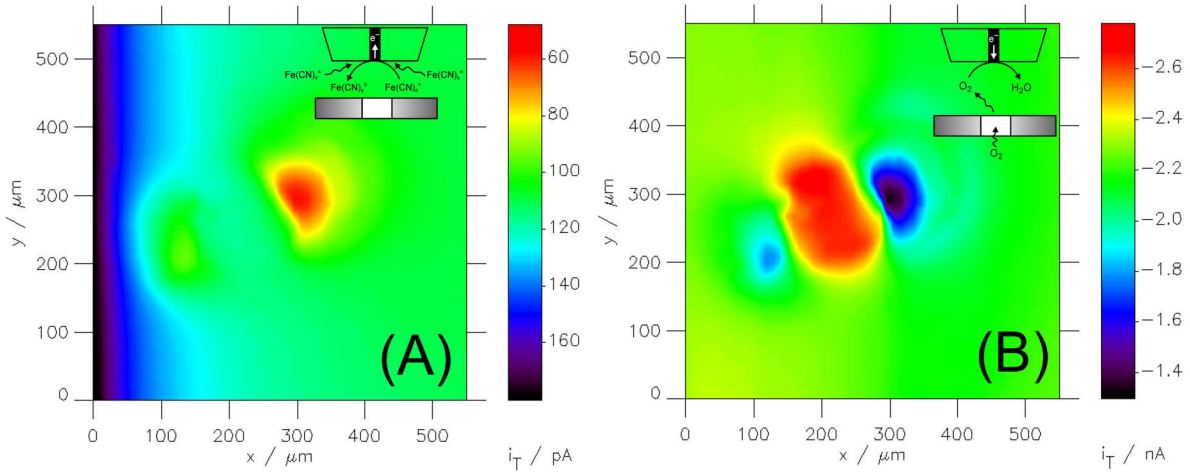

Fig. 15.12. (A) SECM feedback image of a hole in PS plate filled with MTMOS-based silicate; E_T = +0.5 V, (B) - SECM generation-collection mode image of oxygen permeability through silicate; E_T = -0.4 V. Other parameters for both experiments: r_T = 5µm, RG ≈ 32, d = 10 µm, horizontal scan rate v_T = 50 µm s^{-1}, electrolyte was deaerated 0.1 mM $K_4[Fe(CN)_6]$ in 0.1 M phosphate buffer, pH 5.

In order to estimate oxygen concentration above the silicate and the oxygen flux, a cross section above the centre of the silicate has been extracted from a SECM image (Fig. 15.13). The resulting profile has been fitted to the following equations:

$$i_T = 4nFD(O_2)\, r_T\, [O_2]_S\, \zeta \qquad (15.1)$$

These equations were developed for diffusion at an isolated disk-shaped pore [302, 352], where n = 4 is the number of transferred electrons from the microelectrode per O_2 molecule, $D(O_2) = 2.0 \times 10^{-5}$ cm^2 s^{-1} [23] is the diffusion coefficient of oxygen, r_T = 5 µm is the microelectrode radius, r_S is the radius of the silicate hole, $[O_2]_S$ is the additional concentration of oxygen at the silicate surface, and ζ is a dimensionless factor describing the decrease of oxygen concentration as a function of the lateral distance and the vertical distance from the centre of the silicate spot (Section 7.4). Non-linear curve fitting (Fig. 15.13) yields

the following adjustable parameters: $4FDr_Tc_S$ = 0.161 nA, x_0 = 275 µm, d = 10.1 µm, r_S = 79.9 µm, i_{offset} = 2.08 nA.

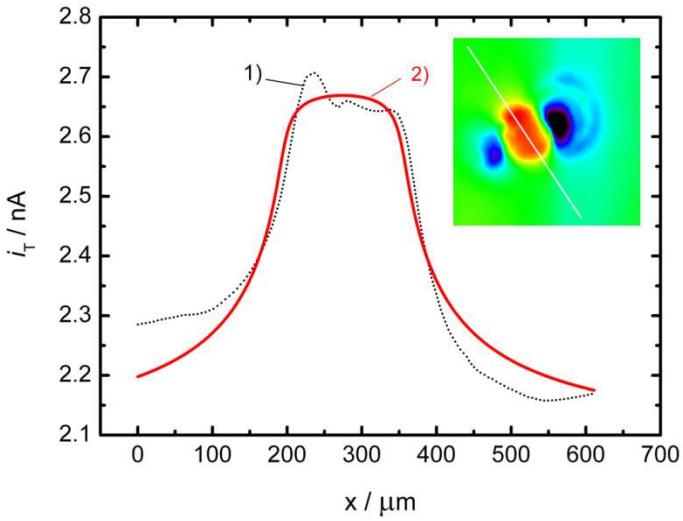

Fig. 15.13. Flux of oxygen emerging from individual hole filled with MTMOS-based silicate. Flux values are obtained from the extracted profile along the white line in the inset and fits to Eqs. (15.1 and 7.16). Dotted line - experimental data, solid line - fitted curve. For more details see the text and the caption of Fig. 15.12.

The fitted value of d agrees well with the distance the microelectrode was retracted from the surface before recording the image. The value of r_S is consistent with the 150 µm hole diameter estimated by optical microscopy. The offset current is a consequence of the presence of oxygen traces in the electrolyte. The additional oxygen surface concentration $[O_2]_S$ can be estimated as 0.0417 mM, i.e. 15.4 % of oxygen concentration under air and atmospheric pressure. From this value, the flux Ω of oxygen from the silicate can be calculated (Section 7.4):

$$\Omega = 4D(O_2)\, r_S\, [O_2]_S = 2.66 \times 10^{-14} \text{ mol s}^{-1} \qquad (15.2)$$

Although there is mass transfer resistance for oxygen diffusion at the entrance of the pore from the gas phase and at the exit from the pore to aqueous solution we supposed that is negligible as compared to that in the pore. Assuming that O_2 partition coefficient between silicate and aqueous solution is equal unity and uniform flux through the silicate the mass-transfer coefficient m for oxygen in MTMOS-based silicate can be estimated from the following equation:

$$m = \frac{\Omega \cdot l}{\pi \cdot r_S^2 \cdot ([O_2]_S' - [O_2]_S)} = 4.66 \times 10^{-5} \text{cm}^2\text{s}^{-1} \qquad (15.3)$$

where l is mass-transport length equal to the sample thickness and $[O_2]_S$' is oxygen surface

concentration at the back side of the sample. If one assume $[O_2]_S' = 2.7 \times 10^{-5}$ mol cm^{-3} (corresponding to an air-saturated aqueous solution [23]), the *m* for oxygen transport in MTMOS-based silicate would be over two times higher than the diffusion coefficient for oxygen in water. Consequently, it can be concluded that the mass transport occurs predominately over the silicate phase as gas diffusion in an interconnected pore system of the electrode material.

Next, the CCGE electrode was examined by SECM in $K_4[Fe(CN)_6]$ aqueous solution and the feedback mode was used to visualise the local electrochemical reaction rate and the electronic conductivity of the CCGE. Although the electrode was polished the topography can still affect this image (Fig. 13.13). First the microelectrode was kept at 0.5 V in order to oxidize $[Fe(CN)_6]^{4-}$. Areas of higher feedback current (red-coloured in Fig. 15.14A) correspond to the locally higher electronic conductivity. After switching the microelectrode potential to -0.4 V, the diffusion-controlled oxygen reduction current at the microelectrode is recorded above the same region. Now red-coloured areas correspond to higher reduction currents (Fig. 15.14B) and represent these fragments of the CCGE surface where more oxygen reaches the electrode|electrolyte interface. Comparison of the SECM images in Figs. 15.14A and 15.14B, reveals that areas of higher conductivity are characterised by lower oxygen supply. Vice versa, lower conductivity areas correspond to higher oxygen ingress. Areas with higher currents in Fig. 15.14A are most likely graphite microparticles providing conductivity but being impermeable for oxygen. The high currents fragments shown in Fig. 15.14B are rich in silicates that provide diffusion paths for oxygen, but have a lower conductivity. The local analysis of transport pathways for electrons and gaseous reactants in composite electrodes provides a new analytical tool for optimising the composite structures of porous electrodes that may be important also for other gas breathing electrodes.

The catalytic activity of the CCGE with adsorbed BOx was examined by cyclic voltammetry (Fig. 15.15) in deaerated buffer. In this experiment oxygen is supplied from the gas phase at the back side of the electrode as illustrated in a scheme in Fig. 15.10. The onset of the cathodic current is observed at 0.45 V. The cathodic current is proportional to the oxygen partial pressure at the back side of the electrode. (Fig. 15.15, lines 2 and 3). This dependence observed at constant total pressure indicates that transport of the oxygen from the gas phase affects the current density of oxygen bioelectroreduction. Interestingly, almost no hysteresis is observed in the voltammograms, what is different than observed for CCE-CNP20 operating in oxygen-saturated solution (Section 15.3). This means that the mass transport through the CCGE can maintain a steady state mass transport. (see ref. [101]).

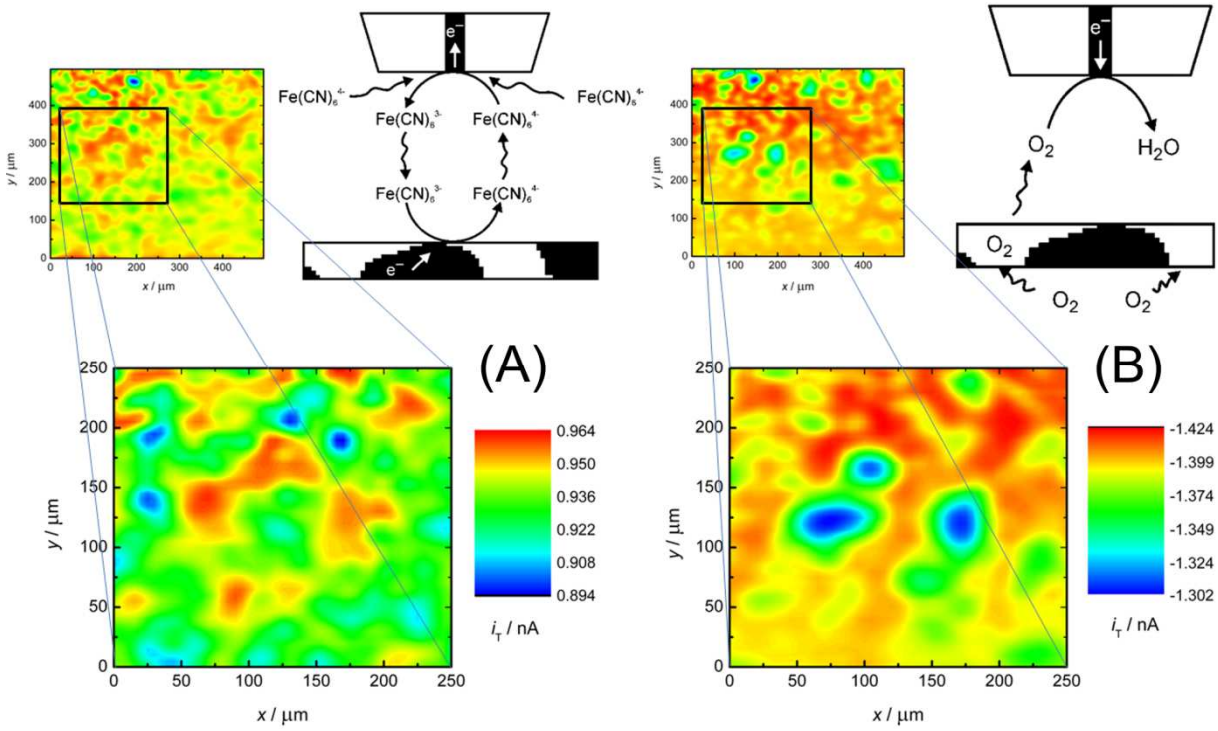

Fig. 15.14. (A) SECM feedback mode image of a CCGE and its schematic representation; E_T = +0.5 V, (B) SECM generation-collection mode image of the measurement of oxygen permeability through the CCGE and its schematic representation. E_T = -0.4 V. Other parameters for both experiments: r_T = 5 µm, RG ≈ 6.8, d ≈ 15 µm, v_T = 25 µm s^{-1}, electrolyte was deaerated 1 mM $K_4[Fe(CN)_6]$ in 0.1 M phosphate buffer pH 5.

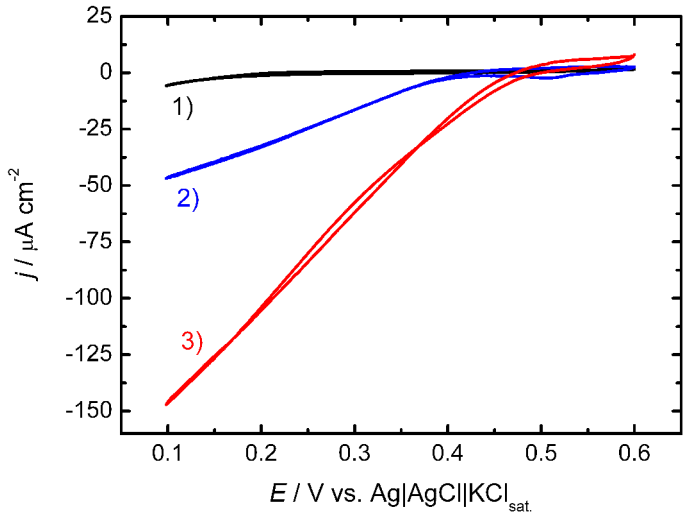

Fig. 15.15. CVs of BOx modified and CNP-enriched CCGE in deaerated 0.1 M phosphate buffer, pH 5. Gaseous oxygen was supplied to the back side of the CCGE at various partial pressures: 1) – 0 atm, 2) – 0.21 atm, 3) – 1 atm. Scan rate: 1 mV s^{-1}.

15.6 Zn-O_2 membraneless hybrid cell

15.6.1 Zn-O_2 cell with oxygen dissolved in electrolyte

CCE-CNP10/BOx was tested as biocathode in Zn-O_2 hybrid cell even at high current densities, when ORR occurs also on carbon material of this composite electrode. To show the influence of CNP on electrocatalysis toward O_2 reduction CCE/BOx and CCE-CNP10/BOx were employed as biocathodes. Current-voltage and current-power characteristics are presented in Fig. 15.16. The cell with CCE-CNP10/BOx exhibits higher voltage and resulting power densities comparing to the cell with CCE/BOx biocathode when the current density is lower than ca. 300 μA cm^{-2}. Above this current density value ORR occurs also on carbon micro- and nanoparticles and the cell with CCE/BOx works effectively. Higher fraction of graphite is on the surface of CCE/BOx than on CCE-CNP10/BOx (see Fig. 15.1). This means that CNPs are more efficient support for BOx, but non-enzymatic ORR occurs more effectively on graphite surface with adsorbed BOx than on CNPs with BOx.

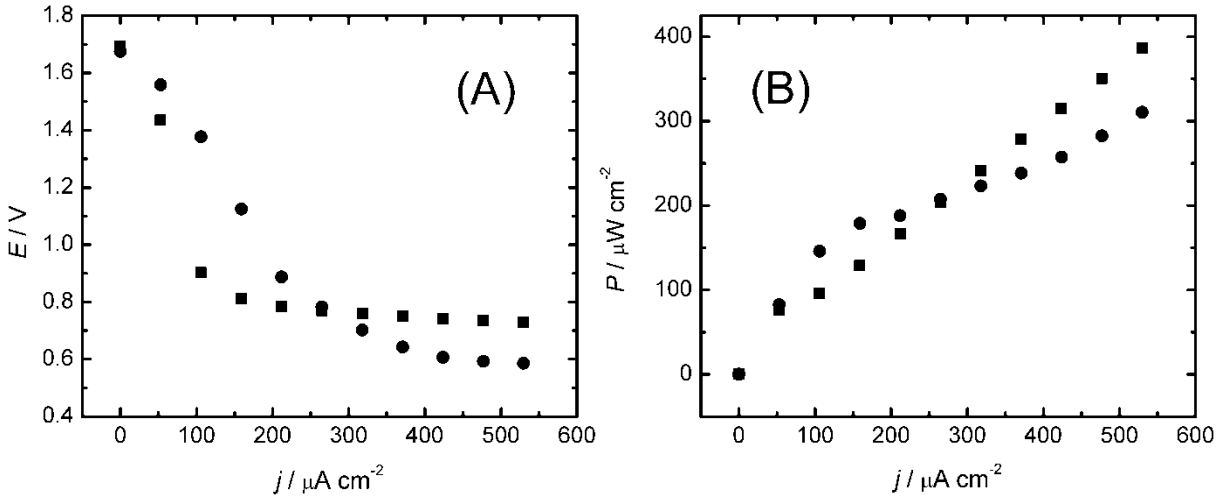

Fig. 15.16. Current density-voltage (A) and current density-power density (B) characteristics of cells consisting of Nafion coated Zn wire and CCE/BOx (■) or CCE-CNP10/BOx (●) immersed in air-saturated 0.1 M phosphate buffer pH 5.

The influence of Nafion layer deposited on zinc surface in Zn-O_2 cell performance was also tested. Characteristics of the cells with bare Zn anode and Nafion-coated Zn anode are presented in Fig. 15.17. At current densities lower than ca. 350 μA cm^{-2} the cell with Nafion-coated anode produce more power. This confirms that Nafion layer preserves zinc against direct oxygen corrosion. However, at higher current densities the cell with bare Zn anode exhibits higher voltage. This is probably because at higher rate of electrooxidation of Zn corrosion does not play any important role and Nafion film is more resistive for produced Zn^{2+} ions than electrolyte.

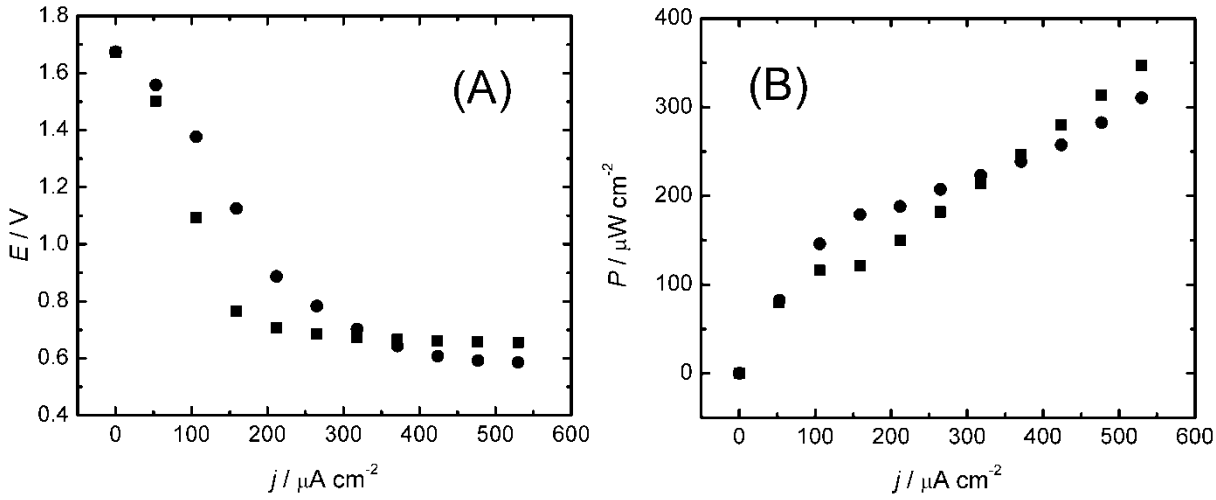

Fig. 15.17. Current density-voltage (A) and current density-power density (B) characteristics of cells consisting of bare Zn wire (■) or Nafion coated Zn wire (●) and CCE-CNP/BOx immersed in air saturated 0.1 M phosphate buffer pH 5.

Keeping in mind potential application of Zn-O_2 hybrid cell as implantable power source the cell consisting of Nafion coated Zn anode and CCE-CNP10/BOx biocathode was tested with two types of electrolytes (Fig. 15.18). Contrary to earlier described cells with laccase-based biocathodes (Section 12.2 and 13.7), here the cell with artificial serum as electrolyte produces more power than the cell with phosphate buffer pH 7.4. This is consistent with the fact that bilirubin oxidase is not sensitive to chloride anions (Section 3.1) and Nafion-coated Zn anode works better in artificial serum that in phosphate buffer [200].

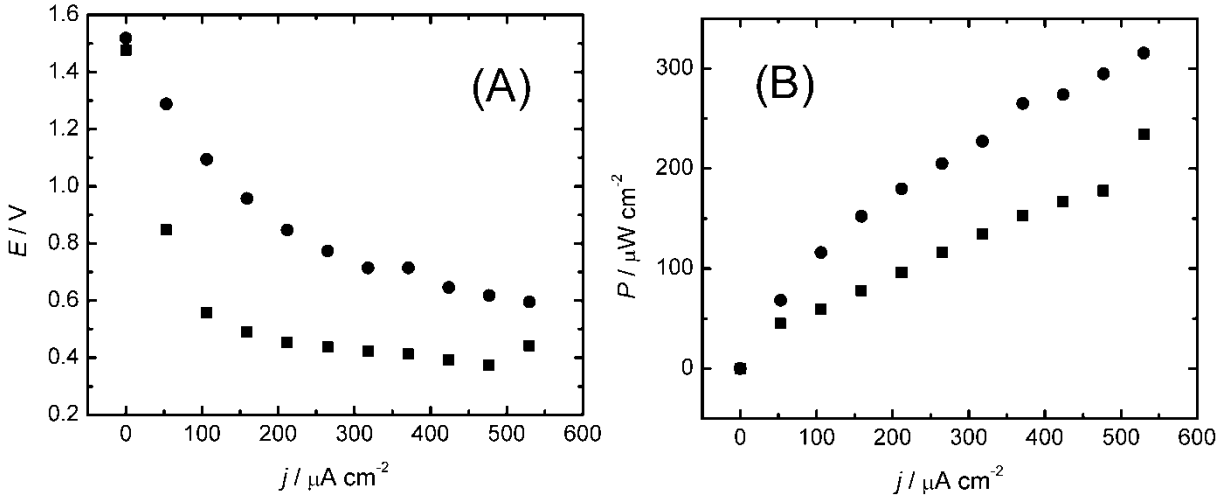

Fig. 15.18. Current density-voltage (A) and current density-power density (B) characteristics of a cell consisting of Nafion coated Zn wire and CCE-CNP10/BOx immersed in air-saturated 0.1 M phosphate buffer pH 7.4 (■)and artificial serum (●).

15.6.2 Zn-O_2 cell with CCGE

Finally, the CCGE was tested as cathode in a Zn-O_2 hybrid cell [103, 201, 202] with external source of oxygen. A non-protected zinc wire could be used as anode. Typical oxygen corrosion of zinc was avoided by using an essentially oxygen-free electrolyte. Current density-voltage and power density-voltage characteristics are presented in Fig. 15.19A and 15.19B respectively. The highest open-circuit voltage (1.095 V) was recorded when pure oxygen was supplied to the back side of the biocathode. The highest power density (41.3 µW cm^{-2}) was recorded under the same conditions at a cell voltage of 0.585 V. Clearly, the cell efficiency strongly depends on the external oxygen partial pressure.

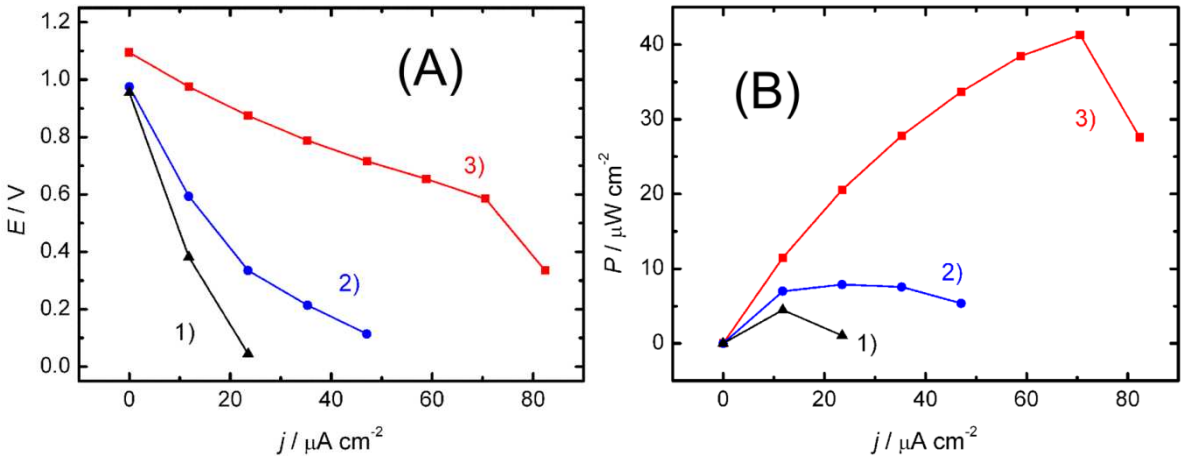

Fig. 15.19. Current-voltage (A) and power-voltage (B) characteristics of zinc-oxygen cell consisting of bare zinc anode and BOx modified CNP-enriched CCGE in deaerated 0.1 M phosphate buffer, pH 5. Gaseous oxygen was supplied to the back side of the electrode at various partial pressures: 1) – 0 atm, 2) – 0.21 atm, 3) – 1 atm. Each data point was recorded 100 s after a galvanostatically controlled current flow had been started.

15.7 Conclusions

BOx can be easily adsorbed on the surface of carbon micro- and nano-particles embedded into MTMOS-based sol-gel processed matrix and this material provides favourable conditions for mediatorless bioelectrocatalytic ORR activity. The oxygen mass transport rate through the MTMOS-based silicate is over two times higher than oxygen diffusion in aqueous solution. The even distribution of the enzyme seems to play important role in BOx electrocatalytic activity. The bioelectrocatalytic activity is further increased by addition of sulfonated carbon nanoparticles to the electrode body. When the back side of this electrode is opened to a oxygen-containing gas phase it can be operated as gas electrode. Then the bioelectrocatalytic current is proportional to the partial pressure of oxygen present in gas phase. Obviously enzyme adsorption is not the best method from the point of view of electrode stability and enzyme loading and other methods of enzyme immobilization should be tested.

The Zn-O_2 cell efficiency is also proportional to the partial pressure of oxygen applied to the back side of CCGE. This feature suggests its application in self-powered oxygen biosensors.

16 Concluding remarks and outlook

From the group of three examined carbon ceramic electrodes for bioelectrochemical oxygen reduction the most promising biocathode for biofuel cells or hybrid devices is CCE modified with carbon nanoparticles and bilirubin oxidase (CCE-CNP/BOx). Compared to the two other examined electrodes – CCE modified with ABTS and laccase (ABTS-CCE/Lc); and CCE modified with syringaldazine and laccase (Syr-CCE/Lc) – it exhibits the highest current density of ORR with low overpotential. ORR occurs effectively on CCE-CNP/BOx at neutral pH and contrary to laccase modified electrodes retains its activity in the presence of chloride. The introduction of hydrophilic CNPs to MTMOS-based hydrophobic gel causes increase of bioelectrocatalytic activity and porosity of the electrode without any substantial loss of its hydrophobicity. Therefore, CCE-CNP/BOx is permeable to gaseous O_2, but not for aqueous electrolyte. This allows its use as a gas electrode for electroreduction of O_2 supplied from gas-phase, which is of practical application for construction of the cell. Namely, an O_2-sensitive anode, such as bare Zn or electrode modified with glucose oxidase, need not to be separated by a membrane. The efficiency of a zinc-oxygen cell with CCE-CNP/BOx biocathode is proportional to the partial pressure of oxygen applied to the back side of this biocathode. This feature suggests application of this cell as a self-powered oxygen sensor. An additional advantage of CCE-CNP/BOx is the lack of mediator as this reduces costs and environmental hazard. Of course enzyme adsorption is not the best method from the point of view of electrode stability and enzyme loading and other methods of enzyme immobilization should be tested in the future.

Another electrode which exhibits bioelectrocatalysis toward ORR at neutral pH is Syr-CCE/Lc. Unfortunately, the ORR overpotential is higher compared to CCE-CNP/BOx and the presence of chloride decreases activity dramatically. Both of which are disadvantageous for biofuel cells applications. Redox potential of syringaldazine depends on pH according to the Nernst equation. This is because of a 2 electrons/2 protons mechanism of the electrode reaction, which was confirmed by Raman spectra of electrochemically treated syringaldazine. This property suggests the use of this electrode for voltammetric pH-sensing. SECM imaging of Syr-CCE/Lc indicates, in contrast to CCE-CNP/BOx, a non-uniform distribution of its enzymatic activity which is probably connected to enzyme aggregation in the sol-gel silicate matrix and/or non-homogeneous distribution of mediator in the electrode material. No H_2O_2 is produced during enzymatic ORR at potentials higher than 0.05 V vs. Ag|AgCl. Despite several imperfections, Syr-CCE/Lc is an efficient biocathode for Zn-O_2 batteries, because

oxygen reduction occurs on its surface at much higher potential than Zn oxidation even at neutral conditions.

ABTS-CCE/Lc also exhibits efficient ORR electrocatalysis, but is less stable than CCE-CNP/BOx and Syr-CCE/Lc. The leaching of mediator and/or probably the $ABTS^{\bullet-}$ radical are responsible for the decrease of ABTS-CCE/Lc activity with time.

Studies of enzymes deposited on flat, insulating surfaces represent an important part of the thesis. The hydrophilic silicate film with immobilized laccase, prepared in the same way as for ABTS-CCE and Syr-CCE modification, exhibits laterally non homogeneous distribution of ORR activity. The edge of the film exhibits the highest activity mainly because of higher surface concentration of laccase caused by the formation of thicker films during evaporation of the continuous phase of the sol drop. Such behaviour is probably connected to hindered diffusion of enzyme and silicate particles close to the border of the sol droplet.

Procedures for SECM imaging and kinetics evaluation proposed in this thesis allow measurement of samples with oxygen-reducing enzymes to be carried out while simultaneously comparison of enzymes activities at the same conditions is carried out. Especially SECM feedback mode imaging with resolution determined by microelectrode size, and with unchanging background signal, can be performed. Such measurements reveal that enzyme in thin silicate film prepared by sol-drop evaporation is concentrated mainly at its edge.

SECM measurement of oxygen transport through the MTMOS-based silicate revealed its favourable property for membranes applications. Namely, the oxygen mass transport rate within this material is over two times higher than oxygen diffusion in aqueous solution.

Generally, all types of CCEs modified with enzymes presented in this thesis are suitable biocathodes for Zn-O_2 primary cells if long-lasting stability is not required. Especially application of CCGE gives the possibility to overcome oxygen mass transfer limitations. In order to extend applicability of these electrodes, further research effort should be put into prolongation of operational- and shelf-live of biocathodes. One possibility could be attained by employment of microbes that are able to continuously renew enzymatic activity on the biocathode surface as is still a challenge.

Another aspect of BFC and biobattery development is the need to increase the efficiency of the electrode process. In the case of biocathodes for O_2 reduction the overpotential is rather difficult to decrease because it depends on redox potential of the prosthetic group what is an

intrinsic property of the enzyme. An increase of ORR current density on biocathode could be attained by increase of enzyme turnover number and its surface concentration. Improvement of the former property is a challenge for genetic engineers and the surface concentration of active sites when the electrode surface would be saturated with properly oriented enzyme molecules is still low because of the huge size of protein molecules. To overcome this problem great effort should be put into isolation of active sites from enzyme and preservation of its activity or the synthesis of such moiety using nature as a template.

17 Bibliography

[1] M. Winter, R.J. Brodd, *What are batteries, fuel cells, and supercapacitors?* Chemical Reviews 104 (2004) 4245-4269.

[2] L. Carrette, *et al.*, *Fuel cells: Principles, types, fuels, and applications.* ChemPhysChem 1 (2000) 162-193.

[3] I. Ivanov, *et al.*, *Recent Advances in Enzymatic Fuel Cells: Experiments and Modeling.* Energies 3 (2010) 803-846.

[4] P. Cinquin, *et al.*, *A Glucose BioFuel Cell Implanted in Rats.* Plos One 5 (2010) e10476.

[5] G. Gun, *et al.*, *Voltammetric Studies of Composite Ceramic Carbon Working Electrodes.* Analytica Chimica Acta 294 (1994) 261-270.

[6] M. Tsionsky, *et al.*, *Sol-Gel-Derived Ceramic-Carbon Composite Electrodes - Introduction and Scope of Applications.* Analytical Chemistry 66 (1994) 1747-1753.

[7] I. Kowaluk, *et al.*, *Li-air batteries: A classic example of limitations owing to solubilities.* Pure and Applied Chemistry 79 (2007) 851-860.

[8] S. Vaddiraju, *et al.*, *Emerging synergy between nanotechnology and implantable biosensors: A review.* Biosensors & Bioelectronics 25 (2010) 1553-1565.

[9] B. Wang, *Recent development of non-platinum catalysts for oxygen reduction reaction.* Journal of Power Sources 152 (2005) 1-15.

[10] B.N. Tarasevich, *et al.*, *Oxygen electrochemistry*, in *Comprehensive treatise of electrochemistry, vol. 7 - Kinetics and mechanisms of electrode processes*, ed. B.E. Conway, (1983), Plenum Press: New York. 301-398.

[11] X.X. Chen, *et al.*, *Electrocatalytic Activity of Spots of Electrodeposited Noble-Metal Catalysts on Carbon Nanotubes Modified Glassy Carbon.* Analytical Chemistry 81 (2009) 7597-7603.

[12] V. Soukharev, *et al.*, *A four-electron O-2-electroreduction biocatalyst superior to platinum and a biofuel cell operating at 0.88 V.* Journal of the American Chemical Society 126 (2004) 8368-8369.

[13] J.H. Wee, K.Y. Lee, *Overview of the effects of rare-earth elements used as additive materials in molten carbonate fuel cell systems.* Journal of Materials Science 41 (2006) 3585-3592.

[14] M.C. Tucker, *Progress in metal-supported solid oxide fuel cells: A review.* Journal of Power Sources 195 (2010) 4570-4582.

[15] J.O. Bockris, A.K.M.S. Huq, *The Mechanism of the Electrolytic Evolution of Oxygen on Platinum.* Proceedings of the Royal Society of London Series a-Mathematical and Physical Sciences 237 (1956) 277-296.
[16] N. Watanabe, M.A.V. Devanathan, *Reversible Oxygen Electrodes.* Journal of the Electrochemical Society 111 (1964) 615-619.
[17] J.P. Hoare, *The Normal Oxygen Potential on Bright Platinum.* Journal of the Electrochemical Society 110 (1963) 1019-1021.
[18] A.C.C. Tseung, H.L. Bevan, *A reversible oxygen electrode.* Journal of Electroanalytical Chemistry 45 (1973) 429-438.
[19] A. Serov, C. Kwak, *Review of non-platinum anode catalysts for DMFC and PEMFC application.* Applied Catalysis B-Environmental 90 (2009) 313-320.
[20] F. Bidault, *et al.*, *Review of gas diffusion cathodes for alkaline fuel cells.* Journal of Power Sources 187 (2009) 39-48.
[21] M.H. Shao, *et al.*, *Superoxide anion is the intermediate in the oxygen reduction reaction on platinum electrodes.* Journal of the American Chemical Society 128 (2006) 7408-7409.
[22] P.W. Atkins, J. De Paula, *Atkins' Physical chemistry*. 8th ed. 2006, Oxford ; New York: Oxford University Press.
[23] Y. Shen, *et al.*, *Detection of Hydrogen Peroxide Produced during Electrochemical Oxygen Reduction Using Scanning Electrochemical Microscopy.* Analytical Chemistry 80 (2008) 750-759.
[24] Z. Chen, *et al.*, *Electrocatalytic activity of nitrogen doped carbon nanotubes with different morphologies for oxygen reduction reaction.* Electrochimica Acta 55 (2010) 4799-4804.
[25] M.O. Davies, *et al.*, *The Oxygen Electrode .1. Isotopic Investigation of Electrode Mechanisms.* Journal of the Electrochemical Society 106 (1959) 56-61.
[26] J.C. Huang, *et al.*, *Oxygen Reduction on Platinum in 85-Percent Ortho-Phosphoric Acid.* Journal of the Electrochemical Society 126 (1979) 786-792.
[27] U.A. Paulus, *et al.*, *Oxygen reduction on a high-surface area Pt/Vulcan carbon catalyst: a thin-film rotating ring-disk electrode study.* Journal of Electroanalytical Chemistry 495 (2001) 134-145.
[28] R.C. Koffi, *et al.*, *Synthesis, characterization and electrocatalytic behaviour of non-alloyed PtCr methanol tolerant nanoelectrocatalysts for the oxygen reduction reaction (ORR).* Electrochimica Acta 50 (2005) 4117-4127.
[29] Y.H. Lin, *et al.*, *Platinum/carbon nanotube nanocomposite synthesized in supercritical fluid as electrocatalysts for low-temperature fuel cells.* Journal of Physical Chemistry B 109 (2005) 14410-14415.
[30] R. Kou, *et al.*, *Enhanced activity and stability of Pt catalysts on functionalized graphene sheets for electrocatalytic oxygen reduction.* Electrochemistry Communications 11 (2009) 954-957.
[31] J. Zhang, *et al.*, *Platinum monolayer electrocatalysts for O-2 reduction: Pt monolayer on Pd(111) and on carbon-supported Pd nanoparticles.* Journal of Physical Chemistry B 108 (2004) 10955-10964.
[32] A.A. Gewirth, M.S. Thorum, *Electroreduction of Dioxygen for Fuel-Cell Applications: Materials and Challenges.* Inorganic Chemistry 49 (2010) 3557-3566.
[33] Y.H. Li, *et al.*, *Oxygen reduction and transportation mechanisms in solid oxide fuel cell cathodes.* Journal of Power Sources 195 (2010) 3345-3358.
[34] V. Neburchilov, *et al.*, *A review on air cathodes for zinc-air fuel cells.* Journal of Power Sources 195 (2010) 1271-1291.
[35] C.J. Zhong, *et al.*, *Nanostructured catalysts in fuel cells.* Nanotechnology 21 (2010) 20.

[36] Y.H. Bing, *et al., Nanostructured Pt-alloy electrocatalysts for PEM fuel cell oxygen reduction reaction.* Chemical Society Reviews 39 (2010) 2184-2202.
[37] J.L. Fernandez, *et al., Thermodynamic guidelines for the design of bimetallic catalysts for oxygen electroreduction and rapid screening by scanning electrochemical microscopy. M-Co (M : Pd, Ag, Au).* Journal of the American Chemical Society 127 (2005) 357-365.
[38] Y. Shen, *et al., Simple preparation method of Pd nanoparticles on an Au electrode and its catalysis for dioxygen reduction.* New Journal of Chemistry 27 (2003) 938-941.
[39] L. Demarconnay, *et al., Electroreduction of dioxygen (ORR) in alkaline medium on Ag/C and Pt/C nanostructured catalysts - effect of the presence of methanol.* Electrochimica Acta 49 (2004) 4513-4521.
[40] I. Yagi, *et al., Electrocatalytic reduction of oxygen to water at Au nanoclusters vacuum-evaporated on boron-doped diamond in acidic solution.* Electrochemistry Communications 6 (2004) 773-779.
[41] M.S. El-Deab, *et al., Oxygen reduction at electrochemically deposited crystallographically oriented Au(100)-like gold nanoparticles.* Electrochemistry Communications 7 (2005) 29-34.
[42] Y.H. Lin, *et al., Electrocatalytic reactivity for oxygen reduction of palladium-modified carbon nanotubes synthesized in supercritical fluid.* Electrochemistry Communications 7 (2005) 267-274.
[43] M.H. Shao, *et al., Pd-Fe nanoparticles as electrocatalysts for oxygen reduction.* Journal of the American Chemical Society 128 (2006) 3526-3527.
[44] K.A. Kurak, A.B. Anderson, *Nitrogen-Treated Graphite and Oxygen Electroreduction on Pyridinic Edge Sites.* Journal of Physical Chemistry C 113 (2009) 6730-6734.
[45] I. Kruusenberg, *et al., Oxygen reduction on carbon nanomaterial-modified glassy carbon electrodes in alkaline solution.* Journal of Solid State Electrochemistry 14 (2010) 1269-1277.
[46] E. Yeager, *Electrocatalysts for O_2 reduction.* Electrochim. Acta. 29 (1984) 1527-1537.
[47] I. Morcos, E. Yeager, *Kinetic Studies of Oxygen-Peroxide Couple on Pyrolytic Graphite.* Electrochimica Acta 15 (1970) 953-&.
[48] B. Lovrecek, *et al., The electrochemical oxygen reduction on the graphite electrode.* Electrochimica Acta 28 (1983) 685-690.
[49] V.A. Garten, D.E. Weiss, *The Quinone Hydroquinone Character of Activated Carbon and Carbon Black.* Australian Journal of Chemistry 8 (1955) 68-95.
[50] Z.W. Zhang, *et al., Oxygen Reduction on Graphite-Electrodes Modified with Quinones in Alkaline-Solution.* Journal of the Electrochemical Society 131 (1984) C112-C112.
[51] Z.W. Zhang, *et al., Electrode-Kinetics of the Oxygen Peroxide Couple on Glassy-Carbon in Alkaline-Solution.* Journal of the Electrochemical Society 130 (1983) C333-C333.
[52] L.H. Tang, *et al., Preparation, Structure, and Electrochemical Properties of Reduced Graphene Sheet Films.* Advanced Functional Materials 19 (2009) 2782-2789.
[53] C.E. Banks, *et al., Electrocatalysis at graphite and carbon nanotube modified electrodes: edge-plane sites and tube ends are the reactive sites.* Chemical Communications (2005) 829-841.
[54] K.S. Novoselov, *et al., Electric field effect in atomically thin carbon films.* Science 306 (2004) 666-669.
[55] C. Berger, *et al., Electronic confinement and coherence in patterned epitaxial graphene.* Science 312 (2006) 1191-1196.
[56] S. Stankovich, *et al., Synthesis of graphene-based nanosheets via chemical reduction of exfoliated graphite oxide.* Carbon 45 (2007) 1558-1565.

[57] F.H. Li, *et al., The synthesis of perylene-coated graphene sheets decorated with Au nanoparticles and its electrocatalysis toward oxygen reduction.* Journal of Materials Chemistry 19 (2009) 4022-4025.

[58] J.P. Collman, *et al., Electrode Catalysis of the 4-Electron Reduction of Oxygen to Water by Dicobalt Face-to-Face Porphyrins.* Journal of the American Chemical Society 102 (1980) 6027-6036.

[59] J.P. Collman, *et al., Effect of electron availability on selectivity of O-2 reduction by synthetic monometallic Fe porphyrins.* Inorganic Chemistry 42 (2003) 4807-4809.

[60] K. Arihara, *et al., Electrocatalytic reduction of oxygen in a novel catalytic system with cobalt phthalocyanines and manganese oxide.* Journal of the Electrochemical Society 151 (2004) A2047-A2052.

[61] W. Chen, *et al., Electrocatalytic Four-Electron Reduction of Dioxygen by Electrochemically Deposited Poly{[meso-tetrakis(2-thienyl)porphyrinato]cobalt(II)}.* Journal of Physical Chemistry C 114 (2010) 8633-8638.

[62] R. Zhang, *et al., Zeolite-encapsulated M(Co, Fe, Mn)(SALEN) complexes modified glassy carbon electrodes and their application in oxygen reduction.* Journal of Electroanalytical Chemistry 643 (2010) 31-38.

[63] S.Q. Liu, *et al., meso-tetrakis(4-N-benzylpyridyl)porphyrin and its supramolecular complexes formed with anionic metal-oxo cluster: spectroscopy and electrocatalytic reduction of dioxygen.* Inorganica Chimica Acta 306 (2000) 87-93.

[64] S. Fukuzumi, *et al., Mechanism of four-electron reduction of dioxygen to water by ferrocene derivatives in the presence of perchloric acid in benzonitrile, catalyzed by cofacial dicobalt porphyrins.* Journal of the American Chemical Society 126 (2004) 10441-10449.

[65] S.L. Gojkovic, *et al., Heat-treated iron(III) tetramethoxyphenyl porphyrin chloride supported on high-area carbon as an electrocatalyst for oxygen reduction - Part II. Kinetics of oxygen reduction.* Journal of Electroanalytical Chemistry 462 (1999) 63-72.

[66] S.V. Mentus, *Oxygen reduction on anodically formed titanium dioxide.* Electrochimica Acta 50 (2004) 27-32.

[67] S.B. Adler, *Mechanism and kinetics of oxygen reduction on porous La1-xSrxCoO3-delta electrodes.* Solid State Ionics 111 (1998) 125-134.

[68] H.Y. Tu, *et al., Ln(0.4)Sr(0.6)Co(0.8)Fe(0.2)O(3-delta) (Ln = La, Pr, Nd, Sm, Gd) for the electrode in solid oxide fuel cells.* Solid State Ionics 117 (1999) 277-281.

[69] S.P. Jiang, *A comparison of O-2 reduction reactions on porous (La,Sr)MnO3 and (La,Sr)(Co,Fe)O-3 electrodes.* Solid State Ionics 146 (2002) 1-22.

[70] Z.P. Shao, S.M. Haile, *A high-performance cathode for the next generation of solid-oxide fuel cells.* Nature 431 (2004) 170-173.

[71] R. Bilewicz, M. Opallo, *Biocathodes for Dioxygen Reduction in Biofuel Cells*, in *Fuel Cell Science: Theory, Fundamentals, and Biocatalysis*, ed. A. Wieckowski, J. Norskov, (2010), John Wiley & Sons, Inc. 169-214.

[72] S. Tsujimura, *et al., Diffusion-Controlled Oxygen Reduction on Multi-CopperOxidase-Adsorbed Carbon Aerogel Electrodeswithout Mediator.* Fuel Cells 7 (2007) 463-469.

[73] A. Christenson, *et al., Direct electron transfer between ligninolytic redox enzymes and electrodes.* Electroanalysis 16 (2004) 1074-1092.

[74] J. Turkova, *Oriented immobilization of biologically active proteins as a tool for revealing protein interactions and function.* Journal of Chromatography B 722 (1999) 11-31.

[75] W. Song, H. Chen, *Protein adsorption on materials surfaces with nano-topography.* Chinese Science Bulletin 52 (2007) 3169-3173.

[76] H.A.O. Hill, N.J. Walton, *Investigation of Some Intermolecular Electron-Transfer Reactions of Cytochrome-C by Electrochemical Methods.* Journal of the American Chemical Society 104 (1982) 6515-6519.

[77] E. Katz, *et al., A non-compartmentalized glucose vertical bar O-2 biofuel cell by bioengineered electrode surfaces.* Journal of Electroanalytical Chemistry 479 (1999) 64-68.

[78] M.K. Wang, *et al., Direct electrochemistry of microperoxidase 11 using carbon nanotube modified electrodes.* Journal of Electroanalytical Chemistry 578 (2005) 121-127.

[79] J. Rogalski, A. Leonowicz, *Laccase*, in *Concise encyclopedia of bioresource technology*, ed. A. Pandey, (2004), Food Products Press: New York. 533-542.

[80] M.R. Tarasevich, *et al., Electrocatalysis of Cathodic Molecular-Oxygen Reduction with Bio-Polymers Enzymes and Their Models.* Journal of Electroanalytical Chemistry 206 (1986) 217-227.

[81] G.T.R. Palmore, H.H. Kim, *Electro-enzymatic reduction of dioxygen to water in the cathode compartment of a biofuel cell.* Journal of Electroanalytical Chemistry 464 (1999) 110-117.

[82] P. Baldrian, *Fungal laccases - occurrence and properties.* Fems Microbiology Reviews 30 (2006) 215-242.

[83] J.A. Cracknell, *et al., Enzymes as working or inspirational electrocatalysts for fuel cells and electrolysis.* Chemical Reviews 108 (2008) 2439-2461.

[84] H.P. Call, I. Mucke, *History, overview and applications of mediated lignolytic systems, especially laccase-mediator-systems (Lignozym(R)-process).* Journal of Biotechnology 53 (1997) 163-202.

[85] S. Shleev, *et al., Electrochemical redox transformations of T1 and T2 copper sites in native Trametes hirsuta laccase at gold electrode.* Biochemical Journal 385 (2005) 745-754.

[86] Reinhamm.Br, T.I. Vanngard, *Electron-Accepting Sites in Rhus-Vernicifera Laccase as Studied by Anaerobic Oxidation-Reduction Titrations.* European Journal of Biochemistry 18 (1971) 463-&.

[87] P. Schneider, *et al., Characterization of a Coprinus cinereus laccase.* Enzyme and Microbial Technology 25 (1999) 502-508.

[88] A. Klonowska, *et al., Characterization of a low redox potential laccase from the basidiomycete C30.* European Journal of Biochemistry 269 (2002) 6119-6125.

[89] S. Shleev, *et al., Comparative spectroelectrochemical studies of lyophilized and nonlyophilized laccases from Cerrena unicolor basidiomycete.* Electroanalysis 19 (2007) 1039-1047.

[90] E. Nazaruk, *et al., Properties of native and hydrophobic laccases immobilized in the liquid-crystalline cubic phase on electrodes.* Journal of Biological Inorganic Chemistry 12 (2007) 335-344.

[91] K. Stolarczyk, *et al., Nanostructured carbon electrodes for laccase-catalyzed oxygen reduction without added mediators.* Electrochimica Acta 53 (2008) 3983-3990.

[92] A.I. Yaropolov, *et al., Laccase - Properties, Catalytic Mechanism, and Applicability.* Applied Biochemistry and Biotechnology 49 (1994) 257-280.

[93] J.W. Gallaway, S.A.C. Barton, *Kinetics of redox polymer-mediated enzyme electrodes.* Journal of the American Chemical Society 130 (2008) 8527-8536.

[94] S. Tsujimura, *et al., Bioelectrocatalytic reduction of dioxygen to water at neutral pH using bilirubin oxidase as an enzyme and 2,20-azinobis*
(3-ethylbenzothiazolin-6-sulfonate) as an electron transfer mediator. Journal of Electroanalytical Chemistry 496 (2001) 69-75.

[95] S. Tsujimura, *et al., Bioelectrocatalysis-based dihydrogen/dioxygen fuel cell operating at physiological pH.* Physical Chemistry Chemical Physics 3 (2001) 1331-1335.

[96] A. Heller, *Miniature biofuel cells.* Physical Chemistry Chemical Physics 6 (2004) 209-216.
[97] N. Mano, *et al.*, *An oxygen cathode operating in a physiological solution.* Journal of the American Chemical Society 124 (2002) 6480-6486.
[98] E.I. Solomon, *et al.*, *Multicopper Oxidases and Oxygenases.* Chemical Reviews 96 (1996) 2563-2605.
[99] P. Ramirez, *et al.*, *Direct electron transfer from graphite and functionalized gold electrodes to T1 and T2/T3 copper centers of bilirubin oxidase.* Biochimica Et Biophysica Acta-Bioenergetics 1777 (2008) 1364-1369.
[100] A. Shimizu, *et al.*, *Myrothecium verrucaria bilirubin oxidase and its mutants for potential copper ligands.* Biochemistry 38 (1999) 3034-3042.
[101] R. Kontani, *et al.*, *Air diffusion biocathode with CueO as electrocatalyst adsorbed on carbon particle-modified electrodes.* Bioelectrochemistry 76 (2009) 10-13.
[102] Y. Miura, *et al.*, *Direct Electrochemistry of CueO and Its Mutants at Residues to and Near Type I Cu for Oxygen-Reducing Biocathode.* Fuel Cells 9 (2009) 70-78.
[103] A. Heller, *Potentially implantable miniature batteries.* Analytical and Bioanalytical Chemistry 385 (2006) 469-473.
[104] S.C. Barton, *et al.*, *The "wired" laccase cathode: High current density electroreduction of O-2 to water at+0.7 V (NHE) at pH 5.* Journal of the American Chemical Society 123 (2001) 5802-5803.
[105] G. Merle, *et al.*, *Electrode biomaterials based on immobilized laccase. Application for enzymatic reduction of dioxygen.* Materials Science & Engineering C-Biomimetic and Supramolecular Systems 28 (2008) 932-938.
[106] F. Mao, *et al.*, *Long tethers binding redox centers to polymer backbones enhance electron transport in enzyme "wiring" hydrogels.* Journal of the American Chemical Society 125 (2003) 4951-4957.
[107] R. Bourbonnais, M.G. Paice, *Oxidation of Nonphenolic Substrates - an Expanded Role for Laccase in Lignin Biodegradation.* Febs Letters 267 (1990) 99-102.
[108] D. Quan, *et al.*, *Characterization of an amperometric laccase electrode covalently immobilized on platinum surface.* Journal of Electroanalytical Chemistry 561 (2004) 181-189.
[109] D. Ivnitski, *et al.*, *Surface characterization and direct electrochemistry of redox copper centers of bilirubin oxidase from fungi Myrothecium verrucaria.* Bioelectrochemistry 74 (2008) 101-110.
[110] L. Brunel, *et al.*, *Oxygen transport through laccase biocathodes for a membrane-less glucose/O2 biofuel cell.* Electrochemistry Communications 9 (2007) 331-336.
[111] J.H. Thomas, *et al.*, *Characterization of ABTS at a polymer-modified electrode.* Electroanalysis 16 (2004) 547-555.
[112] K. Szot, *et al.*, *Bioelectrocatalytic dioxygen reduction at hybrid silicate-polyallylamine film with encapsulated laccase.* Journal of Electroanalytical Chemistry 612 (2008) 1-8.
[113] E. Nazaruk, *et al.*, *Enzymatic biofuel cell based on electrodes modified with lipid liquid-crystalline cubic phases.* Journal of Power Sources 183 (2008) 533-538.
[114] K. Karnicka, *et al.*, *ABTS-modified multiwalled carbon nanotubes as an effective mediating system for bioelectrocatalytic reduction of oxygen.* Analytical Chemistry 80 (2008) 7643-7648.
[115] E. Nazaruk, *et al.*, *Composite Bioelectrodes Based on Lipidic Cubic Phase with Carbon Nanotube Network.* Electroanalysis 21 (2009) 507-511.
[116] M. Jönsson, *et al.*, *Adsorption of 2,2'-Azino-Bis(3-ethylbenzothiazoline-6-sulfonate) on Multiwalled Carbon Nanotubes-Silicate Film: Application to Bioelectrocatalytic Dioxygen Reduction.* Journal of Nanoscience and Nanotechnology 9 (2009) 2346–2352.

[117] J. Pinson, F. Podvorica, *Attachment of organic layers to conductive or semiconductive surfaces by reduction of diazonium salts.* Chemical Society Reviews 34 (2005) 429-439.
[118] S. Shleev, *et al.*, *Direct heterogeneous electron transfer reactions of Trametes hirsuta Laccase at bare and thiol-modified gold electrodes.* Electroanalysis 18 (2006) 1901-1908.
[119] G. Gupta, *et al.*, *Bioelectrocatalysis of oxygen reduction reaction by laccase on gold electrodes.* Electroanalysis 16 (2004) 1182-1185.
[120] S. Tsujimura, *et al.*, *Kinetic study of direct bioelectrocatalysis of dioxygen reduction with bilirubin oxidase at carbon electrodes.* Electrochemistry 72 (2004) 437-439.
[121] S. Shleev, *et al.*, *Direct electron transfer reactions of laccases from different origins on carbon electrodes.* Bioelectrochemistry 67 (2005) 115-124.
[122] J. Lim, *et al.*, *Direct electron transfer in nanostructured sol-gel electrodes containing bilirubin oxidase.* Physical Chemistry Chemical Physics 9 (2007) 1809-1814.
[123] V. Coman, *et al.*, *A Direct Electron Transfer-Based Glucose/Oxygen Biofuel Cell Operating in Human Serum.* Fuel Cells 10 (2010) 9-16.
[124] K. Stolarczyk, *et al.*, *Mediatorless catalytic oxygen reduction at boron-doped diamond electrodes.* Electrochemistry Communications 9 (2007) 115-118.
[125] S. Shleev, *et al.*, *Direct electron transfer between copper-containing proteins and electrodes.* Biosensors & Bioelectronics 20 (2005) 2517-2554.
[126] V. Coman, *et al.*, *A membrane-, mediator-, cofactor-less glucose/oxygen biofuel cell.* Physical Chemistry Chemical Physics 10 (2008) 6093-6096.
[127] C.F. Blanford, *et al.*, *A stable electrode for high-potential, electrocatalytic O-2 reduction based on rational attachment of a blue copper oxidase to a graphite surface.* Chemical Communications (2007) 1710-1712.
[128] C.F. Blanford, *et al.*, *Efficient electrocatalytic oxygen reduction by the 'blue' copper oxidase, laccase, directly attached to chemically modified carbons.* Faraday Discussions 140 (2008) 319-335.
[129] S. Tsujimura, *et al.*, *CueO-immobilized porous carbon electrode exhibiting improved performance of electrochemical reduction of dioxygen to water.* Electrochimica Acta 53 (2008) 5716-5720.
[130] A. Krueger, *The Structure and Properties of Carbon Nanotubes*, in *Strained hydrocarbons : beyond the van't Hoff and Le Bel hypothesis*, ed. H. Dodziuk, (2009), Wiley-VCH: Weinheim. 335.
[131] M. Jonsson-Niedziolka, *et al.*, *Pyrene sulfonate functionalised single-walled carbon nanotubes for mediatorless dioxygen bioelectrocatalysis.* Electrochemistry Communications 11 (2009) 1042-1044.
[132] G. Gobel, F. Lisdat, *Organic interlayers for oxygen reducing electrodes based on bilirubin oxidase and MWCNT modified gold.* Electrochemistry Communications 10 (2008) 1691-1694.
[133] K. Schubert, *et al.*, *Bilirubin oxidase bound to multi-walled carbon nanotube-modified gold.* Electrochimica Acta 54 (2009) 3033-3038.
[134] L. Deng, *et al.*, *Multilayer structured carbon nanotubes/poly-L-lysine/laccase composite cathode for glucose/O-2 biofuel cell.* Electrochemistry Communications 10 (2008) 1012-1015.
[135] Y.M. Yan, *et al.*, *An Ethanol/O-2 Biofuel Cell Based on an Electropolymerized Bilirubin Oxidase/Pt Nanoparticle Bioelectrocatalytic O-2-Reduction Cathode.* Advanced Materials 21 (2009) 4275.
[136] A. Zebda, *et al.*, *Electrochemical performance of a glucose/oxygen microfluidic biofuel cell.* Journal of Power Sources 193 (2009) 602-606.

[137] X.H. Yang, *et al., Covalent immobilization of an enzyme (glucose oxidase) onto a carbon sol-gel silicate composite surface as a biosensing platform.* Analytica Chimica Acta 478 (2003) 67-75.
[138] U. Hanefeld, *et al., Understanding enzyme immobilisation.* Chemical Society Reviews 38 (2009) 453-468.
[139] R.C. Rodrigues, *et al., Immobilization-stabilization of the lipase from Thermomyces lanuginosus: Critical role of chemical amination.* Process Biochemistry 44 (2009) 963-968.
[140] M.M.F. Choi, *Progress in enzyme-based biosensors using optical transducers.* Microchimica Acta 148 (2004) 107-132.
[141] J.J. Gooding, D.B. Hibbert, *The application of alkanethiol self-assembled monolayers to enzyme electrodes.* Trac-Trends in Analytical Chemistry 18 (1999) 525-533.
[142] O. Yehezkeli, *et al., Switchable photochemical/electrochemical wiring of glucose oxidase with electrodes.* Analyst 135 (2010) 474-476.
[143] O. Rudiger, *et al., Enzymatic Anodes for Hydrogen Fuel Cells based on Covalent Attachment of Ni-Fe Hydrogenases and Direct Electron Transfer to SAM-Modified Gold Electrodes.* Electroanalysis 22 (2010) 776-783.
[144] Y.Z. Li, *et al., Characterization of Thiol Self-Assembled Films by Laser Desorption Fourier-Transform Mass-Spectrometry.* Journal of the American Chemical Society 114 (1992) 2428-2432.
[145] W.R. Everett, *et al., Potential-Dependent Stability of Self-Assembled Organothiols on Gold Electrodes in Methylene-Chloride.* Analytical Chemistry 67 (1995) 292-298.
[146] J.J. Gooding, *et al., Platinum-catalyzed enzyme electrodes immobilized on gold using self-assembled layers.* Analytical Chemistry 70 (1998) 2396-2402.
[147] M.A. McRipley, R.A. Linsenmeier, *Fabrication of a mediated glucose oxidase recessed microelectrode for the amperometric determination of glucose.* Journal of Electroanalytical Chemistry 414 (1996) 235-246.
[148] J. Hodak, *et al., Layer-by-layer self-assembly of glucose oxidase with a poly(allylamine)ferrocene redox mediator.* Langmuir 13 (1997) 2708-2716.
[149] E. Katz, *et al., Magnetic field effects on bioelectrocatalytic reactions of surface-confined enzyme systems: Enhanced performance of biofuel cells.* Journal of the American Chemical Society 127 (2005) 3979-3988.
[150] Z.G. Wang, *et al., Enzyme immobilization on electrospun polymer nanofibers: An overview.* Journal of Molecular Catalysis B-Enzymatic 56 (2009) 189-195.
[151] J.F. Fei, *et al., A biopolymer composite that catalyzes the reduction of oxygen to water.* Chemistry of Materials 19 (2007) 1565-1570.
[152] J.W. Gallaway, S.A.C. Barton, *Effect of redox polymer synthesis on the performance of a mediated laccase oxygen cathode.* Journal of Electroanalytical Chemistry 626 (2009) 149-155.
[153] D. Kyprianou, *et al., New reactive polymer for protein immobilisation on sensor surfaces.* Biosensors & Bioelectronics 24 (2009) 1365-1371.
[154] C. Lau, *et al., Development of a Chitosan Scaffold Electrode for Fuel Cell Applications.* Electroanalysis 22 (2010) 793-798.
[155] B. Krajewska, *Application of chitin- and chitosan-based materials for enzyme immobilizations: a review.* Enzyme and Microbial Technology 35 (2004) 126-139.
[156] D.Y. Nadargi, *et al., Synthesis and characterization of transparent hydrophobic silica thin films by single step sol-gel process and dip coating.* Journal of Alloys and Compounds 496 (2010) 436-441.
[157] O. Tammisola, *et al., Spin coating of Blu-Ray disks: modeling, experiments, limitations, and manipulation.* Journal of Coatings Technology and Research 7 (2010) 315-323.

[158] I. Zawisza, *et al.*, *Electrocatalytic reduction of dioxygen by redox mediator and laccase immobilized in silicate thin film.* Journal of Electroanalytical Chemistry 588 (2006) 244-252.
[159] S. Yang, *et al.*, *Simple Approach for Efficient Encapsulation of Enzyme in Silica Matrix with Retained Bioactivity.* Analytical Chemistry 81 (2009) 3478-3484.
[160] H. Frenkel-Mullerad, D. Avnir, *Sol-gel materials as efficient enzyme protectors: Preserving the activity of phosphatases under extreme pH conditions.* Journal of the American Chemical Society 127 (2005) 8077-8081.
[161] Y.K. Choi, *et al.*, *A hybrid biofuel cell based on electrooxidation of glucose using ultra-small silicon nanoparticles.* Biosensors & Bioelectronics 24 (2009) 3103-3107.
[162] J.J. Fornero, *et al.*, *Electric Power Generation from Municipal, Food, and Animal Wastewaters Using Microbial Fuel Cells.* Electroanalysis 22 (2010) 832-843.
[163] S.C. Barton, *et al.*, *Enzymatic biofuel cells for Implantable and microscale devices.* Chemical Reviews 104 (2004) 4867-4886.
[164] E.H. Yu, K. Scott, *Enzymatic Biofuel Cells-Fabrication of Enzyme Electrodes.* Energies 3 (2010) 23-42.
[165] D. Sokic-Lazic, *et al.*, *Oxidation of Biofuels: Fuel Diversity and Effectiveness of Fuel Oxidation through Multiple Enzyme Cascades.* Electroanalysis 22 (2010) 757-764.
[166] W. Gellett, *et al.*, *Biofuel Cells for Portable Power.* Electroanalysis 22 (2010) 727-731.
[167] I. Willner, *et al.*, *Integrated Enzyme-Based Biofuel Cells-A Review.* Fuel Cells 9 (2009) 7-24.
[168] A.K. Sarma, *et al.*, *Recent advances in material science for developing enzyme electrodes.* Biosensors & Bioelectronics 24 (2009) 2313-2322.
[169] M.J. Moehlenbrock, S.D. Minteer, *Extended lifetime biofuel cells.* Chemical Society Reviews 37 (2008) 1188-1196.
[170] S. Kerzenmacher, *et al.*, *Energy harvesting by implantable abiotically catalyzed glucose fuel cells.* Journal of Power Sources 182 (2008) 1-17.
[171] M.J. Cooney, *et al.*, *Enzyme catalysed biofuel cells.* Energy & Environmental Science 1 (2008) 320-337.
[172] S.D. Minteer, *et al.*, *Enzyme-based biofuel cells.* Current Opinion in Biotechnology 18 (2007) 228-234.
[173] Z.W. Du, *et al.*, *A state of the art review on microbial fuel cells: A promising technology for wastewater treatment and bioenergy.* Biotechnology Advances 25 (2007) 464-482.
[174] F. Davis, S.P.J. Higson, *Biofuel cells - Recent advances and applications.* Biosensors & Bioelectronics 22 (2007) 1224-1235.
[175] J. Kim, *et al.*, *Challenges in biocatalysis for enzyme-based biofuel cells.* Biotechnology Advances 24 (2006) 296-308.
[176] R.A. Bullen, *et al.*, *Biofuel cells and their development.* Biosensors & Bioelectronics 21 (2006) 2015-2045.
[177] A. Ramanavicius, *et al.*, *Biofuel cell based on direct bioelectrocatalysis.* Biosensors & Bioelectronics 20 (2005) 1962-1967.
[178] H. Sakai, *et al.*, *A high-power glucose/oxygen biofuel cell operating under quiescent conditions.* Energy & Environmental Science 2 (2009) 133-138.
[179] Y. Kamitaka, *et al.*, *Fructose/dioxygen biofuel cell based on direct electron transfer-type bioelectrocatalysis.* Physical Chemistry Chemical Physics 9 (2007) 1793-1801.
[180] L. Stoica, *et al.*, *Membrane-Less Biofuel Cell Based on Cellobiose Dehydrogenase (Anode)/Laccase (Cathode) Wired via Specific Os-Redox Polymers.* Fuel Cells 9 (2009) 53-62.
[181] G.T.R. Palmore, *et al.*, *A methanol/dioxygen biofuel cell that uses NAD(+)-dependent dehydrogenases as catalysts: application of an electro-enzymatic method to*

regenerate nicotinamide adenine dinucleotide at low overpotentials. Journal of Electroanalytical Chemistry 443 (1998) 155-161.

[182] R.L. Arechederra, S.D. Minteer, *Complete Oxidation of Glycerol in an Enzymatic Biofuel Cell.* Fuel Cells 9 (2009) 63-69.

[183] M. Burchardt, G. Wittstock, *Kinetic studies of glucose oxidase in polyelectrolyte multilayer films by means of scanning electrochemical microscopy (SECM).* Bioelectrochemistry 72 (2008) 66-76.

[184] F. Tasca, *et al.*, *Direct electron transfer at cellobiose dehydrogenase modified anodes for biofuel cells.* Journal of Physical Chemistry C 112 (2008) 9956-9961.

[185] T. Miyake, *et al.*, *Biofuel cell anode: NAD(+)/glucose dehydrogenase-coimmobilized ketjenblack electrode.* Chemical Physics Letters 480 (2009) 123-126.

[186] Y. Kamitaka, *et al.*, *High current density bioelectrolysis of D-fructose at fructose dehydrogenase-adsorbed and Ketjen black-modified electrodes without a mediator.* Chemistry Letters 36 (2007) 218-219.

[187] P.K. Addo, *et al.*, *Evaluating Enzyme Cascades for Methanol/Air Biofuel Cells Based on NAD(+)-Dependent Enzymes.* Electroanalysis 22 (2010) 807-812.

[188] N.L. Akers, *et al.*, *Development of alcohol/O-2 biofuel cells using salt-extracted tetrabutylammonium bromide/Nafion membranes to immobilize dehydrogenase enzymes.* Electrochimica Acta 50 (2005) 2521-2525.

[189] P.C. Pandey, *et al.*, *Studies on glucose biosensors based on nonmediated and mediated electrochemical oxidation of reduced glucose oxidase encapsulated within organically modified sol-gel glasses.* Electroanalysis 11 (1999) 1251-1258.

[190] T. Kuwahara, *et al.*, *Properties of the enzyme electrode fabricated with a film of polythiophene derivative and its application to a glucose fuel cell.* Journal of Applied Polymer Science 104 (2007) 2947-2953.

[191] I. Willner, *et al.*, *Biofuel cell based on glucose oxidase and microperoxidase-11 monolayer-fundionalized electrodes.* Journal of the Chemical Society-Perkin Transactions 2 (1998) 1817-1822.

[192] J. Kim, *et al.*, *Polypyrrole nanowire-based enzymatic biofuel cells.* Biosensors & Bioelectronics 25 (2009) 350-355.

[193] N. Mano, A. Heller, *A miniature membraneless biofuel cell operating at 0.36 V under physiological conditions.* Journal of the Electrochemical Society 150 (2003) A1136-A1138.

[194] N. Mano, *et al.*, *Characteristics of a miniature compartment-less glucose-O-2 biofuel cell and its operation in a living plant.* Journal of the American Chemical Society 125 (2003) 6588-6594.

[195] N. Mano, *et al.*, *A miniature biofuel cell operating at 0.78 V.* Chemical Communications (2003) 518-519.

[196] Y. Liu, S.J. Dong, *A biofuel cell harvesting energy from glucose-air and fruit juice-air.* Biosensors & Bioelectronics 23 (2007) 593-597.

[197] S.C. Wang, *et al.*, *Membrane-less and mediator-free enzymatic biofuel cell using carbon nanotube/porous silicon electrodes.* Electrochemistry Communications 11 (2009) 34-37.

[198] O. Courjean, *et al.*, *Deglycosylation of Glucose Oxidase for Direct and Efficient Glucose Electrooxidation on a Glassy Carbon Electrode.* Angewandte Chemie-International Edition 48 (2009) 5897-5899.

[199] K.G. Lim, G.T.R. Palmore, *Microfluidic biofuel cells: The influence of electrode diffusion layer on performance.* Biosensors & Bioelectronics 22 (2007) 941-947.

[200] W. Shin, *et al.*, *Ionic conduction in Zn-3(PO4)(2)(.)4H(2)O enables efficient discharge of the zinc anode in serum.* Journal of the American Chemical Society 127 (2005) 14590-14591.

[201] M. Smolander, *et al.*, *Development of a printable laccase-based biocathode for fuel cell applications.* Enzyme and Microbial Technology 43 (2008) 93-102.
[202] K. Szot, *et al.*, *Hydrophilic carbon nanoparticle-laccase thin film electrode for mediatorless dioxygen reduction SECM activity mapping and application in zinc-dioxygen battery.* Electrochimica Acta 54 (2009) 4620-4625.
[203] A. Lazarus, *et al.*, *Reduction in energy pacing thresholds by overlapping biphasic stimulation versus conventional bipolar pacing.* Pace-Pacing and Clinical Electrophysiology 21 (1998) 2166-2170.
[204] A.J. Bard, L.R. Faulkner, *Electrochemical methods : fundamentals and applications*. 2nd ed. 2001, New York: Wiley.
[205] R. Adams, *Carbon Paste Electrodes.* Analytical Chemistry 30 (1958) 1576.
[206] L. Rabinovich, O. Lev, *Sol-gel derived composite ceramic carbon electrodes.* Electroanalysis 13 (2001) 265-275.
[207] C.J. Brinker, G.W. Scherer, *Sol-gel science : the physics and chemistry of sol-gel processing*. 1990, Boston: Academic Press.
[208] A.C. Pierre, *Introduction to sol-gel processing*. The Kluwer international series in sol-gel processing. 1998, Boston: Kluwer Academic Publishers.
[209] A. Walcarius, M.M. Collinson, *Analytical Chemistry with Silica Sol-Gels: Traditional Routes to New Materials for Chemical Analysis.* Annual Review of Analytical Chemistry 2 (2009) 121-143.
[210] L.L. Hench, J.K. West, *The Sol-Gel Process.* Chemical Reviews 90 (1990) 33-72.
[211] C.T. Kresge, *et al.*, *Ordered Mesoporous Molecular-Sieves Synthesized by a Liquid-Crystal Template Mechanism.* Nature 359 (1992) 710-712.
[212] Y.N. Xia, *et al.*, *Monodispersed colloidal spheres: Old materials with new applications.* Advanced Materials 12 (2000) 693-713.
[213] J.Y. Wen, G.L. Wilkes, *Organic/inorganic hybrid network materials by the sol-gel approach.* Chemistry of Materials 8 (1996) 1667-1681.
[214] A. Lesniewski, *et al.*, *Carbon ceramic nanoparticulate film electrode prepared from oppositely charged particles by layer-by-layer approach.* Electrochemistry Communications 12 (2010) 83-85.
[215] J. Wang, *et al.*, *Screen-printable sol-gel enzyme-containing carbon inks.* Analytical Chemistry 68 (1996) 2705-2708.
[216] M.D.M. Cordero-Rando, *et al.*, *The Sonogel-Carbon electrode as a sol-gel graphite-based electrode.* Analytical Chemistry 74 (2002) 2423-2427.
[217] A. Abbaspour, A. Ghaffarinejad, *Method for Preparation of a Sol-Gel-Derived Carbon Ceramic Electrode Using Microwave Irradiation.* Analytical Chemistry 81 (2009) 3660-3664.
[218] A.J. Downard, *Electrochemically assisted covalent modification of carbon electrodes.* Electroanalysis 12 (2000) 1085-1096.
[219] G. Shul, *et al.*, *Liquid-liquid interfacial processes at hydrophobic silica carbon composite electrodes: ion transfer at water-nitrobenzene, water-o-nitrophenyloctylether, and at water-o-nitrophenylphenylether interfaces.* Electrochimica Acta 50 (2005) 2315-2322.
[220] E. Rozniecka, *et al.*, *Electroactive ceramic carbon electrode modified with ionic liquid.* Electrochemistry Communications 7 (2005) 299-304.
[221] S. Sampath, O. Lev, *Inert metal-modified, composite ceramic-carbon, amperometric biosensors: Renewable, controlled reactive layer.* Analytical Chemistry 68 (1996) 2015-2021.
[222] L. Rabinovich, *et al.*, *Naphthoquinone-silicate based gas electrodes: chemical-electrochemical mode of operation.* Journal of Electroanalytical Chemistry 504 (2001) 146-159.

[223] T. Rohani, M.A. Taher, *Preparation of a carbon ceramic electrode modified by 4-(2-pyridylazo)-resorcinol for determination of trace amounts of silver.* Talanta 80 1827-1831.
[224] C.X. Lei, *et al.*, *Amperometric immunosensor for probing complement III (C-3) based on immobilizing C-3 antibody to a nano-Au monolayer supported by sol-gel-derived carbon ceramic electrode.* Analytica Chimica Acta 513 (2004) 379-384.
[225] L. Rabinovich, *et al.*, *Fuel-cell type ceramic-carbon oxygen sensors.* Journal of Sol-Gel Science and Technology 8 (1997) 1077-1081.
[226] J.I. Eastcott, E.B. Easton, *Electrochemical studies of ceramic carbon electrodes for fuel cell systems: A catalyst layer without sulfonic acid groups.* Electrochimica Acta 54 (2009) 3460-3466.
[227] H.J. Chen, S.J. Dong, *Direct electrochemistry and electrocatalysis of horseradish peroxidase immobilized in sol-gel-derived ceramic-carbon nanotube nanocomposite film.* Biosensors & Bioelectronics 22 (2007) 1811-1815.
[228] C.X. Lei, *et al.*, *An amperometric hydrogen peroxide biosensor based on immobilizing horseradish peroxidase to a nano-Au monolayer supported by sol-gel derived carbon ceramic electrode.* Bioelectrochemistry 65 (2004) 33-39.
[229] L.D. Zhu, *et al.*, *Sol-gel derived carbon nanotubes ceramic composite electrodes for electrochemical sensing.* Sensors and Actuators B-Chemical 125 (2007) 254-261.
[230] A. Salimi, *et al.*, *Simultaneous determination of ascorbic acid, uric acid and neurotransmitters with a carbon ceramic electrode prepared by sol-gel technique.* Talanta 70 (2006) 823-832.
[231] Q.L. Sheng, *et al.*, *Sol-gel derived terbium hexacyanoferrate modified carbon ceramic electrode: Electrochemical behavior and its electrocatalytical oxidation of ascorbic acid.* Journal of Electroanalytical Chemistry 606 (2007) 39-46.
[232] P. Wang, *et al.*, *Fabrication and electrochemical behavior of a sol-gel-derived carbon ceramic composite electrode entrapping 2 : 18-molybdodiphosphate.* Journal of Non-Crystalline Solids 277 (2000) 22-29.
[233] A. Salimi, *et al.*, *Renewable surface sol-gel derived carbon ceramic electrode modified with copper complex and its application as an amperometric sensor for bromate detection.* Electroanalysis 16 (2004) 1984-1991.
[234] A. Salimi, *et al.*, *Renewable surface sol-gel derived carbon ceramic electrode modified with [Ru(NH3)(5)Cl] (PF6)(2) complex : Application to amperometric detection of chlorate.* Electroanalysis 17 (2005) 2273-2280.
[235] H. Razmi, H. Heidari, *Nafion/lead nitroprusside nanoparticles modified carbon ceramic electrode as a novel amperometric sensor for L-cysteine.* Analytical Biochemistry 388 (2009) 15-22.
[236] A. Salimi, *et al.*, *Electrocatalytic properties of [Ru(bpy)(tpy)Cl]PF6 at carbon ceramic electrode modified with nafion sol-gel composite: application to amperometric detection Of L-Cysteine.* Analytica Chimica Acta 534 (2005) 335-342.
[237] A. Salimi, M. Roushani, *Electrocatalytic oxidation of sulfur containing amino acids at renewable Ni-powder doped carbon ceramic electrode: Application to amperometric detection L-cystine, L-cysteine and L-methionine.* Electroanalysis 18 (2006) 2129-2136.
[238] J. Gun, O. Lev, *Sol-gel derived, ferrocenyl-modified silicate-graphite composite electrode: Wiring of glucose oxidase.* Analytica Chimica Acta 336 (1996) 95-106.
[239] S. Sampath, O. Lev, *Membrane-free, rhodium-modified, methyl silicate-graphite amperometric biosensor.* Journal of Electroanalytical Chemistry 426 (1997) 131-137.
[240] J. Li, *et al.*, *Renewable silica sol-gel derived carbon composite based glucose biosensor.* Journal of Electroanalytical Chemistry 460 (1999) 234-241.

[241] A. Salimi, M. Roushani, *Non-enzymatic glucose detection free of ascorbic acid interference using nickel powder and nafion sol-gel dispersed renewable carbon ceramic electrode.* Electrochemistry Communications 7 (2005) 879-887.
[242] A. Salimi, S. Pourbeyram, *Renewable sol-gel carbon ceramic electrodes modified with a Ru-complex for the amperometric detection of L-cysteine and glutathione.* Talanta 60 (2003) 205-214.
[243] H.R. Zare, *et al., Electrochemical behavior of an indenedione derivative electrodeposited on a renewable sol-gel derived carbon ceramic electrode modified with multi-wall carbon nanotubes: Application for electrocatalytic determination of hydrazine.* Electrochimica Acta 54 (2009) 2828-2836.
[244] Q.F. Sheng, *et al., Hydrogen peroxide determination by carbon ceramic electrodes modified with pyrocatechol violet.* Electrochimica Acta 52 (2007) 7300-7306.
[245] H. Razmi, *et al., Self-Assembled Prussian Blue Nanoparticles Based Electrochemical Sensor for High Sensitive Determination of H2O2 in Acidic Media.* Electroanalysis 21 (2009) 2355-2362.
[246] A. Salimi, *et al., Sol-gel derived carbon ceramic composite electrode containing a ruthenium complex for amperometric detection of insulin at physiological pH.* Journal of Electroanalytical Chemistry 542 (2003) 39-49.
[247] Z.H. Yang, *et al., Sol-gel-derived carbon ceramic electrode containing 9,10-phenanthrenequinone, and its electrocatalytic activity toward iodate.* Fresenius Journal of Analytical Chemistry 371 (2001) 337-341.
[248] S. Sampath, O. Lev, *Electrochemical oxidation of NADH on sol-gel derived, surface renewable, non-modified and mediator modified composite-carbon electrodes.* Journal of Electroanalytical Chemistry 446 (1998) 57-65.
[249] J. Wang, *et al., Low-potential stable detection of beta-NADH at sol-gel derived carbon composite electrodes.* Analytica Chimica Acta 360 (1998) 171-178.
[250] A. Salimi, *et al., Modification of carbon ceramic electrode prepared with sol-gel technique by a thin film of chlorogenic acid: application to amperometric detection of NADH.* Talanta 65 (2005) 888-894.
[251] H. Razmi, *et al., pH-sensing properties of PbO2 thin film electrodeposited on carbon ceramic electrode.* Journal of Solid State Electrochemistry 12 (2008) 1579-1587.
[252] M. Elkaoutit, *et al., Dual laccase-tyrosinase based sonogel-carbon biosensor for monitoring polyphenols in beers.* Journal of Agricultural and Food Chemistry 55 (2007) 8011-8018.
[253] M. El Kaoutit, *et al., The Sonogel-Carbon materials as basis for development of enzyme biosensors for phenols and polyphenols monitoring: A detailed comparative study of three immobilization matrixes.* Biosensors & Bioelectronics 22 (2007) 2958-2966.
[254] B. Haghighi, *et al., Carbon ceramic electrodes modified with laccase from Trametes hirsuta: Fabrication, characterization and their use for phenolic compounds detection.* Electroanalysis 19 (2007) 907-917.
[255] M. ElKaoutit, *et al., Structural characteristics and cyclic voltammetric behaviour of Sonogel-Carbon tyrosinase biosensors. A detailed comparative study of three immobilization matrixes.* Journal of Sol-Gel Science and Technology 45 (2008) 157-163.
[256] M. ElKaoutit, *et al., A comparison of three amperometric phenoloxidase-Sonogel-Carbon based biosensors for determination of polyphenols in beers.* Food Chemistry 110 (2008) 1019-1024.
[257] H. Zejli, *et al., Phenol biosensor based on Sonogel-Carbon transducer with tyrosinase alumina sol-gel immobilization.* Analytica Chimica Acta 612 (2008) 198-203.

[258] H. Razmi, R. Mohammad-Rezaei, *Flow injection amperometric determination of pyridoxine at a Prussian blue nanoparticle-modified carbon ceramic electrode.* Electrochimica Acta 55 (2010) 1814-1819.
[259] M.R. Majidi, *et al.*, *Preparation and electrochemical study of modified carbon ceramic electrode with 5-(4-dimethyl amino benzelyden)-rhodanin for the determination of silver.* Electroanalysis 19 (2007) 364-369.
[260] T. Rohani, M.A. Taher, *Preparation of a carbon ceramic electrode modified by 4-(2-pyridylazo)-resorcinol for determination of trace amounts of silver.* Talanta 80 (2010) 1827-1831.
[261] A. Salimi, *et al.*, *Micromolar determination of sulfur oxoanions and sulfide at a renewable sol-gel carbon ceramic electrode modified with nickel powder.* Electrochimica Acta 51 (2006) 1952-1959.
[262] M. Tsionsky, O. Lev, *Electrochemical Composite Carbon-Ceramic Gas Sensors - Introduction and Oxygen Sensing.* Analytical Chemistry 67 (1995) 2409-2414.
[263] M. Tsionsky, O. Lev, *Investigation of the Kinetics and Mechanism of Co-Porphyrin Catalyzed Oxygen Reduction by Hydrophobic Carbon-Ceramic Electrodes.* Journal of the Electrochemical Society 142 (1995) 2132-2138.
[264] J. Gun, *et al.*, *Electrochemical Characterization and Morphological-Studies of Palladium-Modified Carbon Ceramic Electrodes.* Journal of Electroanalytical Chemistry 395 (1995) 57-66.
[265] L. Rabinovich, *et al.*, *Electrochemical characterisation of Pd modified ceramic vertical bar carbon electrodes: partially flooded versus wetted channel hydrophobic gas electrodes.* Journal of Electroanalytical Chemistry 466 (1999) 45-59.
[266] H. Razmi, E. Habibi, *Electrocatalytic oxidation of methanol on carbon ceramic electrode modified by platinum nanoparticles incorporated in poly (o-phenylenediamine) film.* Journal of Solid State Electrochemistry 13 (2009) 1897-1904.
[267] H. Razmi, *et al.*, *Electrocatalytic oxidation of methanol and ethanol at carbon ceramic electrode modified with platinum nanoparticles.* Electrochimica Acta 53 (2008) 8178-8185.
[268] S. Ranganathan, E.B. Easton, *High performance ceramic carbon electrode-based anodes for use in the Cu-Cl thermochemical cycle for hydrogen production.* International Journal of Hydrogen Energy 35 (2010) 1001-1007.
[269] C.J. Chen, *Introduction to scanning tunneling microscopy*. 2nd ed. Monographs on the physics and chemistry of materials. 2008, Oxford ; New York: Oxford University Press.
[270] J. Kim, K.B. Song, *Recent progress of nano-technology with NSOM.* Micron 38 (2007) 409-426.
[271] M.V. Mirkin, B.R. Horrocks, *Electroanalytical measurements using the scanning electrochemical microscope.* Analytica Chimica Acta 406 (2000) 119-146.
[272] A.L. Barker, *et al.*, *Scanning electrochemical microscopy: beyond the solid/liquid interface.* Analytica Chimica Acta 385 (1999) 223-240.
[273] X. Lu, *et al.*, *Review: Recent applications of scanning electrochemical microscopy to the study of charge transfer kinetics.* Analytica Chimica Acta 601 (2007) 10-25.
[274] G. Wittstock, *et al.*, *Scanning Electrochemical Microscopy for Direct Imaging of Reaction Rates.* Angewandte Chemie, International Edition 46 (2007) 1584-1617.
[275] W.S. Roberts, *et al.*, *Advances in the application of scanning electrochemical microscopy to bioanalytical systems.* Biosensors & Bioelectronics 23 (2007) 301-318.
[276] R.C. Engstrom, *et al.*, *Measurements within Diffusion Layer Using a Microelectrode Probe.* Analytical Chemistry 58 (1986) 844-848.
[277] H.-Y. Liu, *et al.*, *Scanning Electrochemical and Tunneling Ultramicroelectrode Microscope for High-Resolution Examination of Electrode Surfaces in Solution.* Journal of the American Chemical Society 108 (1986) 3838-3839.

[278] A.J. Bard, *et al., Scanning Electrochemical Microscopy. Introduction and Principles.* Analytical Chemistry 61 (1989) 132-138.
[279] J. Kwak, A.J. Bard, *Scanning Electrochemical Microscopy - Theory of the Feedback Mode.* Analytical Chemistry 61 (1989) 1221-1227.
[280] S.E. Pust, *et al., Investigation of Localized Catalytic and Electrocatalytic Processes and Corrosion Reactions with Scanning Electrochemical Microscopy (SECM).* Zeitschrift Fur Physikalische Chemie-International Journal of Research in Physical Chemistry & Chemical Physics 222 (2008) 1463-1517.
[281] B. Csoka, Z. Mekhalif, *Carbon paste-based ion-selective dual function microelectrodes for SECM measurements.* Electrochimica Acta 54 (2009) 3225-3232.
[282] B.R. Horrocks, *et al., Scanning electrochemical microscopy. 19. Ion-celective potentiometric microscopy.* Analytical Chemistry 65 (1993) 1213-1224.
[283] G. Gyetvai, *et al., Solid contact micropipette ion selective electrode for potentiometric SECM.* Electroanalysis 19 (2007) 1116-1122.
[284] S. Amemiya, A.J. Bard, *Scanning electrochemical microscopy. 40. Voltammetric ion-selective micropipet electrodes for probing ion transfer at bilayer lipid membranes.* Analytical Chemistry 72 (2000) 4940-4948.
[285] D.J. Comstock, *et al., Integrated Ultramicroelectrode-Nanopipet Probe for Concurrent Scanning Electrochemical Microscopy and Scanning Ion Conductance Microscopy.* Analytical Chemistry 82 (2010) 1270-1276.
[286] E. El-Giar, D.O. Wipf, *Microparticle-based iridium oxide ultramicroelectrodes for pH sensing and imaging.* Journal of Electroanalytical Chemistry 609 (2007) 147-154.
[287] F.M. Boldt, *et al., Real-time pH microscopy down to the molecular level by combined scanning electrochemical microscopy/single-molecule fluorescence spectroscopy.* Analytical Chemistry 76 (2004) 3473-3481.
[288] K. Stulik, *et al., Microelectrodes. Definitions, characterization, and applications (Technical Report).* Pure and Applied Chemistry 72 (2000) 1483-1492.
[289] M.V. Mirkin, *et al., Scanning Electrochemical Microscopy .13. Evaluation of the Tip Shapes of Nanometer Size Microelectrodes.* Journal of Electroanalytical Chemistry 328 (1992) 47-62.
[290] C.G. Zoski, M.V. Mirkin, *Steady-state limiting currents at finite conical microelectrodes.* Analytical Chemistry 74 (2002) 1986-1992.
[291] J.L. Amphlett, G. Denuault, *Scanning electrochemical microscopy (SECM): An investigation of the effects of tip geometry on amperometric tip response.* Journal of Physical Chemistry B 102 (1998) 9946-9951.
[292] R. Cornut, C. Lefrou, *New analytical approximation of feedback approach curves with a microdisk SECM tip and irreversible kinetic reaction at the substrate.* Journal of Electroanalytical Chemistry 621 (2008) 178-184.
[293] C. Zhao, G. Wittstock, *Scanning electrochemical microscopy for detection of biosensor and biochip surfaces with immobilized pyrroloquinoline quinone (PQQ)-dependent glucose dehydrogenase as enzyme label.* Biosensors & Bioelectronics 20 (2005) 1277-1284.
[294] E.M. Oliveira, *et al., SECM characterization of immobilised enzymes by self-assembled monolayers on titanium dioxide surfaces.* Bioelectrochemistry 71 (2007) 186-191.
[295] Y.H. Yin, *et al., In situ characterization of localized corrosion of stainless steel by scanning electrochemical microscope.* Applied Surface Science 255 (2009) 9193-9199.
[296] C. Gabrielli, *et al., A SECM assisted EQCM study of iron pitting.* Electrochimica Acta 52 (2007) 7706-7714.

[297] E.R. Scott, *et al.*, *Iontophoretic Transport through Porous Membranes Using Scanning Electrochemical Microscopy - Application to Invitro Studies of Ion Fluxes through Skin.* Analytical Chemistry 65 (1993) 1537-1545.
[298] F. Li, *et al.*, *Detection of hydrogen peroxide produced at a liquid/liquid interface using scanning electrochemical microscopy.* Electrochemistry Communications 11 (2009) 473-476.
[299] S.X. Guo, *et al.*, *Microelectrochemical techniques for probing kinetics at liquid/liquid interfaces.* Progress in Reaction Kinetics and Mechanism 29 (2004) 43-166.
[300] P. Liljeroth, *et al.*, *Disk-generation/ring-collection scanning electrochemical microscopy: Theory and application.* Analytical Chemistry 74 (2002) 1972-1978.
[301] J.L. Fernandez, *et al.*, *Analytical methods: Optimization of "wired" enzyme O2-electroreduction catalyst compositions by scanning electrochemical microscopy.* Angewandte Chemie, International Edition 43 (2004) 6355-6357.
[302] Y. Saito, *A Theoretical Study on the Diffusion Current at the Stationary Electrodes of Circular and Narrow Band Types.* Review of Polarography 15 (1968) 177-187.
[303] K. Eckhard, *et al.*, *Redox competition mode of scanning electrochemical microscopy (RC-SECM) for visualisation of local catalytic activity.* Physical Chemistry Chemical Physics 8 (2006) 5359-5365.
[304] K. Karnicka, *et al.*, *Visualisation of the local bio-electrocatalytic activity in biofuel cell cathodes by means of redox competition scanning electrochemical microscopy (RC-SECM).* Electrochemistry Communications 9 (2007) 1998-2002.
[305] P.C. Chen, *et al.*, *Localized Deposition of Chitosan as Matrix for Enzyme Immobilization.* Electroanalysis 21 (2009) 804-810.
[306] O.E. Husser, *et al.*, *Scanning Electrochemical Microscopy - High-Resolution Deposition and Etching of Metals.* Journal of the Electrochemical Society 136 (1989) 3222-3229.
[307] H. Yamada, *et al.*, *Scanning electrochemical microscope observation of defects in a hexadecanethiol monolayer on gold with shear force-based tip-substrate positioning.* Langmuir 22 (2006) 7923-7927.
[308] M. Ludwig, *et al.*, *Topography Feedback Mechanism for the Scanning Electrochemical Microscope Based on Hydrodynamic-Forces between Tip and Sample.* Review of Scientific Instruments 66 (1995) 2857-2860.
[309] B.B. Katemann, *et al.*, *Constant-distance mode scanning electrochemical microscopy (SECM) - Part I: Adaptation of a non-optical shear-force-based positioning mode for SECM tips.* Chemistry-a European Journal 9 (2003) 2025-2033.
[310] G. Wittstock, W. Schuhmann, *Formation and Imaging of Microscopic Enzymatically Active Spots on an Alkanethiolate-Covered Gold Electrode by Scanning Electrochemical Microscopy.* Analytical Chemistry 69 (1997) 5059-5066.
[311] http://www.olympusmicro.com/primer/techniques/confocal/confocalintro.html
[312] Z. Kęcki, *Podstawy spektroskopii molekularnej*. 1972, Warszawa: PWN.
[313] http://en.wikipedia.org/wiki/Scanning_electron_microscope
[314] http://www.wittstock.chemie.uni-oldenburg.de/en/research/methods/afm.html
[315] A. Leonowicz, K. Grzywnowicz, Enzyme and Microbial Technology 3 (1981) 55.
[316] J. Rogalski, *et al.*, *Immobilization of laccase from Cerrena unicolor on controlled porosity glass.* Journal of Molecular Catalysis B-Enzymatic 6 (1999) 29-39.
[317] W. Nogala, *et al.*, *Feedback mode SECM study of laccase and bilirubin oxidase immobilised in a sol–gel processed silicate film.* Analyst 135 (2010) 2051-2058.
[318] C. Nunes Kirchner, *et al.*, *Evaluation of Thin Titanium Nitride Electrodes for Electroanalytical Applications.* Electroanalysis 19 (2007) 1023-1031.
[319] G. Wittstock, *et al.*, *Investigation of ion-bombarded conducting polymer films by scanning electrochemical microscopy (SECM).* Fresenius Journal of Analytical Chemistry 367 (2000) 346-351.

[320] L.M. Ellerby, *et al.*, *Encapsulation of Proteins in Transparent Porous Silicate-Glasses Prepared by the Sol-Gel Method.* Science 255 (1992) 1113-1115.
[321] C. Kranz, *et al.*, *Lateral Deposition of Polypyrrole Lines over Insulating Gaps. Towards the Developlment of Polymer-Based Electronic Devices.* Advanced Materials 7 (1995) 568-571.
[322] W.E. Farneth, *et al.*, *Current densities from electrocatalytic oxygen reduction in laccase/ABTS solutions.* Journal of Electroanalytical Chemistry 581 (2005) 190-196.
[323] W.E. Farneth, M.B. D'Amore, *Encapsulated laccase electrodes for fuel cell cathodes.* Journal of Electroanalytical Chemistry 581 (2005) 197-205.
[324] B. Gründig, *et al.*, *Mediator-modified electrodes for electrocatalytic oxidation of NADH.* Journal of Electroanalytical Chemistry 395 (1995) 143-157.
[325] J.F. Fei, *et al.*, *Two polymerizable derivatives of 2,2 '-azino-bis(3-ethylbenzthiazoline-6-sulfonic acid).* Organic Letters 8 (2006) 3-6.
[326] R.S. Nicholson, I. Shain, *Theory of Stationary Electrode Polarography - Single Scan + Cyclic Methods Applied to Reversible Irreversible + Kinetic Systems.* Analytical Chemistry 36 (1964) 706-&.
[327] C. Fernandez-Sanchez, *et al.*, *Voltammetric monitoring of laccase-catalysed mediated reactions.* Bioelectrochemistry 58 (2002) 149-156.
[328] S.D. Maleknia, *et al.*, *Photochemical and electrophysical production of radicals on millisecond timescales to probe the structure, dynamics and interactions of proteins.* Photochemical & Photobiological Sciences 3 (2004) 741-748.
[329] M.R. Tarasevich, *et al.*, *Fractal and percolation properties of active layer structure at oxygen electrode based on nanocomposite material of dispersed carbon carrier/laccase.* Electrochimica Acta 51 (2005) 418-426.
[330] W. Zheng, *et al.*, *Direct electrochemistry of multi-copper oxidases at carbon nanotubes noncovalently functionalized with cellulose derivatives.* Electroanalysis 18 (2006) 587-594.
[331] S. Scott, *et al.*, *Spectroscopic Parameters, Electrode Potentials, Acid Ionization Constants, and Electron Exchange Rates of the 2,2~-Azinobis(3-ethylbenzothiazolineine-6-sulfonateR)a dicals and Ions.* Journal of Physical Chemistry 97 (1993) 6710-6714.
[332] G. Shul, *et al.*, *Scanning electrochemical microscopy study of ion transfer process across water/2-nitrophenyloctylether interface supported by hydrophobic carbon ceramic electrode.* Journal of Solid State Electrochemistry 12 (2008) 1285-1291.
[333] C. Nunes Kirchner, *et al.*, *Scanning Electrochemical Microscopy (SECM) Based Detection of Oligonucleotide Hybridization and Simultaneous Determination of the Surface Concentration of Immobilized Oligonucleotides on Gold.* Electroanalysis (New York) 19 (2007) 1258-1267.
[334] G. Janusz, *Comparative studies of fungal laccases*, in *Department of Biochemistry*. 2005, Maria Curie-Sklodowska University: Lublin.
[335] M.M. Bradford, *A rapid and sensitive method for the quantitation of microgram quantities of protein utilizing the principle of protein-dye binding.* Analytical Biochemistry 72 (1976) 248-254.
[336] F. Vianello, *et al.*, *A high sensitivity amperometric biosensor using a monomolecular layer of laccase as biorecognition element.* Biosensors & Bioelectronics 20 (2004) 315-321.
[337] Y. Suenaga, C.G. Pierpont, *Binuclear complexes of Co(III) containing extended conjugated bis(catecholate) ligands.* Inorganic Chemistry 44 (2005) 6183-6191.
[338] G. Shul, *et al.*, *Characterisation of biphasic electrodes based on the liquid N,N-didodecyl-N',N'-diethylphenylenediamine redox system immobilised on porous hydrophobic silicates and immersed in aqueous media.* Journal of Electroanalytical Chemistry 582 (2005) 202-208.

[339] M.M.A. Aly, *Infrared and Raman spectra of some symmetric azines.* Spectrochimica Acta Part a-Molecular and Biomolecular Spectroscopy 55 (1999) 1711-1714.
[340] R. Bauer, C.O. Rupe, *Use of Synringaldazine in a Photometric Method for Estimating Free Chlorine in Water.* Analytical Chemistry 43 (1971) 421-&.
[341] R. Bourbonnais, *et al.*, *Electrochemical analysis of the interactions of laccase mediators with lignin model compounds.* Biochimica Et Biophysica Acta-General Subjects 1379 (1998) 381-390.
[342] D.K. Cope, *The edge effect for planar electrodes.* Journal of Electroanalytical Chemistry 439 (1997) 7-27.
[343] C. Bourdillon, *et al.*, *New insights into the enzymic catalysis of the oxidation of glucose by native and recombinant glucose oxidase mediated by electrochemically generated one-electron redox cosubstrates.* Journal of the American Chemical Society 115 (1993) 2-10.
[344] D.T. Pierce, *et al.*, *Scanning Electrochemical Microscopy. 17. Studies of Enzyme - Mediator Kinetics for Membrane- and Surface- Immobilized Glucose Oxidase.* Analytical Chemistry 64 (1992) 1795-1804.
[345] R.D. Deegan, *et al.*, *Capillary flow as the cause of ring stains from dried liquid drops.* Nature 389 (1997) 827-829.
[346] H. Hu, R.G. Larson, *Marangoni effect reverses coffee-ring depositions.* Journal of Physical Chemistry B 110 (2006) 7090-7094.
[347] A. Michniewicz, *et al.*, *The white-rot fungus Cerrena unicolor strain 137 produces two laccase isoforms with different physico-chemical and catalytic properties.* Applied Microbiology and Biotechnology 69 (2006) 682-688.
[348] T. Nakagawa, *et al.*, *Bilirubin oxidase and [Fe(CN)(6)](3-/4-) modified electrode allowing diffusion-controlled reduction of O-2 to water at pH 7.0.* Chemistry Letters 32 (2003) 54-55.
[349] S. Shleev, *et al.*, *Direct heterogeneous electron transfer reactions of bilirubin oxidase at a spectrographic graphite electrode.* Electrochemistry Communications 6 (2004) 934-939.
[350] X. Li, *et al.*, *A Miniature Glucose/O-2 Biofuel Cell With a High Tolerance Against Ascorbic Acid.* Fuel Cells 9 (2009) 85-91.
[351] A.P. Borole, *et al.*, *Three-dimensional, gas phase fuel cell with a laccase biocathode.* Journal of Power Sources 188 (2009) 421-426.
[352] B.D. Bath, *et al.*, *Imaging molecular transport in porous membranes. Observation and analysis of electroosmotic flow in individual pores using the scanning electrochemical microscope.* Analytical Chemistry 70 (1998) 1047-1058.

18 Published papers

The results presented in this thesis are partially published in following papers:

1. “Immobilization of ABTS - laccase system in silicate based electrode for biooelectrocatalytic reduction of dioxygen”
   W. Nogala, E. Rozniecka, I. Zawisza, J. Rogalski, M. Opallo
   Electrochemistry Communications 8 (2006) 1850-1854
2. “pH-sensitive syringaldazine modified carbon ceramic electrode for bioelectrocatalytic dioxygen reduction”
   W. Nogala, E. Rozniecka, J. Rogalski, M. Opallo
   Journal of Electroanalytical Chemistry 608 (2007) 31-36
3. “Scanning electrochemical microscopy study of laccase within a sol-gel processed silicate film”
   W. Nogala, M. Burchardt, M. Opallo, J. Rogalski, G. Wittstock
   Bioelectrochemistry 72 (2008) 174-182
4. “In situ micro-Raman studies of syringaldazine-entrapped composite electrodes modified with laccase”
   G. Zukowska, W. Nogala, Y. Svartsov, M. Marcinek, J. Rogalski, K. Szot, M. Opallo
   ECS Transactions 25 (2010) 29-44
5. “Scanning electrochemical microscopy activity mapping of electrodes modified with laccase encapsulated in sol–gel processed matrix”
   W. Nogala, K. Szot, M. Burchardt, M. Jönsson-Niedziolka, J. Rogalski, G. Wittstock, M. Opallo
   Bioelectrochemistry 79 (2010) 101-107
6. “Bioelectrocatalytic mediatorless dioxygen reduction at carbon ceramic electrodes modified with bilirubin oxidase”
   W. Nogala, A. Celebanska, K. Szot, G. Wittstock, M. Opallo
   Electrochimica Acta 55 (2010) 5719-5724
7. “Feedback mode SECM study of laccase and bilirubin oxidase immobilised in a sol–gel processed silicate film”
   W. Nogala, K. Szot, M. Burchardt, F. Roelfs, J. Rogalski, M. Opallo, G. Wittstock
   Analyst 135 (2010) 2051-2058
8. “Bioelectrocatalytic carbon ceramic gas electrode for reduction of dioxygen and its application in a zinc-dioxygen cell”
   W. Nogala, A. Celebanska, G. Wittstock, M. Opallo
   Fuel Cells (2010) accepted

Other papers with my co-authorship:

1. "SnO_2–poly(diallyldimethylammonium chloride) films: Electrochemical evidence for heme protein absorption, denaturation, and demetallation"
   E. Milsom, H. Dash, T. Jenkins, C. Halliwell, A. Thetford, N. Bligh, W. Nogala, M. Opallo, F. Marken
   Journal of Electroanalytical Chemistry 610 (2007) 28-36
2. "Scanning electrochemical microscopy study of ion transfer process across water/2-nitrophenyloctylether interface supported by hydrophobic carbon ceramic electrode"
   G. Shul, W. Nogala, I. Zakrochemna, J. Niedziolka, M. Opallo
   Journal of Solid State Electrochemistry 12 (2008) 1285
3. "Hydrophilic carbon nanoparticle-laccase thin film electrode for mediatorless dioxygen reduction. SECM activity mapping and appliocation in zinc-dioxygen battery"
   K. Szot, W. Nogala, J. Niedziolka-Jönsson, M. Jönsson-Niedziolka, F. Marken, J. Rogalski, C. Nunes Kirchner, G. Wittstock, M. Opallo
   Electrochimica Acta 54 (2009) 4620-4625